

Inaugural dissertation
for
obtaining the doctoral degree
of the
Combined Faculty of Mathematics, Engineering and Natural Sciences
of the
Ruprecht - Karls - University
Heidelberg

presented by
M.Sc. Alex Cornean
born in: Reșița, Romania
Oral examination: 29.07.2022

The role of the medaka protein O-mannosyltransferase 2 across tissues, development and dystroglycanopathies

Referees: Prof. Dr. Joachim Wittbrodt
Jun.-Prof. Dr. Steffen Lemke

*"When we are no longer able to change a situation,
we are challenged to change ourselves."*
-Viktor E. Frankl (Man's Search for Meaning)

für meine Oma

Abstract

Protein *O*-mannosylation is a conserved modification of proteins with the sugar mannose. Defective *O*-mannosylation of the peripheral membrane protein α -dystroglycan (α -DG) results in a spectrum of congenital diseases called dystroglycanopathies (DGpathies). DGpathies manifest a broad range of symptoms from serious, prenatal changes in the morphology of the brain to adult-onset muscular dystrophy. Consequently, mutations in the genes encoding the protein *O*-mannosyltransferases 1 and 2 (POMT1/2), which catalyse the first steps of *O*-mannosylation, cause the most severe forms of DGpathies. Why different organs are distinctly affected in patients with varying grades of DGpathies is not clear. Moreover, the precise contribution of the known substrates of the POMT1-POMT2 complex, α -DG, SUCO and KIAA1549, to the pathology in DGpathies remains ill-defined. Therefore, the aim of this thesis was to resolve the organismal role of the POMT1-POMT2 complex in DGpathies and to disentangle the contributions of its substrates.

To address these questions, I created a framework for highly efficient base editing to mutate virtually any cytosine or adenine in the teleost fish genome. Using CRISPR/Cas9 and base editors, I established *pomt2* DGpathy models in medaka (*Oryzias latipes*) and characterised these using behavioural, biochemical, histological and transcriptomic analyses. I could show that organs such as the eye and the brain are only affected when POMT-complex function was substantially disrupted. By contrast, the muscles and spine are much more prone to minute changes in the enzymatic properties of the POMTs. Next, I disrupted the POMT-substrates individually using a CRISPR/Cas9 approach. I identified a previously unknown cardiovascular function of α -DG and SUCO, and revealed that SUCO plays an important role in notochord development. Finally, I employed base editing to mutate *O*-mannosylation glycosites on α -DG (T330) and SUCO (S806 and T811), which partially recapitulated respective loss-of-function phenotypes. With this first-ever evidence for the study of glycosites using base editing *in vivo*, I demonstrate the feasibility of this new approach to provide functional insights in a developing organism.

Future studies linking structure-function relationships on the substrate level to tissue-wide developmental consequences in model systems will be instrumental to enable tailored, preclinical drug screens and to provide reliable predictions of disease progressions in DGpathies.

Zusammenfassung

Die *O*-Mannosylierung von Proteinen ist eine konservierte Modifikation von Proteinen mit dem Zucker Mannose. Eine fehlerhafte *O*-Mannosylierung des peripheren Membranproteins α -Dystroglykan (α -DG) führt zu einem Spektrum von angeborenen Krankheiten, die als Dystroglykanopathien (DGpathien) bezeichnet werden. DGpathien weisen eine Vielzahl unterschiedlicher Symptome auf, die von schwerwiegenden pränatalen Veränderungen der Gehirnmorphologie bis hin zur Muskeldystrophie im Erwachsenenalter reichen. Die schwersten Formen von DGpathien werden folglich von Mutationen in Genen, die für die Protein *O*-Mannosyltransferasen 1 und 2 (POMT1/2) kodieren, verursacht, da diese die ersten Schritte der *O*-Mannosylierung katalysieren. Warum verschiedene Organe bei Patienten mit unterschiedlichen Schweregraden von DGpathien unterschiedlich stark betroffen sind, ist noch nicht eindeutig erforscht. Darüber hinaus ist der genaue Beitrag der bekannten Substrate des POMT1-POMT2-Komplexes, α -DG, SUCO und KIAA1549, zum Krankheitsbild von DGpathien nach wie vor nicht klar definiert. Ziel dieser Arbeit war es daher, die organismische Rolle des POMT1-POMT2-Komplexes bei DGpathien zu klären und die Funktionen seiner Substrate zu entschlüsseln.

Um diese Fragen zu beantworten, habe ich eine Methode für hocheffizientes Base Editing etabliert, mit dem im Grunde jedes Cytosin oder Adenin im Genom von Teleostfischen mutiert werden kann. Mithilfe von CRISPR/Cas9 und Base Editoren habe ich *pomt2* DGpathie-Modelle in Medaka (*Oryzias latipes*) etabliert und diese anhand von biochemischen, histologischen, transkriptomischen und Verhaltensanalysen charakterisiert. Ich konnte zeigen, dass Organe wie das Auge und das Gehirn nur dann betroffen sind, wenn die Funktion des POMT-Komplexes erheblich gestört ist. Im Gegensatz dazu sind Muskeln und Wirbelsäule viel anfälliger für geringe Veränderungen der enzymatischen Eigenschaften der POMTs. Anschließend habe ich einzelne Substrate des POMT-Komplexes mithilfe von CRISPR/Cas9 verändert. Dadurch konnte ich eine bislang unbekannte kardiovaskuläre Funktion von α -DG und SUCO identifizieren und zeigen, dass SUCO eine wichtige Rolle in der Entwicklung des Notochords spielt. Schließlich habe ich durch Base Editing *O*-Mannosylierungsstellen in α -DG (T330) und SUCO (S806 und T811) mutiert, was wiederum zu einem partiellen Funktionsverlust führte. Mit dieser erstmaligen Untersuchung von Glykosylierungsstellen durch Base Editing in vivo konnte ich den Nutzen dieses Ansatzes zur Gewinnung funktioneller Erkenntnisse in einem sich entwickelnden Organismus demonstrieren.

Zukünftige Studien, die Struktur-Funktions-Beziehungen auf Substratebene

mit gewebeübergreifenden Entwicklungskonsequenzen in Modellsystemen verknüpfen, werden entscheidend sein, um maßgeschneiderte präklinische Wirkstoffscreens zu ermöglichen und so zuverlässige Vorhersagen über den Krankheitsverlauf bei DGpathien zu liefern.

Contents

Abstract	I
Zusammenfassung	III
Abbreviations	VII
Contributions	XI
1 Introduction	1
1.1 Protein glycosylation	1
1.2 Protein <i>O</i> -mannosylation	3
1.3 Classical <i>O</i> -mannosylated proteins	5
1.4 α -dystroglycan and the dystrophin-glycoprotein complex	6
1.5 The spectrum of DGpathies	8
1.6 Open questions in DGpathies	10
1.7 Vertebrate model systems to study dystroglycanopathy (DGpathy)	11
1.8 Genome editing tools	13
Aims and Approaches	19
2 Results	21
2.1 Precise <i>in vivo</i> functional analysis of protein variants by base editing in medaka	21
2.2 Studying the spectrum of DGpathies with medaka <i>pomt2</i> disease models	35
2.3 Investigating the function of POMT-substrate <i>O</i> -mannosylation sites <i>in vivo</i> by an expanded base editor repertoire	73
3 Discussion	105
3.1 Efficient F0 cytosine and adenine base editing	107
3.2 The effect of differential POMT1-POMT2 (POMT) activity on different organs in DGpathy models	111
3.3 The individual contribution of substrates of the POMT-complex to the spectrum of DGpathies	116

3.4	Delineating the function of individual protein <i>O</i> -mannosylation (<i>O</i> -man) glycosites	119
3.5	Perspective	123
4	Conclusions	127
5	Materials & Methods	129
5.1	Materials	129
5.2	Methods	164
6	References	197
	Publications	225
	Acknowledgments	227
	Declaration	231
	List of Figures	233
	List of Tables	237

Abbreviations

3x pA	three times poly adenylation sequence
ACEofBASEs	a careful evaluation of base edits
A	adenine
ABE	adenine base editor
α-DG	α -dystroglycan
Amplicon-seq	Amplicon deep-sequencing
atoh7	atonal BHLH transcription factor 7
<i>B2M</i>	<i>β2-Microglobulin</i>
bp	base pairs
β-DG	β -dystroglycan
C	cytosine
CBE	cytosine base editor
Cas	CRISPR-associated protein
CDG	congenital disorders of glycosylation
cDNA	complementary DNA
CDS	coding sequence
CMD	Congenital Muscular Dystrophy
CNS	central nervous system
CRISPR	clustered regularly interspaced short palindromic repeat
crRNA	Cas9-CRISPR RNA
CSF	cerebrospinal fluid
DGC	dystrophin-glycoprotein complex
DGpathy	dystroglycanopathy
DGpathies	dystroglycanopathies
DMSO	dimethyl sulfoxide
DNA	deoxyribonucleic acid
dNTP	deoxynucleoside triphosphate
dpf	days post fertilisation
dph	days post hatching
DSB	DNA double-strand break
<i>dag1</i>	<i>dystroglycan</i>

DAG1	<i>dystroglycan</i>
ECM	extracellular matrix
ER	endoplasmatic reticulum
<i>E. coli</i>	<i>Escherichia coli</i>
EGFP	enhanced green fluorescent protein
ERM	embryo rearing medium
Fiji	Fiji is just ImageJ
FL	flexible linker
G	guanine
<i>g</i>	gravitational force equivalent
<i>GAPDH</i>	<i>Glyceraldehyde 3-phosphate dehydrogenase</i>
GCL	ganglion cell layer
gDNA	genomic DNA
gRNA	RfxCas13d guide RNA
GFP	green fluorescent protein
GlcA	glucuronic acid
GPI	glycosylphosphatidylinositol
H2A-mCherry	mCherry coupled to histone2a
HDR	homology-directed repair
HF	homology flank
hpf	hours post fertilisation
indel	insertion or deletion events
INL	inner nuclear layer
IR	infrared
KO	knockout
LGMD	Limb-Girdle Muscular Dystrophy
Man	mannose
MDDG	muscular dystrophy-dystroglycanopathy
LGMD	Limb-Girdle Muscular Dystrophy
mCherry	monomeric cherry fluorescent protein
min	minute(s)
mRNA	messenger RNA
MZT	maternal zygotic mutants
N	any DNA nucleobase
n	sample number
NHEJ	non-homologous end joining
NTP	nucleotide triphosphate

<i>oca2</i>	<i>oculocutaneous albinism II</i>
O-man	protein O-mannosylation
ONL	outer nuclear layer
OPL	outer plexiform layer
PAM	protospacer adjacent motif
PC	principal component
PCA	principal component analysis
PCR	polymerase chain reaction
pegRNA	prime editing guide RNA
PIM	PAM-interacting motif
pGGDest	Golden GATEway destination vector
POMT	POMT1-POMT2
POMT1/2	vertebrate protein O-mannosyltransferases 1 and 2
POMT1-POMT2	protein O-mannosyltransferase 1 and 2 complex
PTC	premature termination codon
PTU	phenylthiourea
qRT-PCR	quantitative reverse transcription PCR
RfxCas13d	<i>Ruminococcus flavefaciens</i> strain XPD3002 Cas13d
RNA	ribonucleic acid
RNASeq	RNA sequencing
rNTP	ribonucleoside triphosphate
RPE	retinal pigmented epithelium
rpm	revolutions per minute
RT-PCR	reverse transcription PCR
SD	splice-donor
SDS-PAGE	sodium dodecyl sulfate polyacrylamide gel electrophoresis
sec	second(s)
Ser	serine (S, Ser)
sgRNA	single guide RNA
SUCO	SUN domain ossification factor
T	thymine
Thr	threonine (T, Thr)
tracrRNA	transactivating CRISPR RNA
TUNEL	terminal deoxynucleotidyl transferase dUTP nick end labeling
UTR	untranslated region

WISH	whole mount <i>in situ</i> hybridisation
WWS	Walker-Warburg Syndrome

Contributions

In the following, people that contributed to the experimental data described in this thesis are listed:

Nithyapriya Kumar helped perform the locomotion assays for the Cab control, the *pomt2*^{S56(*ins*)}, the *pomt1*^{Y33(*ins*)}, and *dag1*^{Q410X/T330M} compound heterozygous lines. She helped with the genotyping, stainings and imaging of the *pomt2*^{Cterm-*fs*} mutant line.

Linda Kloß helped with injections for the generation of the *pomt2*^{ΔMIR2} line and helped identify founders for the *pomt2*^{ΔCterm} and *pomt2*^{Cterm-*fs*} lines. She also helped with the initial setting-up and testing of the Noldus machine.

David Ibberson prepared the library prep and performed the sequencing of bulk transcriptome samples.

Daniel Sturm performed the POMT1 / POMT2 Western Blots.

Thomas Thumberger conceived the knockout-by-knockin strategy to generate the *pomt2*^{S56(*ins*)} and the *pomt1*^{Y33(*ins*)} mutant lines.

Beate Wittbrodt and **Rachel Müller** helped with genotyping of adults fish lines.

Nick Marschlich helped with the Cas13d knockdown experiments.

Base editing part (NGG PAM editors) on next page.

Base editing part (NGG PAM editors)

Bettina Welz (B.W.): cloning of pCS2+_evoBE4max and pCS2+_evoBE4max-NG with me; performed injections and screening with me; performed genotyping (Sanger-sequencing) of most samples; Confocal microscopy with me.

Jakob Gierten (J.G.): selected the *tnnt2a* and *kcnh6a* targets for base editing validation and designed the *kcnh6a* sgRNAs. He performed initial injections with the BE4-Gam base editor using the *kcnh6a* sgRNAs with me.

My contribution to this part: designed and analysed all experiments (with contributions from B.W. for EditR analysis); Figure preparation; synthesis of sgRNAs; performed injections and screening with B.W.; Amplicon-Sequencing; Confocal microscopy with B.W.

*"The barrier to enlightenment
is biochemistry, but you can tunnel
through the barrier
by using genetics."*

Sydney Brenner

1

Introduction

Dystroglycanopathies (DGpathies) are a group of neuromuscular disorders with abnormal glycosylation of α -dystroglycan (α -DG) [Kanagawa, 2021]. Patients show a broad clinical spectrum that ranges from severe central nervous system (CNS) defects at birth to adult-onset muscular dystrophy [Godfrey et al., 2011; Kanagawa, 2021]. At least 18 genes are known to be directly linked to the glycosylation of α -DG. Among these are genes encoding the vertebrate protein O-mannosyltransferases 1 and 2 (POMT1/2) which initialise α -DG glycosylation [Beltrán-Valero de Bernabé et al., 2002; van Reeuwijk et al., 2005]. To date, however, there is no way to treat the disorder effectively or even improve any of the symptoms [Kanagawa, 2021]. Understanding the molecular and cellular consequences of defective *pomt1* or *pomt2* will not only help identify entry points for therapies for DGpathies but also reveal the basic functions of these genes.

1.1 Protein glycosylation

The glycosylation of proteins is a co- and posttranslational process by which monosaccharides or glycans are covalently attached to proteins [Freeze et al., 2015; Moremen et al., 2012]. Protein glycosylation is a highly conserved modification that involves roughly 700 enzymes in humans [Brooks, 2009; Moremen et al., 2012]. This also makes protein glycosylation one of the most complex post-translational modifications [Moremen et al., 2012]. Glycans can carry out structural and modulatory functions. They support protein

folding and its quality control, act as recognition structures in various cell-cell or cell-extracellular matrix (ECM) interactions and may play vital roles in bacterial and viral infections [Haltiwanger and Lowe, 2004; Moremen et al., 2012; Varki, 2017; Wopereis et al., 2006].

In vertebrates, the activity of glycosyltransferases can generate a large diversity of glycans on glycoproteins by using one or several monosaccharides to build linear or branched sugar structures. Among these sugars are mannose (Man), N-acetylglucosamine, N-acetylgalactosamine, galactose and xylose. Many glycoenzymes are expressed in a spatiotemporally controlled manner that is cell type and tissue-specific [Moremen et al., 2012; Varki, 2017]. Therefore, only a fraction of the diversity is present in any given cell. This is the "glycome" of the cell. The resulting differences expand biological diversity. The consequences of different glycomes are best conveyed when comparing genetic defects that affect cell-surface or secreted glycoproteins. These defects often leave cultured cells unaltered [Varki and Kornfeld, 2017]. The same mutations, however, often radically alter a multicellular organism and in the most severe cases can result in developmental lethality [Moremen et al., 2012; Varki, 2017].

In the context of a particular glycoprotein, diversity is also prevalent and glycosylated proteins often carry multiple types of glycans. Under different conditions, particular glycosylation sites may harbor different glycan structures, or none at all [Brooks, 2004]. The major groups of protein glycosylation encompass *N*-glycosylation, *O*-glycosylation, *C*-mannosylation and glycosylphosphatidylinositol (GPI)-anchor formation. *N*-glycans are attached to asparagine side chains via an amide bond and represent the most common structures on glycoproteins. The very diverse *O*-linked glycans are added to hydroxyl groups of amino acid side chains and are further subdivided depending on the initiating monosaccharide [Moremen et al., 2012; Schjoldager et al., 2020]. In the next section I will discuss *O*-mannosylation which is essential for the function of α -DG and highly relevant in DGpathies.

1.2 Protein O-mannosylation

Protein *O*-mannosylation (*O*-man) is an essential and highly conserved modification in eukaryotes [Bausewein et al., 2016; Hang et al., 2022]. It was discovered in fungi and yeast where most secreted and cell wall proteins are *O*-mannosylated [Lommel and Strahl, 2009; Sentandreu and Northcote, 1968]. There, the modification is crucial for cell wall rigidity and cell integrity [Gentzsch and Tanner, 1996]. Protein *O*-mannosyltransferases, PMTs in yeast (PMT1-7) or POMTs in vertebrates (POMT1/2), are ER-resident glycosyltransferases that act as heteroduplexes to initiate *O*-man (Fig. 1.1) [Bai et al., 2019; Gentzsch et al., 1995a,b; Girrbach and Strahl, 2003; Haselbeck and Tanner, 1983; Manya et al., 2004].

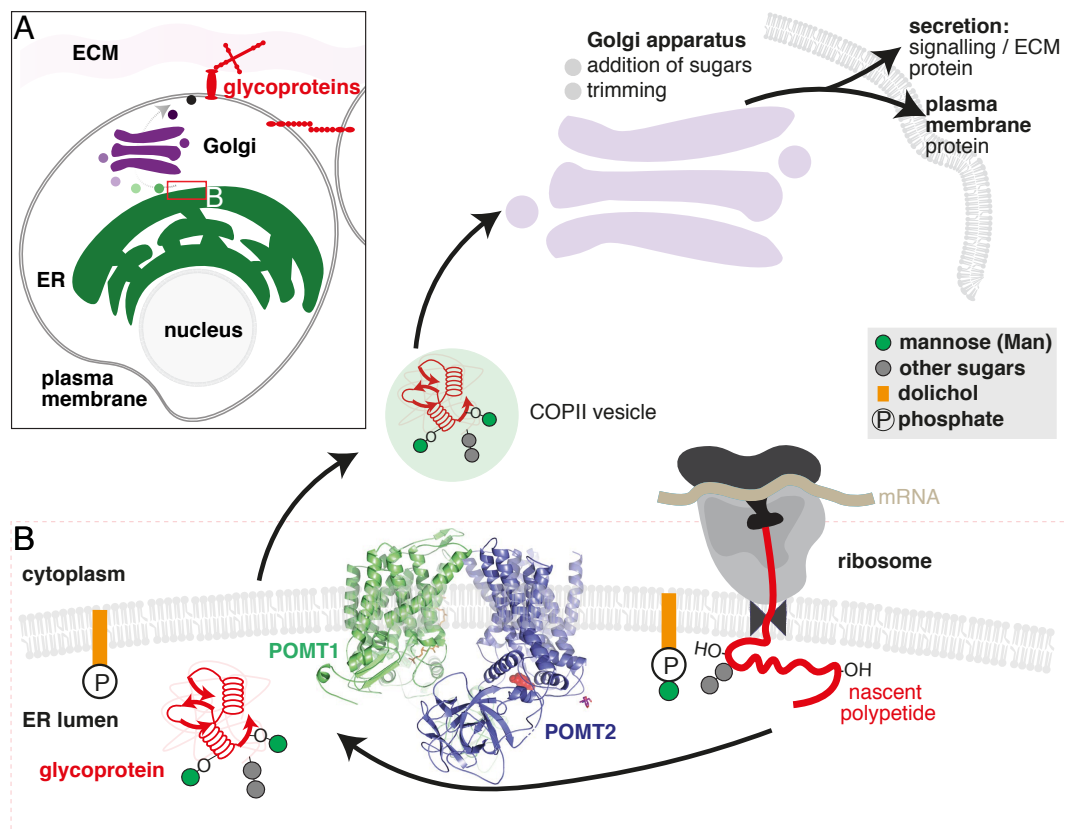


Figure 1.1: Principle of protein *O*-mannosylation by the POMT1-POMT2 complex in vertebrates. (A) Cell surface and secreted glycoproteins need to pass through the secretory pathway and may interact with proteins on other cells or ECM proteins. ER, endoplasmic reticulum; ECM, extracellular matrix. (B) *O*-mannosylation is initiated by a heterodimeric complex of protein *O*-mannosyltransferases 1 and 2 (POMT1/2). The complex covalently links mannose to hydroxyl groups of serine or threonine residues on nascent polypeptides in a co-translational process. Glycoproteins will be shuttled to the Golgi-apparatus, where additional modifications occur. The glycoproteins are either secreted or integrated into the plasma membrane to exert their functions in signalling, cell-cell interaction, cell-adhesion and cell-ECM interaction. Note: the conserved yeast PMT1-PMT2 crystal structure [Bai et al., 2019] was used, with permission, to display the POMT1-POMT2 complex.

Vertebrate POMT1 and POMT2 use dolichol-phosphate mannose as donor substrate to covalently link mannose to hydroxyl groups on the side chains of serine and threonine residues secretory proteins [Akasaka-Manyá et al., 2006; Girrbach and Strahl, 2003; Manyá et al., 2004; Neubert et al., 2016; Willer et al., 2002]. This core mannose (M0) can then be further elongated [Endo, 1999] into linear or branched structures in the ER (core M3) and the Golgi apparatus (core M1, M2 and M3) according to the conformation of the added *N*-acetylglucosamine [Sheikh et al., 2017; Yoshida-Moriguchi et al., 2013]. *O*-man glycoproteins eventually carry out their functions as part of a major communication front in vertebrates, involved in cell-cell recognition, signal transduction and cell migration [Hang et al., 2022].

1.3 Classical *O*-mannosylated proteins

The vertebrate brain contains an abundance of mostly elongated *O*-mannosyl glycans [Chai et al., 1999; Williams et al., 2022]. These glycoproteins are *O*-mannosylated by the protein *O*-mannosyltransferase 1 and 2 complex (POMT1-POMT2) and are often referred to as classical *O*-man glycoproteins [Hang et al., 2022].

Three proteins have been validated as substrates of the POMT1-POMT2. These are the SUN domain ossification factor (SUCO), KIAA1549 and α -DG [Larsen et al., 2017a,b; Vester-Christensen et al., 2013]. SUCO is an ER-resident transmembrane protein and has been shown to be involved in collagen biosynthesis and bone formation [Sohaskey et al., 2010]. KIAA1549 is a plasma membrane-spanning glycoprotein that is heavily *O*-mannosylated that plays a role as a ciliary protein in the retina [De Bruijn et al., 2018]. Due to its direct association with DGpathies, α -DG has been thoroughly characterised. It is the only protein for which not only the glycosites of *O*-mannosyl glycans have been extensively mapped in brain and muscle tissues, but there is also ample evidence for the functions of *O*-mannosyl glycans at specific glycosites [Chiba et al., 1997; Hara et al., 2011; Sasaki et al., 1998; Smalheiser et al., 1998; Stalnaker et al., 2011; Yagi et al., 2013].

1.4 α -dystroglycan and the dystrophin-glycoprotein complex

α -DG is an extracellular, peripheral membrane glycoprotein that is linked to the plasma membrane via β -dystroglycan (β -DG) (Fig. 1.2A). Its mucin-type domain contains at least 19 *O*-man sites in vertebrates with the glycans often constituting more than 50% of its mass [Gomez Toledo et al., 2012; Larsen et al., 2017b; Nilsson et al., 2010; Stalnakker et al., 2010; Vester-Christensen et al., 2013]. α -DG is an essential component of the dystrophin-glycoprotein complex (DGC), linking the cytoskeleton with the ECM by acting as a receptor for many ECM or synaptic proteins [Barresi and Campbell, 2006]. The main α -DG interaction partner is laminin. This interaction is crucial for the maintenance of basement membranes in the CNS, muscles and many other developing and adult tissues [Barresi and Campbell, 2006; Ervasti and Campbell, 1993]. Complex and extended *O*-mannosyl glycans initiated by the POMT1-POMT2 complex play a central role for α -DG-laminin interactions [Kanagawa, 2021; Nickolls and Bönnemann, 2018]. A large polymeric repeat structure, consisting of alternating xylose and glucuronic acid (GlcA), also referred to as matriglycan, functions as the binding site for laminin and other ECM ligands (Fig. 1.2B) [Briggs et al., 2016; Goddeeris et al., 2013; Inamori et al., 2013; Kanagawa et al., 2004].

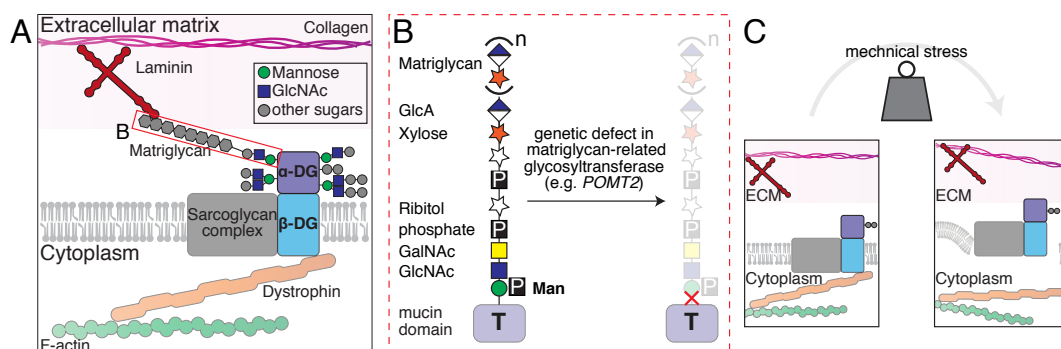


Figure 1.2: The role of *O*-mannosylation for the function of α -dystroglycan (α -DG) and the dystrophin-glycoprotein complex (DGC). (A) α -DG is a key link of the DGC, an essential component of basement membranes. The *O*-mannosyl glycan structures of DGC facilitate the linking of the extracellular matrix (ECM) with cytoskeletal proteins via β -dystroglycan (β -DG). Redrawn after Sheikh et al. [2017]. (B) The complex, extended *O*-mannosyl glycan structure with matriglycan at its end mediates the crucial laminin to α -DG interaction. Defects in enzymes that are involved in the synthesis and extension of these glycan structures reduce or completely abolish α -DG-laminin interaction. (C) The loss of DGC integrity can lead to physical instability of the plasma membrane and even necrosis, especially under mechanical stress, such as the repeated contraction and relaxation of muscles.




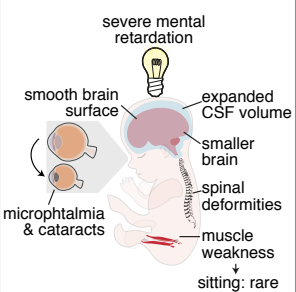
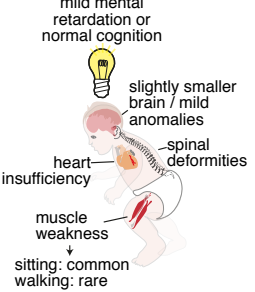
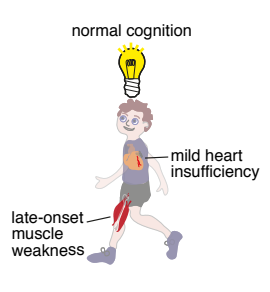
An impairment in the function of any of the glycosyltransferases involved in α -DG *O*-mannosylation and extension, such as POMT2, may reduce or even completely abolish the α -DG-ECM interaction [Michele et al., 2002; van Reeuwijk et al., 2005]. The resulting reduction of basement membrane integrity is proven to have different effects on different tissues. In tissues that are continuously exposed to mechanical forces such as the repeated contractions and extensions in muscles, the sarcolemma (muscle cell membrane) is physically destabilised (Fig. 1.2C) which in the most extreme cases leads to necrosis [Barresi and Campbell, 2006; Ervasti and Campbell, 1993; Han et al., 2009]. In other cells, such as neurons or glial cells, a reduced α -DG-ECM interaction can result in aberrant cell migration [Hang et al., 2022; Walko et al., 2013]. For instance, in the cerebral cortex, α -DG is expressed at the end feet of radial glia cells, which maintain the glia limitans basement membrane complex (pial basement membrane) to prevent neural and glial overmigration. The disruption of the basement membrane was shown to cause neuronal cells to migrate into the subarachnoid space [Hu et al., 2011; Li et al., 2011; Myshrall et al., 2012; Satz et al., 2010]. Consequently, the loss of α -DG *O*-man will result in a wide variety of pathological outcomes in DGpathy patients [Kanagawa, 2021].

1.5 The spectrum of DGpathies

DGpathies are generally characterised by congenital muscular dystrophy and a range of abnormalities of the CNS. Other tissues and organs are often also affected, but the spectrum in which a specific disease is graded on depends mainly on the underlying brain defects [Kanagawa, 2021; Nickolls and Bönnemann, 2018]. The spectrum can be broadly split into three groups of congenital muscular dystrophy-dystroglycanopathy (MDDG) types A-C (Fig. 1.3) [Kanagawa, 2021; Song et al., 2020].

Type A encompasses the most severe forms with cerebral and ocular abnormalities, including the **Walker-Warburg Syndrome (WWS)** which often results from mutations in *POMT1* or *POMT2* [Beltrán-Valero de Bernabé et al., 2002; Clement et al., 2008; Geis et al., 2019; van Reeuwijk et al., 2005]. Most strikingly, WWS patients develop cobblestone lissencephaly (type II lissencephaly) due to the mislocalisation of neuronal cells into the subarachnoid space [Kanagawa, 2021; Nakano et al., 1996]. The result is an abnormally

smooth brain surface and several other cerebral, cerebellar and brain stem defects [Devisme et al., 2012]. The fusion of the two brain hemispheres and hydrocephaly, a condition in which the volume of cerebrospinal fluid (CSF) increases and causes an expansion of the skull, are common comorbidities. These CNS defects cause severe mental retardation and patients rarely live longer than 12 months [Akasaka-Manya et al., 2004; Clement et al., 2008; Dobyns et al., 1989; Manya et al., 2008; Michele et al., 2002; Nickolls and Bönnemann, 2018; van Reeuwijk et al., 2005; Yang et al., 2016].

syndrome	Walker-Warburg Syndrome (WWS)	Congenital Muscular Dystrophy (CMD)	Limb-Girdle Muscular Dystrophy (LGMD)
disease severity	very severe, death shortly after birth (< 1 year)	moderate to severe, wide range of life spans (6-24 years)	mild, late-onset, survival into and beyond early adulthood
age onset			
dominant symptoms			

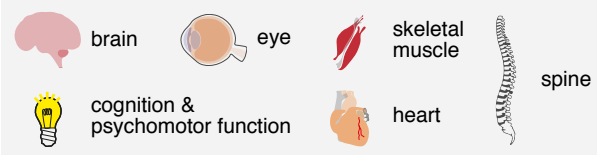


Figure 1.3: Overview of the symptoms in dystroglycanopathies.

The symptoms in Type B disease patients with **Congenital Muscular Dystrophy (CMD)** are less severe compared to the WWS, although mild brain abnormalities can still occur which also affect cognition and psychomotor development. Patients will primarily display muscular dystrophy. Scoliosis or other spinal deformities are common and sometimes accompanied by cardiac and respiratory anomalies. While the symptoms generally begin at or shortly after birth, the life span of CMD patients may vary between 6-24 years [Godfrey et al., 2007; Martinez et al., 2014; Mercuri et al., 2009; Song et al., 2020; Yanagisawa et al., 2007, 2009].

Limb-Girdle Muscular Dystrophy (LGMD) (Type C disease) patients display no mental symptoms and patients are able to walk. Muscular dystrophy only develops later in life (>18 months) in the form of mild muscle weakness and is sometimes accompanied by mild arrhythmias. Patients may live well into adulthood (>42 years) [Balci et al., 2005; Biancheri et al., 2007; Godfrey et al., 2007; Song et al., 2020; Yildirim et al., 2021].

1.6 Open questions in DGpathies

A recent report on a cohort of POMT1-DGpathy patients indicated that all WWS patients had nonsense, frameshift or splice-site mutations, or combinations of those, while LGMD patients predominantly showed missense mutations [Geis et al., 2019]. This suggests that null mutations on the *POMT* genes will result in the complete lack of α -DG, SUCO and KIAA1549 *O*-mannosylation and therefore lead to the most severe symptoms. By contrast, *POMT* genes with hypomorphic mutations retain a certain level of enzymatic activity resulting in milder symptoms.

Why are muscular, spinal or cardiovascular system symptoms present in patients with mild symptoms while they rarely show CNS defects?

I propose that the requirement for *O*-man is different in different tissues. Muscles which are constantly subject to mechanical forces have a larger requirement for the stabilising structures of the DGC in basement membranes. The same is likely true for the role of SUCO in bones, which is why spinal deformities are common. In neurons and glial cells, the POMT-substrates are likely to carry out more modulatory functions, that may not be completely abolished upon a slight reduction in glycosylation. Consequently, this means that only when the function of the POMTs is completely abolished, neuronal migration defects surface. Additionally, a comparative analysis of DGpathy patients revealed that the clinical severity of symptoms does not always match the degree α -DG hypoglycosylation [Jimenez-Mallebrera et al., 2009]. It is, therefore, necessary to establish DGpathy models of the POMT-complex with a range of severities to compare them side-by-side to fully understand the role of *O*-man.

What is the precise contribution of the three known POMT-substrates, α -DG, SUCO and KIAA1549, to the pathology in DGpathy?

The role of α -DG is diverse and spans over different tissues and developmental stages. By contrast, the functions of SUCO and KIAA1549, appear to be more restricted to the bones and cartilages, and the retina, respectively [De Bruijn et al., 2018; Sohaskey et al., 2010]. To attribute symptoms to POMT1/2-substrates *in vivo* their gene functions need to be disrupted. Their resulting phenotypes then need to be matched to those observed in mutants and patients of the POMT-complex, both newly established and published [Beltrán-Valero de Bernabé et al., 2002; Biancheri et al., 2007; Clement et al., 2008; Godfrey et al., 2007; Hu et al., 2011; van Reeuwijk et al., 2005; Rubio-Fernández et al., 2018; Uribe et al., 2021; Yanagisawa et al., 2009].

Are individual *O*-man glycosites of POMT-substrates functional *in vivo*?

As I have alluded to above, there are some indications of a tissue-specific functional significance of the POMT-substrates. By contrast, there is only scant evidence for the role of their individual *O*-mannosyl glycosites during development. Using a precise and highly efficient tool to mutate these sites *in vivo* is crucial to allow to target a vast number of these sites. Consequently, the genetic model system used must: 1) enable the study of the organism-wide deficiency of POMT and POMT-substrate genes; 2) allow easy access and analysis of a large number of mutations in both POMT and POMT-substrate genes; 3) be amenable to highly efficient genome engineering.

1.7 Vertebrate model systems to study DGpathy

Mouse. Major aspects of the organismal basis of DGpathies have been studied in mice. However, the early embryonic lethality in *dystroglycan* (*DAG1*), *POMT1* and *POMT2* null mice [Hu et al., 2011; Willer et al., 2004; Williamson et al., 1997] constrained the analysis to conditional knockout (KO) mouse models to study the neural, glial and muscular aspect of the diseases [Cohn et al., 2002; Hu et al., 2011; Moore et al., 2002; Satz et al., 2008, 2010, 2009]. Additionally, the uterine development of mice makes it difficult to access the early aspects of CNS phenotypes.

Teleost fish such as zebrafish and medaka are excellent to study developmental processes *in vivo*. The extrauterine development of the largely transparent embryos makes them excellent models to investigate embryonic development *in vivo* [Schartl, 2014; Wittbrodt et al., 2002].

Zebrafish. All DGpathy related genes are highly conserved between mammals and fish and are required for functional α -DG glycosylation [Moore et al., 2008; Steffen et al., 2007]. Using both transient approaches [Avşar-Ban et al., 2010; Parsons et al., 2002] and mutant lines [Gupta et al., 2011], DGpathy research using *dystroglycan (dag1)/pomt1/pomt2* zebrafish models have revealed that: 1) the early stages of embryonic development are largely independent of α -DG function in teleost fish; 2) the CNS is only moderately affected in larvae with progressive muscular dystrophy. This merely moderate effect on the CNS may constrain the use of zebrafish as a model for DGpathies to the muscular pathology.

Medaka. The teleost medaka or Japanese rice fish (*Oryzias latipes*) has emerged as another attractive model to study congenital disorders of glycosylation (CDG). The medaka model with a mutation CDG gene *alg2* faithfully recapitulated the multisystemic yet specific phenotypes and explored the molecular basis for organismal hypo-*N*-glycosylation [Gücüm et al., 2021]. Given, the shared advantages of zebrafish and medaka as developmental model systems two aspects of medaka CNS development may make medaka superior in studying the α -DG aspects of DGpathy to zebrafish. First, zebrafish develops much faster during early development, reaching neurulation stages in almost half the time. This may ameliorate neuronal migration defects in zebrafish [Furutani-Seiki and Wittbrodt, 2004]. Second, the zebrafish brain is much more plastic and is able to regenerate as opposed to medaka and mammalian brains [Chowdhury et al., 2022]. With the availability of a versatile genome engineering toolbox, medaka has great potential to become a powerful model for the study of DGpathies.

1.8 Genome editing tools

1.8.1 CRISPR/Cas9 targeted genome engineering

The prokaryotic clustered regularly interspaced short palindromic repeat (CRISPR)/CRISPR-associated protein (Cas) system [Bolotin et al., 2005; Mojica et al., 2005; Pourcel et al., 2005] was initially identified as RNA-mediated acquired immune system in bacteria and archaea protecting these from viral infection [Barrangou et al., 2007]. The ability of the purified Cas9-CRISPR RNA (crRNA) complex to cleave target Cas *in vitro*, laid the foundation for the widespread use of the CRISPR/Cas9 system for targeted genome editing *in vivo* [Cong et al., 2013; Gasiunas et al., 2012; Hsu et al., 2013; Jinek et al., 2012].

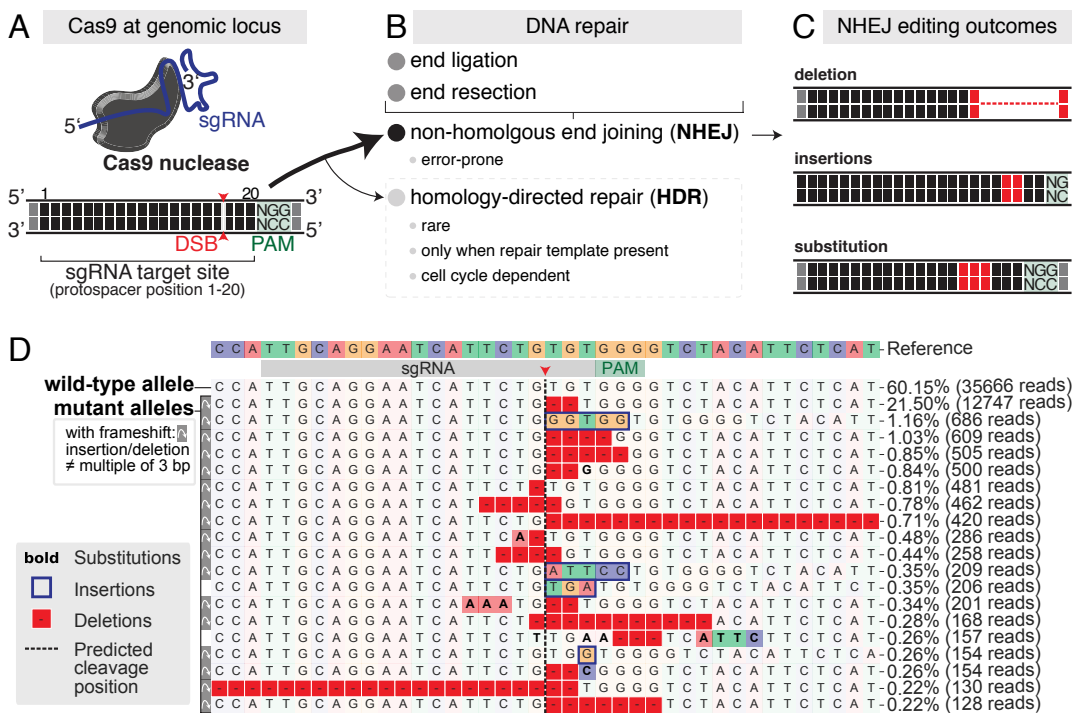


Figure 1.4: CRISPR/Cas9-mediated generation of loss-of-function alleles.

(A) Scheme showing the Cas9-sgRNA complex and the spatial relations between the protospacer adjacent motif (PAM), the DNA double-strand break (DSB) and the protospacer on the genomic target site. (B) DSB-induced repair mechanisms. (C) Non-homologous end-joining (NHEJ) after a DSB results in deletions, insertions, or substitutions of the targeted genomic region. (D) Representative data shows that CRISPR/Cas9 genome editing results in several different outcomes, most of which change the open reading frame. Data taken from Thumberger et al. [2022].

The *Streptococcus pyogenes* (Sp)Cas9 endonuclease is guided to its genomic target site by a single guide RNA (sgRNA), a synthetic fusion of the crRNA and transactivating CRISPR RNA (tracrRNA). The programming of the system is

encoded within a variable 20 nucleotide sequence at the 5' end of the crRNA called protospacer, which corresponds to the target sequence. Importantly, any genomic sequence can be targeted this way. The only requirement is the presence of a recognisable protospacer adjacent motif (PAM), e.g., NGG for SpCas9, next to the target sequence. Following target recognition, the Cas9 enzyme introduces a DNA double-strand break (DSB) 3 nucleotides upstream of the PAM site (Fig. 1.4A) [Hsu et al., 2013; Stemmer et al., 2015]. Endogenous DNA repair pathways, including the error-prone non-homologous end joining (NHEJ) or precise homology-directed repair (HDR), then try to seal the DSB by end ligation and resection processes [Nambiar et al., 2022]. NHEJ mainly results in the deletion, insertion, or substitution of base pairs (Fig. 1.4B-C). By contrast, HDR can seamlessly fix the lesion in the presence of a homologous repair template [Gutierrez-Triana et al., 2018; Seleit et al., 2021]. However, moderate efficiencies limit the in-depth phenotypic analysis in fish to generations F1 or F2.

The Cas9-mediated gene KO is robust which allows to discern gene functions in fish in F0. Both the high Cas9 nuclease efficiency and robust workflows have facilitated the study of gene functions in so called "crispants" [Burger et al., 2016; Hoshijima et al., 2019; Kroll et al., 2021; Thumberger et al., 2022]. While CRISPR/Cas9-mediated KO has been instrumental in establishing the basic functions of target genes through null or hypomorphic alleles, these efficient approaches rarely produce specific alleles. Instead, an allelic series within an edited embryo will emerge, with a large fraction of these leading to frameshift mutations and, ultimately, to a premature termination codon (PTC) (Fig. 1.4D) [Thumberger et al., 2022]. These alleles are then broadly considered loss of function alleles in crispants when analysing F0-level phenotypic outcomes [Hammouda et al., 2021] and laborious genetics is required to isolate a selected allele in the next generations. However, a means to go beyond gene-level analysis to address the functional impact of single amino acid changes directly is highly desirable.

1.8.2 Cytosine and adenine DNA base editors

CRISPR/Cas9-based DNA base editors have recently emerged as single nucleotide rubber and pencil tools [Molla and Yang, 2019; Porto et al., 2020; Ravindran, 2019; Rees and Liu, 2018]. Cytosine (CBE) and adenine base editor (ABE) alike utilise the hydrolytic deamination of target nucleotides within a window of high activity [Anzalone et al., 2020; Huang et al., 2021],

in the absence of DSBs and with only limited activation of DNA damage response pathways or induction of apoptosis [Nambiar et al., 2022]. Both cytosine base editor (CBE)s and ABEs consist of a Cas9-D10A nickase or a dead Cas9 nuclease and an N-terminally linked cytidine or deoxyadenosine deaminase. Programmable DNA targeting of the base editor complex is achieved through the genome searching and targeting ability of the Cas9 nickase.

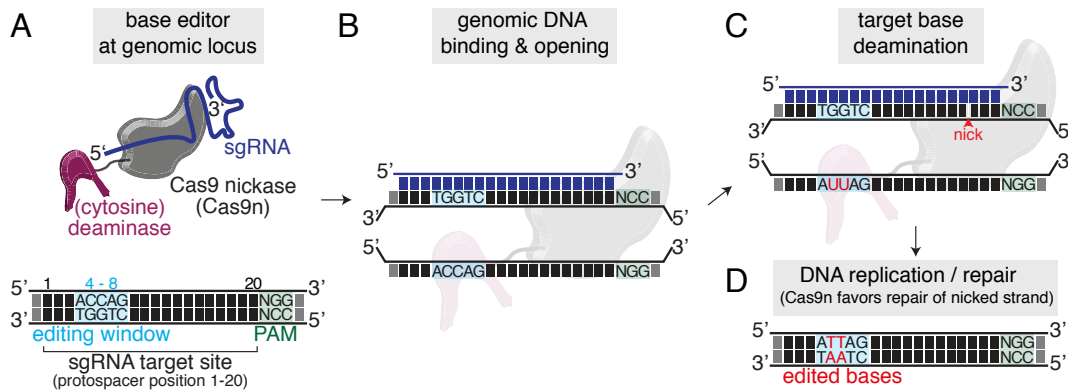


Figure 1.5: The principle of base editing is exemplified by the target C-to-T conversion through cytosine base editors. (A) The cytosine base editor (CBE) complex will be guided to the targeted genomic site by the selected sgRNA. The protospacer adjacent motif (PAM) is essential for target recognition. By contrast, the editing window on the protospacer is more volatile depending on the editor used and resides between positions 4-8 for standard CBEs and ABEs. (B-D) Mechanism of CBE-DNA binding, DNA opening and hydrolytic deamination. Following cellular DNA repair or replication processes target cytosines are converted to thymines.

The deaminases then enable the conversion of cytosine (C) to thymine (T) (C-to-T) or adenine (A) to guanine (G) (A-to-G) within a predefined window of activity on the sgRNA target site. This window typically spans the protospacer positions 4-8. Given the lack of nuclease activity, this approach generally only produces low levels of insertion or deletion events (indel)s, with substantially higher desired editing outcomes (Fig. 1.5). The availability of CBEs and ABEs together enable all transition mutations [Gaudelli et al., 2017; Komor et al., 2016], and as a consequence of various iterations of deaminase improvements *in vitro*, these modifications are achieved with high efficiency [Koblan et al., 2018; Richter et al., 2020; Thuronyi et al., 2019].

DNA base editors have been shown to work efficiently in many model organisms [Molla and Yang, 2019; Nambiar et al., 2022; Rees and Liu, 2018]. Both CBEs and ABEs have been established in zebrafish [Carrington et al., 2020; Qin et al., 2018; Rosello et al., 2021b; Zhang et al., 2017; Zhao et al., 2020], which achieved up to 91% and 40% editing efficiencies in F0, respectively.

Aims and Approaches

The aim of this thesis was to elucidate the organismal role of the POMT1-POMT2 complex in DGpathies and to examine the respective contribution of the three known substrates of the POMT-complex. There is ample evidence from human patient literature but also model organisms that exclusively view defective *POMT1*- or *POMT2*-DGpathies through the lens of α -DG. I wanted to take a step back and first create a baseline for the DGpathy spectrum of *pomt1* and *pomt2* in medaka development. Next, I analysed the loss of function phenotypes of *dag1*, *SUCO* and *KIAA1549* by completely disrupting their gene function or by introducing missense mutations at conserved *O*-man glycosites. I thus aimed to deconvolute, which aspect of *pomt1/pomt2* DGpathies can be attributed to the functions of α -DG, SUCO and KIAA1549. To achieve the overarching goal of this thesis I addressed the following points using the approaches indicated:

- 1. Develop a framework for the efficient installation of point mutations on *O*-mannosyl glycosites.**
I developed a base editing approach to efficiently introduce single amino acid changes and premature stop codons.
- 2. Establish and characterise *pomt2* disease models for DGpathies.**
Using a CRISPR/Cas9-based approach I created *pomt1* and *pomt2* loss-of-function alleles and focused on two *pomt2* alleles that resemble WWS and LGMD patient pathologies to better understand the extremes in the spectrum. To understand the early developmental steps in the pathology of *pomt2* WWS mutants I performed a series of histological experiments to examine the brain and the eyes, which I complemented with whole-transcriptome analysis.
- 3. Identify conserved *O*-man glycosites of α -DG, SUCO and KIAA1549 in medaka and expand the targeting range of existing base editors to allow mutating all *O*-man glycosites.**
I identified highly conserved *O*-man glycosites in medaka by protein sequence alignments across vertebrates using published glycoproteomics annotations. Due to PAM restrictions, I cloned and tested base editor variants that expand the editing range to virtually any site in the genome.
- 4. Disrupt gene and *O*-man glycosite functions of *dag1*, *SUCO* and *KIAA1549* and characterise embryonic and post-embryonic phenotypes.**
I used a CRISPR/Cas9-based approach to create and analyse embryonic and larval phenotypes in F0. To precisely investigate the function of individual *O*-man sites I modified a selection of these using base editors and analysed the respective phenotypes.

2

Results

2.1 Precise *in vivo* functional analysis of protein variants by base editing in medaka

In the next section, I will elaborate on how I established both CBE and ABE DNA base editors in medaka. The section presented is part of a project that we recently published [Cornean et al., 2022]. A detailed description of author contributions for this chapter by my two colleagues, Bettina Welz and Jakob Gierten is given in the Contributions section.

2.1.1 Next-generation cytosine and adenine base editors

A considerable number of functionally relevant phenotypes can emerge from single or multiple nucleotide changes introduced to a gene of interest. These changes can result in PTC that truncate proteins and under certain circumstances cause nonsense-mediated decay events [El-Brolosy et al., 2019]. Moreover, missense mutations will result in the substitution of individual amino acids. While CBEs can biochemically facilitate both types of changes (PTC can emerge from Q, R, and W triplets) [Billon et al., 2017; Komor et al., 2016], ABEs are restricted to amino acid changes [Gaudelli et al., 2017]. To investigate both (PTC and amino acid change by base editing, I selected and tested four state-of-the-art DNA base editors.

First, I compared BE4-Gam [Komor et al., 2017] with two next-generation CBEs, ancBE4max [Koblan et al., 2018] and evoBE4max [Thuronyi et al., 2019], the latter of which had not been previously tested in fish. Second, I tested the highly processive adenine base editor ABE8e (Richter et al., 2020) (Fig. 2.1A),

as I hypothesised that it could overcome the target constraints reported for ABE7.10 in zebrafish [Qin et al., 2018].

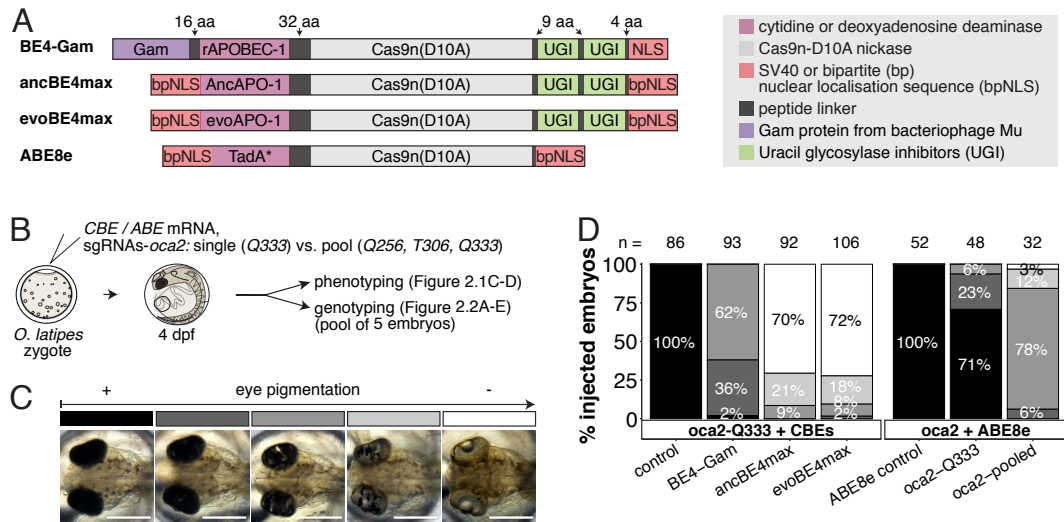


Figure 2.1: Somatic cytosine and adenine base editing at the *oca2* locus allows for direct functional assessment. (A) Structure of cytosine base editors and the adenine base editor ABE8e used. (B) Scheme of the experimental workflow. (C) Phenotypic categories of eye pigmentation phenotypes were obtained at 4 dpf (days post fertilisation) (dorsal view). Scale bar = 400 μ m. (D) Grouped and quantified pigmentation phenotypes for cytosine and adenine base editor experiments. Adapted from Cornean et al. [2022].

Two aspects are essential to probe the function of genes and single amino acids in a developing embryo. First, base editing resulting in the desired editing outcomes needs to happen very early. This is important to ensure that the editing results are homogeneous across the organism when assessing the outcome at a phenotypic level in later stages of development. Second, the efficiency of target nucleotide conversion needs to be high, such that the remaining wild-type alleles can no longer compensate for the mutated alleles.

2.1.2 Biallelic PTC and missense mutations reveal high cytosine and adenine base editing efficiencies

An excellent candidate test gene is *oculocutaneous albinism II* (*oca2*), which is required for the formation of eye pigment. The loss of retinal pigmentation as scorable readout is ideal to address the efficacy of biallelic base editing or Cas9-based KO experiments [Thumberger et al., 2022; Zhang et al., 2017]. A single functional *oca2* allele is sufficient to generate normal retinal pigmentation and therefore both alleles need to be disrupted within a given pigment cell to avoid pigment formation.

I targeted conserved regions in *oca2* using base editor mRNA by injecting 1-cell stage medaka embryos to ensure early editing and hence homogeneity of edits (Fig. 2.1B). Phenotyping of base edited embryos hereafter called “editants”, at 4 days post fertilisation (dpf), revealed a phenotypic spectrum of pigmentation. This spectrum ranged from fully pigmented wild-type eyes to the complete loss of ocular pigmentation which I divided into five arbitrary categories (Fig. 2.1C).

I observed that both ancBE4max and evoBE4max with the *oca2-Q333* sgRNA caused a large fraction of editants to be almost completely devoid of eye pigmentation. This striking effect is a consequence of an introduced PTC (p.Q333X). By contrast, the *oca2-Q333* sgRNA with ABE8e resulted in two missense mutations p.T332A and p.Q333R but was not sufficient to cause substantial pigment loss. Only when combining these missense mutations with editing using *oca2-Q256* and *oca2-T306* sgRNAs (*oca2*-pool) I observed a striking pigment pattern (Fig. 2.1D).

To evaluate the average editing efficiency for each experiment I performed Sanger sequencing of five randomly pooled editants per sample (Fig. 2.2A). Sequencing and peak quantification using editR [Kluesner et al., 2018] reflected the phenotypic trend for CBEs with editing efficiencies at C7 (c.997C>T, i.e., p.Q333X) of $29.3\pm 7.4\%$ (n=3), $93.8\pm 7.9\%$ (n=5), and $93.3\pm 9.8\%$ (n=3) for BE4-Gam, ancBE4max and evoBE4max, respectively (Fig. 2.2B). ABE8e editing resulted in close to homozygous installation of two missense mutations p.T332A ($99.3\pm 0.6\%$, $93.7\pm 11.0\%$) and p.Q333R ($89.0\pm 6.6\%$, $90.3\pm 2.1\%$) by single and pooled *oca2* experiments, respectively. However, most embryos were still partially pigmented (Fig. 2.2C). This was the case even in pooled editants with homozygous p.Q256R (100%) and moderate editing at p.T306I ($52.3\pm 2.3\%$). Two things can be concluded from this. First, missense mutations will more often than not create hypomorphic alleles, in contrast to the null alleles created by PTC. Second, missense mutations can compound the hypomorphic nature of alleles, as shown by the two versus three missense mutations created in *oca2-Q333* and *oca2*-pool injections.

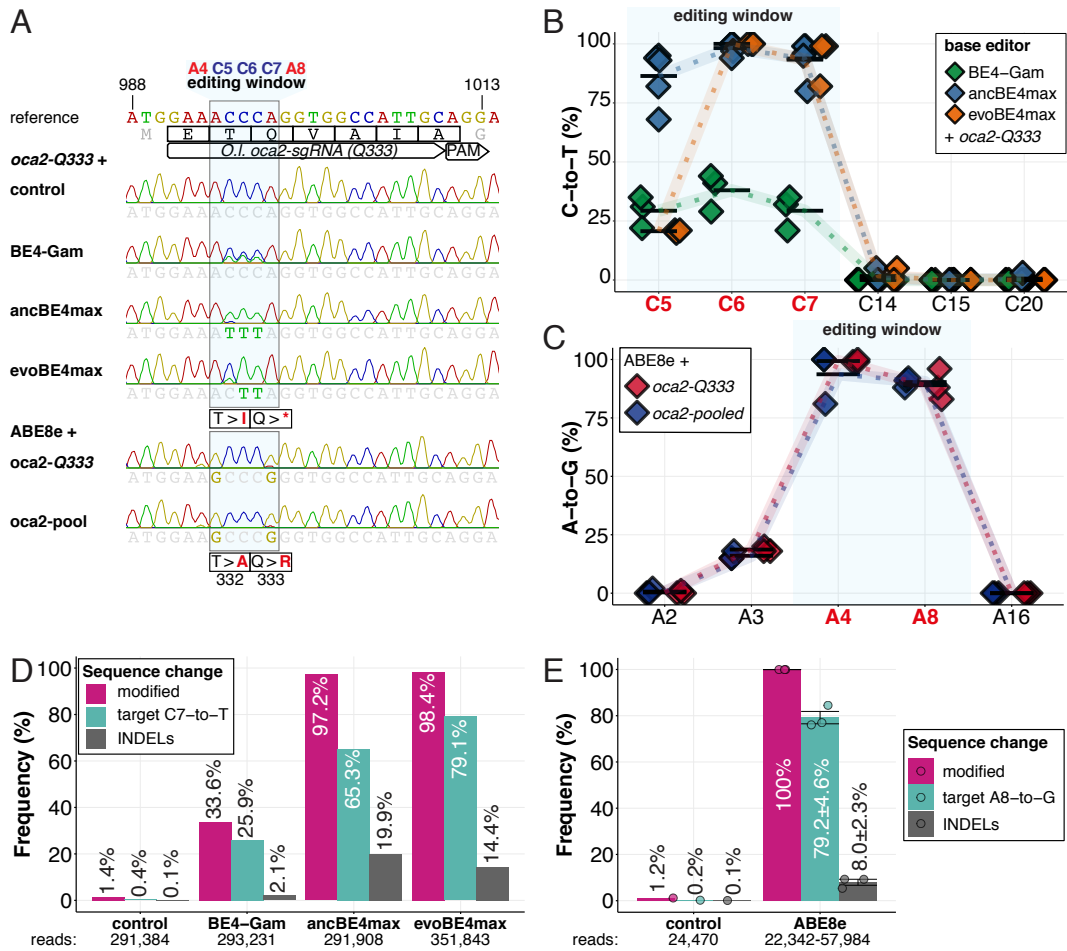


Figure 2.2: Somatic cytosine and adenine base editing at the *oca2* locus is highly efficient. (A) Exemplary Sanger sequencing reads for each experimental condition were obtained from a pool of five randomly selected embryos at the *oca2-Q333* locus. (B-C) Quantification of Sanger sequencing reads (by EditR, Kluesner et al. [2018]) for BE4-Gam (n=3), ancBE4max (n=5) and evoBE4max (n=3) (B); ABE8e for single (n=3) and pooled *oca2-sgRNA* experiments (n=3) (C). (D-E) Amplicon deep-sequencing of cytosine and adenine base editing events at the *oca2-Q333* locus reveals prominent on-target editing efficiencies with low- to moderate levels of indels. Note: for *oca2-Q333* control, BE4-Gam, ancBE4max, and evoBE4max, two pools of five embryos were used as samples. For ABE8e experiments three pools of five embryos were analysed independently. The number of reads shown refers to all aligned Illumina reads per sample. Adapted from Cornean et al. [2022].

Sanger sequencing did not reveal other DNA sequence changes such as indels. However, the method itself is inherently limited in its ability to resolve base calls toward extremes [Kluesner et al., 2018]. To address this limitation, I analysed a subset of editant gDNA samples at the *oca2-Q333* locus using Amplicon deep-sequencing (Amplicon-seq) (Fig. 2.2D-E). The total number of modified alleles resembled the editing efficiencies initially determined by Sanger sequencing. Indel events did, however, contribute to these results in a base editor-dependent manner ranging from 2.1% (BE4-Gam), $8.0 \pm 2.3\%$ (ABE8e), 14.4% (evoBE4max) to 19.9% (ancBE4max).

In summary, the two CBEs ancBE4max and evoBE4max and ABE8e demonstrated remarkable efficiencies of on-target C-to-T or A-to-G conversions, respectively, with low to moderate levels of indels in the *oca2* coding sequence. The CBE mediated introduction of a PTC resulted in a near-complete loss of eye pigmentation in embryos, making it compatible with F0 genotype-phenotype studies. Furthermore, ABE8e can efficiently introduce missense mutations. To examine whether missense mutations can lead to fully penetrant phenotypes in F0, I next addressed the consequences of a missense loss-of-function mutation on transgenic GFP.

2.1.3 Missense mutations are introduced early by ABE8e

Not only can green fluorescent protein (GFP) function be easily analysed, but our understanding of the functions of individual amino acids is also comprehensive [Fu et al., 2015; Li et al., 1997; Patterson et al., 1997]. Specifically, I assayed the loss of GFP fluorescence after the introduction of a p.C71R mutation in a double transgenic line with heart-specific expression of enhanced green fluorescent protein (EGFP) and mCherry (*myl7::EGFP*, *myl7::H2A-mCherry*) [Hammouda et al., 2021]. To understand just how processive ABE8e can be, I performed two experiments. ABE8e mRNA with the *GFP-C71* sgRNA was injected either into 1-cell stage embryos or into a single blastomere at the 4-cell stage (Fig. 2.3A). Since cells in the medaka 4-cell embryo form a syncytium that allows some diffusion, this experiment addresses the speed and efficiency by which the ABE8e-sgRNA complex introduces target deamination.

GFP fluorescence was completely abolished in all hearts assayed at 4 dpf in 1-cell stage injections (n=41; not all founders were homozygous for both GFP and mCherry transgenes). On the other hand, 4-cell stage injections resulted in mosaicism apparent by speckled hearts positive for GFP (23 of 48) (Fig. 2.3B). The GFP speckles can thereby be clearly seen against the expression domain (mCherry) (Fig. 2.3C-E). Sanger sequencing and EditR quantification confirmed the high efficiencies in introducing the intended p.C71R missense mutation ($97.0\pm 4.4\%$ and $90.0\pm 7.8\%$) for 1-cell and 4-cell stage injections, respectively. Additionally, I noticed a bystander edit that introduced a p.V69A missense mutation in both 1- and 4-cell injection experiments ($61.2\pm 9.4\%$ and $12.6\pm 8.1\%$) (Fig. 2.3F-G). Finally, to confirm the biallelic installation of the p.C71R mutation, I performed Amplicon-seq on individual embryos injected at

the 1-cell stage. Similarly, to previous observations with *oca2* editants, the modification of all alleles (100%, n=4) was compounded by the highly efficient on-target edit of $85.9 \pm 15.3\%$ with an indel rate of $15.8 \pm 17.5\%$ (Fig. 2.3H).

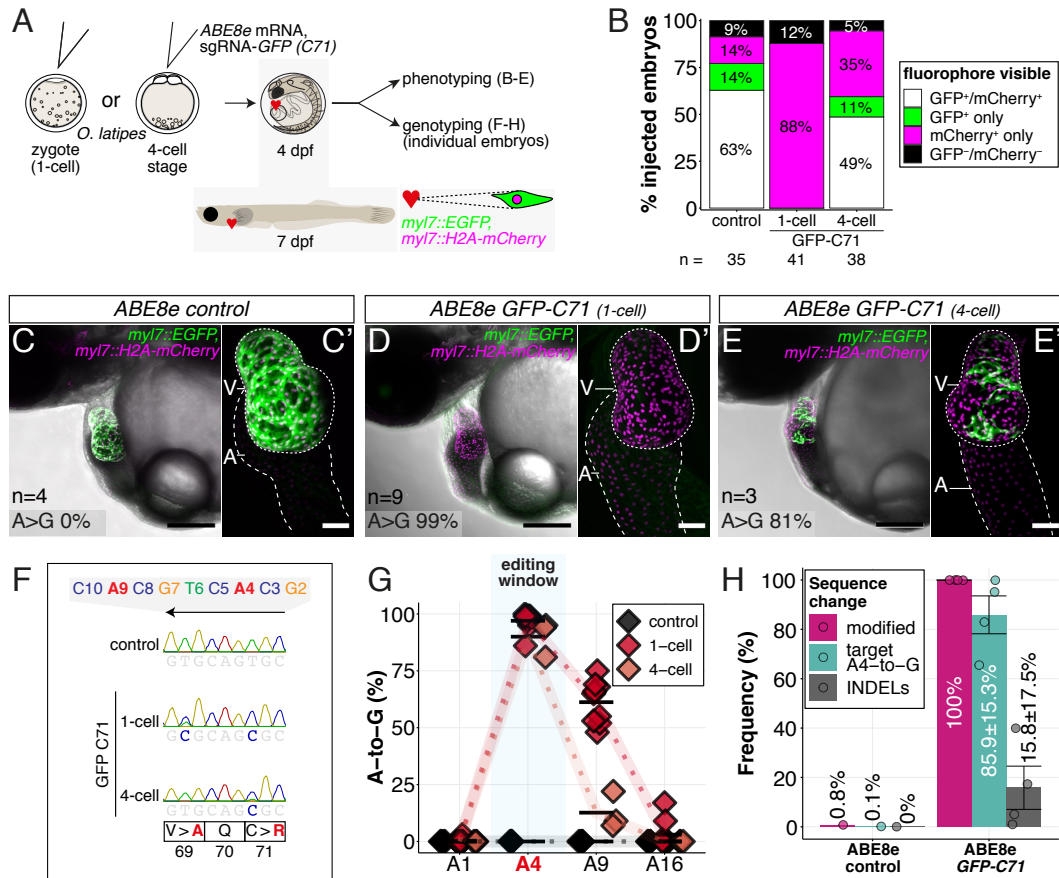


Figure 2.3: ABE8e efficiently introduces a function-altering C71R missense mutation in F0. (A) Scheme of the experimental workflow with injections performed either into a single cell of 1-cell or 4-cell stage medaka embryos (HdrR strain, *myl7::EGFP*, *myl7::H2A-mCherry*). (B) Scoring of GFP and mCherry signal with an epifluorescent microscope in control and *GFP-C71* of 1-cell or 4-cell stage editants displaying heart-specific GFP-signal. (C-E) Confocal microscopy of chemically arrested hearts (representative images) at 7 dpf (lateral view with V = ventricle, A = atrium). Dpf = days post fertilisation. Overview images, overlaid with transmitted light, show maximum z-projections of optical slices acquired with a z-step size of $5 \mu\text{m}$. Scale bar = $200 \mu\text{m}$. (C'-E') Close-up images show maximum z-projections of optical slices acquired with a z-step size of $1 \mu\text{m}$. Note the display of A-to-G conversion rates for A4 causing the p.C71R missense mutation. Scale bar = $50 \mu\text{m}$. (F-G) Quantification of Sanger sequencing reads shows close to homozygosity rates of A-to-G transversions installing the C71R missense mutation. (H) Amplicon-seq of a subset (n=4) of 1-cell stage ABE8e experiment gDNA samples quantifying the outcome of intended base editing and indel formation. Adapted from Cornean et al. [2022].

Together, these experiments are an impressive demonstration of the interrogation of the functional consequences of a missense mutation in F0. Both pigmentation and fluorescence are rather simple, readily scorable phenotypes. To understand the relevance of editants for complex phenotypes, I will in the next two sections demonstrate this by editing two genes involved in cardiac contractility.

2.1.4 evoBE4max can efficiently disrupt heart contractility by editing cardiovascular *troponin T*

I first targeted *troponin T type 2a* (*tnnt2a*) for which fully penetrant and recessive lethal *sih* mutants were previously described in zebrafish, resulting in silent, non-contractile hearts [Sehnert et al., 2002]. Additionally, medaka crispants of *tnnt2a* were recently described, which also show silent hearts in the presence of general developmental defects [Meyer et al., 2020]. I used a published sgRNA (*tnnt2a-Q114*) with CBEs to convert Q114 into a PTC [Meyer et al., 2020] and analysed the resulting phenotypes causing cardiac contractility defects (Fig. 2.4A-B).

The penetrance of the phenotype increased drastically, from BE4-Gam to ancBE4max and evoBE4max (Fig. 2.4C). The phenotypic distribution thereby closely followed the different editing efficiencies determined by Sanger sequencing and quantified by EditR (c.340C8>T resulting in p.Q114X). These were 0% for BE4-Gam, $27.8 \pm 16.8\%$ for ancBE4max and $85.9 \pm 23.5\%$ for evoBE4max, which displayed silent hearts in half of the editants (49%) (Fig. 2.4D-D').

Importantly, the analysis of the editing efficiencies in the silent heart group indicated near homozygous C8-to-T edits (p.Q114X) by evoBE4max. I was able to confirm the high efficiency of these edits by Amplicon-seq on a subset of samples. I observed remarkable efficiencies of $89.3 \pm 6.6\%$ and low indel rates ($7.7 \pm 7.3\%$) (Fig. 2.4E). As a side note, I confirmed the medaka "silent heart" phenotypes of the editors using F0 incrosses that produced genetically homozygous *tnnt2a*^{p.Q114X/p.Q114X} embryos [Cornean et al., 2022].

In summary, I could show that CBE are potent tools for addressing the function of genes involved in complex phenotypes such as heart contraction in F0 by efficiently introducing a PTC in *tnnt2a*.

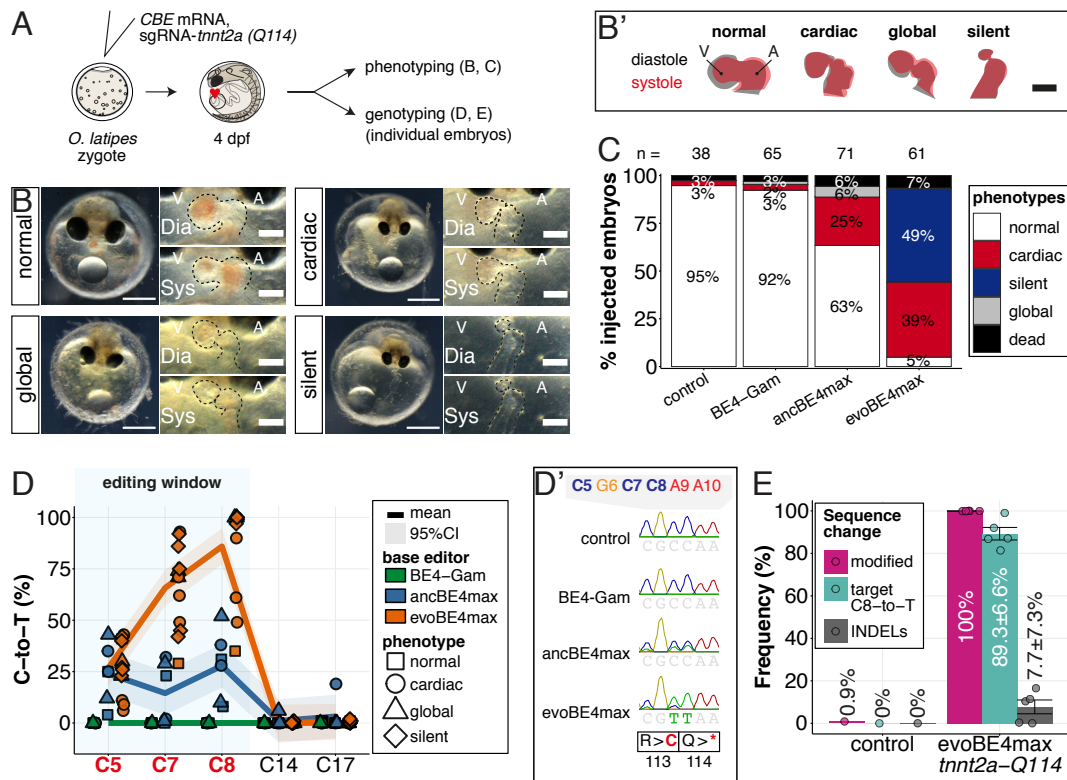


Figure 2.4: Introducing a PTC in *tnt2a* gene accurately recreates complex mutant phenotypes in F0. (A) Scheme of the experimental workflow. (B) Phenotypic categories of heart/developmental phenotypes obtained at 4 dpf. Scale bar = 400 μ m (overview) and 100 μ m (zoom-in). Ventricle (V), atrium (A), diastole (Dia) and systole (Sys) are indicated. Dpf = days post fertilisation. (B') Representative scheme of fractional shortening of the heart chambers in specified phenotype groups highlighting significant morphological consequences (small ventricle) in the silent heart group. (C) Fraction of phenotype scores as a consequence of cytosine base editor injections. (D) Summary of editor type-specific C-to-T conversion efficiencies relative to the target C protospacer position grouped by phenotype for BE4-Gam (n=6), ancBE4max (n=6) and evoBE4max (n=12). CI=confidence interval. (D') Example Sanger sequencing reads of single edited embryos with resulting missense and PTC mutations. (E) Amplicon-seq of a subset (n=5) of evoBE4max edited gDNA samples (single embryos) quantified target C8-to-T editing as well as indel frequencies. Adapted from Cornean et al. [2022].

2.1.5 *In vivo* modelling of heart repolarisation defects

I next targeted a crucial amino acid in the cardiac-specific potassium channel ERG encoded by *kcnh6a* in medaka, essential for cardiac repolarisation [Arnaout et al., 2007; Hassel et al., 2008]. The ERG channel is a homotetramer with each subunit consisting of six α -helical transmembrane domains S1-S4 forming a voltage sensor and the pore-forming domains S5-S6 [Wang and MacKinnon, 2017; Zhang et al., 2004]. Using CBEs, I revealed the loss-of-function phenotype in *kcnh6a* editants by efficiently installing a PTC (p.Q11X) in F0 (Fig. 2.5A-C), and also confirmed this phenotype in F1 [Cornean et al., 2022]. To alter the

voltage-sensing and gating behaviour of the ERG channel *in vivo*, I selected a sgRNA (*kcnh6a-R512*) that facilitates a base conversion with ABE8e to remove a positive charge at a crucial position on the conserved S4 domain [Arnaout et al., 2007].

I used ABE8e mRNA with sgRNA *kcnh6a-R512* in a *myl7::EGFP* reporter [Gierten et al., 2020] to reveal a high frequency of specific heart phenotypes at 4 dpf (81%). The majority of hearts in these editants displayed partially or entirely silent ventricles (Fig. 2.5A-B'). Analysis of the genomic *kcnh6a* locus around R512 in editants by Sanger-sequencing and EditR quantification reproducibly revealed high A8-to-G conversion rates at p.R512G ($91.7 \pm 9.5\%$). The efficiency of editing thereby correlated with the observed phenotype (Fig. 2.5D). Notably, ABE8e-mediated editing achieved homozygosity in three out of four imaged R512G embryos in F0 (Fig. 2.5E). Moreover, I was able to confirm the high on-target editing rates by Amplicon-seq, albeit with heterogeneous indel rates ranging from 0.8-27.8% in different individuals (Fig. 2.5G).

Confocal microscopy of the chemically arrested hearts of p.R512G missense editants at 7 dpf revealed a striking morphological impact of the primary repolarisation phenotype. While atrioventricular differentiation was complete, the ventricular muscle showed major growth and differentiation deficiencies. The ventricles were collapsed and displayed multiple vesicle-shaped, aneurysm-like structures (Fig. 2.5F). This demonstrated that this S4 sensor charge is functionally essential *in vivo* as the p.R512G missense editants recapitulated phenotypes of PTC-truncated *kcnh6a* editants. Whether this structural phenotype is a direct consequence of the R512G missense mutation or a secondary consequence by the lack of forces generated through chamber contractions and directed blood flow remains to be investigated.

Taken together, the precision and remarkable efficiency of ABE8e in medaka embryos allowed me to introduce a single amino change that modified the conserved voltage sensor domain of ERG *in vivo* in F0. Overall, my F0 base editing results in medaka demonstrate the utility of both CBEs and ABE8e to study gene functions at the amino acid level in complex biological processes.

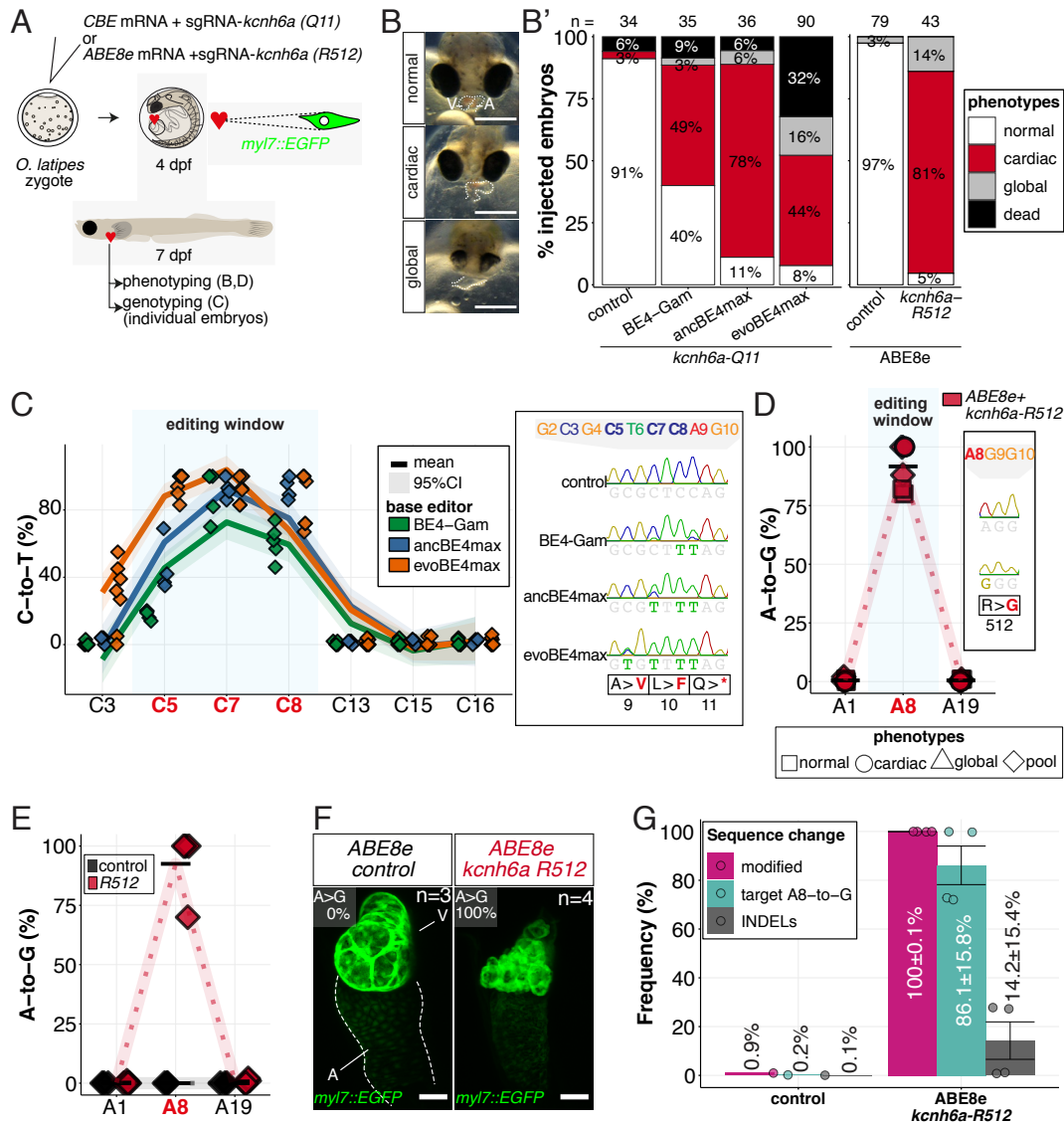


Figure 2.5: *In vivo* cytosine and adenine base editing modelling of the ERG channel gene *kcnh6a* reveals that p.R512G completely abolishes the protein's function. (A) Scheme of the experimental workflow with injections performed into zygotes of medaka embryos (Cab strain, *myl7::EGFP*). (B) Phenotypic categories of heart/developmental phenotypes obtained at 4 dpf. Scale bar = 400 μ m. (B') Fraction of phenotype scores as a consequence of CBE and ABE8e injections. (C) Summary of CBE-specific C-to-T conversion efficiencies and exemplary Sanger sequencing reads for the *kcnh6a-Q11* site relative to the target C protospacer position for BE4-Gam (n=5), ancBE4max (n=4) and evoBE4max (n=7). (D-E) Summary of ABE8e A-to-G conversion efficiencies and exemplary Sanger sequencing reads for the *kcnh6a-R512* site relative to the target A protospacer position separated by phenotype (n=6) (D) and embryo samples after confocal microscopy (n=4) (E). (F) Confocal imaging reveals striking chamber wall defects of non-contractile/spastic ventricles, of which 3 of 4 specimens with 100% A8-to-G conversion quantified by Sanger-sequencing. Images show maximum z-projections of optical slices acquired with a z-step size of 1 μ m. Scale bar = 50 μ m. V = ventricle, A = atrium, dpf = days post fertilisation. (G) Amplicon-seq of the gDNA samples from imaged embryos (single embryos, n=4) quantified target A8-to-G editing and indel frequencies. Adapted from Cornean et al. [2022].

2.2 Studying the spectrum of DGpathies with medaka *pomt2* disease models

2.2.1 *Pomt1* and *pomt2* are broadly, but dynamically expressed across developmental stages

Pomt1 and *pomt2* are widely expressed across developmental stages in both mouse and fish [Avşar-Ban et al., 2010; Lommel et al., 2008; Moore et al., 2008; Willer et al., 2004]. In particular, strong expression was observed in developing neural tissues such as the neural tube and the eyes, but also in somites. To address the developmental expression dynamics of medaka *pomt1/pomt2* I mined published RNA-sequencing data sets [Ichikawa et al., 2017; Li et al., 2020; Marlétaz et al., 2018]. I analysed absolute expression values (TPM, transcripts per million) and intrinsically normalized values (Zscore) from embryonic to postembryonic stages of development (Fig. 2.6A-B).

To confirm the previously described spatial gene expression pattern in medaka I performed whole mount *in situ* hybridisations. *Pomt1* only begins to be expressed at late gastrulation stages and maintains robust expression levels until stage 34. By contrast, *pomt2* appears to be expressed at high levels before the zygotic genome commences transcription. The tissue-specific gene expression of both paralogues follows a similar pattern across developmental stages. At early stages the expression is moderately high in neural tissues and the notochord (stages 24 and 28). Later, gene expression in the retina is confined to retinal pigmented epithelium (RPE) and retinal stem/progenitor cells for *pomt1* and amacrine and stem/progenitor cells for *pomt2* (stages 34 and 39) (Fig. 2.6C-E). To assess how well transcript levels of *pomt1* and *pomt2* are translated into protein levels I used developmental stages with peak (stage 34) and reduced gene expression to perform POMT1 and POMT2 immunoblots. Similar to reduced gene expression levels after stage 34 for both *pomt1* and *pomt2*, the level of protein is substantially lower in postembryonic larvae (Fig. 2.6F). This suggests dynamic functional regulation at the transcript and protein level. Together, the requirement for *O*-mannosyltransferase activity across stages may be differentially adjusted. In the next section, I will describe how I used several mutant alleles for *pomt2* in medaka to study the spectrum of DGpathies.

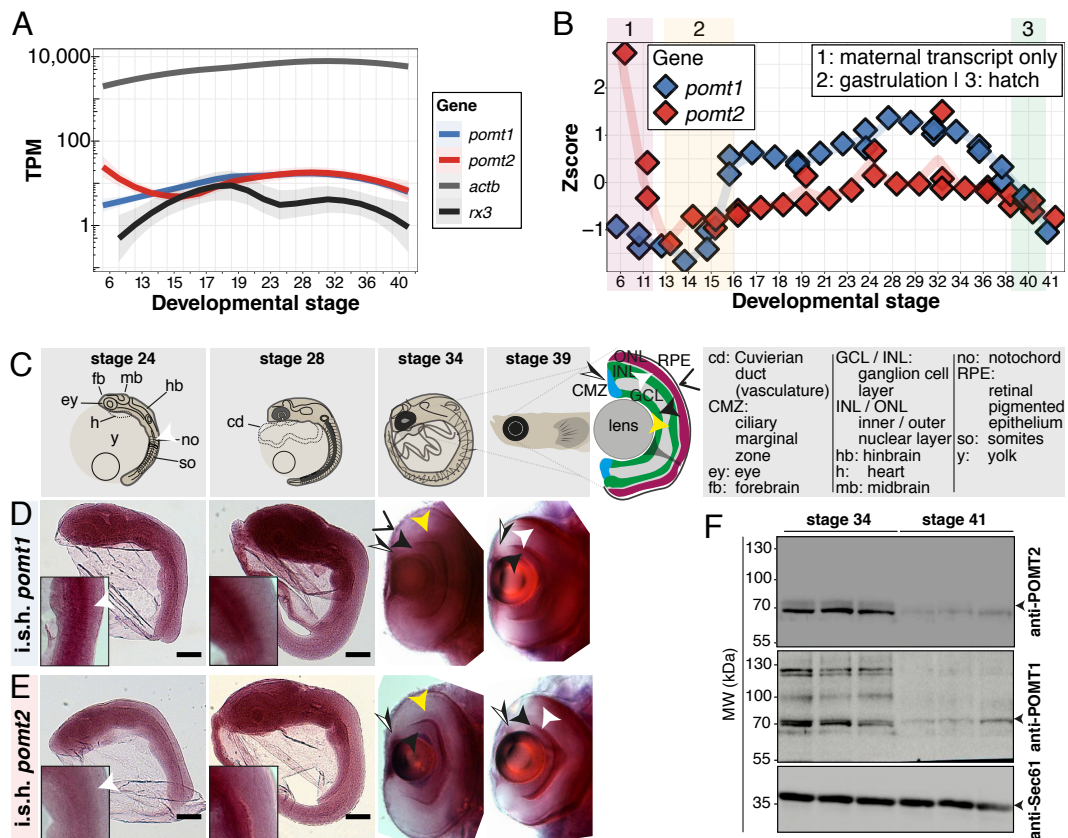


Figure 2.6: Expression of the substrates of the POMT1-POMT2 complex across stages and tissues. (A-B) Gene expression data for *pomt1* and *pomt2* at embryonic stages from published datasets [Ichikawa et al., 2017; Li et al., 2020; Marlétaz et al., 2018] with absolute, log-scaled transcripts per million (TPM, A) counts and normalised (gene-intrinsic) Zscore ((B). Note: zygotic genome activation in medaka happens around stages 7-8 (32 to 64-cell stages; [Kraeussling et al., 2011]). (C-E) Tissue-specific gene expression by *in situ* hybridisation for *pomt1* and *pomt2* at early brain/eye development and somitogenesis stages (24 and 28), completion of somitogenesis and retinal differentiation (34) and hatching stages (39). Scale bar = 100 μ m. (F) Immunoblot on 30 μ g membrane fractions from wild-type medaka stage 34 and 41 embryos, detecting Sec61 (loading control), POMT1 and POMT2.

2.2.2 Medaka *pomt1* and *pomt2* mutants capture a spectrum of DGpathies

To better understand which POMT1 and POMT2 domains are functionally crucial and which are dispensable I wanted to confirm that the POMT1-POMT2 complex recapitulates the general structure of the yeast PMT1-2 complex [Bai et al., 2019]. The AlphaFold2 algorithm has been praised for predicting the structures of uncharacterised proteins [Jumper et al., 2021]. I retrieved the structures for both human POMT1 and POMT2 proteins from the AlphaFold Protein Structure Database [Varadi et al., 2022] and annotated regions and domains of interest, including the N- and C-termini and the MIR domains (Fig. 2.7A-B).

Notably, while the N-terminus of both POMT1 and POMT2 reside within the cytoplasm, the C-terminal domain lies in the ER lumen. The functional centres, including the proposed active site with the highly conserved acidic DE motif and the MIR domains, localise to the ER lumen [Akasaka-Manyá et al., 2011; Bai et al., 2019; Bausewein et al., 2016; Chiapparino et al., 2020; Lommel et al., 2011]. This suggests that modifying the C-terminus rather than the N-terminus will cause greater functional alterations.

In mice, the function of the POMT1-POMT2 complex is essential for the formation of the rodent specific early basement membrane called Reichert's membrane [Hu et al., 2011; Willer et al., 2004]. This makes the study of embryonic development complex and reliant on complicated conditional KO experiments that, while insightful to the specific function of the POMTs within a particular tissue, cannot fully recapitulate the patient's pathophysiology. Previous work in zebrafish indicated that early teleost fish development can progress even in the absence of POMT function. Moreover, the high levels of maternal *pomt2* in medaka will provide an additional buffer for early development. I speculated that by overcoming the early POMT-functional necessities I could specifically study processes of embryonic development that are inaccessible in patients and mouse models of DGpathy. In particular, brain and retinal development. I therefore focused on *pomt2* to study DGpathies. I established four different *pomt2* mutant alleles, and additionally one mutant allele for *pomt1* (Fig. 2.7C-C'). These alleles can be categorised by the position of altered amino acids within the protein:

- N-terminal, close to the DE motif (alleles 1 and 1*)
- a change in the MIR motif region (allele 2)
- C-terminal with disruption of the 3'UTR (alleles 3 and 4)

Additionally, the nature of the mutation distinguishes the alleles: Both *pomt1*^{Y33(*ins*)} and *pomt2*^{S56(*ins*)} are N-terminal, insertional alleles, that would theoretically introduce an early PTC due to a frameshift or lead to changes in splicing or alternative ATG usage. Five conserved amino acids, IRLEH are deleted between I416 and H420 in the MIR mutant *pomt2*^{ΔMIR2} allele. Finally, both *pomt2*^{ΔCterm} and *pomt2*^{Cterm-fs} contain large deletions removing the last two exons or large parts of the 3'UTR, respectively.

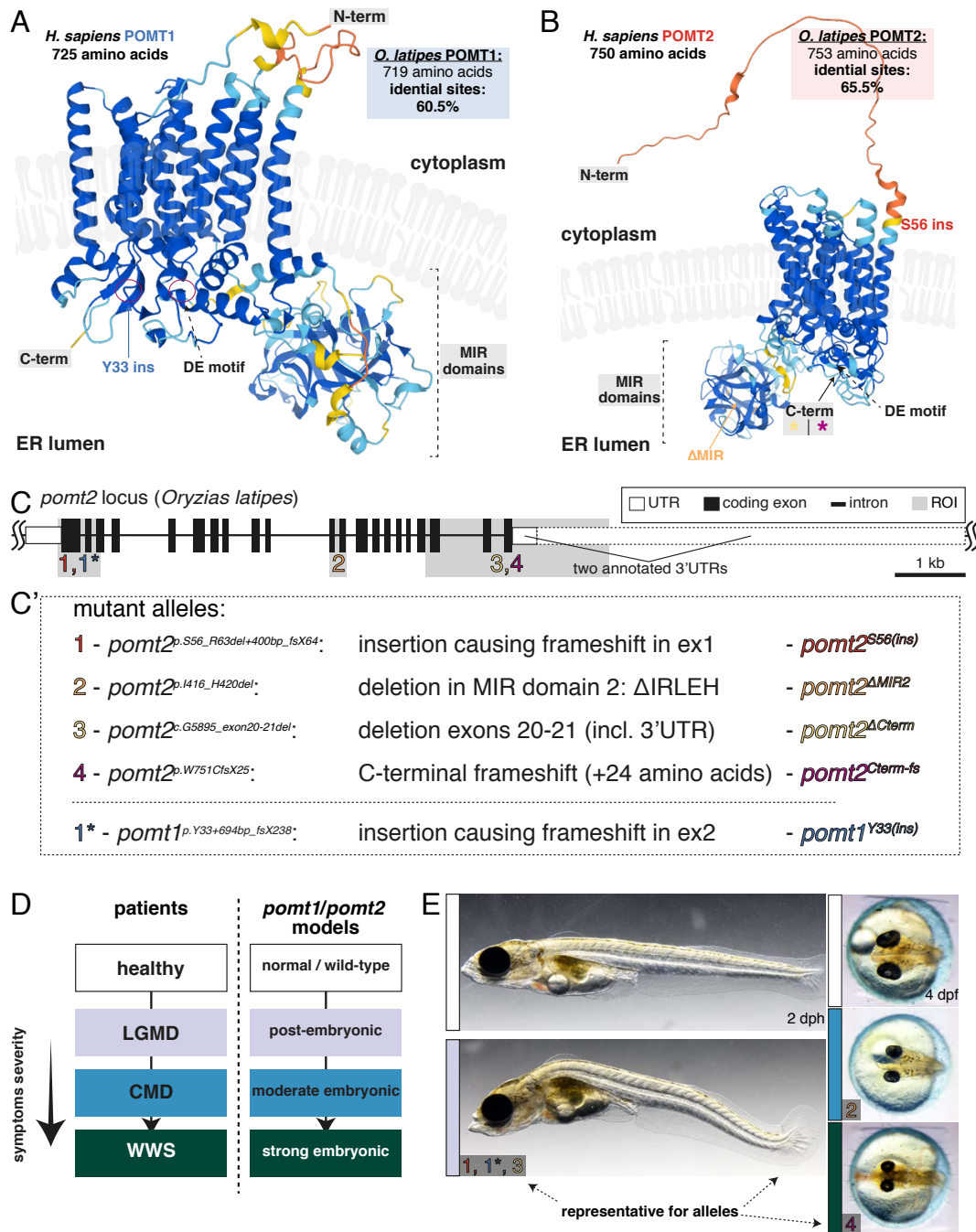


Figure 2.7: Overview of *potm1* and *potm2* mutant medaka alleles generated in this thesis. (A-B) Structures of human POMT1 (UniProt Q9Y6A1) (A) and POMT2 (UniProt Q9UKY4) (B) predicted by AlphaFold2 [Jumper et al., 2021; Varadi et al., 2022]. Note the annotation of mutations of mutant alleles summarised in (C'). (C) The medaka *potm2* gene locus. Regions referring to the mutants alleles in (C') are highlighted in gray. (C') A total of four stable *potm2* alleles (1-4), as well as one *potm1* allele (1*) were investigated. Alleles 1 and 1* are insertional alleles, leading to a frameshift or changes in pre-mRNA splicing. Alleles 2-4 are deletion alleles. (D-E) Side by side comparison of *POMT1/POMT2*-based DGpathy and medaka models, with exemplary mutants shown for each category. LGMD, Limb-Girdle Muscular Dystrophy; CMD, Congenital Muscular Dystrophy; WWS, Walker-Warburg Syndrome. (E) Alleles 1, 1* and 3 were not fully penetrant and not all homozygotes resulted in a phenotype. Dpf/dph = days post fertilisation/hatching.

Since its stop codon was removed it is unclear how the $pomt2^{\Delta Cterm}$ allele would be regulated on a transcript level. Following the deletion of three highly conserved amino acids WDF $pomt2^{Cterm-fs}$ results in a frameshift just before the STOP codon which adds a net total of 21 amino acids to the protein. In the process of establishing these alleles, I noticed two things. First, a similar, though, always variable spectrum of phenotypes reminiscent of DGpathies emerged. I observed this both in the stable lines and in compound heterozygous mutants (Fig. 2.7D-E). Second, neither the nature of the mutation (frameshift, in-frame deletion, insertion) nor the region of the gene mutated, were sensible predictors of phenotype severity.

Milder mutant alleles (1, 1* and 3) always displayed a varying combination of spinal deformities and reduced swimming capacity, and sometimes, but not always an enlarged yolk. These phenotypes indicated muscular dystrophy-like alterations and scoliosis-like (scoliosis and kyphosis) appearances with metabolic changes, reminiscent of the mild muscular dystrophy symptoms seen in Limb-Girdle Muscular Dystrophy patients (Fig. 2.7D-E). Notably, not all homozygotes and compound heterozygotes showed these phenotypes, indicating incomplete penetrance. I will discuss the statistics in the next section. On the other hand, the more severe embryonic brain and eye defects I saw in $pomt2^{\Delta MIR2}$ and $pomt2^{Cterm-fs}$ mutants were fully penetrant, and resemble the Congenital Muscular Dystrophy and Walker-Warburg Syndrome groups of disorders, respectively. Together, these mutants constitute an attractive resource to study dystroglycanopathies.

In the next three sections, I will look at the spectrum of dystroglycanopathies using the following the approaches:

- Analysing the mild Limb-Girdle Muscular Dystrophy-like $pomt2^{S56(ins)}$ allele (subsection 2.2.3).
- Using a base editing approach to disrupt the splice-donor of $pomt1$ and $pomt2$ to investigate Congenital Muscular Dystrophy -like phenotype (subsection 2.2.4) as fish of the $pomt2^{\Delta MIR2}$ allele were difficult to maintain and genotype.
- Characterising the Walker-Warburg Syndrome-like $pomt2^{Cterm-fs}$ allele (subsection 2.2.5, subsection 2.2.6).

Additionally, I performed several experiments that do not neatly fit into the flow of the following three sections and I have added them to the end of this chapter (subsection 2.2.7). This includes:

- Establishing a swim assay to assess dystroglycanopathy phenotypes.
- Using this assay to quantify the swimming behaviour of Limb-Girdle Muscular Dystrophy-like *pomt1*^{Y33(*ins*)} and *pomt2*^{S56(*ins*)} mutants.
- Knockdown of early *pomt2* transcripts.
- Using base editing to investigate the function of POMT2 aspartate (D) 92 of the DE motif in development.

2.2.3 LGMD-like *pomt2*^{S56(*ins*)} mutants are characterised by mild muscular dystrophy with muscle fibre ruptures but no retinal abnormalities

I have established the *pomt2*^{S56(*ins*)} mutants in my master's thesis [Cornean, 2017], in an attempt to generate translational null alleles. In brief, a linker-GFP-3x polyA cassette was constructed with a 5' homology flank, homologous to the end of the first coding exon of *pomt2*. The aim was to trigger the endogenous repair machinery by CRISPR/Cas9-induced DSBs. The repair pathways would recognise the repair template and insert it (Fig. 2.8A). Since I did not use a 3' homology flank, I assumed that several copies of the template could concatemerise, such that several of these insert one after the other from 5' to 3'. With the polyA signal present, the ribosomes would abort translation.

The allele that was isolated, however, did not contain the full donor sequence, but rather the 3' end of *EGFP* and the 5' end of the 3x pA signal (Fig. 2.8B). A PCR with primers flanking the insertion site can easily assess the presence of the mutant allele (Fig. 2.8C). Importantly, in addition to the insertion, five amino acids (P57-P62) were deleted out of frame, which leads to a downstream PTC 192 bp after the deletion site (Fig. 2.8D).

A central aspect of muscular dystrophy, muscle degeneration, has a progressive effect on the capacity to move the skeletal apparatus in vertebrates [Barresi and Campbell, 2006]. I therefore, established an assay that would allow me to quantify the swimming behaviour of *pomt2*^{S56(*ins*)} larvae (subsection 2.2.7). Interestingly, *pomt2*^{S56(*ins*)} mutants were mostly unaffected across stages, both under constant light and light-induced stress.

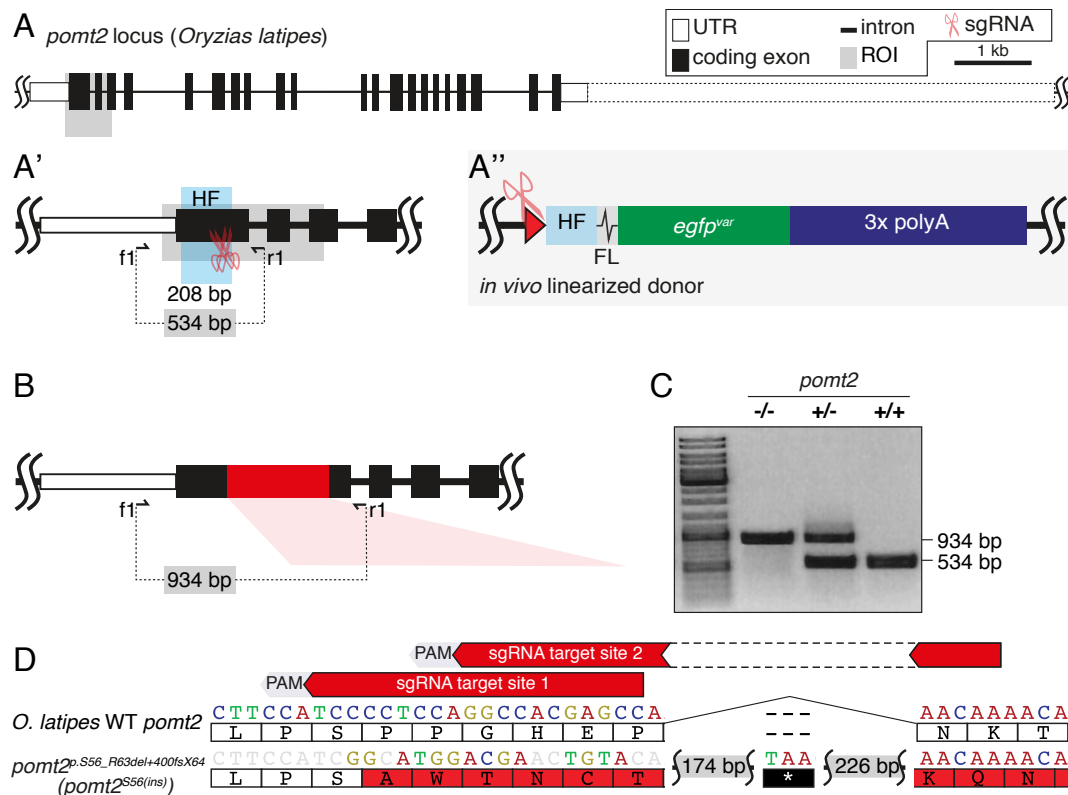


Figure 2.8: The *pomt2* knockout by knockin strategy used to generate N-terminal mutant alleles results in a *pomt2^{S56(ins)}* allele with mild postembryonic phenotypes. (A-A'') A 208 bp homology flank from the first coding exon of *pomt2* was cloned to generate a donor construct, containing a flexible linker (FL), the *EGFP^{var}* coding sequence and a triple polyA signal (A''). (B) The *pomt2^{S56(ins)}* allele in a stable fish line contains five out of frame deletions and the insertion of a 3' GFP to 5' 3x polyA 421 bp fragment. (C) A *pomt2* exon 1 locus flanking PCR can distinguish between insertion and wild-type allele. (D) The deletion/insertion in the *pomt2^{S56(ins)}* allele leads to a downstream PTC.

MZT *pomt2^{S56(ins)}* mutants display high rates of embryonic death and postembryonic muscular, skeletal and patterning defects

To overcome the compromising effect of penetrance in the mild mutants, I decided to investigate the phenotypic consequences of *pomt2^{S56(ins)}* in maternal zygotic mutants (MZT). I argued that the high levels of early *pomt2* transcripts, deposited by the mother were compensating for apparent phenotypes. I therefore, raised homozygotes to adulthood with the aim to cross these with each other. To identify homozygous *pomt2^{S56(ins)}* female carriers I genotyped 42 adult fish from fin clips. I identified only one homozygous escaper fish (2.4%), a female that allowed me to create MZT mutants. This suggests that 90% of *pomt2^{S56(ins)}* homozygotes died before they reached adulthood. I hypothesise that similar to DGpathy patients, mutant larvae will experience cardiac or respiratory arrest and cause premature death.

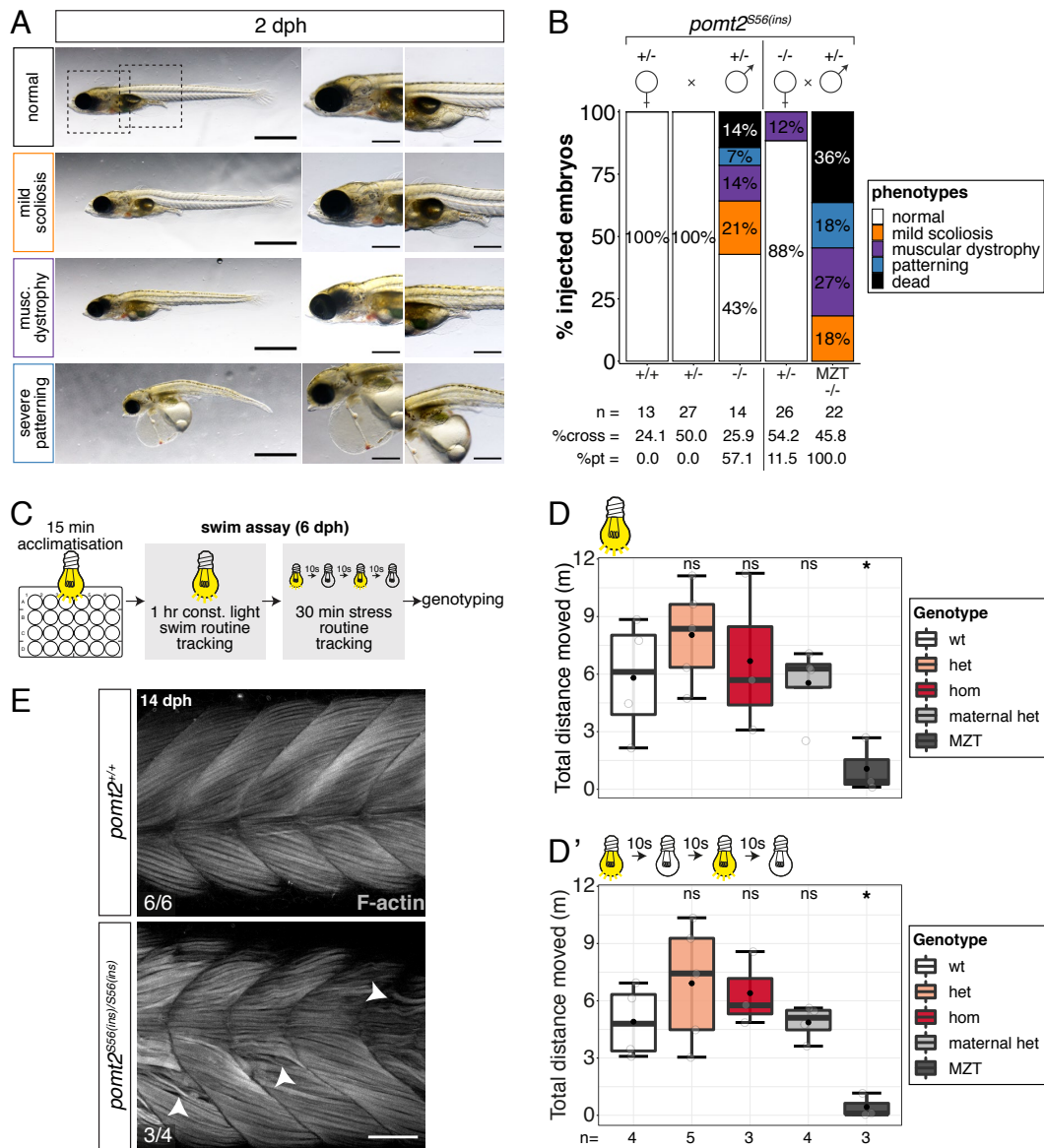


Figure 2.9: MZT *pomt2*^{S56(ins)} mutants display severe developmental defects. (A-B) Phenotype profile and quantification of phenotypes of *pomt2*^{S56(ins)} zygotic and maternal-zygotic (MZT) crosses at 2 dph. Scale bar = 1 mm, scale bar zoom in = 400 μ m. (C) Swim assay set-up of *pomt2*^{S56(ins)} zygotic and maternal-zygotic (MZT) crosses at 6 dph. (D-D') Quantification of larval movement by tracking larval locomotion in a 24-well plate under constant light for 1 hour at 6 dph. Bold line=median. Black circle=mean. Statistical analysis was performed in R using the one-way ANOVA test with wild-type larvae as the reference group. Global: D, $p = .048$; D', $p = .0099$. $p = .047$ (*, constant light MZT, D); $p = .013$ (*, stress MZT, D'). (E) Tails of 14 dph *pomt2*^{S56(ins)} zygotic mutants stained with phalloidin (actin) to visualise the degeneration of muscle bundles (white arrowheads). Scale bar = 100 μ m. Dph = days post hatching.

Of the remaining fish, 17 were wild-type for the *pomt2* gene (40.5%) and 24 were heterozygotes (57.1%) (see %cross). I next set up two crosses. The first cross was a heterozygous *pomt2*^{S56(ins)} incross, which expectedly, only led to 8 of 14 homozygotes to display phenotypes at 2 dph (Fig. 2.9A-B). These phenotypes were mostly mild displays of scoliosis / kyphosis (3 of 14), muscular

dystrophy with an apparent reduction of swimming capacity (2 of 14) and embryonic lethality (2 of 14). Importantly, neither wild-type nor heterozygotes from this cross showed any phenotypes. On the other hand, crossing a heterozygous *pomt2*^{S56(*ins*)} male to the homozygous female, resulted in aberrant phenotypes or embryonic death in all MZT mutants. A substantial fraction (8 of 22) died before hatching. I saw signs of scoliosis / kyphosis in 4 MZT larvae, whereas 6 MZT mutants had an evident muscular dystrophy phenotype, with signs of deterioration and were unable to swim. The most severe phenotypes (4 of 22) were observed in hatchlings that combined a wide range of phenotypes, including cardiac edema with a streaky, tubular heart, craniofacial and forebrain defects, and deformed lens, spinal and muscular deformities and global tissue damage. Interestingly, it seems that the lack of maternal *pomt2* alone can result in muscular dystrophy phenotypes in zygotic heterozygotes, pinpointing a tight temporal regulation on the level of the POMT complex.

To confirm the lack of swimming ability I performed the swim assay with MZT mutants at 6 dph. Here, I tracked larval movement over 1 hour with constant light, followed by 30 min of light on/off stress (Fig. 2.9C). During the swim assay with constant light, MZT displayed close to no movement averaging 1.1 ± 1.4 m over one hour ($p=.047$), as opposed to 5.8 ± 3.1 m and 6.7 ± 4.2 m by wild-type and homozygous larvae, respectively. I observed the same trend under light-induced stress with 0.4 ± 0.6 m travelled by MZT ($p=.0099$), and 4.9 ± 1.9 m and 6.4 ± 1.9 m by wild-type and homozygous larvae, respectively (Fig. 2.9D-D'). I next wanted to understand, whether normally swimming homozygous *pomt2*^{S56(*ins*)} larvae developed and maintained muscles normally or whether the muscular defects were insufficient to impair movement. I assessed the integrity of muscle fibres in 14 dph homozygotes using phalloidin to stain for filamentous (F-)actin. Muscle fibres appeared disrupted in various instances, however, not overall affected in 3 of 4 larvae (Fig. 2.9E).

These results show that mutant allele levels greatly impact the phenotypic outcome, with the lack of early *pomt2* turning mild LGMD-like mutant characteristics into severe CMD-like phenotypes. I next addressed the functional consequences on the retina in *pomt2*^{S56(*ins*)} larvae.

The retinal architecture is unaffected in *pomt2*^{S56(*ins*)} mutants – splicing to the rescue?

I used cryosections of 14 dph larvae to analyse the structure of the retina in *pomt2*^{S56(*ins*)} homozygotes. Interestingly, the structure of the retina and in particular the photoreceptors, labelled by Rx2, appeared unaltered (Fig. 2.10A-B). It is worth noting that the retina of zebrafish *pomgnt1* mutants was normal at 2 months. Photoreceptors-loss was only observed in 6 month old fish [Liu et al., 2020]. Moreover, the conditional, retina-specific KO of mouse *pomt1* only resulted in modest structural alterations of the retina, in particular, a thinning of the photoreceptor layer in adult mice [Rubio-Fernández et al., 2018; Uribe et al., 2021].

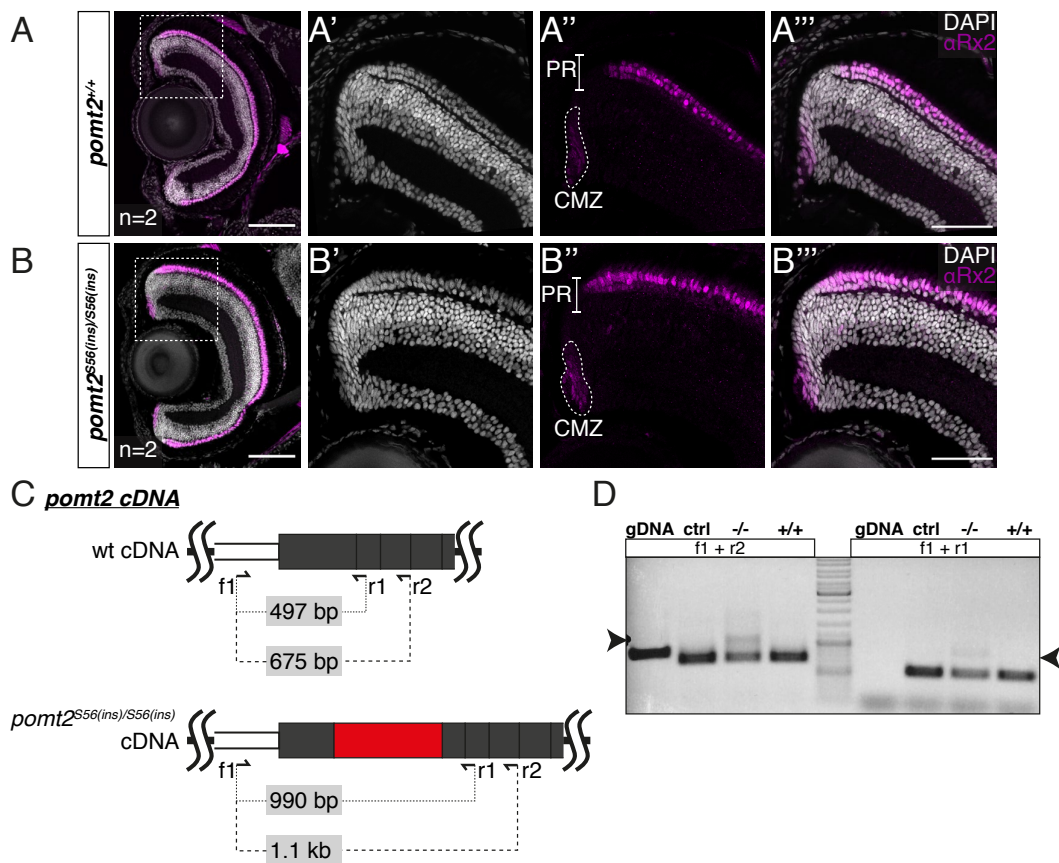


Figure 2.10: Normal retinal architecture in zygotic *pomt2*^{S56(*ins*)} mutants is accompanied by changes in splicing. (A-B) Cryosections of wild-type (A) homozygous *pomt2*^{S56(*ins*)} mutant (B) retinæ of 14 dph larvae stained for Rx2 (magenta; A'', B'') with DAPI counterstaining highlighting nuclei (grey; A', B'). Overlays are shown in panels A, A'' and B, B'' for overview images and zoom-in images on the dorsal retina. The dotted area indicates the stem and progenitor zone, CMZ (ciliary marginal zone), whereas the vertical bar indicates the photoreceptors in the outer nuclear layer. Scale bar = 100 µm, scale bar zoom in = 50 µm. Dph = days post hatching. (C-D) cDNA analysis of wild-type and homozygous *pomt2*^{S56(*ins*)} mutant hatchlings without apparent phenotype reveals alternative splicing of the insertion. The PCR product of mutant cDNA containing the insertion is indicated by arrowheads run on a 1% agarose gel (D).

To address the possibility that one of the factors that leads to milder or absent phenotypes in some *pomt2*^{S56(*ins*)} homozygotes is a change in splicing, I analysed the cDNA of homozygous hatchlings (2 dph) without apparent phenotype (Fig. 2.10C). Homozygotes express the mutant transcript, containing the PTC, however, these mutants express a larger fraction of a wild-type sized allele (Fig. 2.10D). This change can stem from the use of an alternative splice donor-acceptor pair, that may have emerged on the boundary of the insertion, but needs further scrutiny.

In conclusion, maternal transcription and splicing may impact the phenotypic outcome of DGpathy models as highlighted by *pomt2*^{S56(*ins*)} homozygotes. This yet again strengthens the notion that cellular and molecular machineries, wherever possible, are compensating to overcome any aberrant cellular consequences in cells harbouring mutations.

2.2.4 Splice-donor *pomt2* editants recapitulate embryonic CMD-like phenotypes

I next used the base editors I introduced earlier to probe the function of both *pomt1* and *pomt2* by generating null alleles. To achieve this I decided to introduce splice-donor (SD) mutations as these were suggested to be the most efficient type of mutation to disrupt a gene's function [Kluesner et al., 2021]. I designed sgRNAs aimed at the complementary strand that would install SD mutations changing the -GT- to a -GC- using ABE8e. I targeted the first exon-intron boundary of *pomt1* and the second exon-intron boundary of *pomt2* (Fig. 2.11A).

Interestingly, in *pomt2-e2-SD* editants I observed phenotypes that are highly reminiscent of CMD-like embryonic phenotypes (Fig. 2.7) in 34 of 52 embryos (brain and patterning groups). Among these were brain alterations in the forebrain and midbrain (brain/eye group, n=23), which were more severe in embryos with altered patterning (n=11). The changed position and arrangement of guanophores indicates changes in cellular movements during preceding developmental stages (Fig. 2.11B-C). Disrupting the exon1-SD in *pomt1*, however, did not result in obvious malformations. Surprisingly, editants with both *pomt1-e1-SD* and *pomt2-e2-SD* point mutations showed lower rates of phenotypes, such as CMD-like brain alterations, than *pomt2-e2-SD* editants alone. Only 14 of 62 showed CMD-like brain abnormalities.

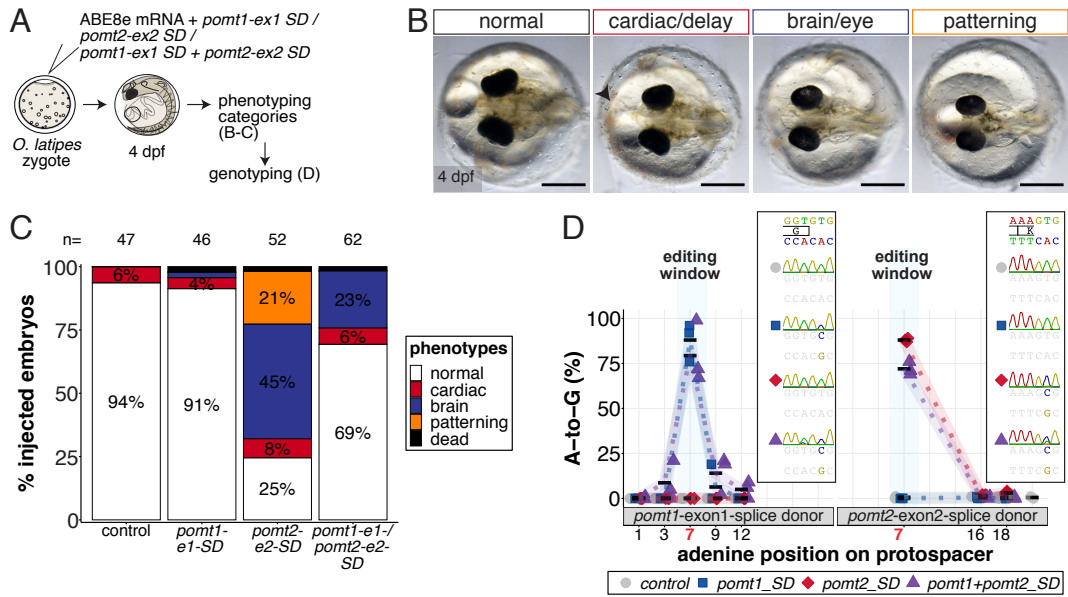


Figure 2.11: Splice-donor editants of *pomt2* recapitulate moderate embryonic, CMD-like phenotypes (A) Experimental setup to investigate the effects of *pomt1* and *pomt2* splice donor (SD, GT) mutations at the exon1-intron and exon2-intron boundary, respectively, in editants. (B) Phenotype profile of *pomt1-ex1-SD*, *pomt2-ex2-SD* and *pomt1/pomt2-SD* editants at 4 dpf. Scale bar = 400 μ m. (C) Quantification of phenotypes of editants at 4 dpf. (D) Adenine base editing efficiency quantified from Sanger sequencing reads of target amplicons using EditR analysis. Dpf = days post fertilisation.

These observations can be, at least in part, explained by the slightly reduced base editing efficiencies in the double gene editants. I achieved editing at both sites simultaneously with an average -GT- to -GC- efficiency of $79.3 \pm 17.2\%$ at *pomt1* and $72.0 \pm 3.6\%$ at *pomt2* (n=3, each) (Fig. 2.11D). By contrast, I could edit the *pomt1-ex1-SD* alone with $88.0 \pm 10.6\%$ efficiency (n=3) and *pomt1-ex1-SD* alone with $88.0 \pm 1.0\%$ efficiency (n=3). Considering that the disruption led to frequent CMD-like phenotypes a reduction of 16% of editing may account for the reduced frequency of phenotypes. These results also suggest that the function of *pomt1* may be less important than that of *pomt2* during vertebrate development. More likely, however, is that some sort of compensation occurred at the level of splicing.

2.2.5 Disrupted cell migration causes severe WWS-like, embryonic brain and eye defects in *pomt2*^{Cterm-fs} mutants

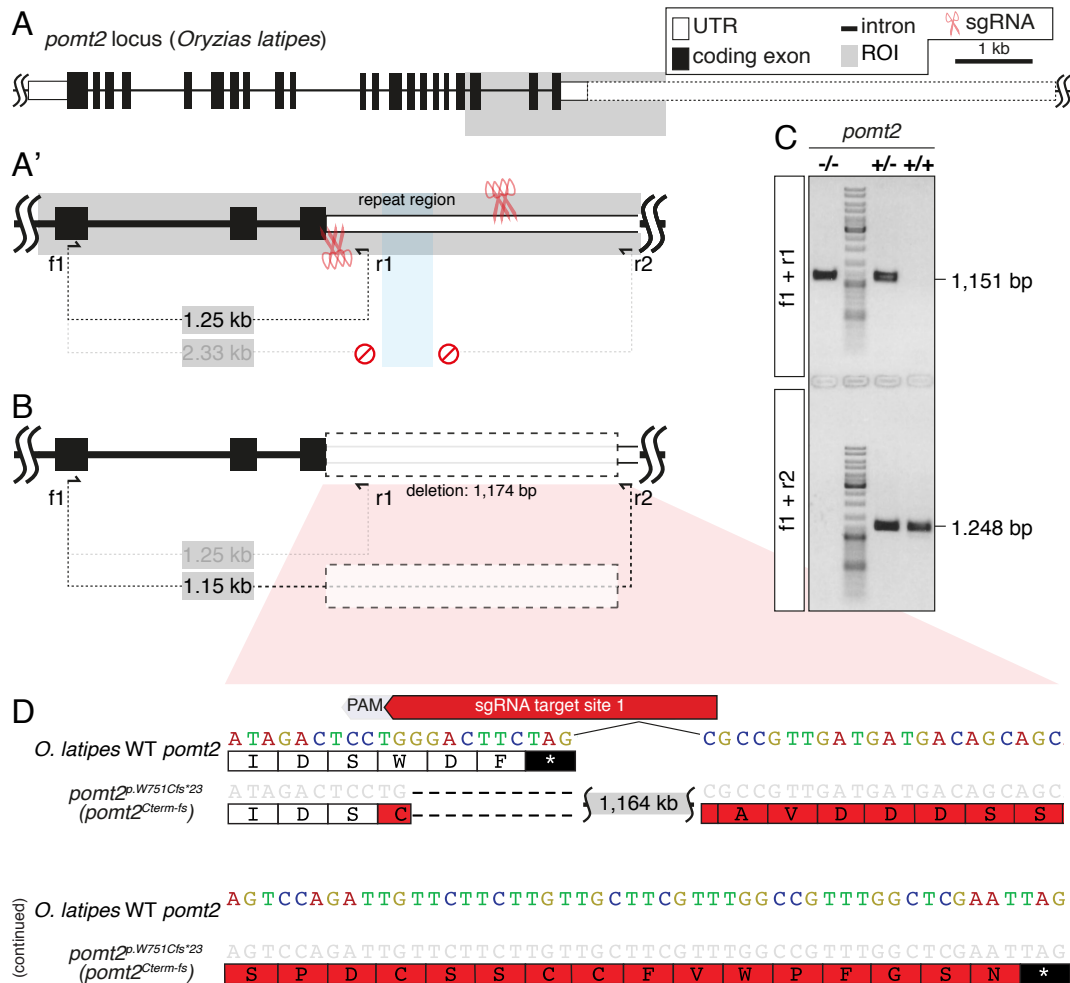


Figure 2.12: A 3'UTR deletion strategy leads to the isolation of the severe *pomt2*^{Cterm-fs} allele. (A) Four sgRNAs, two at the 3' end of the *pomt2* coding sequence and two sgRNAs within the 3'UTR were used to create CRISPR/Cas9 based deletion mutations. Note: while the f1+r1 primer combination can amplify the wild-type sequence of *pomt2* at the 3' end, it is not possible to amplify the region including a repeat region (light blue) using f1+r2 primer pairs. (B) The CRISPR/Cas9 deletion strategy results in the deletion of an almost 1.2 kb sized DNA segment including the last two amino acids and a substantial part of the 3'UTR. The absence of the repeat region allows amplifying over the boundaries of the deletion site with f1+r2, while the binding site for r1 is now missing. (C) The combination of f1+r1 and f1+r2 PCR allows to easily distinguish the wild-type and the mutant allele. (D) Sequencing of genomic DNA and cDNA, isolated from homozygotes, indicates a frameshift after the highly conserved tryptophan 751 residue accompanied by a deletion, that replaces the C-terminal amino acids WDF with a 24 residue serine and glutamate-rich peptide.

The C-terminus of POMT2 is highly conserved, resides within the endoplasmic reticulum (ER) in the vicinity of the mannosyltransferase (Fig. 2.7B) and

several mutations associated with severe DGpathies indicate its essential role in POMT1 and POMT2 function [Bai et al., 2019; Geis et al., 2019]. I decided to create a mutant allele that contains larger deletions of this region, including a deletion of the 3' UTR, which would likely perturb the mRNA-based downstream process [Mayr, 2019].

I used a CRISPR/Cas9 strategy with four sgRNAs, two at the 3' end of the *pomt2* coding sequence and two roughly 1 kb downstream. Following this approach I isolated several alleles in the following generations. These included *pomt2*^{ΔCterm} and *pomt2*^{Cterm-fs} (Fig. 2.7C). To understand the processes that lead to the WWS-like phenotypes I decided to focus on *pomt2*^{Cterm-fs} (Fig. 2.12A). A large portion of the 3' UTR is deleted including the last 7 nucleotides of the coding sequence and the STOP codon (Fig. 2.12B). This results in a frameshift that virtually replaces the last three amino acids WDF with a 24 amino acid peptide stretch, rich in serines and glutamates (Fig. 2.12D). I observed this as well on cDNA isolated from homozygotes. A repeat region on the deleted segment of the 3' UTR typically prevents PCR amplifying across this region. Since this repeat region is deleted in the mutant I could use a set of two PCRs to easily distinguish wild-type and mutant alleles (Fig. 2.12C).

The C-terminal extension of POMT2 results in diminished global levels of the POMT1/POMT2 complex in *pomt2*^{Cterm-fs} embryos

To assess the effect of the frameshift mutation in *pomt2*^{Cterm-fs} mutants on *pomt1/pomt2* expression I next performed a semi-quantitative RT-PCR on RNA isolated from stage 34 mutants. To normalise transcripts I used the housekeeping gene *GAPDH*. Interestingly, while *pomt2* transcripts were slightly reduced to 73±4% in homozygotes (93±38% in heterozygotes), *pomt1* mRNA levels were almost halved in homozygotes (53±19%) and moderately reduced in heterozygotes (65±21%) (Fig. 2.13A). I next assessed whether the change in protein size, by the net addition of 21 amino acids, is visible as a 2-3 kD band shift on a Western blot. I observed a clear upward shift and a striking reduction in POMT2 levels accompanied by almost absent levels of POMT1 in the homozygotes (Fig. 2.13B).

These results indicate that the C-terminal protein extension of POMT2 dramatically destabilises the protein complex and diminishes POMT1 protein in the *pomt2*^{Cterm-fs} mutant. Moreover, the reduction in *pomt1* mRNA in heterozygotes suggests that the mutant allele might be dominant-negative. Even heterozygous levels of mutant POMT2 may reduce the level of the POMT1/POMT2 complex.

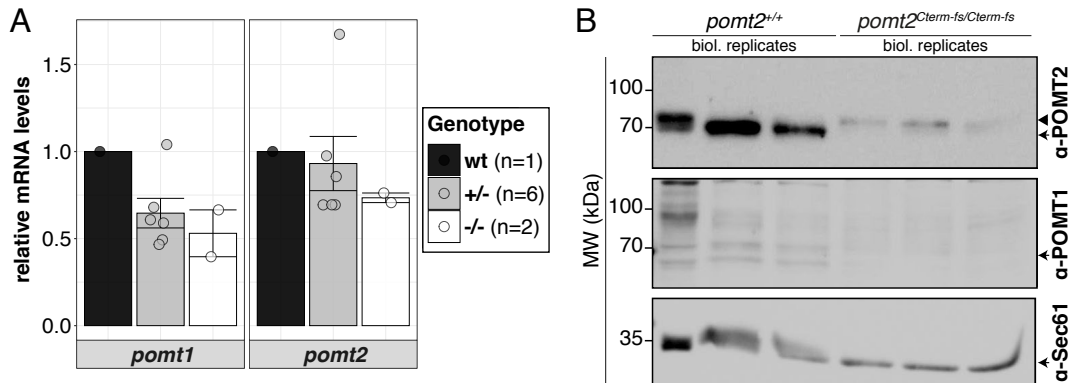


Figure 2.13: Reduced levels of *pomt1/pomt2* transcript and POMT1/POMT2 protein in stage 34 *pomt2*^{Cterm-fs} mutants. (A) Semi-quantitative RT-PCR analysis of wild-type, heterozygous and homozygous *pomt2*^{Cterm-fs} mutant cDNA from single stage 34 embryos (5 days post fertilisation). Approximately 200 bp exon spanning PCR products for *pomt1* and *pomt2* cDNA were run on a 2% agarose gel and bands were normalised to *GAPDH*. The error bar indicates the mean with the standard error. (B) Immunoblot on 30 μ g membrane fractions from stage 34 wild-type (pool of 20 per sample) and mutant embryos (pool of 40 per sample), detecting Sec61 (loading control), POMT1 and POMT2. Arrow, wild-type protein band. Triangle, mutant protein band. Note the reduction of POMT1 and POMT2 and the size increase of remaining POMT2 protein detected in homozygotes.

A time course of *pomt2*^{Cterm-fs} development reveals clear defects in midbrain, forebrain and eye development with secondary heart defects

I next investigated the morphological changes that occurred in the central nervous system in developing *pomt2*^{Cterm-fs} mutants. I followed the development of embryos from a heterozygous cross starting before the striking phenotypes emerge, usually between stages 27-29 (Fig. 2.14A-D). At stage 20 the three regions of the brain, forebrain, midbrain and hindbrain are already spatially established. This process is initiated during gastrulation and the three brain regions become more defined by stage 22.

While embryos develop normally otherwise the interhemispheric fissure appears to be less pronounced. This observation is suggestive of a mild form of holoprosencephaly, a disorder in which the embryonic forebrain fails to properly

develop into two hemispheres. At stage 24 the isthmus fold at the midbrain-hindbrain boundary is visibly less pronounced with overall flattened midbrain. By stage 29 both forebrain and midbrain defects are very apparent, which is accompanied by a strong reduction in eye size and brain-wide cell or tissue death. These changes are consolidated in later developmental stages and persist until the hatching stage when embryos typically die. Mutants become trapped between partially dissolved chorion (eggshell) and are unable to move to break free.

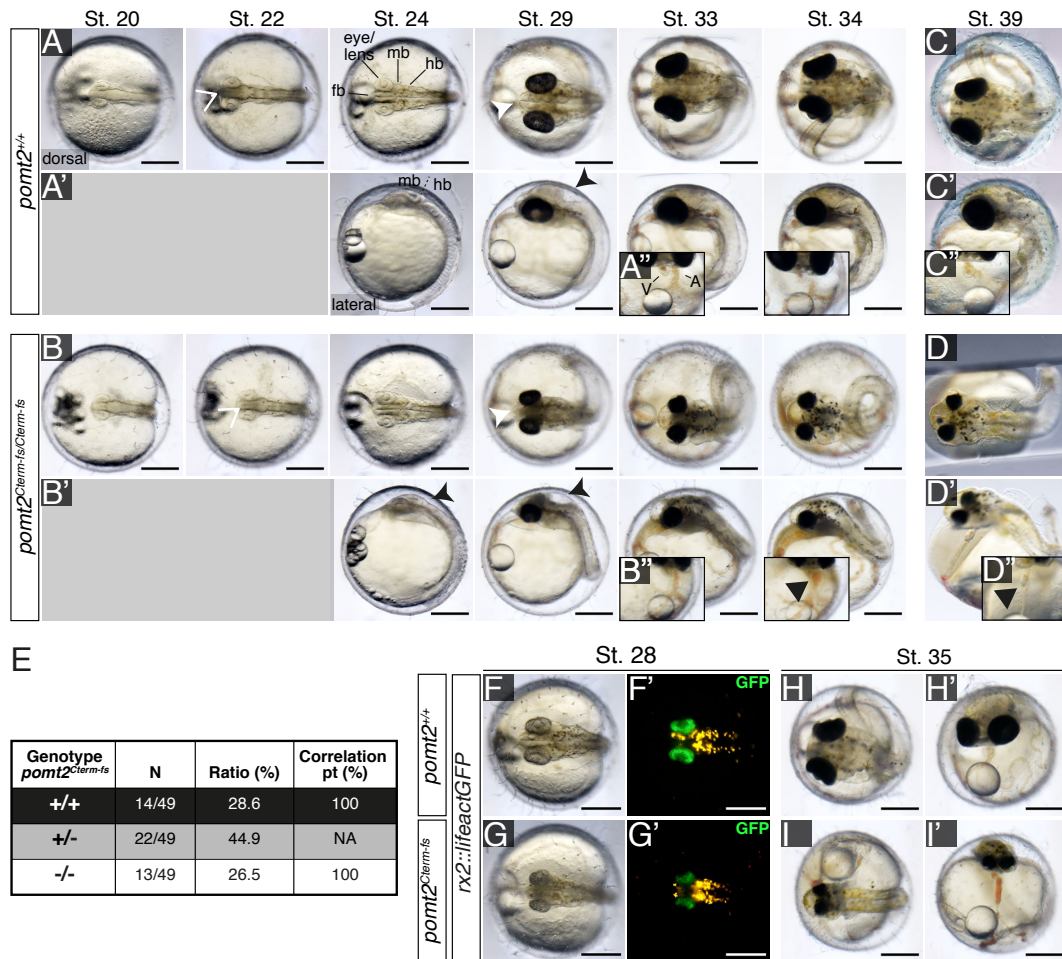


Figure 2.14: Time course of $pomt2^{Cterm-fs}$ mutant embryonic development. (A-D'') Wild-type (A-A'', C-C'') and $pomt2^{Cterm-fs}$ mutant (B-B'', D-D'') development from early brain regionalisation stages (stage 20) to hatching stage (stage 39, C-C'' and D-D''). Fb = forebrain, mb = midbrain, hb = hindbrain. Note: clear changes in the interhemispheric fissure along the entire brain axis (white arrow) at stage 22 (B), in midbrain development (black arrowhead) at stages 24 and 29 (B'), forebrain development (white arrowhead) at stage 29 and secondary changes of the ventricle (black triangle) beginning at stage 34 (B'') resulting in a highly tubular, streaky heart (D'-D''). (E) Genetics of $pomt2^{Cterm-fs}$ mutants reveal a 100% correlation of homozygotes with the phenotype. (F-I') Wild-type (F-F', H-H') and $pomt2^{Cterm-fs}$ mutant (G-G', I-I') development in a retinal cell reporter ($rx2::lfeactGFP$) background. Scale bar = 400 μ m. Note: stage 22 = 1.5 dpf; stage 29 = 3 dpf; stage 34 = 5 dpf; stage 39 = 8-9 dpf. Dpf = days post fertilisation.

Interestingly, the heart develops normally until stage 33, but then the atrium begins to stretch downwards, away from the ventricle and becomes tubular by stage 39 (Fig. 2.14A-D", H-I'). Unlike the milder *pomt2*^{S56(*ins*)} mutants, the phenotype was fully penetrant and I could see the severe brain and eye phenotypes in all examined homozygous *pomt2*^{Cterm-fs} mutants (n=13) (Fig. 2.14E). Moreover, heterozygotes appeared to be unaffected which contradicts my initial hypothesis of the *pomt2*^{Cterm-fs} being dominant-negative. I next crossed the *pomt2*^{Cterm-fs} mutants to a *rx2::lifeactGFP* reporter to visualise developing retinal cells at early developmental stages. Both the size of the eye but also the density of retinal cells, evident by the drop in fluorescence intensity signal are affected in stage 28 mutants (Fig. 2.14F-G).

To visualise the interhemispheric fissure defects at greater resolution, I next performed antibody stainings on wholemount heads from stage 22 wild-type and mutant embryos. While both the retina and the midbrain appeared normally developed, there was a modest, though apparent change in the width of the forebrain fissure. In particular the interhemispheric fissure fold appeared to be absent (Fig. 2.15A-B).

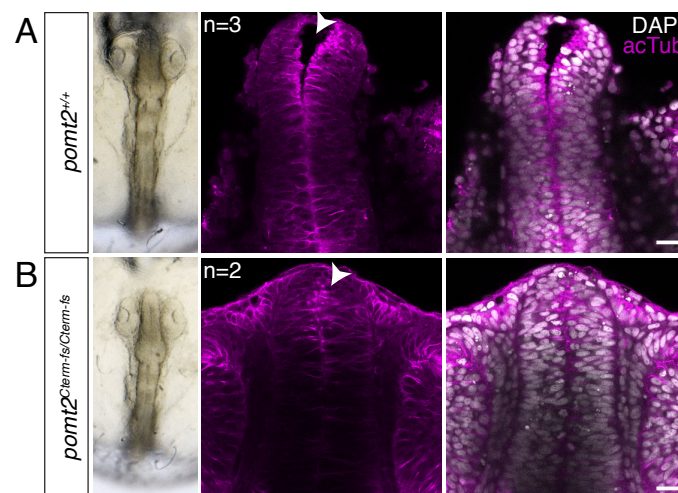


Figure 2.15: *Pomt2*^{Cterm-fs} mutants display inter-hemispheric fissure defects in the forebrain at stage 22. (A-B) Heads of stage 22 control (A) and *Pomt2*^{Cterm-fs} mutants (B) staining neurites with acetylated tubulin (magenta). DAPI was used as counterstain to label nuclei (gray). Single optical section, with white arrowheads indicating the absence of interhemispheric fissure fold of the forebrain in mutants (B). Scale bar = 50 μ m.

These results are in accordance with previous observations on a DGC-dependent loss of cerebral morphology in both glial cell-specific *DAG1* and brain-specific *POMT2* knockout mice [Hu et al., 2011; Moore et al., 2002]. Evidence suggests that these forebrain defects are a result of aberrant neuronal cell migration and resemble those observed in cobblestone lissencephaly in severe DGpathy patients [Nakano et al., 1996; Nickolls and Bönemann, 2018]. I hypothesise that neuronal cell migration is also the cause of the early brain defects in *pomt2*^{Cterm-fs}.

By stage 24, the morphological changes of the forebrain became more striking and were accompanied by increased rates of apoptosis (Fig. 2.16A-D). In addition to the absence of a diencephalic ventricle (Fig. 2.16D), *pomt2*^{Cterm-fs} mutants also showed changes in midbrain morphology, and the isthmus fold of the midbrain-hindbrain boundary (Fig. 2.16A-B). Moreover, mutant retinæ were more loosely packed and showed widespread signs of apoptotic cells, suggesting that migratory defects are also a cause of the severe retinal alterations (Fig. 2.16E-F).

These suggestive migratory defects resulted in a widespread disorganisation of the central nervous system at later stage 28 *pomt2*^{Cterm-fs} mutants (Fig. 2.17A-D). The dorsal midbrain displayed high levels of apoptosis and the tectal ventricle was absent. Moreover, the diencephalic ventricle shrank substantially. These changes coincided with a massive disorganisation of the retina. While fish do not have a cerebral cortex the strong dorsal directionality of the brain phenotype strikingly resembles that of cobblestone lissencephaly phenotypes of *DAG1* and *POMT2* mouse models of DGpathies [Hu et al., 2011; Satz et al., 2010]. In addition to high levels of apoptosis as seen by TUNEL positive cells, it was striking that a large fraction of the central retina displayed evident signs of pyknosis. Pyknosis is a conserved process of irreversible condensation of chromatin that occurs in both apoptosis and necrosis [Burgoyne, 1999; Hou et al., 2016].

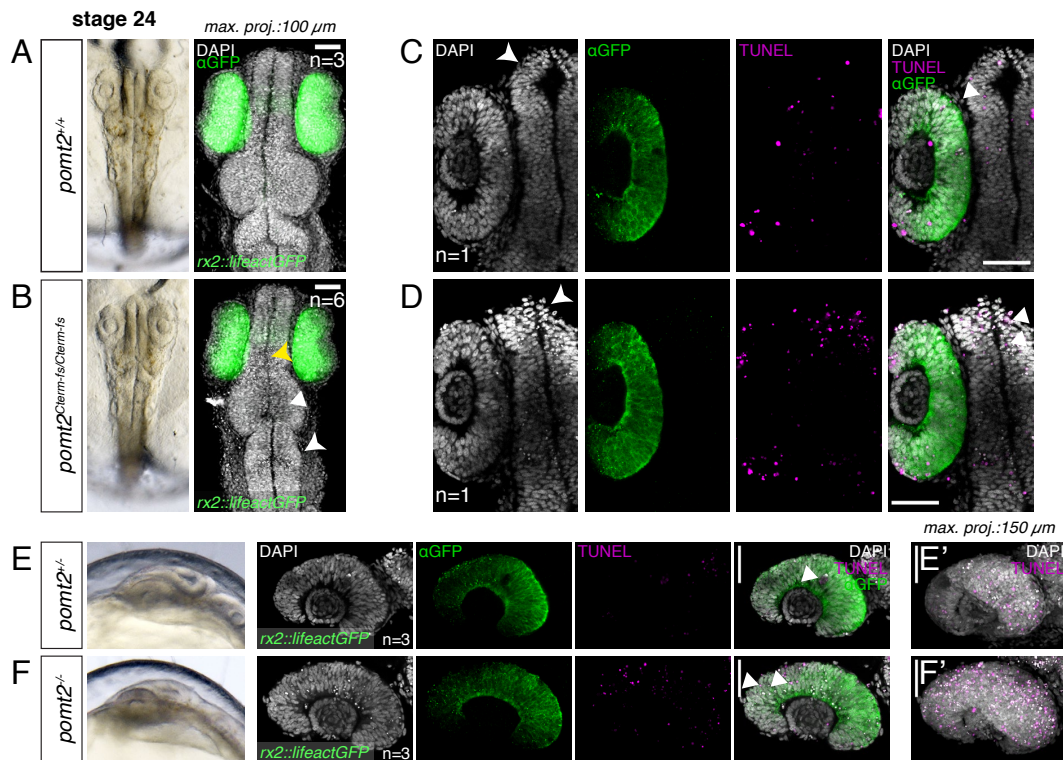


Figure 2.16: Striking forebrain and midbrain defects of stage 24 *pomt2*^{Cterm-fs} mutants are accompanied by increased levels of apoptosis in the brain and the retina. (A-F) Heads and retinas of stage 24 control (A, C, E) and homozygous *pomt2*^{Cterm-fs} mutants (B, D, F) in a retinal cell reporter (*rx2::lfeactGFP*) background, staining retinal cells with GFP (green) and apoptotic cells using the TUNEL assay (magenta). DAPI was used as counterstain to label nuclei (gray). (A-B) Maximum projection of 100 optical sections with a z-step size of 1 μm . White arrowhead indicates defects in the isthmus fold. White triangle and yellow arrowhead indicate morphological changes in the midbrain. (C-D) Single optical section, with white arrowheads indicating the clear absence of interhemispheric fissure fold and diencephalic ventricle of the forebrain in mutants that is accompanied by increased levels of apoptotic cells (white triangles) (D). (E-F') Lateral view on single optical sections of the retina and maximum projections (E',F'), with increased levels of retinal apoptosis (white triangles). Scale bar = 100 μm .

As these strongly condensed nuclei showed only weak terminal deoxynucleotidyl transferase dUTP nick end labeling (TUNEL) signal they were either cells at the beginning of apoptosis before widespread DNA fragmentation occurred or necrotic cells. The latter would suggest that the severe phenotypes I observed in my DGpathy *pomt2* model are not only a final consequence of widespread apoptosis but also necrosis. Interestingly, in addition to the high levels of apoptosis in the dorsal part of the brain, the central part shows signs of pyknotic cells (Fig. 2.17B). As I did not see these nuclear condensations at stage 24 when I observed increased levels of apoptosis, apoptosis and pyknosis may be the endpoints of two different cellular processes malfunctioning. Necrosis has been previously only described for the muscular dystrophy symptoms in DGpathy patients [Martin, 2005]. It will be exciting to further define these cell

death processes, as non-steroidal anti-inflammatory drugs such as ibuprofen may help ameliorate the most severe symptoms in WWS patients when given prenatally [Cheung and Tidball, 2003].

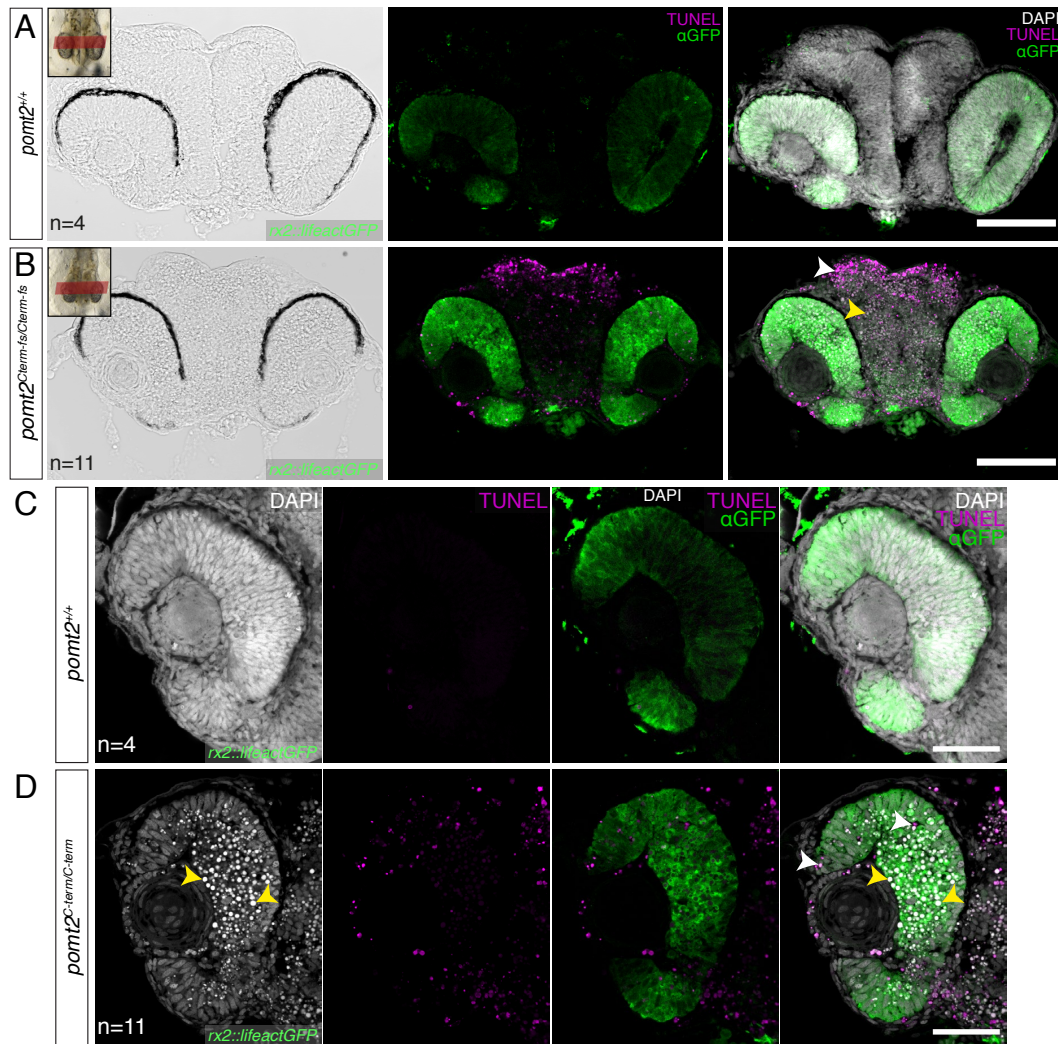


Figure 2.17: Striking brain and eye defects in stage 28 *pomt2^{Cterm-fs}* mutants are a consequence of widespread cell death. (A-D) Transverse sections of stage 28 control (A, C) and homozygous *pomt2^{Cterm-fs}* mutants (B, D) in a retinal cell reporter (*rx2::lfeactGFP*) background. Retinal cells were stained with GFP (green) and apoptotic cells were visualised using the TUNEL assay (magenta). DAPI was used as counterstain to label nuclei (gray). Note the increase of apoptotic cells in the optic tectum of the dorsal midbrain (white arrowheads) and the absence of the tectal and diencephalic ventricles in mutants with pyknotic cells (yellow arrowheads) (B). Mutant retinæ show broad and widespread apoptosis (white arrowheads) and high levels of pyknotic cells (yellow arrowheads) in the central retina as seen by bright DAPI signal (D). Scale bars = 200 µm (A-B), 100 µm (C-D).

2.2.6 RNA-sequencing analysis of *pomt2*^{Cterm-fs} mutant development

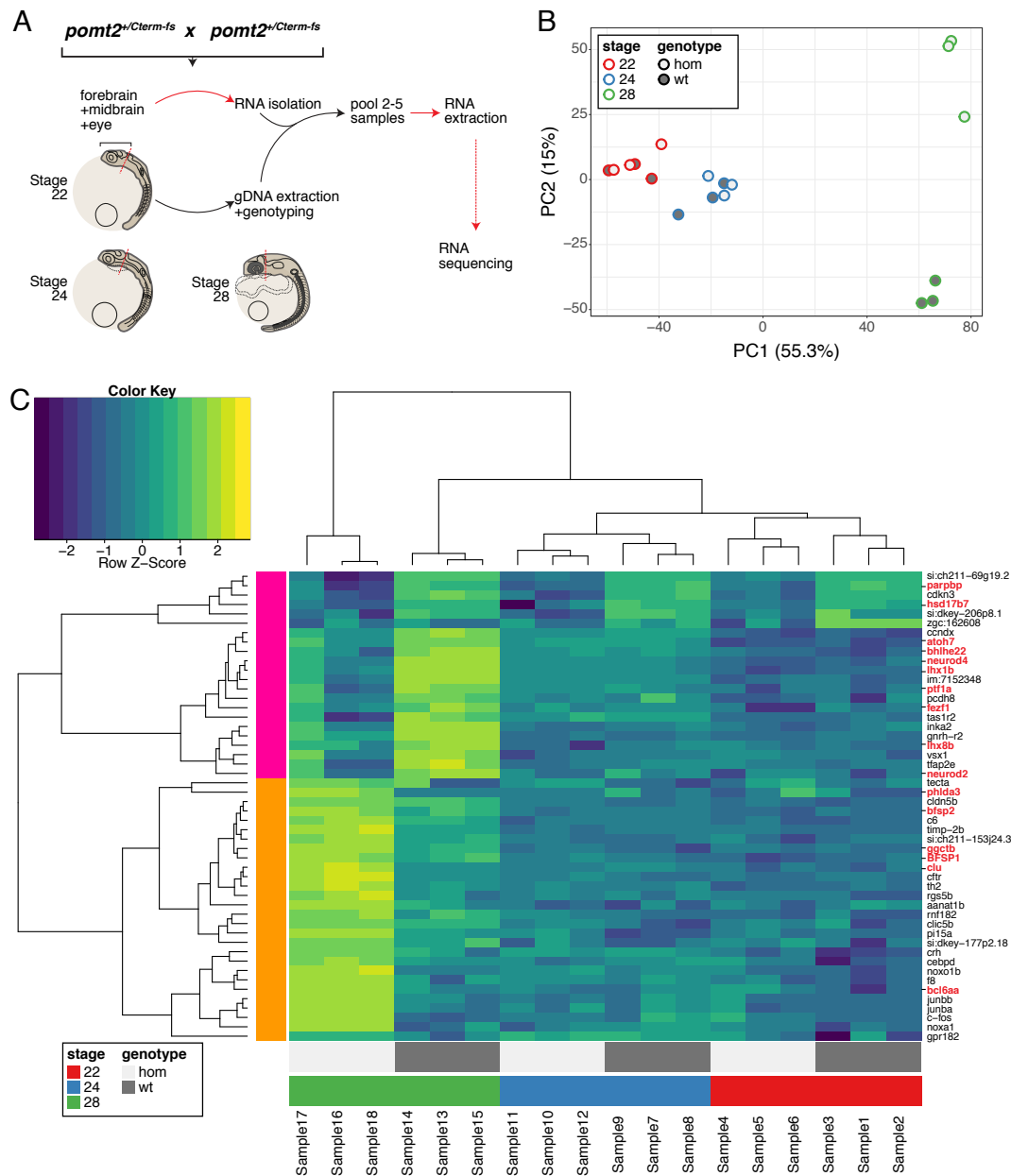


Figure 2.18: A transcriptome of *pomt2*^{Cterm-fs} mutant development. (A) RNA isolation and sequencing (RNAseq) approach of stage 22, stage 24 and stage 28 wild-type (wt) and homozygous *pomt2*^{Cterm-fs} mutant (hom) pooled tissues of forebrain, midbrain and eyes. Each condition was sampled in triplicates. (B) Principal component analysis (PCA) of RNASeq datasets obtained brain samples of stage 22 (red circle), stage 24 (blue circle) and stage 28 (green circle) wild-type (dark grey fill) and homozygous (light-grey fill) embryos. (C) Heatmap of log₂-transformed expression values of genes with FDR < 0.01 and log₂ fold change ≥ 2. Unsupervised hierarchical clustering of genes using the Pearson method and unsupervised hierarchical clustering of samples using the Spearman method. Yellow denotes high expression and blue low expression.

To complement these structural insights of the *pomt2*^{Cterm-fs} mutant model with mechanistic insights of *pomt2*-based DGpathies I assessed the transcriptome of brains of stage 22, stage 24 and 28 wild-type and homozygotes. Specifically, I dissected the brain at the midbrain-hindbrain boundary to perform whole transcriptome RNA sequencing (RNASeq) on brain/eye samples excluding the hindbrain (Fig. 2.18A).

Preliminary analysis of the data indicates that stages 22 and 24 cluster closely together and no clear transcriptome-wide difference is present between wild-type and homozygous brains (Fig. 2.18B). Since only 6 hours separate these stages temporally, it is not surprising that they are not highly different (stage 22, 1 day 14 hours post fertilisation (hpf); stage 24, 1 day 20 hpf; Iwamatsu [2004]). By contrast, stage 28 (2 days 16 hpf) is clearly distinct from the other stages and wild-type and homozygous samples separately clearly. Moreover, I identified several differentially expressed genes, however, this still need to be examined in more detail (Fig. 2.18C). In brief, unsupervised hierarchical clustering identified two groups of genes of which the log₂-transformed expression values fulfilled the following, very stringent requirements: FDR < 0.01 (after Benjamini–Hochberg adjustment) and log₂ fold change ≥ 2. These were a total of 50 genes, with on the one hand downregulated (pink) and upregulated genes in homozygotes (orange).

A subgroup of the pink cluster was already present at stage 22 and included DNA repair (*parpbbp*) and cholesterol biosynthesis/homeostasis (*hsd17b7*) genes [Marijanovic et al., 2003; Moldovan et al., 2012]. Interestingly, several of the genes downregulated in homozygous stage 28 samples were involved in neural (*ccndx*, *lhx1b*, *neurod2*, *neurod4*, *fezf1*) or retinal (*ptf1a*, *atoh7*, *bhlhe22*, *neurod4*) precursor differentiation/development [Ganz et al., 2011; Ivanov, 2019; Lien et al., 2016; Lust et al., 2016; Runge et al., 2021; Saturnino et al., 2018; Shimizu and Hibi, 2009]. By contrast, there was an increase in apoptosis-related (*clu*, *phlda3*) and lens/cataract (*BFSP1*, *bfsp2*) associated gene expression in homozygous stage 28 mutant samples [Kim et al., 2011; Liu et al., 2021; Song et al., 2009]. These results confirm the presence of increased apoptotic gene expression programs in stage 28 mutants as well as a striking downregulation of neural and retinal differentiation programs.

Taken together, I have shown that the *pomt2*^{Cterm-fs} mutants are an excellent model to further investigate the early neurodevelopmental defects occurring in WWS patients. I demonstrated that uncharacterised processes result in the progressive misdeveloping of both the forebrain and the midbrain and I hypothesise defective cell migration to be the main cause. Moreover, these defects are later intensified by high levels of apoptosis in the brain and apoptosis and necrosis in the retina. I detected the molecular signatures for these apoptotic events by forebrain/midbrain/retina-wide transcriptome analysis and revealed that the brains of these mutants significantly reduced neural differentiation and proliferation programs. Whether the cell death processes are a direct consequence of defective cell migration or perhaps an ancillary mechanism that may involve defect signalling pathways remains to be addressed. This first demonstration of necrosis would open the door to the very first treatments of central nervous system symptoms in severe DGpathy patients. Finally, the secondary heart defects in my WWS model have not been previously described and may be useful to better understand the WWS pathophysiology.

In this chapter, I have used a combination of CRISPR-based genetic models to study the extremes in the spectrum of DGpathies and transient approaches to further elucidate particular developmental functions of *pomt2*. The data I have presented here highlights a *pomt2*^{S56(ins)} mutant that displays post-embryonic muscular dystrophy phenotypes and, or scoliosis / kyphosis. Transcriptional regulation, however, results in incomplete penetrance of this allele, only overcome in MZT mutants. This raises the question of whether healthy patients may be carriers for homozygous or compound heterozygous mutant *POMT1* or *POMT2* alleles that are compensated by splicing processes. The WWS *pomt2*^{Cterm-fs} model faithfully recapitulates the CNS defects and I revealed that widespread cell death pathways are a large contributor to the pathophysiology.

In the next chapter (section 2.3), I will take a step forward and take a closer look at the known substrates of the POMT1-POMT2 complex. I use both highly efficient CRISPR/Cas9 gene editing and precise base editing. With these tools, I take a look at the general function of these proteins, their contributions toward DGpathy phenotypes and the function of annotated *O*-man sites.

2.2.7 Appendix

A swim assay to assess DGpathy phenotypes

I conceived an experimental set-up that would allow assaying the swimming capacity of freely swimming medaka larvae in consecutive stages of postembryonic development (Fig. 2.19). A similar, albeit one dimensional assay, was recently used to assess the swimming behaviour of a *fkrp*^{-/-} zebrafish mutant model of LGMD [Serafini et al., 2018]. Larvae from 2 dph onwards are transferred to transparent 24-well plates and placed inside an observation chamber (DanioVision, Noldus) (Fig. 2.19A-A”).

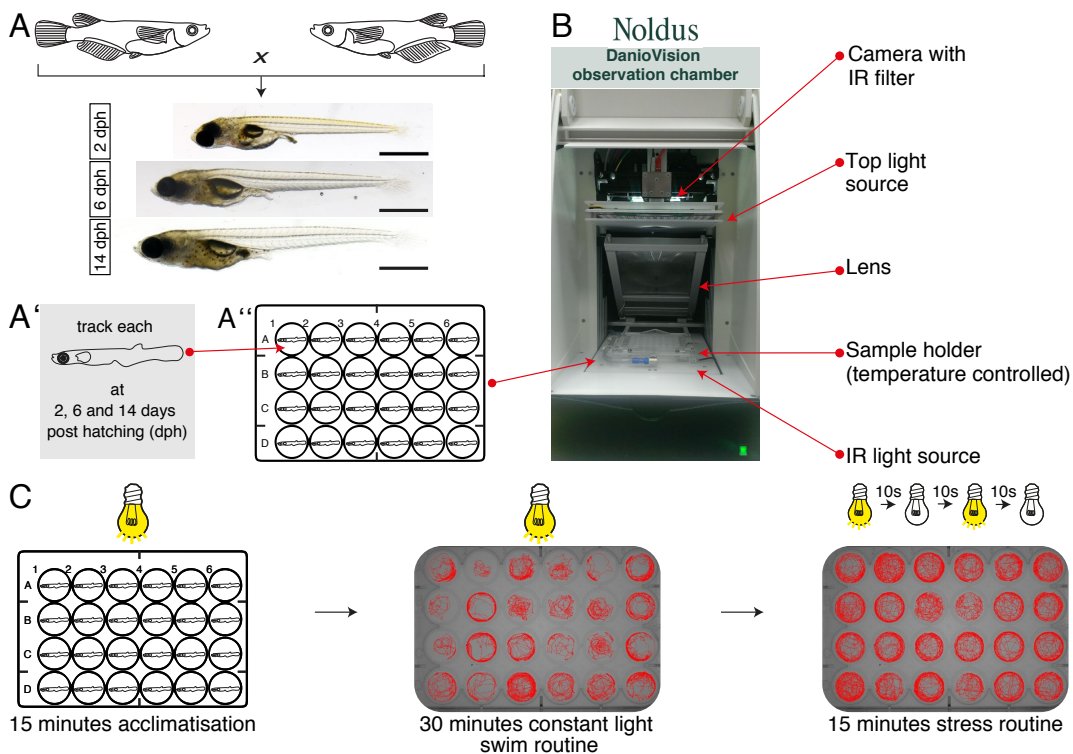


Figure 2.19: A simple locomotion assay can determine the swimming behaviour of freely swimming medaka larvae. (A-A”) Medaka embryos are raised to hatching and larvae are assayed at three time points in a transparent 24-well plate. After each assay, larvae are kept separate until the next time point to assay, e.g. from 2 to 6 dph, and fed daily. Scale bar = 1 mm. (B) The DanioVision system allows on-line tracking of freely swimming larvae placed within a central arena in a multi-well plate. By using an infrared (IR) light source and IR camera that is directly coupled to a computer running the tracking software (EthoVision, Noldus) the system can directly output parameters including distance travelled, average velocity and others. The observation chamber is fully light isolated, which allows to control and program an internal light source. Additionally, the sample holder is connected to a water flow system that maintains a set temperature by a temperature control unit. (C) Larvae acclimatise in the chamber for 15 min and then tracking begins for 30 min with constant top light. Afterwards, the light is programmed to switch from on to off mode every 10 seconds and the swimming behaviour is tracked for 15 min. Dph= days post hatching.

This chamber uses infrared (IR) light that is detected by an IR camera to

monitor the movement of larvae and can do so both in light and darkness. The camera is coupled to a computer running a commercial tracking software (EthoVision, Noldus) that will output metrics such as distance moved, average velocity or the number of movements in a given time window (Fig. 2.19B). Since these metrics capture essentially the same physiological phenotype, I chose to focus on the total distance that the hatchlings moved. After larvae acclimatised in the chamber, their movement was tracked for 30 min with constant top light and then 15 min during 10 sec light on / 10 sec light off stressor routine (Fig. 2.19C). I then kept the 2 dph larvae separate until 6 dph, repeated the assay, kept them separate until 14 dph and repeated the assay a final time.

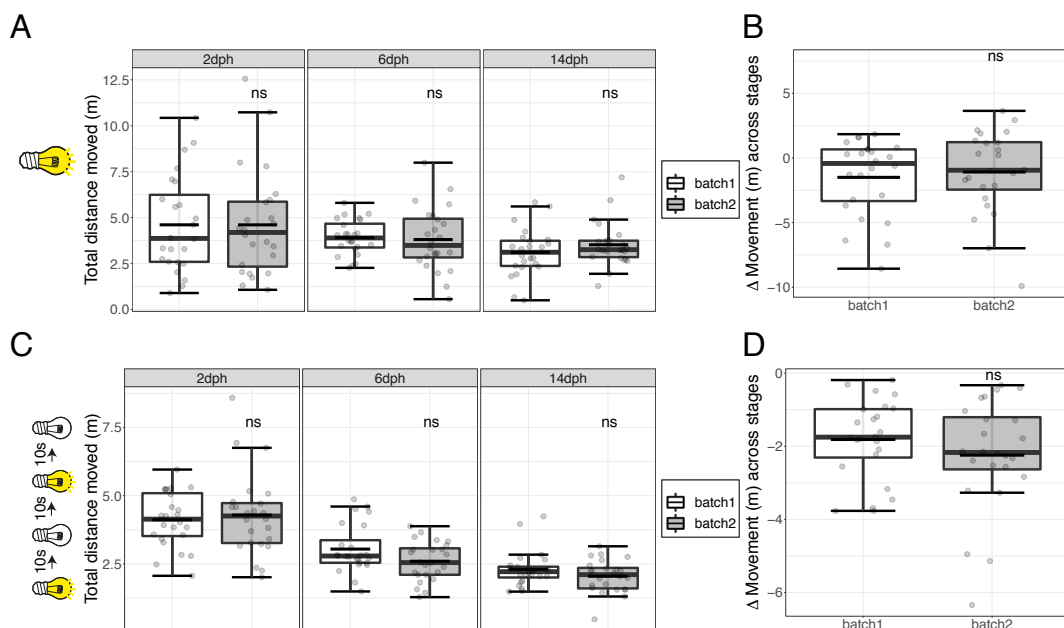


Figure 2.20: Larval movement across post-embryonic stages in wild-type medaka. (A,C) Quantification of larval movement of two larvae from two separate clutches (batch 1 and 2; $n=24$, each) at 2, 6 and 14 dph under constant light (A) and during a stress routine (C). (B,D) Movement change between 2 dph and 14 dph under constant light (B) and during a stress routine (D). Δ Movement was calculated as the difference between the Total distance moved at 14 dph and 2 dph for individual larvae. Gray full line = median. Black halfline = mean. Statistical analysis was performed in R using the Student's T test with batch 1 larvae as the reference group. ns indicates statistically insignificant p values: ns $p > .05$. Dph = days post hatching.

I could obtain developmental changes in movement across stages that were reproducible for wild-type animals during both constant and stressed conditions (Fig. 2.20A, C). Moreover, the results I obtained from two independent clutches (batch 1 and 2) were also reproducible when assessing the increase or decrease in swimming behaviour from 2 dph to 14 dph. I calculated this change as

14 dph distance (m) – 2 dph distance (m) (Δ Movement (m)), per individual, for both constant and stress conditions (Fig. 2.20B, D).

LGMD-like *pomt1*^{Y33(*ins*)} and *pomt2*^{S56(*ins*)} mutants show no reproducible reduction in swimming behaviour

I next used the established assay to investigate the phenotypic consequences of the two mild *pomt1*^{Y33(*ins*)} and *pomt2*^{S56(*ins*)} alleles on muscular function. As I indicated earlier, however, potential phenotypes in homozygous mutants did not surface in larvae. Instead, both *pomt1*^{Y33(*ins*)} (blue) and *pomt2*^{S56(*ins*)} (red) mutants were unaffected in almost all conditions across stages, both under constant light (Fig. 2.21A-A') and stressed conditions (Fig. 2.21B-B'). Interestingly and unexpectedly, *pomt2*^{S56(*ins*)} homozygotes showed an increase in swimming capacity under constant light at 2 dph of 4.7 ± 2.9 m vs 2.6 ± 0.8 m in wild-type siblings and of 5.1 ± 1.6 m vs 3.4 ± 1.5 m at 14 dph. The changes across development from 14 dph vs. 2 dph (14 dph distance (m) – 2 dph distance (m), per individual) were also comparable in wild-type and both mutants (Fig. 2.21C-D).

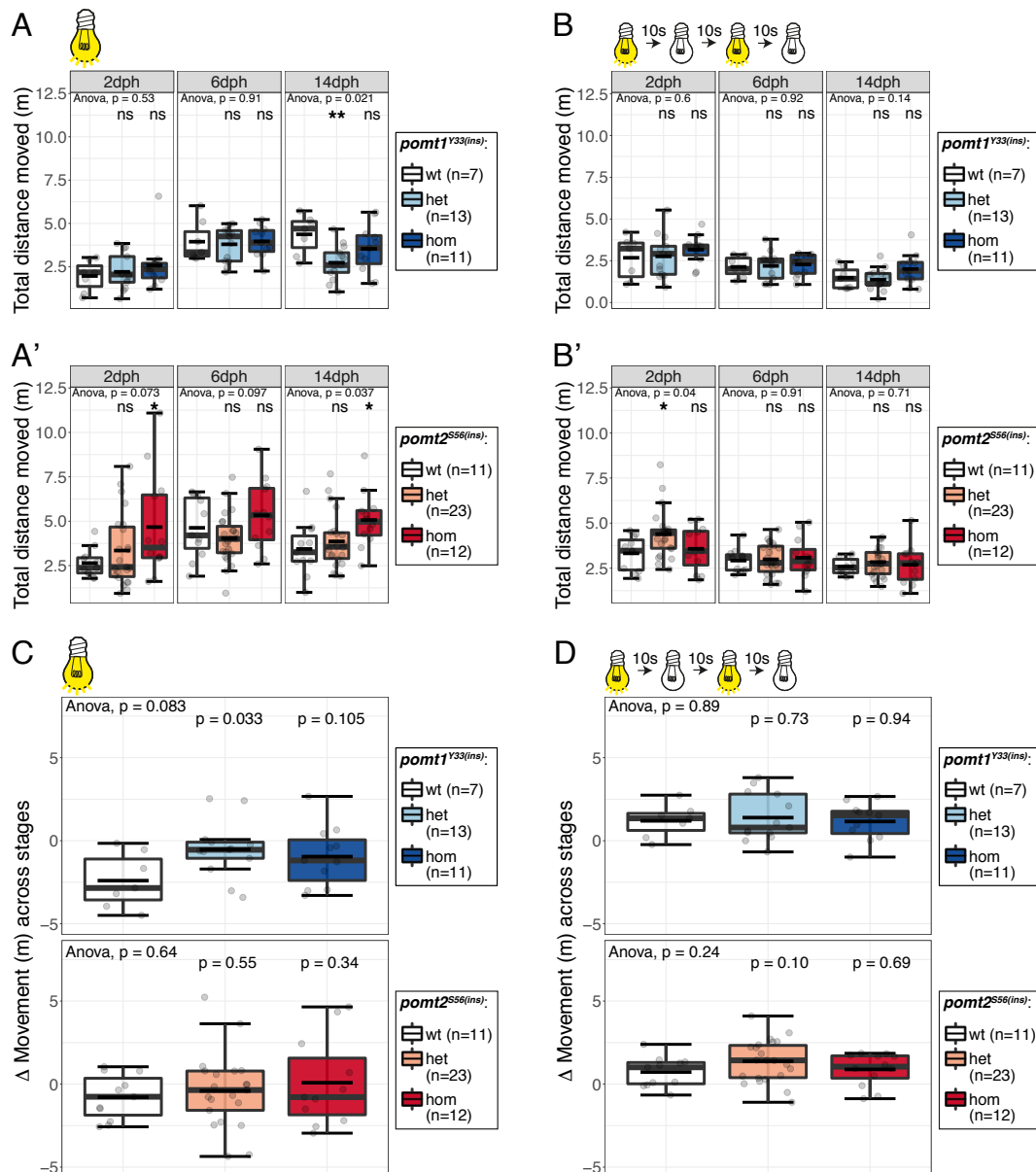


Figure 2.21: Larval movement across post-embryonic stages in *pomt1*^{Y33(*ins*)} and *pomt2*^{S56(*ins*)} mutants shows no quantifiable changes. (A-B) Quantification of larval movement of offspring from heterozygous *pomt1*^{+/Y33(*ins*)} and *pomt2*^{+/S56(*ins*)} incrosses at 2, 6 and 14 dph under constant light (A-A') and during a stress routine (B-B'). (C-D) Movement changes between 2 dph and 14 dph under constant light (C) and during a stress routine (D). Δ Movement was calculated as the difference between the Total distance moved at 14 dph and 2 dph for individual larvae. Gray full line = median. Black half line = mean. Statistical analysis was performed in R using the one-way ANOVA test with wild-type (wt) larvae as the reference group. Asterisks indicate p values: ** $p \leq .01$, * $p \leq .05$, ns $p > .05$. Dph = days post hatching.

A reduction of maternal *pomt2* transcript leads to a low frequency of DGpathy-like phenotypes

The few cases of phenotypes resulting from heterozygous *pomt2*^{S56(*ins*)} mutants without maternal *pomt2* suggested that differential expression levels are crucial

when it comes to *O*-man. To address the role of maternal *pomt2* transcript, I used the *Ruminococcus flavefaciens* strain XPD3002 Cas13d (RfxCas13d) system to transiently knockdown *pomt2* [Koner mann et al., 2018]. The use of three RfxCas13d guide RNA (gRNA)s was suggested to efficiently result in the knockdown of early transcripts in medaka [Kushawah et al., 2020]. I, therefore, used three gRNAs spread across the *pomt2* transcript to reduce the levels of *pomt2* mRNA (Fig. 2.22A). I verified the success of the knockdown by qRT-PCR on stage 9 embryos and observed a 0.48 ± 0.06 fold reduction of *pomt2* (Fig. 2.22B).

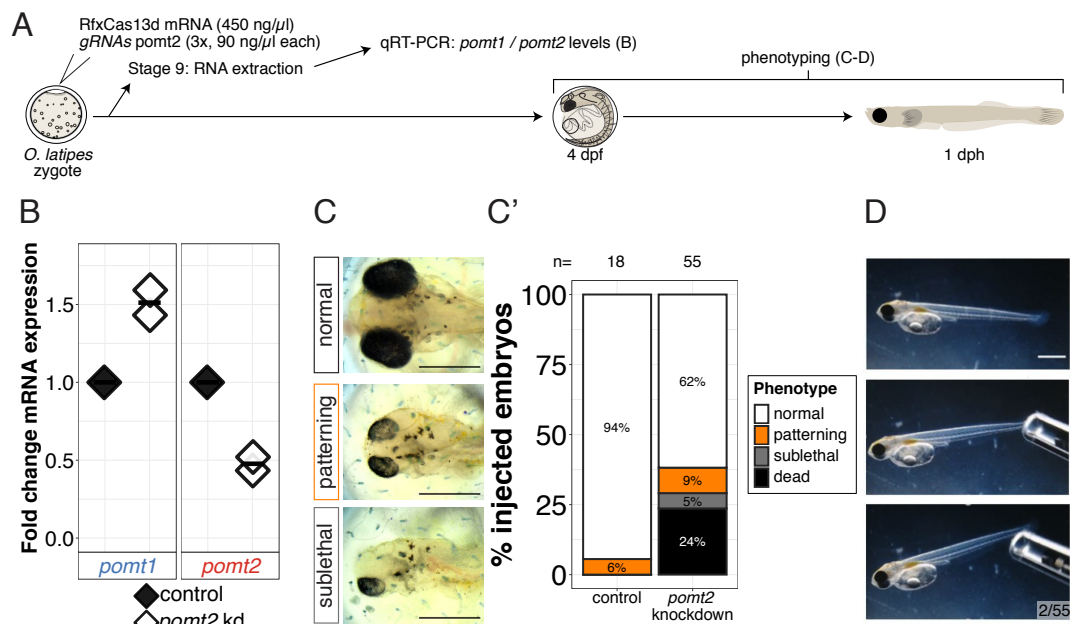


Figure 2.22: Reducing maternal *pomt2* transcript results in a low frequency of DGpathy phenotypes. (A) Microinjection of RfxCas13d and *pomt2* gRNAs for mRNA knockdown into zygotes is followed by RNA extraction at stage 9 (late morula) with subsequent RT-qPCR analysis (B), or phenotyping at 4 dpf (C) and hatching, respectively (D). (B) Transcript analysis of *pomt1* and *pomt2* following *pomt2* knockdown by RT-qPCR. Control (RfxCas13d only), n=1; *pomt2* knockdown, n=2. (C) Phenotyping following *pomt2* knockdown reveals early embryonic phenotypes as a consequence of defective gastrulation and neurulation. Scale bar = 400 μ m. (D) *Pomt2* knockdown hatchlings show rare muscular dystrophy phenotypes and are non-responsive to touch. Scale bar = 1 mm.

Interestingly, as a possible compensatory mechanism, *pomt1* levels increased 1.51 ± 0.11 fold, which indicates that net levels of *pomt1/pomt2* remained unaltered. As the zygotic genome becomes active between stages 7-8 [Kraeussling et al., 2011], compensation may indeed play a role. In line with the moderate reduction in *pomt2* levels and possible compensation, not all knockdown embryos and only a small fraction of hatchlings showed phenotypes. 13 of 55 embryos died during early development and only 8 embryos showed developmental defects (patterning or sublethal) at 4 dpf (Fig. 2.22C-C'). Finally, at hatching

stage 7 larvae showed sublethal phenotypes and were unable to hatch, while I observed the loss of mobility in 2 larvae (Fig. 2.22D). These results suggest that maternal *pomt2* mRNA may play a role during early developmental processes of gastrulation or neurulation.

The POMT2 aspartate (D) 92 residue of the DE motif is dispensable for embryonic and early postembryonic muscle and retinal function

Given the high efficiency of ABE8e, I decided to investigate the developmental function of the highly conserved DE motif [Lommel et al., 2011], for which a critical role has been ascribed to both POMT1 and POMT2. Experiments with the yeast orthologue of *pomt1*, *pmt4*, showed that p.D80A results in a relative enzyme activity of only 3% *in vitro*.

I assessed the phenotypes of p.D92G editants by assaying their movement at 14 dph over the course of 1 hour with constant light (Fig. 2.23A). Surprisingly, the total distances that control and p.D92G editants swam, were very similar with 25.3 ± 6.9 m and 26.8 ± 7.4 m (Fig. 2.23B). I also could not see a correlation between the editing efficiency and the phenotypic consequence for a subset of larvae that I genotyped. I mapped the efficiencies of p.D92G onto the distance on the y axis that an individual moved on a blue (0%) to yellow (100%) colour space (Fig. 2.23C). I observed average efficiencies of $78.3 \pm 12.8\%$, which may not have been sufficient to cause substantial changes to muscular function (Fig. 2.23D). To assess the retinal phenotype I used the heads of editants with high editing efficiencies (99% and 100%) to perform cryosections of the retina. Immunoreactivity of Zpr1 which labels photoreceptors did not indicate any photoreceptor-specific alterations (Fig. 2.23E-G). Moreover, I could not see any changes in glycosylated α -DG (IIH6C, green), stem and progenitor cells (Rx2, magenta) or general retinal architecture (DAPI, nuclei and F-actin) (Fig. 2.23H-I).

Since yeast PMT4 forms a homodimer the strong drop in activity in p.D80A mutants may stem from the fact that in these dimers two of four acidic amino acids are removed. This is in contrast to the situation in vertebrates and would suggest that to address this problem I would have to simultaneously mutate the DE motif of both *pomt1* and *pomt2*. Alternatively, mutating both amino acids on *pomt2* may result in the same outcome.

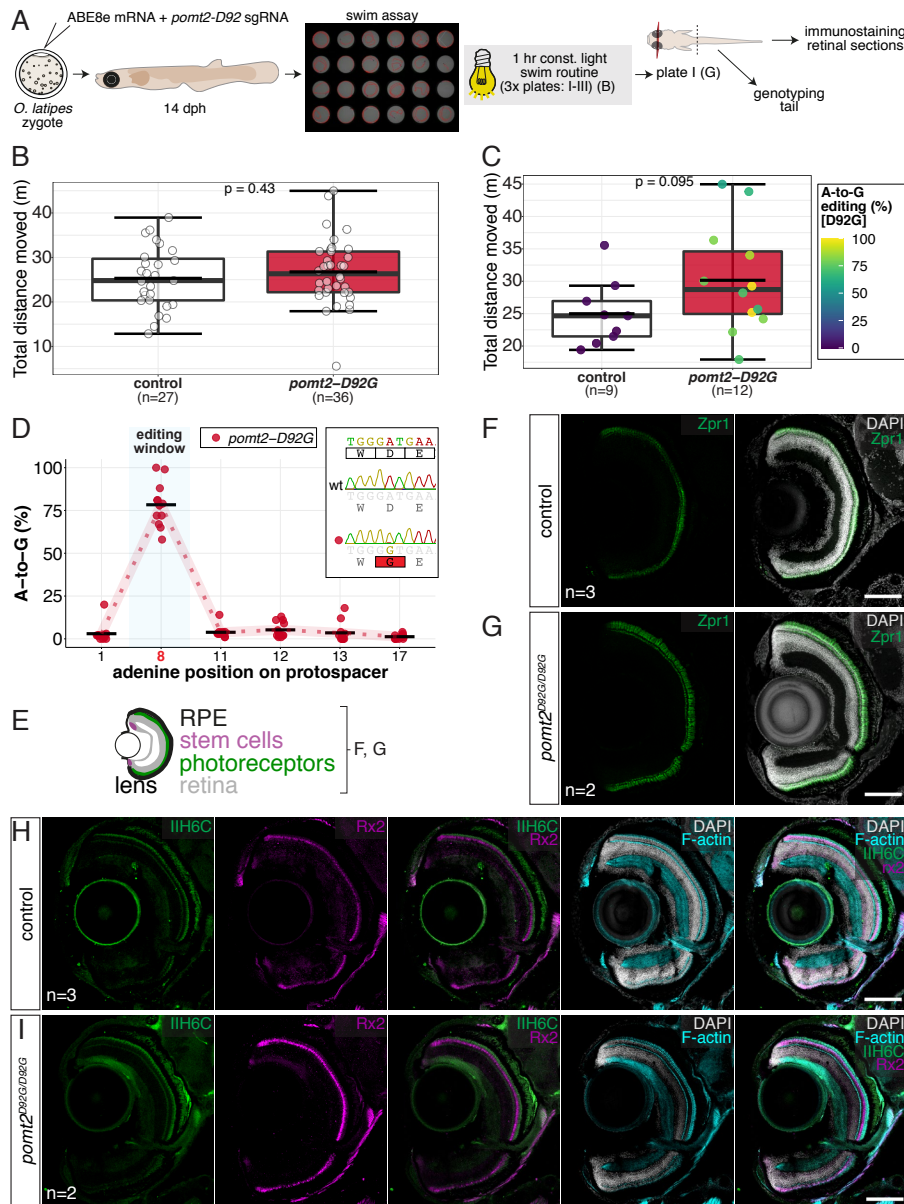


Figure 2.23: Zygotic aspartate 92 of the POMT2 acidic DE motif is dispensable for muscular and retinal function in post-embryonic medaka larvae. (A) Experimental setup to investigate the effects of a D92G missense mutation on the function of postembryonic POMT2 in muscular physiology and retinal structure in editants. Controls were injected with ABE8e mRNA only. (B) Quantification of larval movement by tracking larval locomotion in a black-wall 24-well plate under constant light for 1 hour at 14 dph. (C) Quantification of larval movement of a subset of hatchlings from (B) that were genotyped after tracking, with p.D92G base editing efficiencies mapped onto datapoints. Bold line = median. Black circle = mean. Statistical analysis was performed in R using the Student's test with the control injection larvae as the reference group, p values $> .05$ are considered insignificant. (D) Adenine base editing efficiency quantified from Sanger sequencing reads of target amplicons using EditR analysis. (E) Cartoon depicting the structure of the retina, with the green area corresponding to photoreceptors stained with Zpr1 in F and G and additionally, the stem and progenitor cell zone being highlighted by Rx2 signal in H and I. Note: Rx2 also labels photoreceptors. (F-I) Cryosections of control (F, H) homozygous $pomt2^{D92G}$ editants (G, I) retinas of 14 dph larvae. Sections were stained for the photoreceptor marker Zpr1 (green) (F-G) or glycosylated α -DG (IIH6C) (green), the stem/progenitor and photoreceptor marker Rx2 (magenta) and F-actin (phalloidin; cyan) (H-I). DAPI was used as counterstain in both experiments to label nuclei. Scale bar = 100 μ m. Dph = days post hatching.

2.3 Investigating the function of POMT-substrate *O*-mannosylation sites *in vivo* by an expanded base editor repertoire

In the previous chapter, I have introduced medaka *pomt2* disease models resembling the extremes in patients with DGpathies. In a CMD/LGMD medaka model, I could show that post-embryonic onset of muscular dystrophy is accompanied by scoliosis or kyphosis. By contrast, a WWS model displays early brain and retinal developmental defects that are accompanied by high rates of cell death.

Three substrates of the POMT-complex, α -DG, SUCO and KIAA1549, are confirmed so far in vertebrates [Larsen et al., 2017a,b; Vester-Christensen et al., 2013]. In the following, I will first address the question of their conservation in medaka and identify conserved sites of *O*-man. To allow for unrestricted base editing, thereby making all conserved α -DG sites accessible, I established SpRY base editors. Finally, to address the molecular mechanism underlying POMT-based DGpathies, I disrupted the genes encoding the three substrates. I used Cas9-induced NHEJ to produce loss-of-function phenotypes. Finally, by specifically mutating the annotated *O*-man sites, I achieved an unprecedented resolution in the interrogation of glycosylation sites *in vivo*.

2.3.1 Expression and *O*-man sites of the substrates of POMT1/2

Dag1 is a highly conserved gene in vertebrates [Bigotti and Brancaccio, 2021] that is expressed as a precursor protein and cleaved by proteolytically processing into α -DG and β -DG [Holt et al., 2000]. In zebrafish *dag1* is broadly expressed across all stages, as early as the 1-cell stage with more pronounced expression in the presomitic mesoderm and later myotomes, the immature notochord, the brain and eye [Gupta et al., 2011; Moore et al., 2008; Parsons et al., 2002]. Moreover, *dag1* mutant phenotypes indicate expression in ganglion cells, the lens, and the cornea [Gupta et al., 2011]. In medaka similar to several branches of teleost fish, two copies of *dystroglycan*, *dag1* and *dag1b*, are expressed [Pavoni et al., 2007].

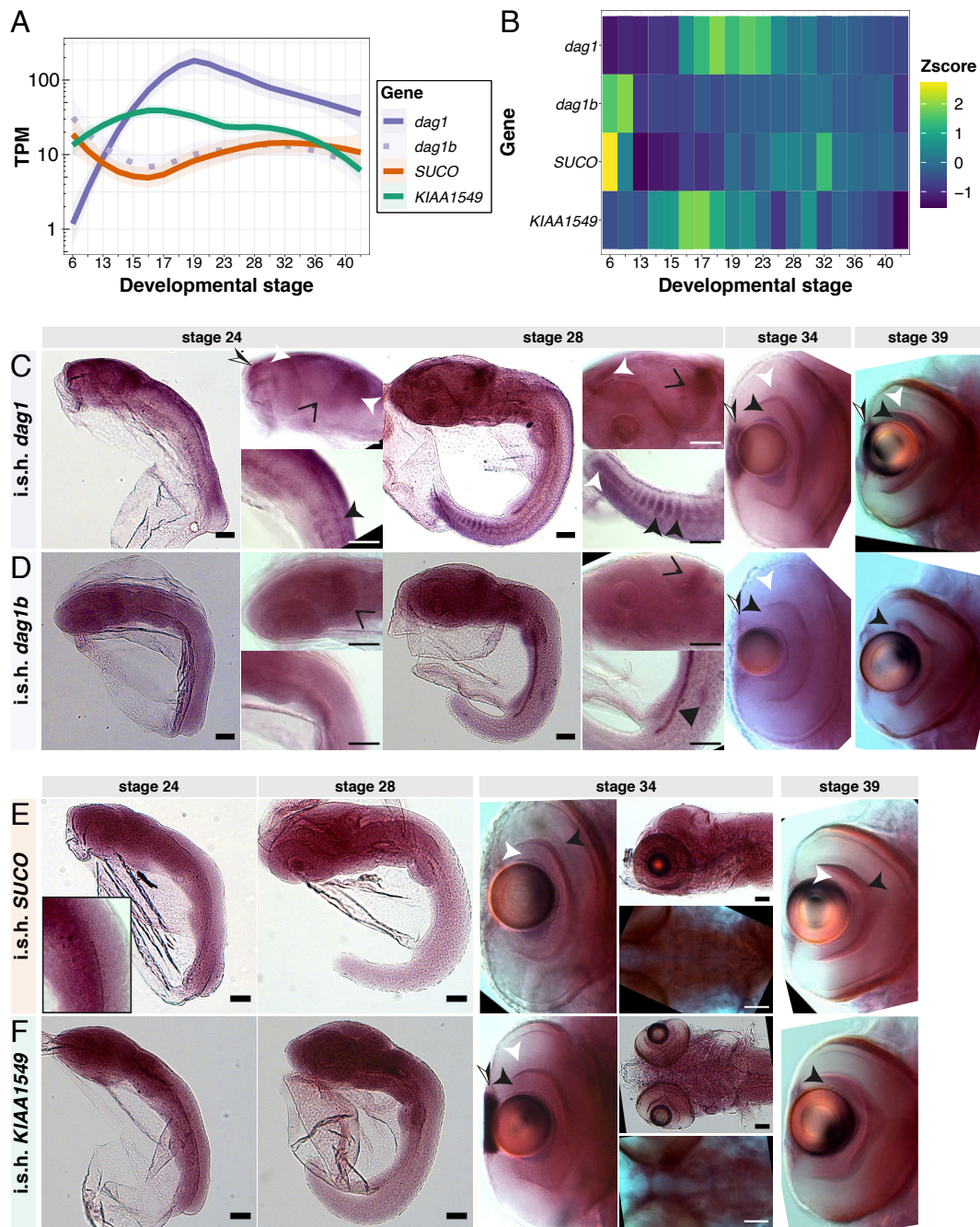


Figure 2.24: Expression of the substrates of the POMT1/2 complex across stages and tissues. (A-B) Gene expression for *dag1*, *dag1b*, *SUCO* and *KIAA1549* at embryonic stages extracted from published datasets [Ichikawa et al., 2017; Li et al., 2020; Marlétaz et al., 2018] with absolute, log-scaled transcripts per million (TPM, **A**) counts and normalised (gene-intrinsic) Zscore (**B**). (C-F) Tissue-specific gene expression by *in situ* hybridisation for *dag1*, *dag1b*, *SUCO* and *KIAA1549* at early brain/eye development and somitogenesis stages (24 and 28), completion of somitogenesis and retinal differentiation (34) and hatching stages (39). Scale bar = 100 μ m.

Making use of published RNA expression data sets [Ichikawa et al., 2017; Li et al., 2020; Marlétaz et al., 2018] I observed that *dag1* and *dag1b* are expressed mutually exclusive throughout development (Fig. 2.24A-B). *Dag1* is expressed

only after activation of the zygotic genome with peak expression during the stages of neurulation and organogenesis. By contrast, *dag1b* is primarily expressed maternally with weaker late embryonic expression, potentially restricting its function to the very early stages of development.

Dag1 is expressed in the eye, brain and somites at stage 24, and including the immature notochord at stage 28, in line with previous observations [Gupta et al., 2011; Moore et al., 2008; Parsons et al., 2002]. Later, global transcript levels are more moderate in the eye and brain with stronger expression in the cornea, ganglion and amacrine cells at stages 34 and 39 (Fig. 2.24C). *Dag1b* transcription is confined to the eye, the midbrain and the pronephric duct during early stages. Later gene expression in the eye is confined to the retinal ganglion and amacrine cells, as well as the putative stem cell domain (Fig. 2.24D).

The rough ER protein *SUCO* is ubiquitously expressed during early and post-embryonic mouse development with high skeletal expression in chondrocytes and osteoblasts/-clasts/-cytes [Sohaskey et al., 2010]. In medaka *SUCO* is expressed in two waves, once before gastrulation and then again beginning with neurulation it is moderately expressed until post-embryonic stages (Fig. 2.24A-B). During early stages no strong tissue-specificity can be seen for *SUCO* transcripts other than moderately elevated levels in the brain, eye and notochord (stages 24 and 28). In later stages, *SUCO* expression can be observed in the cartilage forming regions of the head, as well as in the ganglion and amacrine cells in the retina (stages 34 and 39) (Fig. 2.24E).

KIAA1549 is expressed in two isoforms in humans, a long transcript with dominant expression in the brain and a short transcript that appears to be specific to the retina. Within the retina, *KIAA1549* protein was localised to the connecting cilium of photoreceptors and the outer plexiform layer [De Bruijn et al., 2018]. In medaka *KIAA1549* is expressed throughout development, however, the strongest expression can be observed during late gastrulation and neurulation stages of development (Fig. 2.24A-B). Across stages, *KIAA1549* expression is confined to the brain and the eye, including the cornea, ganglion and amacrine cells (Fig. 2.24F). Altogether, the gene expression profiles support the idea of *dag1*, *SUCO* and *KIAA1549* as key substrates of the POMT-complex with high functional relevance.

Next, I examined the conservation of the amino acids that hold the *O*-man glycans for the three substrates and how accessible these are to base editing in medaka (Fig. 2.25 and Fig. 2.26). First, I retrieved sequence information on the position of the *O*-man peptides analysed in human and CHO cells [Larsen et al., 2017b; Vester-Christensen et al., 2013]. By alignment to the medaka sequence, I observed that of the 79 *O*-man peptides across all substrates 37 are conserved between human or chinese hamsters and medaka (47%) (Fig. 2.25A).

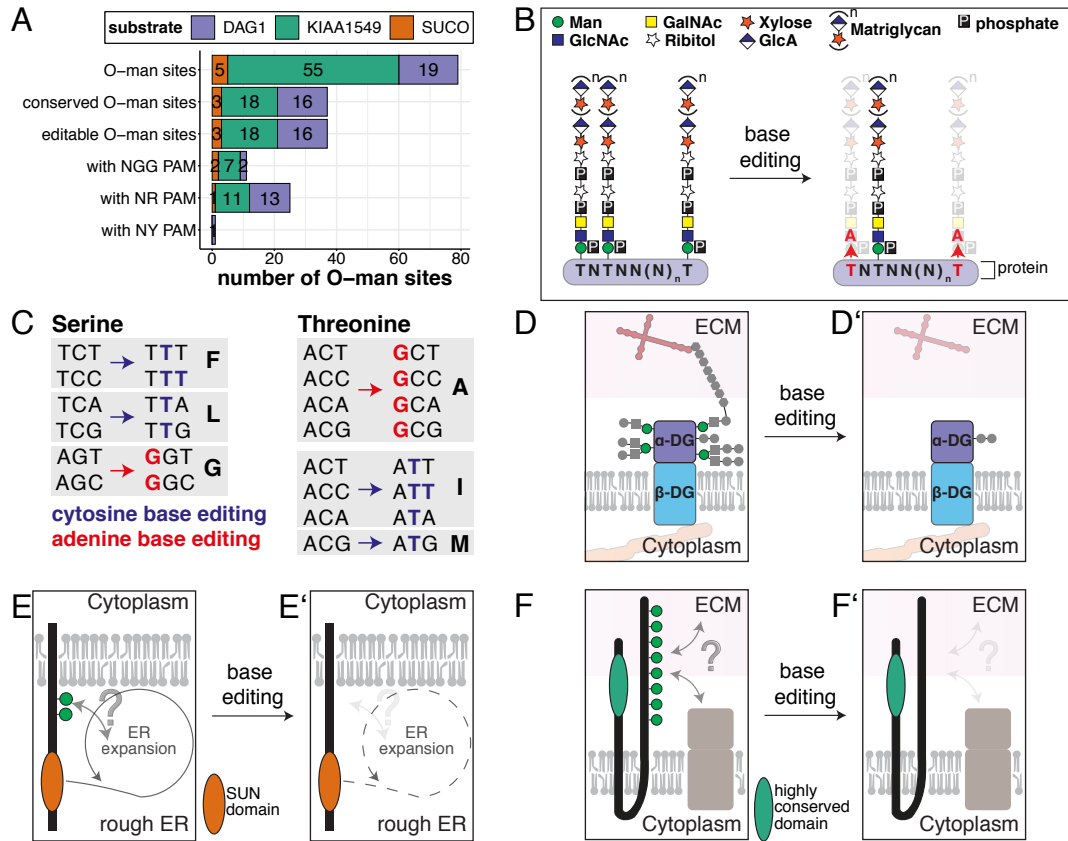


Figure 2.25: Conservation of *O*-mannosylation sites and concept of *O*-man site base editing. (A) All *O*-man sites (Thr / Ser) were retrieved from the published glycoproteomics data sets that identified *O*-mannosyl glycopeptides in human and CHO cells [Larsen et al., 2017b; Vester-Christensen et al., 2013]. Sites were aligned for conservation to medaka and analysed for the usability of cytosine or adenine base editors with NGG, NG / NA (NR) or NC / NT (NY) PAMs to introduce point mutations in the conserved Thr / Ser. Note: if a Ser / Thr was aligned to a Thr / Ser in medaka it was considered to be conserved. (B) The general idea in using base editing to study the role of *O*-mannosylated amino acids. (C) Overview of all codon changes on Ser or Thr that can be introduced by CBEs or ABEs. (D-F) Schematics showing the localisation and function of α -DG (D), SUCO (E) and KIAA1549 (F) and the hypothesised impact of a lack of *O*-mannosylation on function (schemes redrawn after Sheikh et al. [2017], Sohaskey et al. [2010] and De Bruijn et al. [2018], respectively).

In particular, α -DG conservation is remarkably high (84%), which is in accordance with high overall conservation of the entire α -DG protein, and specifically the *O*-man peptide containing mucin domain required for laminin recognition (Fig. 2.26A). Not only is α -DG highly conserved, but also all enzymes involved in its *O*-man, as well as matriglycan synthesis, are highly conserved in vertebrates [Bigotti and Brancaccio, 2021]. Together with substantial evidence of the conservation of *O*-man glycan structures on α -DG in mammals [Gomez Toledo et al., 2012], this suggests that the glycosylation of the conserved Thr/Ser residues may also be conserved.

By contrast, *O*-man site conservation in SUCO and KIAA1549 is much lower at 60% and 3%, respectively, which generally reflects the overall modest conservation of the *O*-man region (Fig. 2.26B). Given the nature of Ser and Thr codons (Fig. 2.26C), all conserved *O*-man sites can be converted to a non-*O*-man amino acid by combining cytosine and adenine base editors (Fig. 2.25A). Base editing can thereby facilitate the study of the function of individual *O*-man sites with high precision (Figures 2.3.2B-F). However, standard base editors introduced in the first chapter of this thesis (section 2.1) utilise NGG PAM-interacting motifs (PIMs) and can only access 30% of conserved *O*-man sites.

Recently, by engineering Cas9 variants a variety of PIMs have been explored for the use of Cas9-mediated NHEJ and base editing alike [Nishimasu et al., 2018; Walton et al., 2020]. The engineering effort led to the identification of NG and SpRY PIM variants, the latter of which can hypothetically be used to localise the sgRNA:Cas9 (or base editor) complex to virtually any site of the genome. Editing of NGN or NAN (R = G or A) can thereby be achieved with high efficiency, and even NCN or NTN (Y = C or T) showed editing, albeit at lower levels [Walton et al., 2020]. Therefore, to make all *O*-man sites accessible to base editing, in the next section I will describe experiments with which I tested and established these SpRY base editors in medaka.

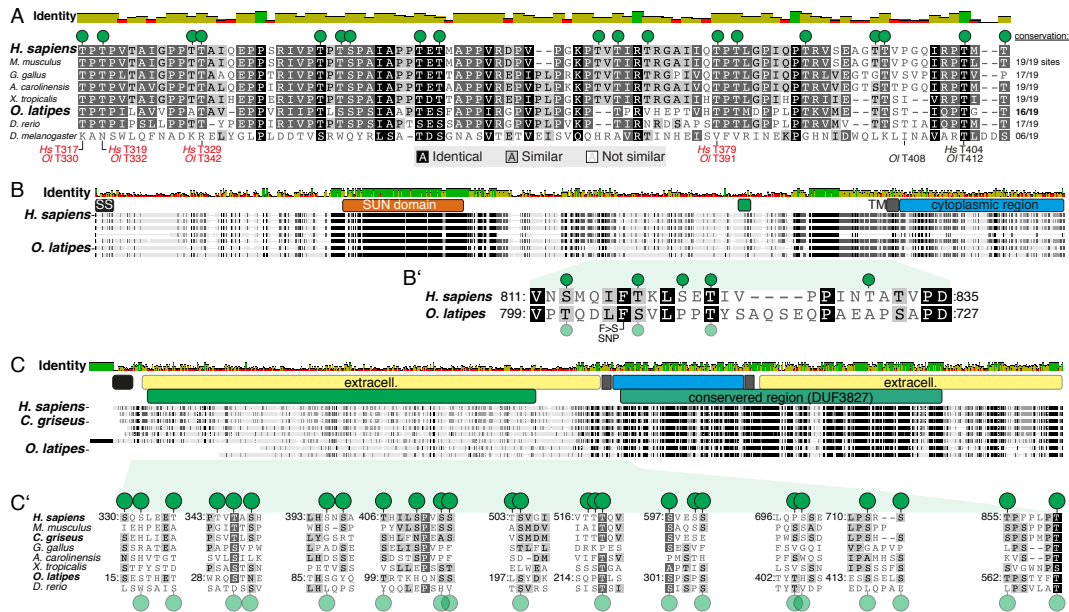


Figure 2.26: Conservation of O-mannosylation sites. (A) Protein alignment of the laminin-binding region of the mucin domain of α -DG across vertebrates with *D. melanogaster* as outgroup and annotation of the O-man sites. Annotated positions highlight relevant Thr residues that will be later experimentally investigated and /or have been shown to be required for laminin binding (red) [Hara et al., 2011; Yagi et al., 2013]. (B) Alignment of the entire SUCO protein sequence across vertebrates (same order as in A), highlighting high conservation in the SUN domain region, and by contrast lower conservation in the region of O-man sites (B'). (C) Alignment of the entire KIAA1549 protein sequence across vertebrates, highlighting high conservation in the DUF3827 region, and only low conservation in the region of α -DG sites (C'). Note that the blocks displayed in (C') do not encompass all annotated human α -DG sites, excluding those blocks without any Ser / Thr. Annotation of α -DG sites after Vester-Christensen et al. [2013] and Larsen et al. [2017b].

2.3.2 Expanding the limits of *in vivo* base editing

I have described that the two CBEs ancBE4max and evoBE4max can mediate near homozygous C-to-T conversions of NGG PAM sites in medaka. Likewise, ABEe achieves remarkable A-to-G editing efficiencies using NGG sgRNAs. I chose to test the published NG editors for evoBE4max-NG and ABEe-NG [Richter et al., 2020; Thuronyi et al., 2019], and clone ancBE4max-NG as well as all three base editors with SpRY PIM [Walton et al., 2020]. Using synthetic sgRNAs as crRNA::tracrRNA duplex (crRNAs), base editing was achieved at high efficiencies in zebrafish editants with NGG CBEs [Rosello et al., 2021b] and with BE4max-SpRY at a NAN PAM site [Rosello et al., 2021a].

Thus, I wanted to identify the optimal non-NGG PAM base editing conditions in medaka. I performed mRNA injections with NGG, NG and SpRY base editors into zygotes using both sgRNAs and synthetic crRNAs. I designed sgRNAs/crRNAs such that CBEs would introduce PTCs in the *oca2* gene. The same sgRNA should install a missense mutation with ABE8e. The resulting loss of *oca2* function can then be scored by assessing the eye pigmentation phenotype.

***oca2* NGG PAM base editing**

I performed the first tests using the *oca2-Q333* NGG PAM sgRNA (Fig. 2.27A). All CBE-PIM versions with both sgRNAs and synthetic crRNAs generated, at least a fraction, of pigment-free eyes (Fig. 2.27B-C). The crRNAs were consistently more efficient in obtaining eye pigmentation editants. Both ancBE4max and evoBE4max showed high, comparable efficiencies with all PIM versions. In fact, 19 of 21 normally developed embryos injected with evoBE4max-SpRY mRNA and the *oca2-Q333* crRNA were close to completely pigment-free (Fig. 2.27D). However, both evoBE4max-NG and evoBE4max-SpRY injections with the crRNA generated a large fraction of dead or aberrant embryos by 4 dpf (80% and 49%, respectively) (Fig. 2.27D). The coinjections of ancBE4max-SpRY with the crRNA, therefore, stand out with both high efficiency (24 of 35 close to pigment-free) and comparably low dead or aberrant levels (22%) (Fig. 2.27C-D).

ABE8e showed low-to-moderate levels of editing as indicated by the fraction of embryos with any loss of eye pigment across all conditions, and up to 96% with ABE8e-NGG/crRNA. However, ABE8e-SpRY seems to induce high levels of lethality and abnormal embryos. I hypothesise, that the increased genome-wide targeting range of both NG and SpRY PAM editors will likewise also increase the available off-targeting range.

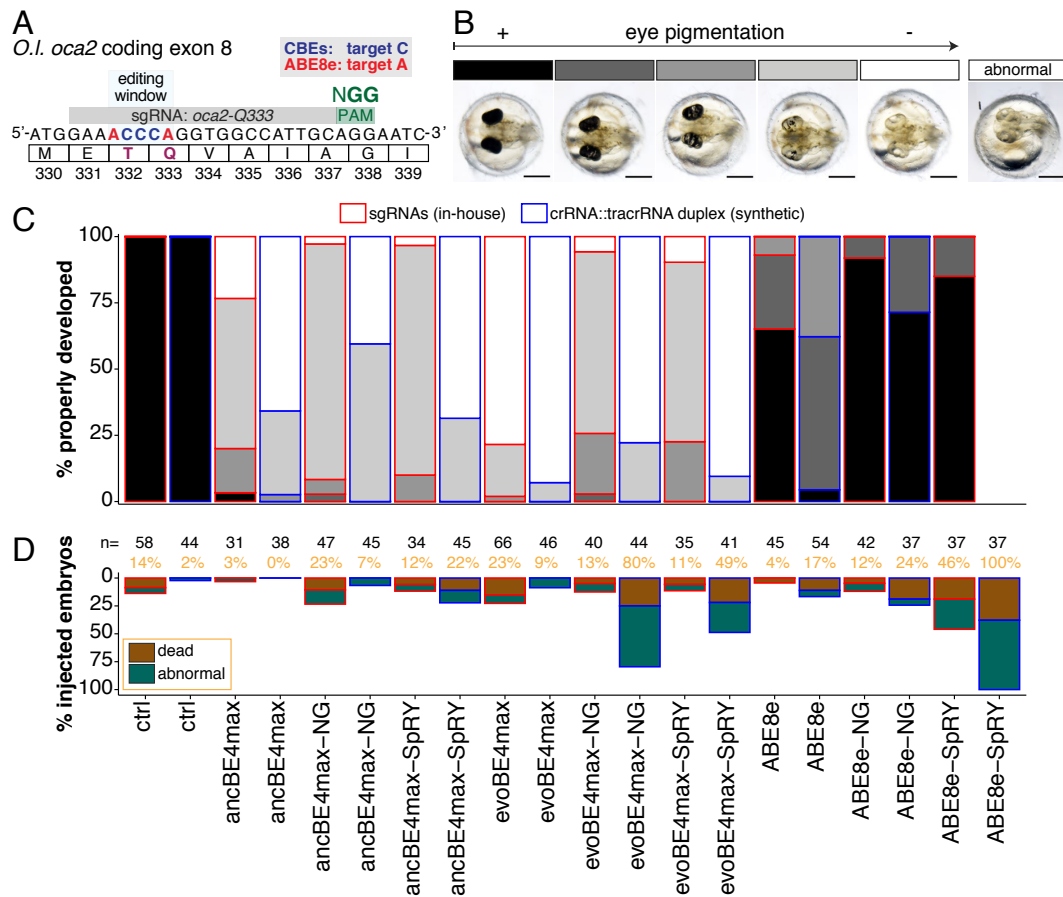


Figure 2.27: Synthetic crRNAs achieve higher base editing efficiencies of the *oca2* gene as indicated by the loss of eye pigmentation. (A) *oca2-Q333* locus with target C or A. (B) Phenotypic categories of eye pigmentation phenotypes obtained at 4 days post-fertilisation (dorsal view). Scale bar = 400 μ m. (C) Grouped and quantified pigmentation phenotypes for cytosine and adenine base editor experiments showing the percentage of embryos that fall into the "normal" category in (D). (D) Scoring of all non-eye-pigment-related phenotypes for cytosine and adenine base editor experiments. Abnormal embryos either showed developmental delay or sublethal phenotypes. The percentage in orange shows the combined fraction of embryos with either dead or abnormal phenotypes.

oca2 NGN PAM base editing

Next, I tested the NG PAM sgRNA *oca2-Q22*, which expectedly, did not result in any apparent editing with NGG editors using the sgRNA. The NGG-CBEs, only generated moderate levels of overall pigment loss using the corresponding crRNA. By contrast, both NG and SpRY variants were able to cause high levels of pigmentation phenotypes in the sgRNA setup and close-to absolute levels with the corresponding crRNA (Fig. 2.28A-C). Both ancBE4max-SpRY and evoBE4max-SpRY experiments with the *oca2-Q22* crRNA led to a high fraction of embryos, 27 of 33 and 20 of 24 respectively, that were almost devoid of pigment. While ABE8e-NG and -SpRY experiments in the crRNA setup produced a fraction of embryos with pigmentation loss

(4 of 31 and 2 of 8, respectively), ABE8e-SpRY editing also caused substantial unwanted phenotypes and death (79%) (Fig. 2.28D)

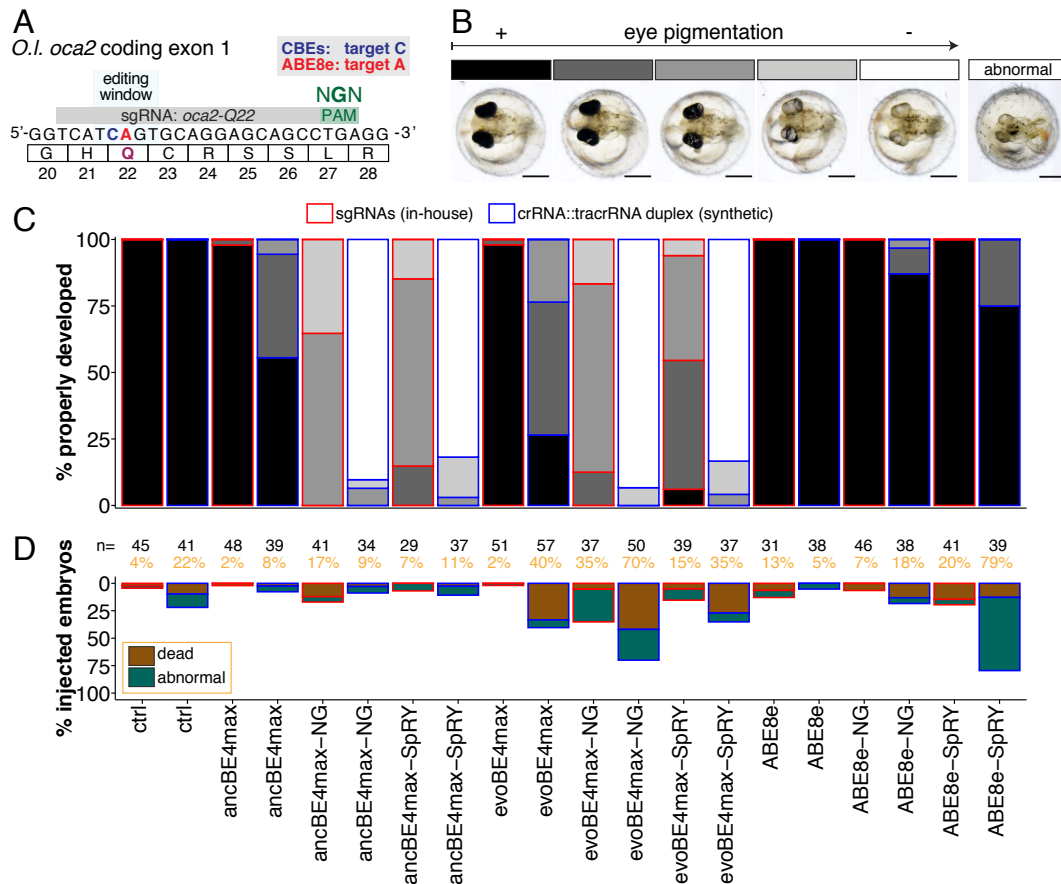


Figure 2.28: NG and SpRY CBEs can efficiently edit *oca2* NGN PAM as indicated by the loss of eye pigmentation. (A) *oca2-Q22* locus (NGN PAM site) with target C or A. (B) Phenotypic categories of eye pigmentation phenotypes obtained at 4 days post-fertilisation (dorsal view). Scale bar = 400 μ m. (C) Grouped and quantified pigmentation phenotypes for cytosine and adenine base editor experiments showing the percentage of embryos that fall into the "normal" category in (D). (D) Scoring of all non-eye-pigment-related phenotypes for cytosine and adenine base editor experiments. Abnormal embryos either showed developmental delay or sublethal phenotypes. The percentage in orange shows the combined fraction of embryos with either dead or abnormal phenotypes.

oca2 NAN PAM base editing

I next tested the editing efficiencies of the SpRY base editors using the NA PAM sgRNA *oca2-Q271* (Fig. 2.29A). Here, both ancBE4max- and evoBE4max-SpRY led to a significant fraction (45 of 45 and 33 of 35, respectively) of embryos that showed some loss of eye pigment (Fig. 2.29B-C). Notably, this remarkable editing occurred with only marginal levels (12% and 26%) of undesired phenotypes (Fig. 2.29D). By contrast, ABE8e-SpRY mediated *oca2* base editing did not result in any pigment-loss, in the

presence of high (45%) levels of unwanted phenotypes. It is important to not directly compare the true editing efficiency of the CBEs with ABE8e at this point, as introduced missense mutations may not lead to a strong loss of function. My previous comparison of NGG ancBE4max/evoBE4max and ABE8e indicated comparable efficiencies by Sanger and Illumina sequencing.

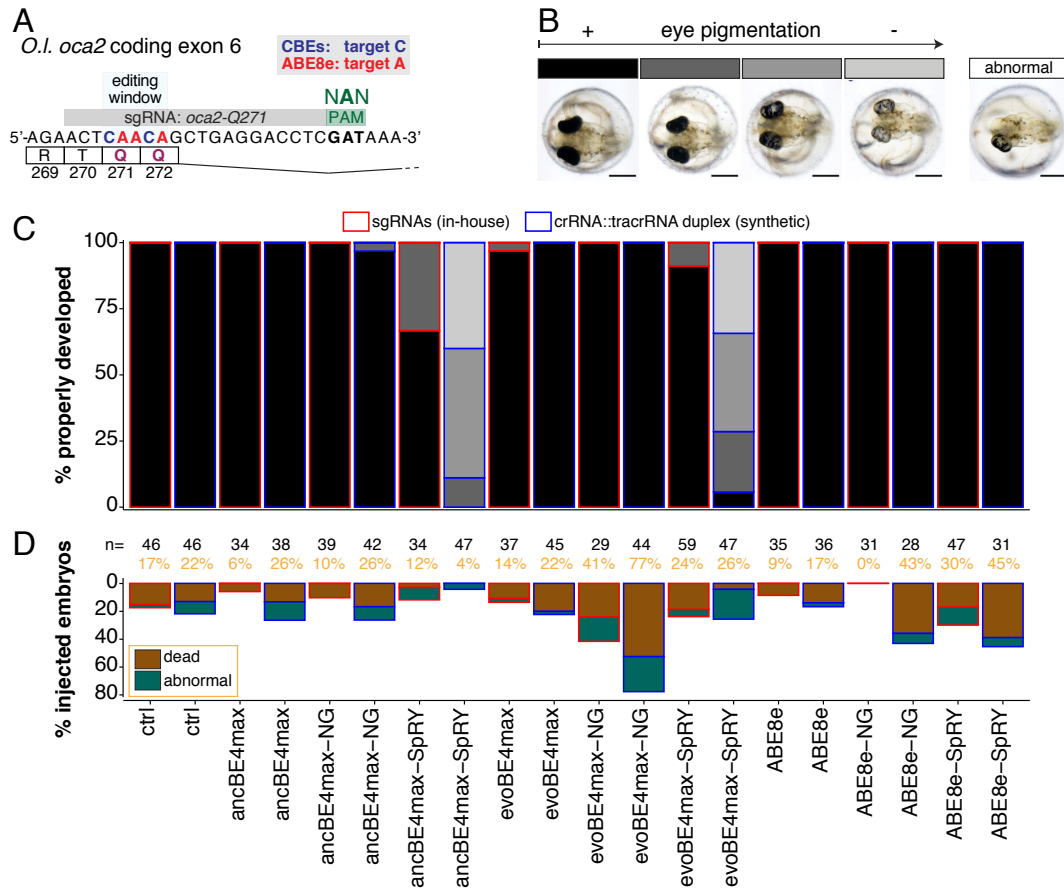


Figure 2.29: SpRY base editor variants can efficiently edit *oca2* NAN PAM sites as indicated by the loss of eye pigmentation. (A) *oca2-Q271* locus (NAN PAM site) with target C or A. (B) Phenotypic categories of eye pigmentation phenotypes obtained at 4 days post-fertilisation (dorsal view). Scale bar = 400 μ m. (C) Grouped and quantified pigmentation phenotypes for cytosine and adenine base editor experiments showing the percentage of embryos that fall into the "normal" category in (D). (D) Scoring of all non-eye-pigment-related phenotypes for cytosine and adenine base editor experiments. Abnormal embryos either showed developmental delay or sublethal phenotypes. The percentage in orange shows the combined fraction of embryos with either dead or abnormal phenotypes.

oca2 NCN and NTN PAM base editing

Finally, I used the same *oca2* pigment assay to explore the full capabilities of SpRY editors *in vivo*. SpRY base editors have been previously shown to edit NAN PAM genomic targets in zebrafish [Rosello et al., 2021a]. However, to date, no report on NCN or NTN (NYN) PAM base editing has demonstrated

their *in vivo* potential to edit these sites. To test NCN and NTN PAMs I designed and injected *oca2-Q15* (NCN) and *-W385* (NTN) crRNAs together with SpRY CBEs and ABE8e (Fig. 2.30A). In spite of previously reported, reduced efficiencies of these NYN PAMs *in vitro* [Walton et al., 2020], both ancBE4max- and evoBE4max-SpRY led to substantial fractions (35 of 35 and 22 of 29, respectively) of normally developed embryos with pigmentation phenotype at the NCN PAM locus (Fig. 2.30B-C). Importantly, these editing events occurred with only low-to-moderate concomitant unwanted phenotypes (22% and 45%) (Fig. 2.30D).

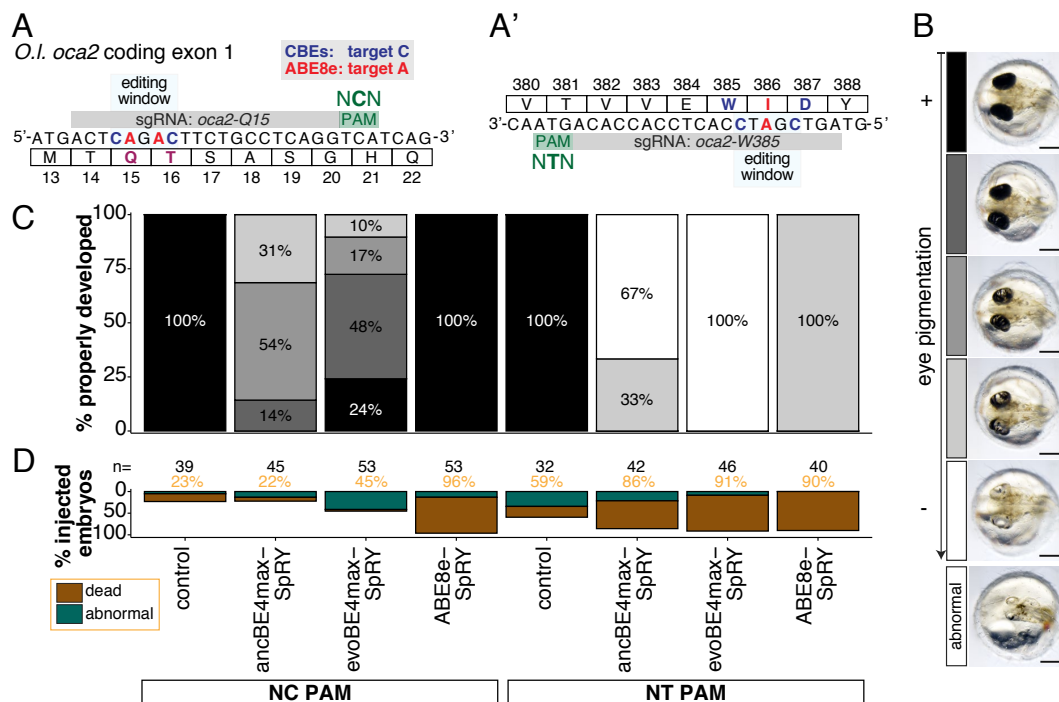


Figure 2.30: SpRY base editor variants can efficiently edit *oca2* NCN and NTN PAM sites using synthetic crRNAs. (A) *oca2-Q15* locus (NCN PAM site) with target C or A. (A') *oca2-W385* locus (NTN PAM site) with target C or A. (B) Phenotypic categories of eye pigmentation phenotypes obtained at 4 days post-fertilisation (dorsal view). Scale bar = 400 μ m. (C) Grouped and quantified pigmentation phenotypes for cytosine and adenine base editor experiments showing the percentage of embryos that fall into the "normal" category in (D). (D) Scoring of all non-eye-pigment-related phenotypes for cytosine and adenine base editor experiments. Abnormal embryos either showed developmental delay or sublethal phenotypes. The percentage in orange shows the combined fraction of embryos with either dead or abnormal phenotypes.

Almost all ancBE4max- and evoBE4max-SpRY edited, normally developed embryos of the NTN PAM site were pigment-free, indicating that NTN targets can be edited efficiently. However, the majority of injections led to unwanted phenotypes with rates of 86% for ancBE4max-SpRY and 91% for evoBE4max-SpRY. Likewise, ABE8e-SpRY editing of both sites was

accompanied by 90-96% aberrant or dead embryos, while only NTN editing produced loss of pigmentation phenotypes (4 of 4 normally developed) (Figure 2.3.7B-D).

Taken together, using the *oca2* gene as a test site I have shown that base editing using SpRY-base editors can access virtually any site in the genome. Editing capabilities are now expanded to any NR and NY site. However, these editors lead to unwanted phenotypes at higher levels than previously observed with NGG PAM base editors. F0 and F1 base editing experiments will therefore need careful consideration, to avoid misinterpreting "off-target" phenotypes as the phenotype that is being scored.

NAN, NCN and NTN PAM base editing of the *tbxta* gene

No-tail or tailless mutant phenotypes have been extensively described and used to score the efficiency of CRISPR/Cas9 editing in zebrafish using the *ntl* gene [Hoshijima et al., 2016; Vicencio et al., 2022]. *Ntl* or *tbxta* is a T-box transcription factor, essential for notochord and posterior mesoderm development [Halpern et al., 1993], with its loss of function leading to posterior truncations of the embryonic body. *Ntl / tbxta* is highly conserved and medaka *tbxta* shares 87.7% identical sites with zebrafish *ntl*. To test the SpRY base editors with a different gene I designed three crRNAs with NAN, NCN and NTN PAMs in *tbxta* that would introduce PTCs when coinjected with CBE-SpRY mRNA (Fig. 2.31A). ABE8e-SpRY base editing did not lead to any posterior phenotype at any PAM site. By contrast, I observed three tailless embryos in each, evoBE4max- and ancBE4max-SpRY experiment (7% and 6%) and overall 52% and 79% posterior phenotypes using the NA PAM crRNA (Fig. 2.31B-C). Additionally, the ancBE4max-SpRY was able to produce posterior phenotypes using the NT PAM crRNA, but not the NC PAM crRNA. Finally, efficient NCN and NTN PAM editing was achieved with the evoBE4max-SpRY editor using the corresponding crRNA leading 36.6% and 34.8% posterior phenotypes (Fig. 2.31B-C).

In summary, I have shown that base editing can now also be applied to virtually any target sequence of the genome, given that target-C or -A nucleotides are present within the base editing window. Whether experiments can be conducted in F0 or require the crossing to F1 or F2 to dispose of potential off-target phenotypes, will depend on the locus, the efficiency and

importantly the change that is being installed. However, these results are promising as now all conserved *O*-man sites can theoretically be accessed by base editing and thereby enable studying their role in F0 or later generations.

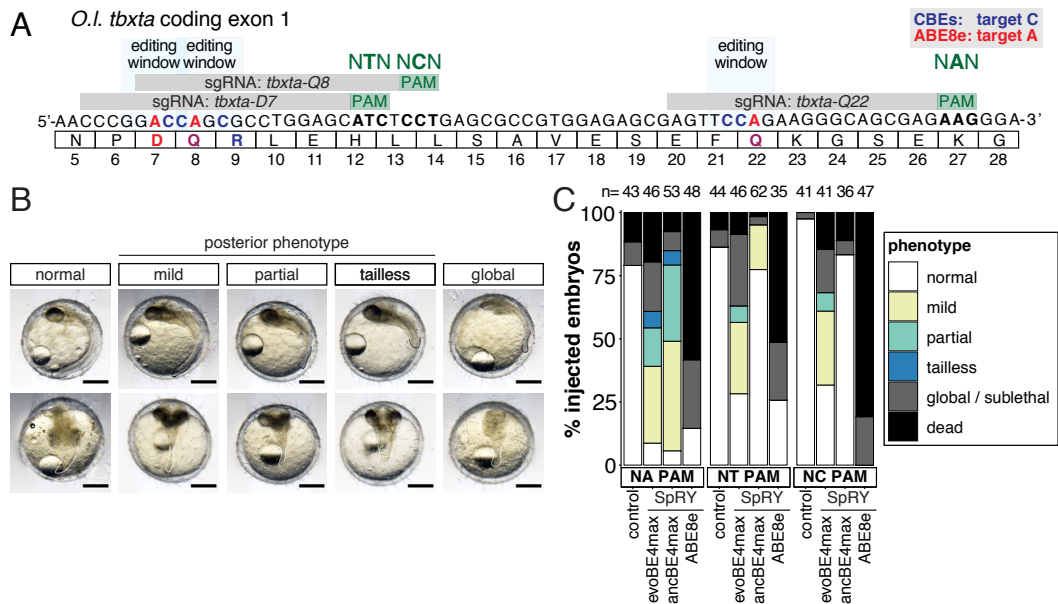


Figure 2.31: SpRY cytosine base editor variants are versatile tools that allow PAM-decoupled base editing of *tbxta* NAN, NCN and NTN PAM sites. (A) Coding exon 1 of the *tbxta* locus showing the *tbxta-D7* (NTN PAM site), *tbxta-Q8* (NCN PAM site) and *tbxta-Q22* (NAN PAM site) crRNA target sites, with target C or A. (B) Phenotypic categories of posterior "tailless" phenotypes obtained at 3 days post-fertilisation (dorsal view). Scale bar = 400 μ m. (C) Grouped and quantified "tailless" phenotypes for cytosine and adenine base editor experiments.

2.3.3 Advanced genome engineering tools provide entry points to functional *in vivo* analysis of *O*-man sites

The *in vivo* function of *dag1* and α -DG *O*-man sites

Zebrafish *dag1* knockdown and hypomorphic mutants have indicated that the reduction of dystroglycan function leads to a postembryonic onset of phenotypes. While muscular dystrophy becomes apparent during the first postembryonic days of larvae and worsen quickly, the CNS is only mildly affected [Gupta et al., 2011; Parsons et al., 2002]. Therefore, our understanding of the extent of embryonic *dag1* function is incomplete.

dag1 crispants.

To obtain an overview of the function of *dag1* in medaka I performed Cas9 KO experiments by microinjecting Cas9 mRNA together with two *dag1-crispr-sgRNAs* (Fig. 2.32A-B). First, to assess that *dag1* function is

effectively disrupted I performed immunoblots against β -DG on pools of 1 dpf *dag1* crispants. The lack of β -DG immunoreactivity confirms the loss of *dag1* in the crispants. I concluded that these crispants provide a good approximation for dystroglycan-less embryos (Fig. 2.32C). I hypothesised that similar to observations in zebrafish *dag1* crispants will show prominent phenotypes after the development of muscles. Therefore, I scored crispant phenotypes after hatch (3 dph) and observed a clear dystrophic phenotype in 24 of 48 of the larvae (Fig. 2.32D). The dystrophic crispants had a curved body axis and were either completely immobile or showed reduced motility. This result highlights the potential of medaka to further investigate the function of dystroglycan and provide entry points to bridge the gap to the understanding of *pomt2* mutants.

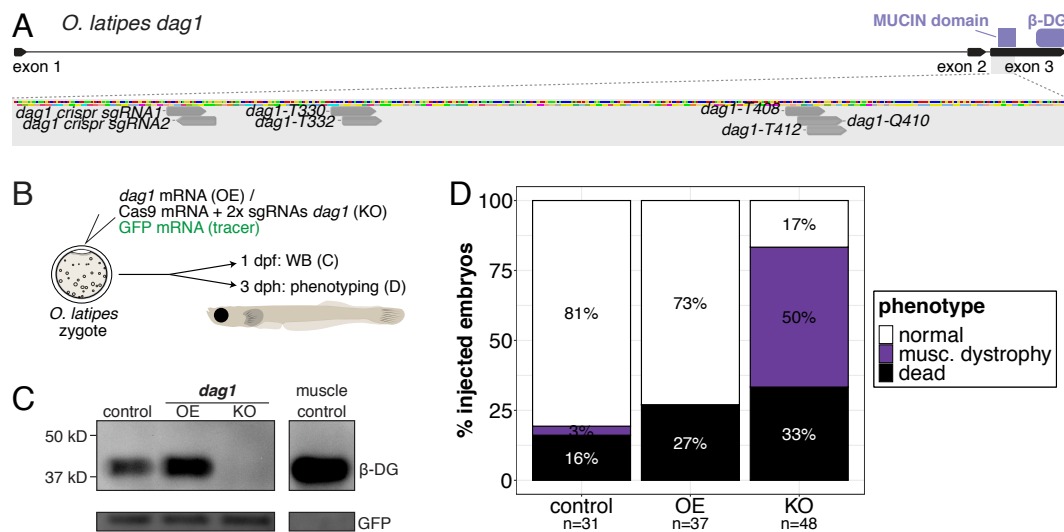


Figure 2.32: Medaka *dag1* crispants reveal DGpathy-like phenotypes in post-embryonic development. (A) Overview of the *dag1* locus with coding exons highlighting the sgRNAs used to disrupt the *dag1* gene by Cas9 mediated KO or base editing. (B) Experimental setup to validate the loss of *dag1* function in crispants. (C) Immunoblot on control, *dag1* overexpression, and *dag1* crispant pooled embryo lysates obtained at 1 dpf with β -dystroglycan (β -DG, 43 kD) and GFP (27 kD) antibodies. For each sample, 20x embryos were pooled. Dissected adult muscle tissue was used as a positive control. (D) The loss of *dag1* function results in embryonic and post-embryonic lethality and a large fraction of muscular dystrophy-like 3 dph old larvae displaying abnormal muscle structures, accompanied by reduced or absent motility. Dpf / dph = days post fertilisation / hatching.

dag1 cytosine base editing.

Next, I used the highly efficient cytosine base editors to install point mutations that introduce missense changes in the *dag1* coding sequence. I selected presumptive *O*-man amino acids as targets and characterised the resulting phenotypes in injected editants (Fig. 2.32A and Fig. 2.33A). Specifically, I targeted two conserved threonines T330 and T332, as well as one control threonine T408 (Fig. 2.26A).

Notably, T330 and T332 were previously shown to be necessary for the formation of laminin-binding matriglycan on α -DG (corresponding to human T317 and T319, respectively). While T317A/T319A almost completely abolished laminin-binding in cell culture, single point mutations led to a slight but noticeable reduction [Hara et al., 2011; Yagi et al., 2013]. I performed different sgRNA/CBE microinjections, phenotyped embryos and hatchlings and extracted genomic DNA for sequence analysis (Fig. 2.33A). Base editing using the evoBE4max CBE with *dag1-T330*, *dag1-T332* and *dag1-T408* mainly led to unexpected, out-of-the-editing-window base conversions as quantified by EditR (Fig. 2.33B). These edits resulted in the installation of p.P331L, p.P333F and a silent nucleotide change of the T408 codon, respectively. Although these changes were not the desired missense mutations, the efficiencies were nevertheless remarkable with $99.3\pm 1.2\%$ editing leading to p.P331L (n=3), $84.0\pm 5.3\%$ to p.P333F (n=3) and a silent point mutation of T408 with an efficiency of $99.7\pm 0.6\%$ (n=3).

By contrast, ancBE4max mediated cytosine base editing resulted in all desired mutations, albeit at lower efficiencies. With *dag1-T330* sgRNA alone or in combination with *dag1-T408* p.T330M was installed with $56.7\pm 4.5\%$ (n=3) and $53.0\pm 3.2\%$ (n=4) efficiency, respectively. The *dag1-T330/-T408* double editants displayed $42.5\pm 9.0\%$ (n=4) efficiency in installing p.T408I. Finally, ancBE4max mRNA together with the *dag1-Q410* sgRNA resulted in the installation of a PTC p.Q410X with $64.0\pm 1.7\%$ (n=3) efficiency. Cytosine base editing is highly context-dependent with different characteristics of evoBE4max and ancBE4max reported *in vitro* [Arbab et al., 2020; Huang et al., 2021; Komor et al., 2016] and *in vivo* [Cornean et al., 2022]. Indeed, I also observed that ancBE4max is superior in editing cytosines that follow an adenine.

I analysed the phenotypes for all editants at 4 dpf and observed that all but *dag1-T408*silent and *dag1-P333F* only showed moderate levels of aberrant phenotypes, coinciding with highly efficient editing rates in those two cases (Fig. 2.33C-D). The silent mutation may have led to a destabilisation of the transcript or reduction in translation efficiency leading to 44% aberrant or dead editants. By contrast, *dag1-P333F* lies in the highly conserved region adjacent to two matriglycan sites, and will likely disrupt the local structure and thereby impede laminin binding.

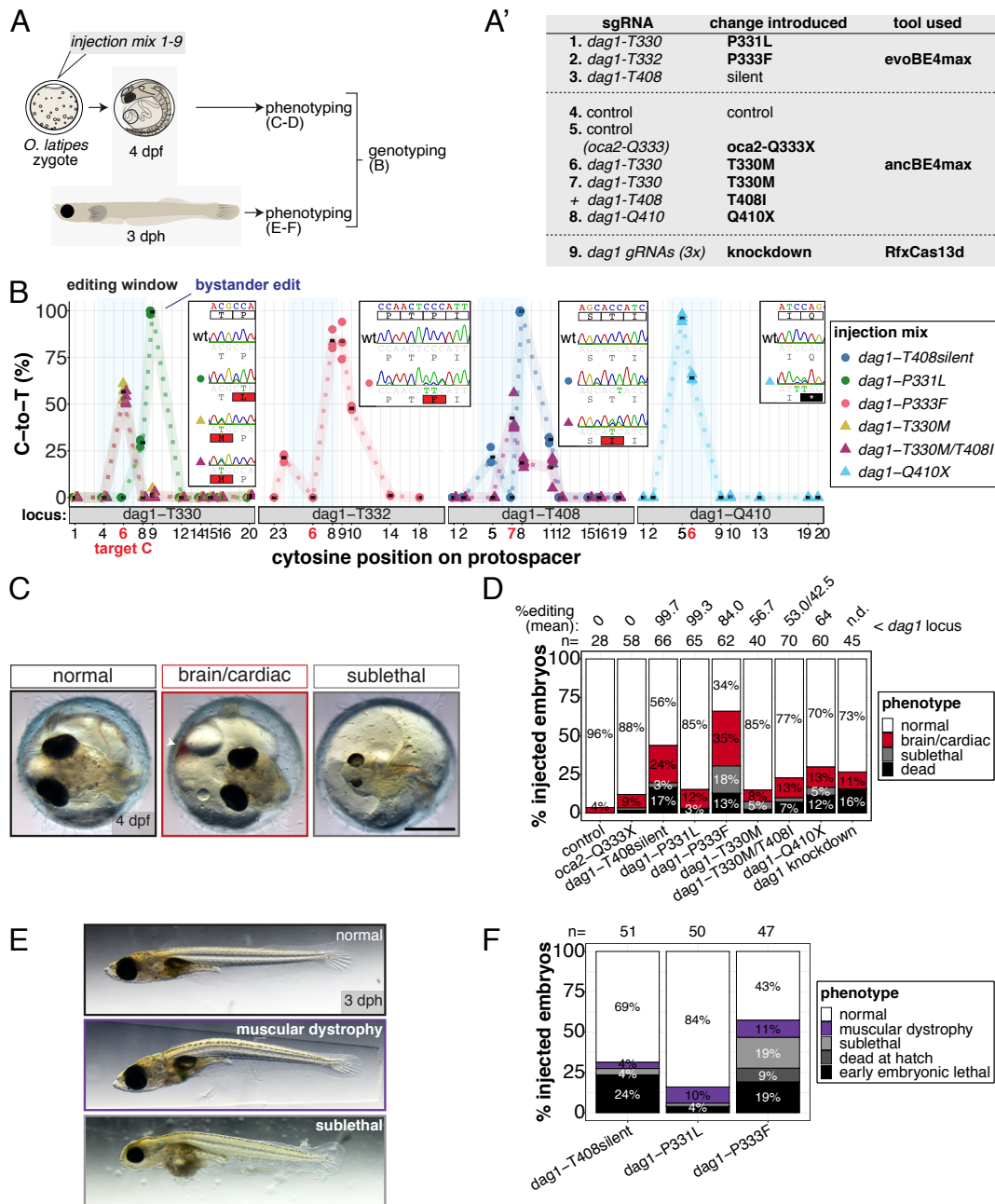


Figure 2.33: Cytosine base editing of the *dag1* gene reveals the functional importance of a proline at position 333 in F0. (A) Experimental setup to investigate the effects of CBE-introduced missense mutations on the function of *dag1* in F0. (B) Cytosine base editing efficiency quantified from Sanger sequencing reads of target amplicons following CBE experiments using EditR. (C) Phenotype profile of *dag1* editants at 4 dpf. Scale bar = 400 μ m. (D) Quantification of phenotypes of *dag1* editants at 4 dpf. (E) Post-embryonic phenotype profile of *dag1* evoBE4max editants at 3 dph. (F) Quantification of phenotypes of *dag1* evoBE4max editants at 3 dph. Dpf/dph = days post fertilisation/hatching.

Interestingly, the knockdown of early *dag1* transcript using the RfxCas13d system also did not lead to notable levels of embryonic phenotypes. This observation is in fact in line with the low-level expression and likely moderate role of *dag1* during the early stages of embryogenesis. Postembryonic larvae of both p.P331L and p.P333F resulted in 5 of 50 and 5 of 47 editants, respectively to display a dystrophic phenotype with aberrant swimming behaviour. Additionally, 19% of p.P333F hatchlings were completely immobile with no response to touch and widespread, apparent cell death (“sublethal”, Fig. 2.33E-F). Taken together, these results show that the phenotypic analysis of *dag1* editants to study individual α -DG amino acids is possible, however, requires the careful selection the base editor tools.

***dag1* adenine base editing.**

I hypothesised that ABE8e might be less prone to context-dependent editing efficiencies, as earlier data suggests, making it more reliable in installing *O*-man missense mutations. Moreover, to better understand the pathophysiology in dystroglycan-deficient embryos I decided to characterise *dag1* crispants in more detail and compound the *dag1* crispant phenotype by coinjecting a *dag1b-crispr-sgRNA*. To achieve a higher phenotypic impact, I assessed the phenotypes of editants with *dag1*-T330A / T408A double missense mutations with those of ABE8e control injections, *dag1* crispants and *dag1 / dag1b* crispants. I first scored phenotypes during early development and after the hatching stage and then performed a constant light swim assay to quantitatively compare the phenotypes (Fig. 2.34A).

At 4 dpf, a large fraction of both *dag1* and *dag1 / dag1b* crispants were developmentally affected (Fig. 2.34B). Defects ranged from mild delays in development to structural heart abnormalities with coagulation, abnormal brain and eye morphology and severe patterning defects (Fig. 2.34C). All of these phenotypes were scored on a graded scale, and while the cardiovascular system scored the most frequent in crispants (20 of 72 and 14 of 52, for single and double KOs), no phenotypic aspect stood out. This spectrum is in fact a powerful representation of DGpathies. Moreover, the phenotypic profile was very similar between *dag1* and *dag1 / dag1b* double crispants, indicating that *dag1b* may only play a minor role during embryonic development. By contrast, cardiac abnormalities in 10 of 58 embryos were the only phenotype in *dag1*-T330A / T408A editants.

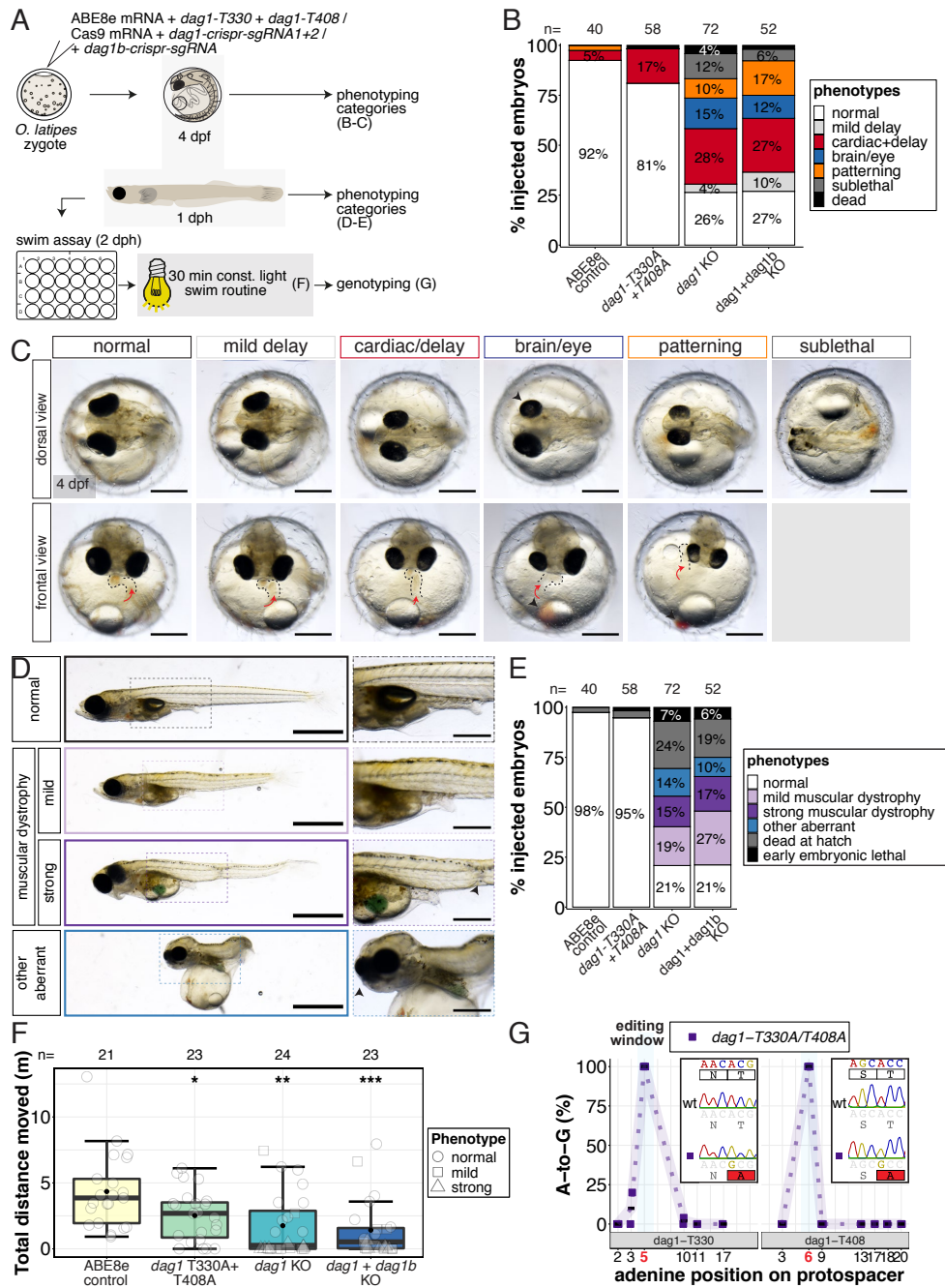


Figure 2.34: The loss of *dag1* function by CRISPR/Cas9-mediated NHEJ or ABE8e single amino acid change can be assayed with great precision in F0. (A) Experimental setup to investigate the effects of *dag1* missense mutations and of *dag1* and *dag1/dag1b* crispants on the function of dystroglycan in early and postembryonic development in F0. (B) Quantification of phenotypes of *dag1* editants / crispants at 4 dpf. (C) Phenotype profile of *dag1* editants / crispants at 4 dpf. Scale bar = 400 μ m. Red arrows indicate the direction of blood flow. (D) Phenotype profile of *dag1* editants / crispants at 1 dph. Scale bar = 1 mm, scale bar zoom in = 400 μ m. (E) Quantification of phenotypes of *dag1* editants / crispants at 1 dph. (F) Quantification of larval movement by tracking larval locomotion in a 24-well plate at 2 dph (constant light, 30 min). Individual data points are shown as phenotypic categories. Bold line = median. Black circle = mean. Statistical analysis was performed in R using the one-way ANOVA test with ABE8e control as the reference group. Global $p = .0004$. $p = .0210$ (*, *dag1-T330A+T408A*); $p = .0023$ (**, *dag1 KO*); $p = .0006$ (***, *dag1+dag1b KO*). (G) Adenine base editing efficiency quantified from Sanger sequencing reads of target amplicons using EditR analysis. dpf/dph=days post fertilisation/hatching.

It was striking that both *dag1* single and *dag1 / dag1b* crispants showed substantial levels of dystrophic hatchlings and additional aberrant characteristics which, in both cases only left 21% of normally developed larvae (Fig. 2.34D-E). In *dag1* crispants 11 larvae showed mild muscular dystrophy with a curved body axis, muscles that appear to be degenerating and reduced swimming. Moreover, 14 of 72 larvae showed a strong muscular dystrophy phenotype, characterised by complete immobility and a constriction of the notochord / spinal cord halfway along the body axis. By comparison to single *dag1* crispants, there was only a slight increase in the numbers of mild (14 of 52) and strongly dystrophic (9 of 52) hatchlings in *dag1 / dag1b* crispants.

Notably, a recent report has demonstrated the role of *dag1* function in *X. laevis* notochord development [Buisson et al., 2014]. The notochord, a defining feature of all chordate embryos, acts as a midline axial structure between the neural tube and developing inner organs that provides the main physical support structure during development [Scott and Stemple, 2004]. In addition to the muscular defects that are prominent, it is likely that a destabilised notochord will compound the morphological defects observed in strongly dystrophic and aberrant larvae and also result in defects in cartilages similar to a previously reported *alg2* mutant [Gücüm et al., 2021]. By contrast, all surviving *dag1*-T330A / T408A editants (95%) were normally developed normally. However, these normal *dag1*-T330A / T408A editants showed a clear reduction in the total distance they swam over the course of 30 min (Fig. 2.34F). Control larvae swam 4.3 ± 2.9 m ($n=21$), whereas 2.5 ± 2.0 m ($p = .0210$, $n=23$) were covered by *dag1*-T330A / T408A editants. This clear indication of muscular dystrophy was further substantiated by the fact that both edits p.T330A and p.T408A were introduced with 100% efficiency ($n=2$, each) (Fig. 2.34G). The effect on single and double crispants was even more striking, with only 1.8 ± 2.3 m ($p = .0023$, $n=24$) and 1.4 ± 2.2 m ($p = .0006$, $n=23$) covered, respectively.

In summary, I demonstrated that early signs of muscular dystrophy in medaka hatchlings can be easily quantified in a statistically meaningful manner. I could show that the complete loss of *dag1* function leads to a striking degeneration of muscles and potentially the notochord / spinal cord which leads to obvious impairment and even absence of locomotion in larvae. Moreover, the base editing efficiency of ABE8e introduced p.T330A, a hypothetical matriglycan site of α -DG, and p.T408A was exceptionally high. These

promising F0 experiments open the door for investigations of additional α -DG O-man sites, individually or in a combinatorial fashion.

Cytosine base editing of a highly conserved α -DG O-man site.

I have shown earlier that ancBE4max-SpRY can edit genomic sites with NAN PAMs efficiently, without increased rates of off-target phenotypes. I therefore decided to mutate a highly conserved α -DG O-man site (T412) using ancBE4max-SpRY (Fig. 2.35A-B). Analysing the genomic locus by Sanger sequencing and EditR quantification revealed that the average editing efficiency was $8.2 \pm 9.1\%$ ($n=10$) (Fig. 2.35C). Since the desired mutation was installed in the absence of bystander mutations, albeit at a very low frequency, the injected siblings can be raised to investigate the phenotypic effects in a stable genetic line. In the next section, I will provide some analysis of two genetically stable *dag1* point mutations.

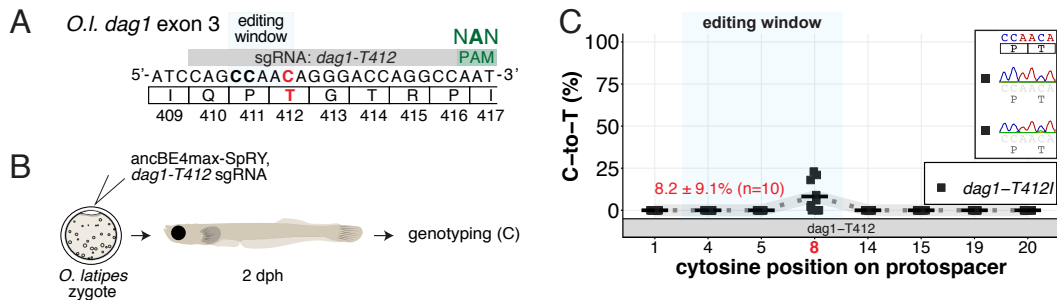


Figure 2.35: ancBE4max-SpRY mediates editing of a highly conserved T412 O-man site with a NAN PAM. (A) *Dag1-T412* locus (NAN PAM site) with target C8 at the T412 O-man. (B) Experimental setup. (C) Cytosine base editing efficiency quantified from Sanger sequencing reads of target amplicons using EditR analysis.

Dag1 p.T330M causes quantifiable changes in locomotion.

To overcome the limitations of reduced cytosine base editing of the T330 O-man site, I decided to assess the phenotypic consequences of p.T330M quantitatively in F2. For this purpose, I set up two different F1 crosses. I incrossed *dag1*^{+/T330M} fish and additionally, I crossed *dag1*^{+/T330M} males to *dag1*^{+/Q410X} females to analyse the effects of the p.T330M missense mutation over a null allele (Fig. 2.36A). I then used the wild-type, heterozygous, compound heterozygous and homozygous F2 offspring to perform locomotion analysis of individual larvae at 2, 6 and 14 dph (Fig. 2.36B-C). As introduced earlier (subsubsection 2.2.7), the swimming capacity of freely moving larvae is a good measure for the state of muscular dystrophy. Muscular dystrophy, with the disruption of muscle fibres and their attempted repair is a progressive phenotype. Therefore, performing this assay across several post-embryonic

stages can reflect the state of muscular dystrophy in a quantifiable manner. After acclimatisation of larvae in the imaging set-up in a 24-well plate, I tracked the swimming behaviour under constant light and light on/off alternating stress conditions. To be able to observe changes in swimming capacity as a measure of muscular dystrophy I maintained larvae separate in-between measurements.

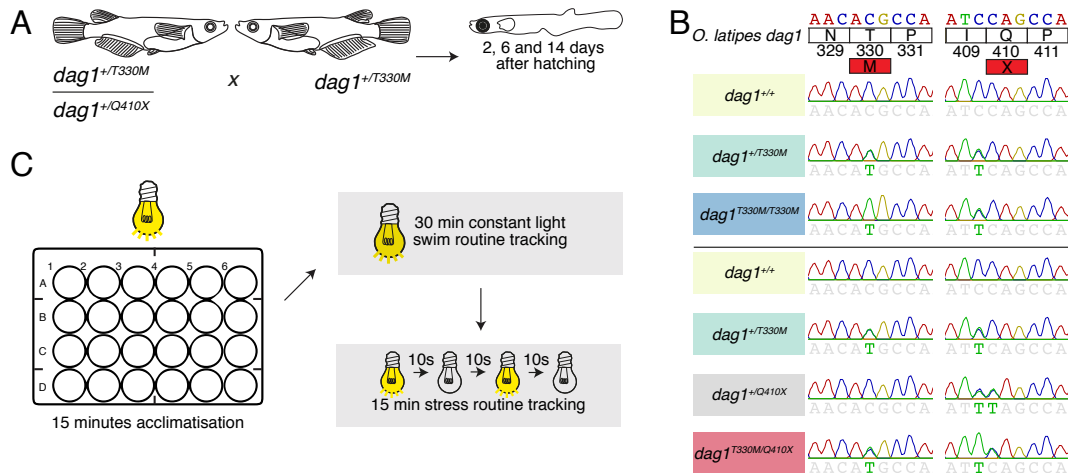


Figure 2.36: $dag1^{+/T330M}$ and $dag1^{+/Q410X}$ crossing schemes and genotyping in F2. (A-B) Heterozygous F1 p.T330M founders were increased to generate a mendelian ratio of wild-type, heterozygous and homozygous p.T330M fish in F2. Additionally to produce compound heterozygotes, heterozygous F1 p.T330M males were crossed to heterozygous F1 p.Q410X females. (C) Larvae at 2, 6 and 14 dph were subjected to a swimming assay. After transfer to a 24-well plate, larvae were acclimatised in the enclosed tracking system at constant light and temperature conditions (28°C) for 15 min. Tracking of the freely moving was then conducted for 30 min with constant light. Then the larvae were subjected to a 15 min light stress routine in which the top light was turned off after every 10 sec then on again for 10 sec. Tracked 2 dph larvae were kept separately and fed daily until 6 dph, where they were subjected to the same tracking routine. Finally, 6 dph larvae were raised separately to 14 dph with daily feeding and tracked (constant light and stress) prior to genotypic analysis. Dph = days post hatching.

In fact, I observed no significant effect of the p.T330M on the swimming behaviour under constant light conditions, nor in stress conditions when analysing stage by stage (Fig. 2.37A-C). Clear effects were only apparent in the cross-stage comparison under stress (Fig. 2.37D). The difference in distance that individual larvae travelled during 15 min stress at 14 dph versus 2 dph, i.e. 14 dph distance (m) – 2 dph distance (m), was relatively constant for wild-type animals (0.2 ± 1.3 m, $n=13$). By contrast, both heterozygotes and homozygotes moved considerably less at 14 dph, as indicated by negative Δ Movement values. These were -1.0 ± 1.5 m ($p = .0101$, $n=22$) for heterozygotes and -1.9 ± 1.6 m ($p = .0054$, $n=10$) for homozygotes. These results indicate minute, but nevertheless measurable effects of the p.T330M *O*-man site mutation. While the contact of α -DG to laminin in $dag1^{T330M}$ mutants appears

to be sufficient to maintain robust mobility under constant, relaxed conditions, not enough stability is given to allow the greater exertion of effort when stressed.

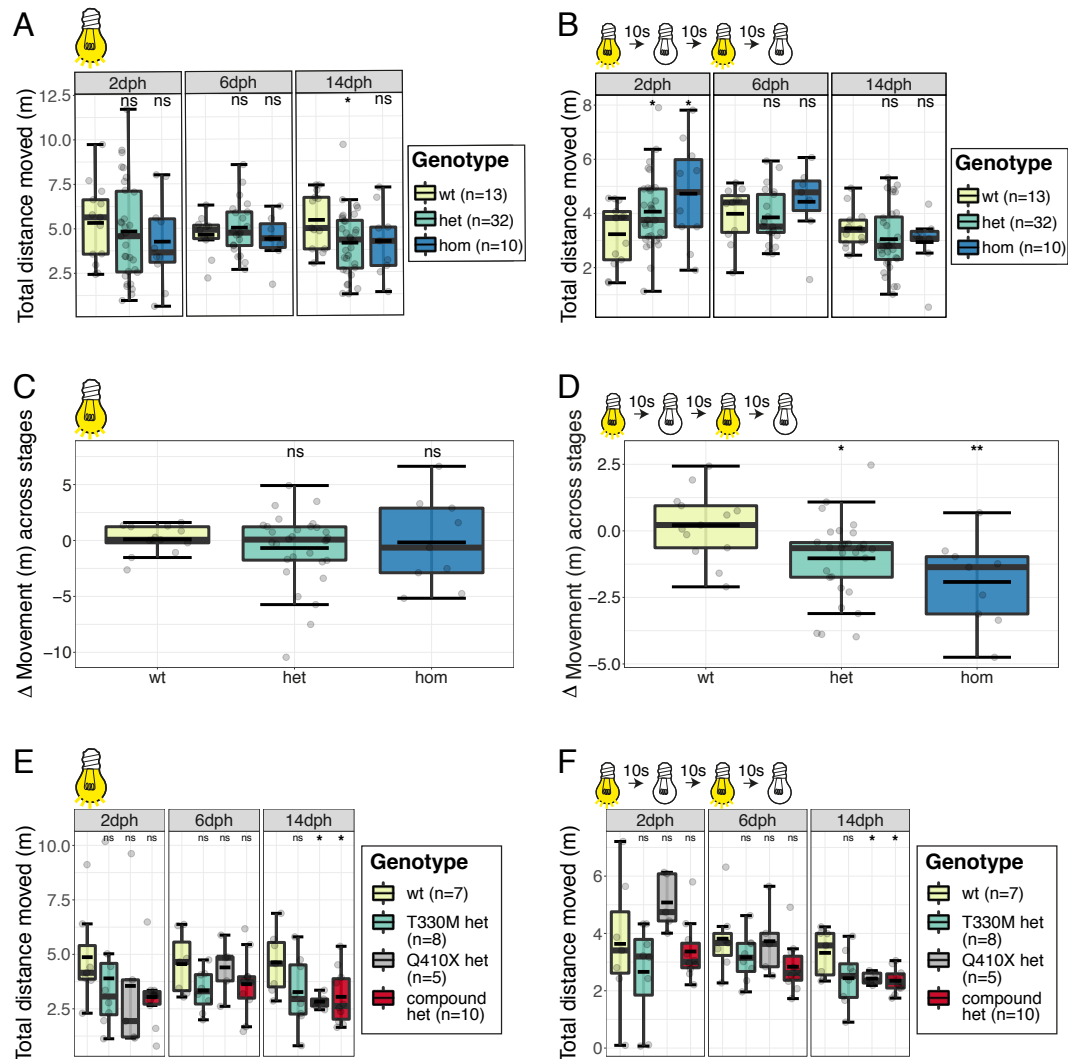


Figure 2.37: F2 analysis on the progressive effect of *dag1* p.T330M and a p.Q410X on larval locomotion. (A-B) Quantification of larval movement of offspring from heterozygous F1 p.T330M incrosses at 2, 6 and 14 dph under constant light (A) and during a stress routine (B). (C-D) Movement change between 2 and 14 dph under constant light (C) and during a stress routine (D) of offspring from heterozygous F1 p.T330M incrosses. Δ Movement was calculated as the difference between the Total distance moved at 14 dph and 2 dph for individual larvae. (E-F) Quantification of larval movement of offspring from heterozygous F1 p.T330M x p.Q410X incrosses at 2, 6 and 14 dph under constant light (A) and during a stress routine (B). Gray full line = median. Black half line = mean. Statistical analysis was performed in R using the one-way ANOVA test with wild-type (wt) larvae as the reference group. Asterisks indicate *p* values: ** $p \leq .01$, * $p \leq .05$, ns $p > .05$. Dph = days post fertilisation.

Finally, I observed that both $dag1^{+/Q410X}$ and compound heterozygotes $dag1^{T330M/Q410X}$ displayed significantly reduced swimming behaviour at 14 dph under both constant and stressed conditions (Fig. 2.37E-F). Under constant light wild-type animals moved 4.6 ± 1.4 m ($n=7$) over 30 min. By contrast,

dag1^{+/*Q410X*} swam only 2.8±0.3 m ($p = .016$, $n=5$) and *dag1*^{*T330M/Q410X*} 3.1±1.3 m ($p = .038$, $n=10$). Stressed wild-type animals on the other hand swam 3.3±0.8 m over the course of 15 min, with the movement of *dag1*^{+/*Q410X*} (2.4±0.2 m, $p = .027$) and *dag1*^{*T330M/Q410X*} (2.4±0.4 m, $p = .020$) being impaired similarly.

In summary, by using a sensitive, indirect assay of motor unit function I have shown that the T330 *O*-mannosylation site is functionally important *in vivo*. I have shown the effects are minute, such that I can only observe differences across stages when forcing the larvae to swim faster by introducing a light stressor. In addition, I could show that both, the complete loss of one functional *dag1* allele as well as the p.T330M in a null background similarly show a quantifiable phenotype at 14 dph.

SUCO plays a role in notochord development and heart function

The consequences of basal lamina disruption in neural tissues and skeletal muscles through the loss of functional α -DG have been described extensively [Nickolls and Bönnemann, 2018]. However, little is known about the pathophysiology of the vertebral columns and cartilages that may lead to scoliosis and scoliosis-like phenotypes seen in patients and that I observed in *pomt2*^{*S56(ins)*} mutants (Fig. 2.9). There is ample evidence suggesting that the notochord plays a role in spine development [Ellis et al., 2013; Gray et al., 2014] and a recent report revealed that a wavy and malformed notochord sheath can lead to scoliosis in zebrafish [Sun et al., 2020].

I have shown that *dag1* is expressed in the notochord during medaka development (Fig. 2.24C), and provided evidence for impaired notochord function in *dag1* crispants. However, relying on the disruption of α -DG function alone may not suffice to fully explain the scoliosis-like phenotypes in the spectrum of *pomt1* / *pomt2* mutants. The notochord sheath is rich in collagen [Scott and Stemple, 2004], whose synthesis and deposition are influenced by the function of *SUCO* [Sohaskey et al., 2010]. Based on the expression of *SUCO* in the notochord and the cartilage forming regions of the head (Fig. 2.24E), I hypothesised its loss of function to contribute to the phenotypes observed in *pomt1* / *pomt2* mutants.

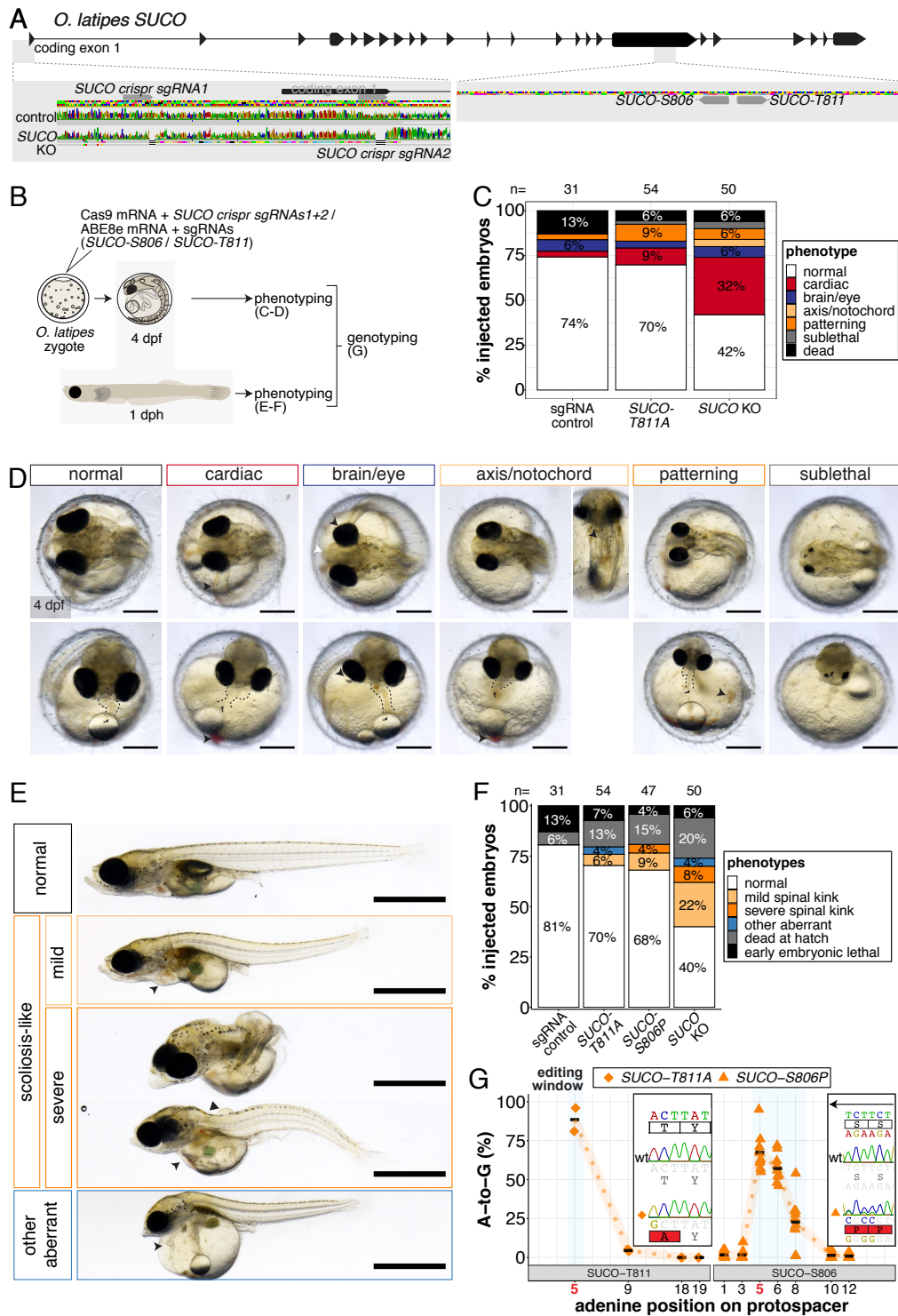


Figure 2.38: *SUCO* crispants and editants show striking spinal abnormalities. (A) Overview of the *SUCO* locus with coding exons highlighting the sgRNAs used to disrupt the *SUCO* gene by Cas9 mediated KO in exon 1 and by base editing in the *O*-mannosylated region. Note: *SUCO-S806* was a crRNA. (B) Experimental setup to investigate the effects of *SUCO* missense mutations and of *SUCO* crispants in early embryonic and postembryonic development in F0. (C) Quantification of phenotypes of *SUCO* editants / crispants at 4 dpf. (D) Phenotype profile of *SUCO* editants/crispants at 4 dpf. Scale bar = 400 μ m. (E) Phenotype profile of *SUCO* editants / crispants at 1 dph. Scale bar = 1 mm. (F) Quantification of phenotypes of *SUCO* editants / crispants at 1 dph. (G) Adenine base editing efficiency quantified from Sanger sequencing reads of target amplicons using EditR analysis. Dpf / dph = days post fertilisation / hatching.

To generate *SUCO* null phenotypes I designed two sgRNAs would cause an excision of the transcriptional start site and the first exon or result in a frameshift. Moreover, I decided to foster the previously successful strategy of introducing two missense mutations in conserved *O*-man sites using ABE8e (Fig. 2.38A-B). In accordance with its broad expression pattern I observed a spectrum of defects in *SUCO* crispants at 4 dpf (Fig. 2.38C-D). Heart morphology changes that were accompanied by coagulation (16 of 50) were most frequent but I also saw axis and patterning defects that are suggestive of defective notochord development. Although I observed a spectrum in the p.T811A editants, the phenotypes were less frequent. In hatchlings, 15 of 50 *SUCO* crispants displayed a scoliosis-like phenotype (scoliosis / kyphosis). Interestingly, I observed these phenotypes in both p.T811A (3 of 54) and p.S806P (6 of 47) editants, suggesting that the *O*-man of these amino acids may be functional *in vivo* (Fig. 2.38E-F). I validated that p.T811A was installed with a high efficiency of $88.5 \pm 10.6\%$ (n=2) in F0. By contrast, the efficiency of p.S806P editing was more modest ($67.5 \pm 11.5\%$, n=10) and occurred in the presence of a bystander edit introducing p.S805P ($22.7 \pm 15.3\%$).

In summary, I was able to provide evidence for a role of *SUCO* in notochord function. Moreover, I demonstrated that using state of the art base editing tools the underlying functions of *SUCO* and its *O*-man sites will be accessible in follow up studies at the amino acid level.

No role for *KIAA1549* beyond the retina?

To investigate the developmental function *KIAA1549* I created *crispants* using Cas9/sgRNA injections. Additionally, I mutated a single *O*-man amino acid (T568) using ancBE4max-SpRY and a T568-crRNA (with NAN PAM) (Fig. 2.39A-B). Despite the exceptional base editing efficiency of $97.7 \pm 6.2\%$ introducing p.T568I in editants I only observed few, unspecific phenotypes (7 of 71), that may suggest functions in neural, heart and notochord development. Since the rate of these phenotypes was even lower in *KIAA1549* crispants (3 of 56) these may, however, be injection artefacts (Fig. 2.39C-E). A recent study linked *KIAA1549* malfunction to Retinitis pigmentosa and suggests that it plays a role in the retina [De Bruijn et al., 2018]. In-depth characterisation of the retina in *KIAA1549* crispants and editants at larval stages will confirm and expand upon its role in the vertebrate eye and disease.

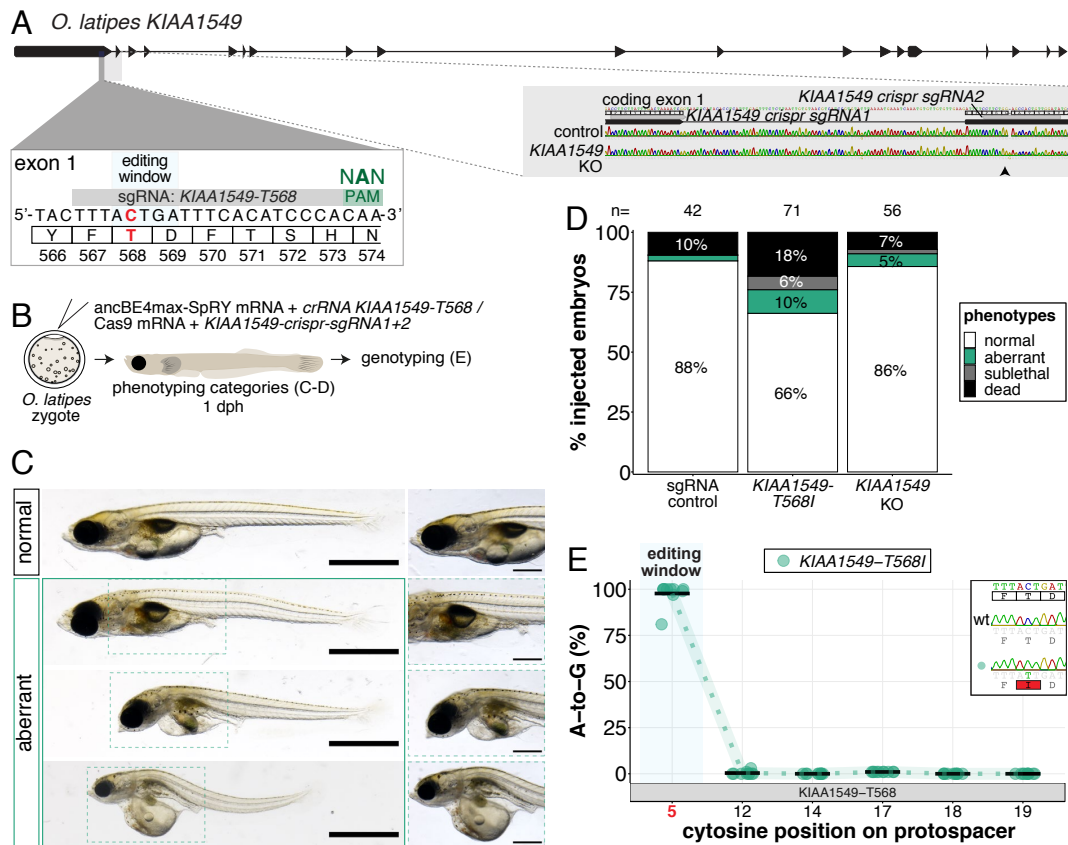


Figure 2.39: Low levels of unspecific developmental defects in *KIAA1549* editants and crispants indicate a dispensable role during early embryogenesis. (A) Overview of the *KIAA1549* locus with coding exons highlighting the sgRNAs used to disrupt the *KIAA1549* gene by Cas9 mediated KO between exons 1 and 2 and by base editing of the *O*-mannosylated region of exon 1 with a NAN PAM. (B) Experimental setup to investigate the effects of the *KIAA1549* p.T568I missense mutation and of *KIAA1549* crispants in development in F0. (C) Quantification of phenotypes of *KIAA1549* editants / crispants at 1 dph. Scale bar = 1 mm, scale bar zoom in = 400 μ m. (D) Quantification of phenotypes of *KIAA1549* editants / crispants at 1 dph. (E) Cytosine base editing efficiency quantified from Sanger sequencing reads of target amplicons using EditR analysis. Dpf / dph = days post fertilisation / hatching.

In summary, I have analysed both the complete loss of function via crispants and *O*-man site editant phenotypes for the three known POMT substrates. The base editing efficiencies presented here suggest that the functions of individual *O*-man sites can be investigated in F0. The muscular dystrophy and notochord phenotypes in *dag1* crispants and in parts in *dag1* editants, as well as the scoliosis-like phenotypes observed for *SUCO* crispants and editants alike, expand our understanding of the molecular contributors of DGpathies.

"No great discovery
was ever made
without a bold guess."

Isaac Newton

3

Discussion

In this work, I elucidated the organismal role of the POMT1-POMT2 complex in DGpathies and examined the respective contributions of the three known substrates of the POMT-complex. I used the following experimental approaches:

1. I developed an efficient cytosine and adenine base editing framework to enable the installation of point mutations in medaka (section 2.1).
2. I established and characterised WWS and LGMD *pomt2* models for DGpathies using CRISPR/Cas9 approaches and used base editing to install splice donor mutations in *pomt2* to examine CMD-like phenotypes (section 2.2).
3. I identified conserved *O*-man glycosites of α -DG, SUCO and KIAA1549 by protein sequence alignments and expanded the targeting range of existing base editors to allow mutating any *O*-man glycosites (section 2.3).
4. I disrupted the gene and *O*-man glycosite functions of *dag1*, *SUCO* and *KIAA1549* by CRISPR/Cas9 and base editing approaches and characterised embryonic and postembryonic phenotypes (section 2.3).

In the next section, I discuss and provide an outlook for selected findings of this thesis.

3.1 Efficient F0 cytosine and adenine base editing

3.1.1 Efficient introduction of PTC and amino acid changes in F0

My experiments with both CBEs and ABE8e demonstrated that base editing is remarkably efficient in medaka. I showed that the function of genes and even specific amino acids can be interrogated in F0. With these tools *in vivo* base editing can be harnessed to install PTCs and missense mutations with precision. This makes it easy to study the functional consequences of selected gene disruptions in an organismal context.

To probe the *in vivo* functions of genes that play a more pleiotropic role in embryonic development I chose two genes, *tnnt2a* and *kcnh6a*. Both genes were reported to play roles in cardiac contractility [Arnaout et al., 2007; Hassel et al., 2008; Meyer et al., 2020; Sehnert et al., 2002]. Introducing a PTC in *tnnt2a* (p.Q114X) with evoBE4max resulted in a large fraction of editants with completely silent heart chambers (49%) (Fig. 2.4B-C), reminiscent of *tnnt2a* crispants [Meyer et al., 2020]. By using efficient CBEs and ABE8e to interrogate *kcnh6a* I could highlight the essential function of a single p.R512G amino acid (Fig. 2.5B-B') to support a normal heartbeat. An early stop codon (p.Q11X) revealed the loss-of-function phenotype in CBE *kcnh6a* editants. With ABE8e I installed the p.R512G missense mutation which removed a positive charge of the conserved ERG channel S4 domain [Wang and MacKinnon, 2017]. This charge removal resulted in non-contractile ventricles in embryonic hearts similar to previous observations of null mutants in zebrafish [Hoshijima et al., 2016]. Using high-resolution imaging I revealed that the ventricles of p.R512G editants consistently collapsed which highlights an unexplored aspect of ERG functionality (Fig. 2.5F). These efficient base editing tools now allow to rapidly probe a larger number of individual base changes to efficiently identify relevant sites already in the injected generation. Point mutations in disease-relevant genes can thus be efficiently interrogated. Moreover, single amino acid editing facilitates studying structure-function relationships.

Compared to previous reports for cytosine base editing in fish [Rosello

et al., 2021b; Zhang et al., 2017; Zhao et al., 2020], I observed a surge in editing efficiency and reliability (Fig. 2.2, Fig. 2.3F-H, Fig. 2.4D-E, Fig. 2.5C-E,G). ABE8e efficiencies in both medaka and zebrafish [Cornean et al., 2022] markedly exceeded previously reported ones for ABE7.10 in zebrafish [Qin et al., 2018].

3.1.2 Genotyping: Sanger sequencing versus Amplicon-deep sequencing

The highest rates of editing efficiencies I determined by Sanger sequencing ranged from 94 to 100% and were overall comparable for ancBE4max, evoBE4max, and ABE8e [Cornean et al., 2022]. This suggests that bi-allelic editing is possible in the injected generation. I confirmed the efficacy of these base editors by examining both cytosine and adenine base editing outcomes with deep Amplicon-sequencing (Illumina sequencing). I then compared the averaged editing efficiency that I determined by Sanger vs. Amplicon-sequencing of the identical samples. The efficiencies were $77.8 \pm 20.8\%$ vs. $71.7 \pm 22.3\%$ for evoBE4max and $92.9 \pm 3.7\%$ vs. $83.7 \pm 3.9\%$ for ABE8e. EditR which uses peak heights of Sanger sequencing reads is inherently limited [Kluesner et al., 2018]. Not only can editing $<5\%$ not be resolved, but a dominant allele peak will often mask other alleles in the pool, which may imply a higher rate of editing than actually present. Sanger-sequencing results will tell us what the average composition of the analysed DNA sample was. To obtain information on the allele composition, Amplicon-sequencing is required. This also revealed the frequency of indels which was $9.0 \pm 4.9\%$ and $12.7 \pm 4.1\%$, respectively for evoBE4max and ABE8e across loci.

Which method to use to validate base editing will depend on the biological question and how the experiment is designed. Amplicon-seq allows identifying the frequency of edited alleles, which is of interest if the alleles are rare or present together with various other editing events [Cornean et al., 2022]. Sanger sequencing, though rapid and more straightforward, overestimates the editing frequency at the intended position and will not detect low-to-moderate indel levels in a F0 editant [Cornean et al., 2022; Kluesner et al., 2018]. Moderate indel frequencies can be mostly neglected as long as the desired editing event is very frequent and does not change the overall conclusion derived from phenotype profiles.

3.1.3 Limitations of *in vivo* base editing

There are several issues regarding the fidelity of base editing. These are indel events, off-target DNA editing and by-stander mutations. We have extensively discussed the issue of by-stander mutations and the context-dependent efficiency of base editors *in vivo* [Cornean et al., 2022]. I have already alluded that indels at rates presented in this thesis may be negligible, given a high rate of desired edits. Off-target DNA editing may become an issue when characterising unknown gene functions without the ability to predict the phenotypic outcome. A careful evaluation of **base edits** (ACEofBASEs), which we recently developed and incorporated into our base editing framework, is a sgRNA design tool for base editing that can provide off-target prediction information [Cornean et al., 2022]. It assesses the probability of a given sgRNA to bind anywhere else in the genome and allows us to choose sgRNAs with the fewest *in silico* predicted mismatches. Additionally, there is a growing toolbox of base editors [Anzalone et al., 2020; Huang et al., 2021], with engineered editing windows to minimise by-stander editing and reduce off-target DNA editing such as YE1 CBE variants [Doman et al., 2020] or the fusion of the bacterial Gam Mu protein, as in BE4-Gam, to reduce indel formation [Komor et al., 2017]. Such modifications, however, come at a cost, often in the form of reduced efficiencies and need to be carefully considered.

3.1.4 Alternatives to *in vivo* base editing

There are two alternative options for altering a short stretch of DNA efficiently in F0, which deserve mention. 1) **HDR-based Cas9 knock-in** approaches and 2) **prime editing**. HDR-based approaches are currently the method of choice to insert, modify or replace a stretch of several hundred bp efficiently. The use of efficient Cas9 variants [Thumberger et al., 2022] with chemically modified DNA donors now facilitates the rapid generation of a large variety of knock-in fish lines [Gutierrez-Triana et al., 2018; Seleit et al., 2021]. However, these approaches are constrained by significant byproducts that are consequences of Cas9-induced DSBs, i.e. indels. This makes base editors more attractive when F0 experiments are used for the sake of throughput, cost, time and ease. This is not to say that HDR-based approaches cannot compete with base editing tools when it comes to single or several amino acid alterations. On the contrary, I propose the complementary use of these methods. For

example, introducing several missense mutations, such as in *O*-man glycosites, in close proximity may accentuate indel frequencies when applying base editors and therefore require the crossing of fish to F1 or F2 anyways. Moreover, while C-to-G/C-to-A base editors work in principle [Chen et al., 2021, 2022; Koblan et al., 2021; Kurt et al., 2021], their efficiencies remain modest and are accompanied by unwanted base changes. This means transversion mutations are still beyond reach for F0 applications and therefore make HDR-based approaches indispensable.

I introduced the SpRY base editor variants (subsection 2.3.2) and showed that using *oca2* and *tbxta* as test candidates both cytosine and adenine base editing is possible across all sites across the genome in F0 (Fig. 2.27, Fig. 2.28, Fig. 2.29, Fig. 2.30, Fig. 2.31). This is in line with previously observed efficient editing at NA PAM sites in zebrafish using SpRY editors [Rosello et al., 2021a]. CBE and ABE experiments are therefore no longer limited to the conventional Cas9-based NGG PAM site. The efficiency may vary greatly, however, and F0 experiments with these SpRY editors should consider the potential rise in aberrant phenotypes due to increased DNA off-target effects (Fig. 2.29, Fig. 2.30, Fig. 2.31). Depending on the phenotype scored it may be necessary to titrate the editor:crRNA complex and perform the phenotypic analysis in the F1 generation.

Finally, prime editing may within the next years present itself as a useful genome engineering tool that holds certain merits over base editing. Prime editors are universal gene editing tools and can be used to install any desired DNA change, such as insertions, deletions, and all possible base conversions with precision. Prime editors consist of a Cas9 nickase protein with a C-terminally fused reverse transcriptase. This fusion complex is capable of rewriting DNA sequences at will, using prime editing guide (peg)RNAs that specify the target and encode the desired modification [Anzalone et al., 2019]. The application of prime editors has recently been demonstrated in zebrafish [Petri et al., 2021]. However, modest editing efficiencies, as well as the need for elaborate design and optimisation, currently limit their benefit over other tools, e.g. base editors and CRISPR/Cas9-based HDR. Although, recent improvements in the primed editing technology may overcome some these limitations [Chen et al., 2021; Ferreira da Silva et al., 2022; Nelson et al., 2021; Song et al., 2021], there is as of now no benefit of using these prime editors over base editors or HDR-based approaches *in vivo*.

3.2 The effect of differential POMT activity on different organs in DGpathy models

The two CRISPR-based *pomt2* mutant alleles I have established, *pomt2*^{S56(*ins*)} and *pomt2*^{Cterm-*fs*}, provided insight into the differential O-mannosylation requirement of different developing tissues and organs. Moreover, splice-donor editants of *pomt2* expanded this model (Fig. 2.7, Fig. 3.1).

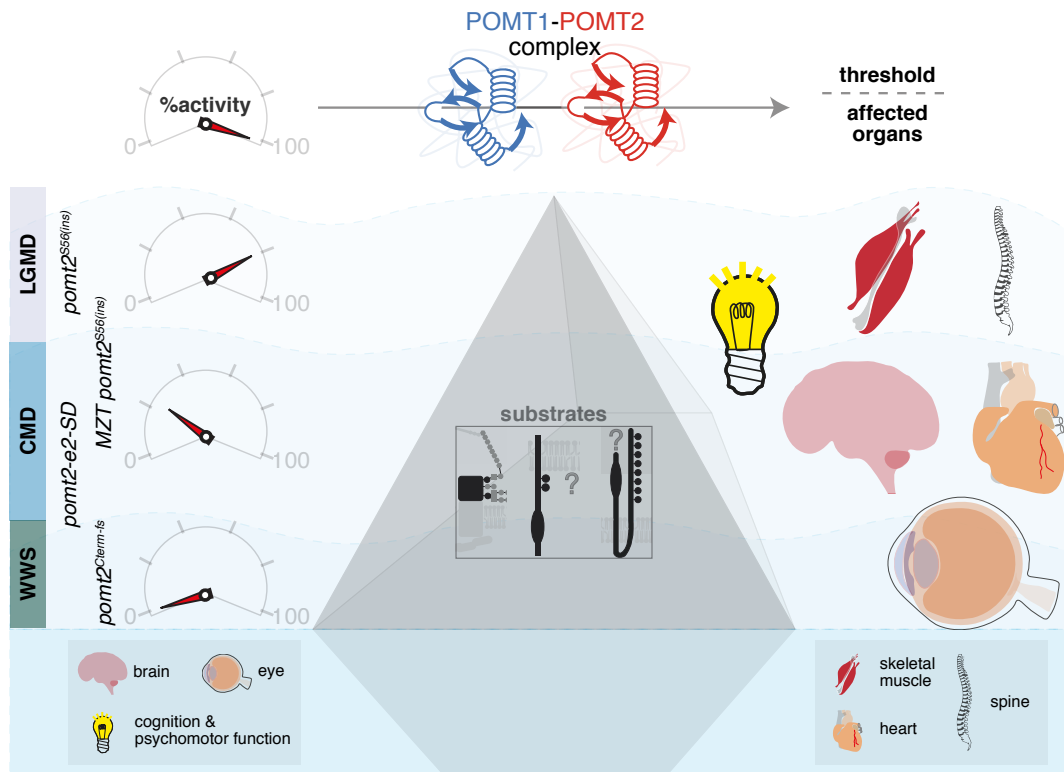


Figure 3.1: Differential POMT-complex activity requirements of organs affected in DGpathies. Note: Swimming capacity in medaka models was used as proxy for psychomotor function. WWS, Walker-Warburg Syndrome; CMD, Congenital Muscular Dystrophy; LGMD, Limb-Girdle Muscular Dystrophy.

3.2.1 A modest reduction in POMT activity primarily affects the muscles and spine

The *pomt2*^{S56(*ins*)} mutant displays comparably mild symptoms in homozygous larvae reminiscent of LGMD patients. These phenotypes are restricted to mild muscle fibre ruptures and scoliosis-like spinal deformities, and are not penetrant across all homozygotes (Fig. 2.9). I saw no retinal morphology alterations and the photoreceptor layer remained intact in 2-week-old larvae (Fig. 2.10A-B). Since 90% of homozygotes did not reach adulthood, it appears

that mild cellular and tissue-specific defects accrue over time and may affect other organ systems in juveniles. This indicates POMT2 is still functional in the *pomt2*^{S56(*ins*)} mutants, likely due to alternative splicing or transcriptional compensation mechanisms [Kontarakis and Stainier, 2020]. Removing maternal proteins or transcripts from homozygotes in MZT mutants appears to abolish this compensatory effect. In these MZT mutants, I saw a clear impact of the reduction of POMT2 function beyond the muscles and spine. The phenotypes extended to the entire body axis, with clear effects on the CNS, heart looping and cardiac edema (Fig. 2.9). While the muscle fibre ruptures did not impair the swimming ability of homozygotes, MZT larvae were almost immobile. This suggests a certain hierarchy in the dependency of tissues on POMT-based *O*-man. Muscles and the spine thereby reside at the tip of this metaphorical iceberg, while the heart and nervous tissues lie underneath the surface. What does this mean? I would argue that unlike as is the case in muscles, the nervous system can buffer the hypoglycosylation of POMT-substrates (e.g. α -DG) to some extent. Additionally, its functional requirement is not as imminent, as in neuronal or glial cells. Mechanically induced damage to the sarcolemma will shortly result in necrosis. By contrast, variations in the anyways, highly buffered neuronal connectivity will only be detrimental when aggravated over time or if glycosylation is completely lost. It is interesting that in the brain α -DG is less glycosylated than in muscle and also shows reduced ligand binding affinity (Nickolls and Bönnemann 2018, Development). There must therefore be a tight regulation of the context-specific function of the *O*-mannosyl glycoprotein and the extent of its glycosylation. Higher ligand binding affinities of neuronal α -DG to ECM proteins such as laminin may not be desirable, as this may deprive these cells of functionally relevant plasticity.

3.2.2 A strong reduction of POMT function impacts the heart and brain

To probe deeper down this iceberg of glycosylation I took a base editing approach to obtain more severe loss-of-function phenotypes. I disrupted the *pomt2-exon2 splice donor* by changing a single base change at an average efficiency of 88% (Fig. 2.11). I observed a range of phenotypes during the early embryonic stages of development in these editants. These ranged from mild cardiovascular defects to more severe midbrain and forebrain alterations. Such phenotypes are likely a consequence of altered cell migrations processes. Macroscopically, the

eye appeared unaltered which indicates that this CMD-like model reveals the next step towards the bottom in the iceberg metaphor, which is the brain.

3.2.3 Abolishing POMT enzyme activity leads to WWS phenotypes with morphological heart, brain and eye defects

Finally, *pomt2*^{Cterm-fs} mutants show a depletion of POMT1 and POMT2 protein levels. The C-terminal POMT2 extension may result in POMT-complex function being completely abolished (Fig. 2.13), resulting in very early WWS-like CNS defects. These start out with the absence of a defined interhemispheric fissure fold and then progress to include alterations in the midbrain, especially the isthmus fold of the midbrain-hindbrain boundary (Fig. 2.14, Fig. 2.15, Fig. 2.16). The phenotypic similarities to mouse models of DGpathy and WWS patients imply that impaired neuronal cell migration is a major driver of these defects [Hu et al., 2011; Moore et al., 2002; Nakano et al., 1996; Nickolls and Bönemann, 2018; Satz et al., 2008, 2010].

The morphological defects become very striking by stage 28 when I also observed a strong separation of wild-type and mutant transcriptomes (Fig. 2.17, Fig. 2.18). A major feature of these mutants was the presence of both apoptotic and pyknotic cells in both the brain and the retina. Apoptosis is common in neurons, especially during early CNS development when neurons fail to form robust synaptic connections. In addition, cell-intrinsic pathways, such as ER stress may also result in apoptosis [Brady and Morfini, 2010; Bredesen et al., 2006; Dekkers et al., 2013]. In yeast, the *O*-man machinery is also involved in protein quality control [Xu et al., 2013]. It is exciting to speculate on a link between the accumulation of misfolded proteins in the ER due to perturbed *O*-man with the ensuing ER stress triggering apoptosis. In fact, in *pomt2*^{Cterm-fs} mutants the increase in gene expression of cell-intrinsic apoptotic genes such as the nuclear isoform of the glycoprotein coding gene clusterin *clu* [Kim et al., 2011] indicates a factual link. Moreover, *phlda3*, which was also upregulated in *pomt2*^{Cterm-fs} mutants is a regulator of ER stress and differentially regulated by adaptive and apoptotic unfolded protein response mediators [Bensellam et al., 2019; Liu et al., 2021].

The pyknotic nuclei I have observed in stage 28 mutants are more difficult to explain. Such cells may be the endpoints of necrosis. Work comparing the morphology of apoptotic and necrotic pyknosis in *Drosophila* argues, however, that these pyknotic nuclei are in fact the endpoints of apoptosis [Hou et al., 2016]. Alternatively, there is physiological evidence for such occurrences in the retina. It was speculated that in nocturnal animals, such as mice, strong nuclear condensation may be involved in converting these nuclei into micro-lenses to enhance vision in near-darkness [Daghsni and Aldiri, 2021]. Molecular signatures of increased gene expression of the two lens-specific genes *BFSP1* and *bfsp2* in *pomt2*^{Cterm-fs} mutants indicate that lens filament gene expression is upregulated to potentially increase lens transparency [Song et al., 2009]. This is in line with a modest alteration of the lens morphology in mutants, perhaps due to increased lens fibre formation. It is intriguing to contemplate that a loss or reduction of synaptic projections from retinal ganglion cells to the optic tectum may have induced a physiological adaptation, wherein on the one hand the lens morphology changes and retinal nuclei become micro-lenses.

Finally, in addition to the CNS phenotypes, I observed the appearance of secondary heart defects with severe edema in *pomt2*^{Cterm-fs} mutants that were previously not observed in other WWS models (Fig. 2.13).

3.2.4 Molecular hallmarks of WWS-like DGpathy

Considering all molecular features of the WWS-like *pomt2*^{Cterm-fs} model it appears that the majority of phenotypes can in fact be explained from the perspective of defective α -DG glycosylation as follows:

1. Disrupted basement membranes in the CNS result in aberrant neural cell migration defects with cells overshooting across tissue boundaries, consequently populating brain ventricles and the interhemispheric fissure [Hu et al., 2011; Li et al., 2011; Moore et al., 2002; Nguyen et al., 2013; Satz et al., 2008, 2010; Sudo et al., 2018]. Moreover, disrupted retinal basement membranes, e.g., the inner limiting membrane likely contribute to aberrant migration within the retina [Clements et al., 2017; Hu et al., 2010; Satz et al., 2008, 2009].
2. The disruption of the glia limitans in the brain may obstruct the flow of cerebrospinal fluid via defective AQP4 water channels which can result in hydrocephaly [Satz et al., 2008, 2010; Tham et al., 2016; Verkman

et al., 2017]. A comparable mechanism of fluid homeostasis deregulation may be the cause for the epicardial edemas and associated tubular heart structure in *pomt2*^{Cterm-fs} mutants, reminiscent of zebrafish *tbx5* morphants [Chen, 2013].

3. Defects in cell differentiation or proliferation in both the brain and the retina may be consequences of perturbed signaling pathways, that reside downstream of α -DG such as Notch or MAPK signaling [McClenahan et al., 2016; Spence et al., 2004]. Radial glia expressed dystroglycan inhibits Notch signaling and thereby promotes oligodendrocyte differentiation in brain white matter [McClenahan et al., 2016]. In fact, Notch signaling regulates the retinal differentiation gene *atoh7* by lateral inhibition, which is downregulated in mutant transcriptomes [Lust et al., 2016; Saturnino et al., 2018]. Interestingly, my transcriptome analysis also revealed the downregulation of the neural differentiation/specification gene *neurod2* in *pomt2* mutant brain samples. *Neurod2* KO mice brains were shown to exhibit an overmigration of cortical neurons [Runge et al., 2021] corroborating the DGpathy phenotypes.
4. The increase in neuronal apoptosis may generally alter the neural-glial homeostasis by triggering an increase in microglial precursor colonisation of the midbrain in later stages of brain development [Xu et al., 2016].
5. Finally, cellular consequences of apical-basal polarity sensing in the retina may lead to the observed, high levels, of apoptosis in the retina [Clements et al., 2017].

3.3 The individual contribution of substrates of the POMT-complex to the spectrum of DGpathies

In the previous section, I discussed the three broad stages of DGpathy and the diverse effects of reducing or abolishing POMT-complex function on particular organs or tissues. I concluded that a majority of WWS-symptoms in the severe *pomt2*^{Cterm-fs} model may be ascribed to defective α -DG *O*-man. However, α -DG may not be the only cause, but rather the main driver. If and how the functions of the two other validated POMT-substrates, SUCO and KIAA1549, are linked to WWS symptoms is unclear. I hypothesised that scoliosis or kyphosis phenotypes observed in LGMD-like mutants are a consequence of impaired spine and notochord development. On the one hand defective α -DG

O-man destabilises notochord basement membranes [Buisson et al., 2014], while defective *SUCO* *O*-man leads to alterations in the notochord sheath by depleting the synthesis of the ECM component collagen [Sohaskey et al., 2010]. I also investigated the embryonic function of *KIAA1549* by examining the gross morphology of *KIAA1549* crispants (Fig. 2.39). However, I did not observe any substantial phenotypes, suggesting that its function is indeed restricted to the postembryonic retina [De Bruijn et al., 2018]. I will therefore, not further elaborate on *KIAA1549* crispant experiments.

3.3.1 *Dag1* loss-of-function phenotypes

I have shown that *dag1* and *dag1/dag1b* double crispants follow a similar overall phenotype distribution (Fig. 2.24), which I explain by their different spatio-temporal gene expression levels (Fig. 2.24). *Dag1b* appears to have acquired a subfunctionalised role during early embryonic development, as well as specialised functions in tissues such as the pronephric duct. I would therefore argue that *dag1b* function is negligible in the discussion of DGpathy phenotypes. Interestingly, the wide range of both embryonic and postembryonic phenotypes I observed in *dag1* crispants is by itself be a good representation of the spectrum of DGpathy (Fig. 2.34B-E). From the bottom to the top of the iceberg, I observed:

- Very severe phenotypes with microphthalmia, microcephaly and overall delayed development.
- Slightly less severe phenotypes with brain and eye defects, resembling those in *pomt2-e2-SD* CMD-like editants, typically accompanied by mild-to-moderate cardiovascular defects.
- Among the embryos with developmental delay and looping defects of the heart, that were able to hatch, were many that showed muscular dystrophy phenotypes by altered morphology and substantially alleviated swimming capacity. Interestingly, among the more strongly affected of these LGMD-like larvae were some which also showed constrictions of the notochord, in line with the reported function of α -DG in notochord development [Buisson et al., 2014].

As the notochord serves as the main physical support structure it is not surprising that, like muscular and spinal phenotypes, notochord phenotypes surface already at the least disruption of α -DG.

3.3.2 *SUCO* loss-of-function phenotypes

As I hypothesised, *SUCO* crispants showed a spectrum of phenotypes that included a substantial fraction (30%) of larvae with scoliosis or kyphosis phenotypes that were accompanied by epicardial edema (Fig. 2.38). The involvement of *SUCO* in collagen synthesis and the abundance of collagen in the notochord sheath [Scott and Stemple, 2004; Sohaskey et al., 2010], make a clear case for a functional role of *SUCO* in notochord development or maintenance. Additionally, my observation of the widespread expression of *SUCO* in various tissues makes a point for a role in heart function (Fig. 2.26), as collagen is an essential component of the late embryonic and postembryonic heart ECM [Silva et al., 2021].

3.3.3 Other classical *O*-man glycoproteins

A second group of protein *O*-mannosyltransferases, the TMTCs (1-4) has been recently reported. The main substrates of the TMTCs appear to be cadherins and protocadherins that do not possess elongated *O*-mannosyl glycan structures [Larsen et al., 2017a]. There are, however, several additional *O*-mannosyl glycoproteins with elongated structures that are, to date, not directly linked to the POMT1-POMT2 complex. These glycoproteins play important roles in the brain, and their glycans make up a large number of core M1 and M2 structures in the cerebellum and hippocampus of mice [Williams et al., 2022]. Among them are several members of the lectican family which interact with hyaluronan and ECM proteins to form the perineuronal net that provides structural stability to the brain [Bartels et al., 2016; Hang et al., 2022; Pacharra et al., 2013]. Moreover, several cell adhesion molecules with neuronal functions in synaptic plasticity and the formation of nodes of Ranvier have been identified. These include CD24 [Bleckmann et al., 2009], Neurofascin186 [Pacharra et al., 2013], and neurexin3 [Bartels et al., 2016]. Finally, the two receptor tyrosine phosphatase receptors PTPRZ1 and RPTP ζ /phosphacan (also known as RPTP β) were shown to be important for neuronal cell adhesion and migration processes in the developing CNS [Bartels et al., 2016; Dwyer et al., 2012; Trinidad et al., 2013]. This suggests that in the least, the function of the POMT-complex is essential for normal brain function beyond α -DG, including a role in perineuronal nets, cell adhesion and neurite outgrowth and several glial-specific functions.

3.3.4 A comprehensive substrate-centric model of DGpathies

Synthesising our understanding on the functional consequences of POMT-substrate disruption including α -DG interactors and putative POMT-substrates frames the following, comprehensive picture (Fig. 3.2). α -DG via laminin is essential in maintaining the integrity of basement membranes in muscles and astrocyte endfeet. Additionally, it maintains normal development of the eye/retina, the heart, the spine, and likely also of the notochord. The interaction with synaptic proteins extends the α -DG function to the neuromuscular junction, neural cell adhesion and the synapses of photoreceptors in the retina. To date, the only known function of KIAA1549 is also restricted to the photoreceptors. By contrast, I was able to show that SUCO likely plays a role not only in bone formation of the spine by positively influencing collagen biosynthesis but also in the heart and the notochord. Finally, there are several *O*-man glycoproteins with extended branched and linear structures which specifically contribute to the function of neurons via various routes. There is, to date, no direct experimental evidence that these proteins are substrates of the POMT1-POMT2 complex. However, due to the extended *O*-man glycans on these glycoproteins POMT1-POMT2 are their most likely glycosyltransferases.

3.4 Delineating the function of individual *O*-man glycosites

Protein glycosylation is a complex modification and it is still a technically challenging endeavour to establish cause and consequence of glycan structures on glycoproteins [Varki and Kornfeld, 2017]. What is particularly intriguing is the idea of differential spatio-temporal glycan composition on a specific glycoprotein. I have already alluded to different glycan compositions of α -DG in different tissues [Nickolls and Bönemann, 2018; Satz et al., 2010; Williams et al., 2022] and have extensively discussed the roles that α -DG plays in these tissues. However, what if it is not only the composition but also the glycosite that is differentially used at different developmental stages or across tissues? To probe this problem, it is crucial to have a versatile and efficient tool to mutate glycosites one by one at first and then combinations these. This is where base editors become remarkably valuable.

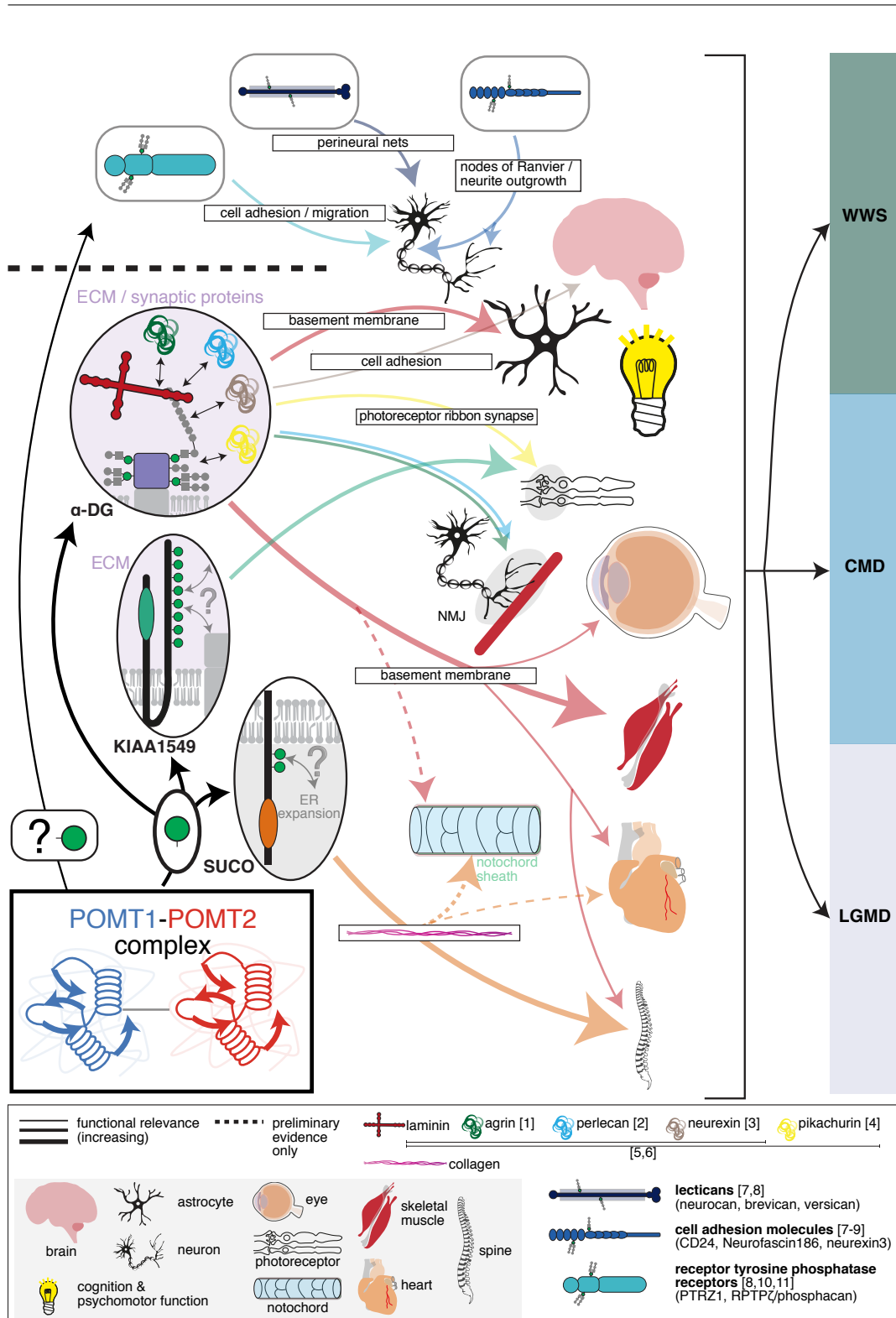


Figure 3.2: Comprehensive overview of the functional roles of POMT substrates in DGpathy. In addition to the three confirmed substrates -DG, SUCO and KIAA1549, the functional implications of the other potential substrates of the POMT-complex are shown. NMJ, neuromuscular junction. [1] Gee et al. [1994]; [2]Peng et al. [1998]; [3] Sugita et al. [2001]; [4] Sato et al. [2008]; [5] Nickolls and Bönnemann [2018]; [6] Endo [2015]; [7] Pacharra et al. [2013]; [8] Bartels et al. [2016]; [9] Bleckmann et al. [2009]; [10] Dwyer et al. [2012]; [11] Trinidad et al. [2013].

In the final chapter of this thesis, I used the comprehensive glycoproteomics data available to map all glycosites identified in human and chinese hamster experiments [Larsen et al., 2017b; Vester-Christensen et al., 2013] to the medaka orthologue of α -DG, *SUCO* and *KIAA1549* (Fig. 2.25, Fig. 2.26). These were a total of 37 O-man glycosites (47%), all of which can be mutated using SpRY-CBEs or -ABE8e and I selected several glycosites to mutate across all three substrates. My results provided the first-ever evidence for the *in vivo* function of individual glycosites. In particular, I presented preliminary evidence for the role of the medaka α -DG T330 glycosite (T317 in human) which had been identified as an essential matriglycan-binding site *in vitro* [Hara et al., 2011; Yagi et al., 2013]. Using a sensitive behavioural swimming assay, I showed that both the missense mutation p.T330A (with a p.T408A background mutation) in editants (Fig. 2.34), and p.T330M in a stable line significantly impacted larval swimming capacity (Fig. 2.37). These two independent experiments suggest an organismal role for the glycosite in muscular function or at the neuromuscular junction. Considering that a missense mutation may by itself alter the three-dimensional conformation and consequently the function of a protein, using different missense mutants or editants is essential. Importantly, CBEs and ABEs perfectly complement one another in this regard, allowing to address the function of a single glycosite from two structural perspectives with the same sgRNA. It is exciting to consider that mutating the T332 glycosite (T319 in human) in a p.T330A or p.T330M background using ABE8e may compound the muscular dystrophy phenotype. *In vitro* experiments have hinted toward a stronger decrease in laminin binding with the two point mutations [Hara et al., 2011; Yagi et al., 2013].

Additionally, I have introduced two point mutations p.S806P and p.T811A individually in the *SUCO* gene (Fig. 2.38). These mutations recreated the notochord, heart and spinal phenotypes of *SUCO* crispants, albeit at modest frequencies, likely due to incomplete editing of the glycosites. Yet, these results provide a good foundation to further characterise the role of these two O-man glycosites *in vivo*. Finally, I have introduced a p.T568I glycosite missense mutation in the *KIAA1549* gene with near-biallelic efficiency using a SpRY-CBE (Fig. 2.39). Given, the predicted retina-specific function of *KIAA1549* [De Bruijn et al., 2018], I was not able to appreciate any functional effects of the point mutation by gross-morphology characterisation of larvae.

Given the technical challenges, the field has largely assessed the com-

position of glycoproteins in tissues with strong enrichment such as the muscle in the case of α -DG [Nilsson et al., 2010; Stalnaker et al., 2010], or relied on cell lines to map glycosites at scale and to identify novel glycoproteins [Larsen et al., 2017b; Vester-Christensen et al., 2013], which at best, is a useful predictor of *in vivo* function. Coupling such approaches with base editing, however, to functionally delineate glycosite functions *in vivo* will lead to a synergy with unprecedented structure-function predictive power.

3.5 Perspective

Elaborating on all promising future experiments would go beyond the scope of this thesis. I will, however, briefly list the short term and discuss long term experiments that I find the most exciting.

1. Address the retinal, postembryonic functions of *KIAA1549* and its glycosite editant. This would complement recent work on a retina-specific *POMT1* KO mouse model where *KIAA1549* was found to be depleted [Uribe et al., 2021]. Since there is still no mutant model for *KIAA1549*, this is crucial.
2. Characterise the *dag1*^{Q410X} null mutant line by histology and transcriptomics and directly compare gene expression profiles with those in *pomt2*^{Cterm-fs} mutants to identify molecular programs that are exclusive to the *pomt2* mutant. These would highlight functionalities that go beyond α -DG.
3. Perform F0 base editing experiments on *dag1*^{T330M/T330M} mutants to alter the predicted matriglycan sites T332 and T391 (T319 and T379 in human) [Hara et al., 2011; Yagi et al., 2013], in a combinatorial fashion by F0 base editing and repeating the quantitative behavioural assays.
4. Address the relevance of defective Notch signalling in *pomt2*^{Cterm-fs} mutants downstream of *dag1* function. For this purpose, the Notch-reporter *tp1-MmHbb::d2GFP* transgenic line in medaka is the ideal tool [Lust et al., 2016], as minute spatio-temporal changes can be followed live, *in vivo*.
5. Investigate the link between ER stress in the brain of *pomt2*^{Cterm-fs} mutants by monitoring ER stress protein levels (e.g., IRE1 and Xbp1) in consecutive stages using immunoblots and quantitatively correlating these with the number of TUNEL positive cells [Ishikawa et al., 2017].

In a long-term perspective, I foresee three separate streams of experiments providing the most exciting insights into DGpathy pathogenesis and biology.

In light of the pleiotropy of phenotypes in DGpathy models such as the *pomt2*^{Cterm-fs} mutant a means to disentangle the effect on different tissues is crucial. Traditionally, this was performed in mice using conditional KO models. However, these models are limited by the use of Cre lines, which are often not accurately expressed in the target tissue alone, or only in a subset of this tissue. Moreover, in organs and tissues harbouring stem cells the re-population of the tissue with cells containing intact copies of the gene of interest may reduce the value of this tedious approach [Becher et al., 2018]. By contrast, organoids have recently emerged as an exceptionally attractive model to study developmental processes and shed light on disease [Kim et al., 2020]. Patient-derived induced pluripotent stem cells were used to derive brain organoids to investigate DGpathies, which recapitulated the abnormal radial glial fibre migration [Taniguchi-Ikeda et al., 2021]. To complement the study of DGpathy-derived human organoids I propose the use of fish organoids recently established [Zilova et al., 2021]. These organoids rapidly assemble into anterior neural structures and can, combined with CRISPR/Cas9 and base editing tools, allow to study DGpathy models within a confined, yet complex organ space. Deriving retinal organoids from *pomt2*^{Cterm-fs} mutants will enable delineating the retinal defects in this WWS-model in an uncoupled manner from the severe brain defects.

I have raised the point to understand the differential functions of *O*-man glycosites across developmental stages and tissues. To achieve this goal, it is necessary to have adequate downstream protocols for the isolation of the studied glycoproteins and mapping of the glycosites. Although, I have attempted to isolate glycosylated α -DG from postembryonic tissue in sufficient amounts for glycoproteomics (in collaboration with Valerian Grote, Rapp lab, MPI Magdeburg), these efforts were technically challenging and did not provide sufficient enrichment to map *O*-man glycosites. The complexity of the α -DG glycan composition and consequently, limitations of current enrichment protocols make it difficult to study the *O*-man glycan composition of α -DG from larval samples. There have been efforts to establish α -DG-knockin models (e.g., myc-tag) [Morlacchi et al., 2012; Palmieri et al., 2017], however, the three dimensional complexity has, to date, not allowed identifying precise tagging location and tag sizes for *in vivo* experiments. I, therefore, propose

the use of SUCO and KIAA1549 as more accessible substrate models. Using previously established endogenous tagging strategies [Gutierrez-Triana et al., 2018; Seleit et al., 2021], I suggest to introduce the small ALFA-tag for affinity purification [Götzke et al., 2019] at the less conserved N-termini of the two candidates and establish endogenously tagged medaka lines. These lines would be excellent resources to perform base editing experiments of individual or multiple glycosites. Investigating the phenotypic effects of these mutations on the notochord, heart or retina and followed up by analytical methods to purify and identify the presence and absence of glycopeptides from the respective organs will allow to correlate glycan structures and glycosites with tissue specific functions.

Finally, to widen our understanding of the CNS in DGpathies I would expand the POMT-substrate KO experiments to the other potential substrates such as neurocan, Neurofascin186 and PTRZ1. Moreover, I would perform combinatorial experiments targeting *dag1*, *SUCO* and *KIAA1549* at the same time and directly compare the phenotypic outcomes to those of the *pomt2* DGpathy models I have established.

4

Conclusions

The results of this thesis suggest a hierarchy in the necessity of POMT-complex activity in different organs. Using three different approaches to disrupt *pomt2* function I could show that depending on the nature of the mutation, the functional consequences will separate along a phenotypic range. Within this range, organs such as the eye and the brain were only affected when POMT-complex function was substantially disrupted. By contrast, muscles and the spine were much more prone to even minute changes in the enzymatic properties of the POMTs. My characterisation of the *pomt2*^{Cterm-fs} WWS-model leaves me to postulate that a combination of neural migration defects, fluid homeostasis deregulation, signaling pathways changes, ER-stress and a change in apical-basal polarity of neural cells drive the pleiotropic CNS defects. I disrupted the functions of the three POMT-substrates individually. Thereby, I identified a previously unknown role of α -DG and SUCO in cardiovascular function, confirmed the necessity of α -DG in notochord function and revealed that likewise SUCO plays an important role in notochord development. Around these results I framed a model that disentangles the contributions of all POMT-substrates, both confirmed and predicted, towards cellular and organ-specific functions. Finally, I established efficient cytosine and adenine base editors that can in principle, mutate virtually any C or A site in the genome. By applying these tools to mutate *O*-man glycosites on α -DG (T330) and SUCO (S806 and T811) I provide the first-ever demonstration of the feasibility of this new approach in providing functional insight in a developing organism. My results show that to fully grasp all aspects of DGpathy we need to take a holistic approach. Future studies linking structure-function relationships on the substrate level to tissue-wide developmental consequences in model organisms will be instrumental to enable tailored, preclinical drug screens and to provide reliable predictions of disease progressions in DGpathies.

5

Materials & Methods

5.1 Materials

5.1.1 Organisms

Fish lines

Table 5.1: Fish lines used in this thesis.

Fish line name	Internal stock numbers	Source
wild-type Cab F67-F75	7524, 7796, 8072, 8368, 8617, 8813, 9170, 9406, 9698	Lab stock, Loosli et al. [2000]
<i>pomt1</i> ^{Y33(<i>ins</i>)}	7741, 8155, 8613, 8765, 9119, 9454, 10047, 10048	This work, Cornean [2017]
<i>pomt2</i> ^{S56(<i>ins</i>)}	7747, 8010, 8063, 8064, 8151, 8614, 8615, 8766, 9067, 9421, 9928	This work, Cornean [2017]
<i>pomt2</i> ^{ΔMIR2}	8824, 9044, 9045, 9222, 9488, 9991, 9992	This work
<i>pomt2</i> ^{Cterm-fs}	8770, 8947, 9221, 9476	This work
<i>pomt2</i> ^{Cterm-fs} , <i>rx2::lifeactGFP</i>	9482, 9937, 9938	This work
<i>rx2::lifeactGFP</i>	9260	Lust and Wittbrodt, unpublished
<i>pomt2</i> ^{ΔCterm}	8770, 8947, 9190, 9475	This work
HdrR, <i>cmlc2::GFP</i> , <i>cmlc2::H2A-mCherry</i> (<i>cmlc2=myl7</i>)	9341	Hammouda et al. [2021]

Fish line name	Internal stock numbers	Source
Cab, <i>cmlc2::GFP</i> (<i>cmlc2=myl7</i>)	9257	Gierten et al. [2020]
<i>dag1</i> ^{T330M}	9461, 9774, 10058	This work
<i>dag1</i> ^{Q410X}	9463, 9773, 10032	This work

All mutant fish lines were generated by injection into one-cell stage medaka embryos. The following lines were generated using the CRISPR/Cas9 system: *pomt1*^{Y33(*ins*)}, *pomt2*^{S56(*ins*)}, *pomt2*^{ΔMIR2}, *pomt2*^{Cterm-fs} and *pomt2*^{ΔCterm}. The following lines were generated using the cytosine base editor ancBE4max: *dag1*^{T330M} and *dag1*^{Q410X}.

Bacteria

Table 5.2: Bacteria used in this thesis.

Designation	Source
Mach1T1 T1 phage resistant chemically competent <i>E. coli</i>	Thermo Fisher Scientific
NEB Turbo Competent <i>E. coli</i>	New England Biolabs

5.1.2 Plasmids

Table 5.3: Plasmids used for mRNA synthesis in this thesis.

Internal plasmid number	Plasmid	Source
#5197	pCS2+_heiCas9	Lab stock / Thumberger et al. [2022]
#5400	pGGEV_4_BE4-Gam	This work / Thumberger et al. [2022]
#5797	pCS2+_evoBE4max	This work / Cornean et al. [2022]
#5811	pCMV_AncBE4max	Addgene #112094, Koblan et al. [2018]

Internal plasmid number	Plasmid	Source
#5812	pCMV_ABE8e	Addgene #138489, Richter et al. [2020]
#5800	pCS2+_evoBE4max-NG	This work
#5868	pCS2+_evoBE4max-SpRY	This work
#5869	pCS2+_ancBE4max-NG	This work
#5867	pCS2+_ancBE4max-SpRY	This work
#5862	pCMV_ABE8e-NG	Addgene #138491, Richter et al. [2020]
#5866	pCS2+_ABE8e-SpRY	This work
#5810	pT3TS_RfxCas13d-HA	Addgene #141320, Kushawah et al. [2020]
#5628	pCS2+_dag1-CDS	This work

Table 5.4: Plasmids used for sgRNA synthesis in this thesis.

Internal plasmid number	Plasmid	sgRNA alias	Source
#5296	DR274_sgRNA275_pomt2_hinten_T3	<i>pomt2-hinten-T3</i>	This work
#5297	DR274_sgRNA276_pomt2_hinten_T4	<i>pomt2-hinten-T4</i>	This work
#5357	DR274_sgRNA_57_Oca2_ex9_T1	<i>oca2-Q333</i>	Lischik et al. [2019]
#5444	DR274_sgRNA18_OI_kcnh6a_e1_stop_T3	<i>kcnh6a-Q11</i>	Cornean et al. [2022]
#5445	DR274_sgRNA19_OI_kcnh6a_e8_S4_T2	<i>kcnh6a-R512</i>	Cornean et al. [2022]
#5584	DR274_sgRNA_DAG1a_T2	<i>dag1-crispr-sgRNA1</i>	This work
#5585	DR274_sgRNA_DAG1b_T2	<i>dag1b-crispr</i>	This work
#5604	DR274_sgRNA325_OI_tnnt2a_T6	<i>tnnt2a-Q114</i>	Meyer et al. [2020]

Internal plasmid number	Plasmid	sgRNA alias	Source
#5607	DR274_sgRNA_GFP_BE_T4	<i>GFP-C71</i>	Hammouda et al. [2021]
#5623	DR274_sgRNA_pomt2-tag-C_T7	<i>pomt2-tag-C-T7</i>	This work
#5624	DR274_sgRNA_pomt2-tag-C_T9	<i>pomt2-tag-C-T9</i>	This work
#5683	DR274_sgRNA_pomt2_MIRmotif_T2	<i>pomt2-MIRmotif-T2</i>	This work
#5684	DR274_sgRNA_pomt2_MIRmotif_T3	<i>pomt2-MIRmotif-T3</i>	This work
#5687	DR274_aDG_O-man_conversion_T14	<i>dag1-T330</i>	This work
#5688	DR274_aDG_O-man_conversion_T31	<i>dag1-T332</i>	This work
#5826	DR274_sgRNA_DAG1a_T3	<i>dag1-crispr-sgRNA2</i>	This work
#5827	DR274_sgRNA_SUCO_TSSregion_T1	<i>SUCO-crispr-sgRNA1</i>	This work
#5828	DR274_sgRNA_SUCO_TSSregion_T9	<i>SUCO-crispr-sgRNA2</i>	This work
#5829	DR274_sgRNA_pomt2_ex2_ABE_T1	<i>pomt2-D92</i>	This work
#5850	DR274_sgRNA_SUCO_ABE_O-man_T1	<i>SUCO-T811</i>	This work
#5880	DR274_sgRNA_pomt2_ex2_SD	<i>pomt2-ex2-SD</i>	This work
#5882	DR274_sgRNA_pomt1_ex1_SD	<i>pomt1-ex1-SD</i>	This work
#5692	DR274_aDG_O-man_conversion_T33	<i>dag1-T408</i>	This work
#5693	DR274_aDG_O-man_conversion_STOP_T36	<i>dag1-Q410</i>	This work
#5870	DR274_oca2-Q22_NGN	<i>oca2-Q22</i>	This work
#5875	DR274_oca2-Q271_NAN	<i>oca2-Q271</i>	This work
#6093	DR274_sgRNA_KIAA1549_ex2_T2	<i>KIAA1549-crispr-sgRNA2</i>	This work
#6094	DR274_sgRNA_KIAA1549_ex1_T13	<i>KIAA1549-crispr-sgRNA1</i>	This work

Table 5.5: Plasmids used for *in situ* probe synthesis in this thesis.

Internal plasmid number	Plasmid	Source
#5820	pGEM-Teasy(O.I._pomt1_partial_cDNA_ISH)	This work
#5821	pGEM-Teasy(O.I._pomt2_partial_cDNA_ISH)	This work
#5822	pGEM-Teasy(O.I._KIAA1549_partial_cDNA_ISH)	This work
#5964	pGEM-Teasy(O.I._dag1_partial_cDNA_ISH)	This work
#5968	pGEM-Teasy(O.I._dag1b_partial_cDNA_ISH)	This work

Table 5.6: Miscellaneous plasmids used in this thesis.

Internal plasmid number	Plasmid	Source
#221	pCS2+	Rupp et al. [1994]
#3632	DR274_sgRNA_backbone	Addgene plasmid #42250, Hwang et al. [2013]
#3240	pGGEV4	Lab stock, Kirchmaier et al. [2013]
#5386	pCMV_BE4_Gam	Addgene #100806, Komor et al. [2017]
#5394	pJET1.2_BE4-Gam_SV40NLS	This work / Thumberger et al. [2022]
#5399	pGGEV4_BE4-Gam_BamHI_EcoRV_half	This work / Thumberger et al. [2022]
#5697	pBT375_evoAPOBEC1-BE4max-NG	Addgene #125616, Thuronyi et al. [2019]
#5698	pBT281_evoAPOBEC1-BE4max	Addgene #122611, Thuronyi et al. [2019]
#5861	pCMV_ABEmax-SpRY	Addgene #140003, Walton et al. [2020]

5.1.3 Oligonucleotides and primers

All oligonucleotides and primers designed in this work were ordered from Eurofins Genomics via a custom FileMaker script from the lab.

Table 5.7: Genotyping and Sanger sequencing primers used in this thesis with sequences in 5' to 3' direction.

Internal stock number	Alias	Oligo sequence
JW1408	locus_eGFP_reverse_seq_primer	AAACGCTCGACCAGGATGGGCA
JW1458	GFP_noStart_F	GTGAGCAAGGGCGAGGAGCT
JW1459	GFP_noSTOP_R	CTTGTACAGCTCGTCCATGC
JW1955	seq primer ggw dest sc -atg	ATTACCGCCTTTGAGTGAGC
JW3078	seq primer ggw dest_backbone	AAACTAACGTGAGTTACGCGTC
JW3120	seqPolyA	CACTGCATTCTAGTTGTG
JW3292	OCA2_T7_F	GTTAAAACAGTTTCTTAAAAAGA
JW3293	OCA2_T7_R	AGCAGAAGAAATGACTCAACATT
JW5566	PomT1_seq_F	ATTATAGTTCCGATCACGCACCA
JW5567	PomT1_seq_R	ACTGGCCATAATACACTTCATCG
JW5574	PomT2_seq_F	AAGTCAGTGGGAGAGTTATGTCAC
JW5575	PomT2_seq_R	CTTAACAGAAAAGAACGGCCACAT
JW6835	PomT1_RT-PCR_5'UTR_F1	TCGGAACCGAGCAACACATT
JW6837	PomT1_RT-PCR_ex3_4_R	GCCCATGGGATACTCTGCTC
JW6841	PomT2_RT-PCR_5'UTR_F1	AAGCCACAAATTCAACCGGC
JW6842	PomT2_RT-PCR_ex1_2_R	GTTTCATCCCAGCACACGTG
JW6846	PomT2_RT-PCR_3'UTR_R	GGTGACAACCTCCAGTGCATC
JW6969	PomT2_condi_locus_intern5_F	CCGCGTCCTGTACTATCACC
JW6971	PomT2_condi_seq_F	CTTCTACAAGTTAGCAGAGC
JW6972	PomT2_condi_seq_R	TGTAGCACTGATGCTAATTCG
JW7050	PomT2_RT-PCR_exon3_R	TCCTCTCATCCCGAGATAGTTG
JW8063	dag1a_exon2_seq_F	GAAGACCACTTGGATGCCGA
JW8064	dag1a_exon3_seq_R	CGTAAATTGGCCTGGTCCCT
JW8065	dag1b_intron2_seq	GCACCAAACCTTTTACGTCTTCCT

Internal stock number	Alias	Oligo sequence
JW8066	dag1b_exon2_seq	ATGCCAACCAACCACAGGAT
JW8071	SUCO_TSSregion_seq_F	TGACGTAAGCAGTAGCAGGT
JW8072	SUCO_TSSregion_seq_R	ACAACAACAATATTTAATGCTGGAG AC
JW8418	OI_kcnh6a_e1_seq_F	CGACTCCTTTTTGCGTGTGTC
JW8419	OI_kcnh6a_e1_seq_R	AATGCAGCACACACACACAC
JW8430	OI_kcnh6a_e8_seq_F	GCTTTGCAAGGTATAGAGCACAG
JW8431	OI_kcnh6a_e8_seq_R	AACGTTGCCAAAACCCACAC
JW9028	Dag1a_base_edit_seq_F	ACTTGGGTGTTCCTTTAGACCAGA
JW9029	Dag1a_base_edit_seq_R	TGGTAGTAGAGGACTTGAAGGT
JW9317	pomt2_MIRmotif_seq_F	TTAATTGAACAGGGCGGCCT
JW9318	pomt2_MIRmotif_seq_R	CTCCGCAGTACCTTCACCAG
JW9319	pomt2_DEmotif_seq_R	AGCAGCATACTCCTCTCATC
JW9474	pomt2_3'UTR_seq_F	AGTTGGTGGGAATGTAAAGGCA
JW9475	pomt2_3'UTR_seq_R	TCGTCTTAGAAATTGTAGTACGAACA
JW9557	tnnt2a_Base_edit_seq_F	TGGAGAAAGACCTGATGGAGC
JW9558	tnnt2a_Base_edit_seq_R	TTCCCGCTCCTCTTCTCTGT
JW10422	SUCO_O-man_F	AACCTCCCCGCCCTTATAGT
JW10423	SUCO_O-man_R	CCCTGAGGAAAAGCTGCAGA
JW10795	pomt1_ex2_DEmotif_F	CCCCTTGTGGTCACAGTTCA
JW10796	pomt1_ex2_DEmotif_R	GGTTCCACACAAAGTTGCCG
JW10962	KIAA1549_ex1_2_seq_F	AGGGACGAAAGGTGCTTCTG
JW10963	KIAA1549_ex1_2_seq_R	CCTGGAGCTCCACTGATTTGT
JW10964	KIAA1549_ex1_seq_F	TGTTCCAGGACTGAGTCAACAG
JW10965	KIAA1549_ex1_seq_R	GAGGAATTAGGAGGCCTGTCCG
JW11047	KIAA1549_ex1_seq_2_F	TACACCACCCAATAACCAAGG
JW11048	KIAA1549_ex1_seq_2_R	CAGAAGCACCTTTCGTCCCT

Table 5.8: Illumina sequencing primers with adapter sequence used in this thesis with sequences in 5' to 3' direction.

Internal stock number	Alias	Oligo sequence
JW10815	oca2_Q333_HTS_genewiz_F	ACACTCTTCCCTACACGACGCTC TTCCGATCTCGTTAGAGTGGTATG GAGAACTGT
JW10816	oca2_Q333_HTS_genewiz_R	GACTGGAGTTCAGACGTGTGCTC TTCCGATCTATGGTCCTCACATCA GCAGC
JW10817	GFP_C71_HTS_genewiz_F	ACACTCTTCCCTACACGACGCTC TTCCGATCTTCCGATCTCGTAAAC GGCCACAAGTTCAG
JW10818	GFP_C71_HTS_genewiz_R	GACTGGAGTTCAGACGTGTGCTCT TCCGATCTTGGCGTCCTCCTTGA AGTC
JW10819	kcnh6a_S4domain_HTS_genewiz_F	ACACTCTTCCCTACACGACGCT CTTCCGATCTAGTTTGCTGTGTA CCTCCAGTT
JW10820	kcnh6a_S4domain_HTS_genewiz_R	GACTGGAGTTCAGACGTGTGCTC TTCCGATCTATCTTCATACCGCC CACACG
JW10821	tnnt2a_Q114_HTS_genewiz_F	ACACTCTTCCCTACACGACGCT CTTCCGATCTTGAGAGCAGAAA GAAAGAGGAGG
JW10822	tnnt2a_Q114_HTS_genewiz_R	GACTGGAGTTCAGACGTGTGCTC TTCCGATCTTGGCGTCATC CTCTGCTCTC

Table 5.9: Oligonucleotides for sgRNA cloning used in this thesis with sequences in 5' to 3' direction.

Internal stock number	Alias	Oligo sequence
JW6951	PomT2_hinten_T3_F	TAGgAACATTTTCATTGAGACTA
JW6952	PomT2_hinten_T3_R	AAACTAGTCTCAATGAAATGTT

Internal stock number	Alias	Oligo sequence
JW6953	PomT2_hinten_T4_F	TAggTATGGTGGGCTTAAATAA
JW6954	PomT2_hinten_T4_R	AAACTTATTTAAGCCCACCATA
JW8055	DAG1a_T2_F	TAggCCAAGCTGGGATACCCTG
JW8056	DAG1a_T2_R	AAACCAGGGTATCCCAGCTTGG
JW8057	DAG1a_T3_F	TAggCCACAGGGTATCCCAGCT
JW8058	DAG1a_T3_R	AAACAGCTGGGATACCCTGTGG
JW8061	DAG1b_T2_F	TAggAAGGTTTCATATCGTATCT
JW8062	DAG1b_T2_R	AAACAGATACGATATGAACCTT
JW8067	SUCO_TSSregion_T1_F	TAggCCGGTTATCACGGTAGAT
JW8068	SUCO_TSSregion_T1_R	AAACATCTACCGTGATAACCGG
JW8069	SUCO_TSSregion_T9_F	TAggTATATAGCTGTAGTATGC
JW8070	SUCO_TSSregion_T9_R	AAACGCATACTACAGCTATATA
JW8635	PomT2_C-terminal_tagging_T7_F	TAggAGGATAACTAGAAAGTCCC
JW8636	PomT2_C-terminal_tagging_T7_R	AAACGGGACTTCTAGTTATCCT
JW8637	PomT2_C-terminal_tagging_T11_F	TAggTGACATCTTAATCAAACA
JW8638	PomT2_C-terminal_tagging_T11_R	AAACTGTTTGATTAAGATGTCA
JW9005	pomt2_MIRmotif_T2_F	TAggATGGAGACATCATTCGAC
JW9006	pomt2_MIRmotif_T2_R	AAACGTCGAATGATGTCTCCAT
JW9007	pomt2_MIRmotif_T3_F	TAggTTTTTCAGGTGACCGGCTA
JW9008	pomt2_MIRmotif_T3_R	AAACTAGCCGGTCACCTGAAAA
JW9013	aDG_O-man_conversion_T14_F	TAggACACGCCAACTCCCATTC
JW9014	aDG_O-man_conversion_T14_R	AAACGAATGGGAGTTGGCGTGT
JW9015	aDG_O-man_conversion_T31_F	TAGgCAACTCCCATTCTGGCAG
JW9016	aDG_O-man_conversion_T31_R	AAACCTGCCAGAATGGGAGTTG
JW9024	aDG_O-man_conversion_T33_F	TAggAGCACCATCCAGCCAACA
JW9025	aDG_O-man_conversion_T33_R	AAACTGTTGGCTGGATGGTGCT
JW9026	aDG_O-man_conversion_STOP_T36_F	TAggATCCAGCCAACAGGGACC

Internal stock number	Alias	Oligo sequence
JW9027	aDG_O-man_conversion_STOP_T36_R	AAACGGTCCCTGTTGGCTGGAT
JW10142	pomt2_ex2_ABE_T1_F	TAggCTGGGATGAAACGCACTT
JW10143	pomt2_ex2_ABE_T1_R	AAACAAGTGCGTTTCATCCCAG
JW10420	SUCO_ABE_O-man_T1_F	TAGgCCACTTATTCTGCTCAAT
JW10421	SUCO_ABE_O-man_T1_R	AAACATTGAGCAGAATAAGTGG
JW10665	sgRNA87_oca2-STOP_1_NG PAM_F	TAggATCAGTGCAGGAGCAGCC
JW10666	sgRNA87_oca2-STOP_1_NG PAM_R	AAACGGCTGCTCCTGCACTGAT
JW10675	sgRNA92_oca2-STOP_3_SpRY PAM_F	TAggTCAACAGGTGAGGACCTC
JW10676	sgRNA92_oca2-STOP_3_SpRY PAM_R	AAACGAGGTCCTCACCTGTTGA
JW10958	sgRNA105_KIAA1549_ex2_T2_F	TAggTCCAACAGTGGCTCCAGA
JW10959	sgRNA105_KIAA1549_ex2_T2_R	AAACTCTGGAGCCACTGTTGGA
JW10960	sgRNA106_KIAA1549_ex1_T13_F	TAggTTCTTATTTGACTAAAAT
JW10961	sgRNA106_KIAA1549_ex1_T13_R	AAACATTTTAGTCAAATAAGAA

Table 5.10: qRT-PCR primers used in this thesis with sequences in 5' to 3' direction.

Internal stock number	Alias	Oligo sequence
JW7492	b2m_qPCR_FW	AATGGAAATGAGCTGCCCGG
JW7493	b2m_qPCR_RV	TGGAGTGAAAGGAGCGTGTTC
JW9106	pomt2_RT-PCR_1_F	AACAAAAGTGGGCCCGGTG
JW9107	pomt2_RT-PCR_1_R	GCTGTAACCTGCTGTTGCTT
JW9906	pomt1_RT-PCR_1_F	CAGTGCTGCTCCTGCTAGAA
JW9907	pomt1_RT-PCR_1_R	ACAGGAGACGCCACAGAGGA

Table 5.11: Primers for semi-quantitative RT-PCR analysis used in this thesis with sequences in 5' to 3' direction.

Internal stock number	Alias	Oligo sequence
JW7490	gapdh_qPCR_FW	AAAGTCATTCACGATAACTTTGGCA
JW7491	gapdh_qPCR_RV	TAGGACCATCCACTGTCTTCTGAG
JW9108	pomt2_RT-PCR_2_F	GGAAAGACTCTTCCAAAATGGGG
JW9109	pomt2_RT-PCR_2_R	TCAAGCCACTGTTTCCCTTTA
JW9908	pomt1_RT-PCR_2_F	CGTCTCGCTTCCCTCAACAGT
JW9909	pomt1_RT-PCR_2_R	GACCAGTCGCACATCAGACA

Table 5.12: Oligonucleotides for fill-in PCR for gRNA (Cas13d) donors used in this thesis with sequences in 5' to 3' direction.

Internal stock number	Alias	Oligo sequence
JW9731	Cas13d_Universal_t7	TAATACGACTCACTATAGGAACCCCTACCAA CTGGTCGGGGTTTGAAAC
JW9913	pomt2_Cas13d_gRNA_1	CGGGAAAATGCTGATTGTTTTGTTTCAAA CCCCGACCAGTT
JW9914	pomt2_Cas13d_gRNA_2	TTCAACCAGCAGAGATACAGGCGTTTCAAA CCCCGACCAGTT
JW9915	pomt2_Cas13d_gRNA_3	TGCTTGCTCGAGTGGCTGGGCTGTTTCAAA CCCCGACCAGTT
JW10041	dag1_Cas13d_gRNA_1	GGTTTGGTTCTCGCTGCAGCGGGTTTCAAA CCCCGACCAGTT
JW10042	dag1_Cas13d_gRNA_2	GGTGGAGGATTCTTACATGGGGTTTCAAA CCCCGACCAGTT
JW10043	dag1_Cas13d_gRNA_3	GCACAATTCTGCAGGGTCTGCCGTTTCAAA CCCCGACCAGTT

Table 5.13: Miscellaneous cloning primers used in this thesis with sequences in 5' to 3' direction.

Internal stock number	Alias	Oligo sequence
JW7663	BamHI_koz_BE4Gam	GCCGGATCCAACATGGCTAAACCAGCAAAACG TATCAAG
JW7665	XbaI_SV40_R	GCCTCTAGATTAGACTTTCTCTTCTTCTTGGGA
JW8193	UGI-oNLS_KpnI_R	GCCGGTACCTTAGTCCAGCCTGGGCCTTGG GAGGGGGAGAACCACCAGAGAG
JW8194	SV40NLS-KpnI_R	GCCGGTACCTTAGACTTTCTCTTCTTCTTGGG
JW8195	BamHI_koz_BE4-Gam_EV4_F	GCCGGATCCAACATGGCTAAAC
JW8823	Dag1_CDS_XhoI_F	CCGGCTCGAGCAAATGTGCAATAAGGAGCGGC
JW8824	Dag1_CDS_XbaI_R	CCGGTCTAGATTAGGGTGGCACATAGGGAG
JW8893	pomt1_insitu_Fwd	CTGTGGAGGGTGGACATCAC
JW8894	pomt1_insitu_Rev	AGGGCAGGCAGGTAGTGATA
JW8895	pomt2_insitu_Fwd	AACAACCTCGAACCTCCACG
JW8896	pomt2_insitu_Rev	GGTGATAGTACAGGACGCGG
JW9274	pCS2+_HiFi_fwd	GCCTCTAGAACTATAGTGAGTCCG
JW9275	pCS2+_HiFi_rev	ATGGGATCCTGCAAAAAGAACAAG
JW9298	dag1_insitu_Fwd	CTGCCCGATCTTGACCAAGT
JW9299	dag1_insitu_Rev	GGTATTCAGGGGGAGGGAGT
JW9567	evoBE4max_HiFi_ins1_Fwd	GTTCTTTTTGCAGGATCCCATTTACCATGAAAC GGACAGCCGAC
JW9568	evoBE4max_HiFi_ins1_Rev	CAGGAAGTCCTTGTCCTTG
JW9569	evoBE4max_HiFi_ins2_Fwd	CAAGGACAAGGACTTCCTG
JW9570	evoBE4max_HiFi_ins2_Rev	CTCACTATAGTTCTAGAGGCTTAGACTTTCTC TTCTTCTTGG
JW9708	KIAA1549_insitu_F	CAGCCTGTAGAGAAGGTGGC
JW9709	KIAA1549_insitu_R	CACCTGGATCTGTTCTGCGT
JW10174	dag1b_instu_1_F	GGGCCACCTACAGCTATTCC
JW10175	dag1b_instu_1_R	CGAACAGGGGGAGCAGAAAT

Internal stock number	Alias	Oligo sequence
JW10695	Nterm_Cas9n-SpRY_Hifi_ins1_Rev	GGCCGATGCTGTACTTCTT
JW10696	Nterm_Cas9n-SpRY_Hifi_ins2_Fwd	AAGAAGTACAGCATCGGCC
JW10697	Cterm_SpRY_Rev	CAGCTGAGACAGGTCGAT
JW10698	Cterm_SpRY-UGI_Fwd	ATCGACCTGTCTCAGCTG
JW10976	SUCO_probe_F	CCACATGAGCCGCCTTATCA
JW10977	SUCO_probe_R	CTGCAGGGGTTTCAGCATGTA

5.1.4 RNAs

sgRNAs (Cas9 and base editing)

Table 5.14: sgRNAs used in this thesis with sequences in 5' to 3' direction.

Alias	target sequence (incl. PAM)	Source
<i>pomt2-hinten-T3</i>	GTAACATTTTCATTGAGACTATGG	This work
<i>pomt2-hinten-T4</i>	ACTATGGTGGGCTTAAATAAGGG	This work
<i>oca2-Q333</i>	GAAACCCAGGTGGCCATTGCAGG	Lischik et al. [2019]
<i>kcnh6a-Q11</i>	GGCGCTCCAGAACACCTATTTGG	Cornean et al. [2022]
<i>kcnh6a-R512</i>	ACTGCTCAGGTTGGTGCGAGTGG	Cornean et al. [2022]
<i>dag1-crispr-sgRNA1</i>	AACCAAGCTGGGATACCCTGTGG	This work
<i>dag1b-crispr</i>	TAAAGGTTTCATATCGTATCTTGG	This work
<i>tnnt2a-Q114</i>	AGAGCGCCAAAAACGTCTTGAGG	Meyer et al. [2020]
<i>GFP-C71</i>	AGCACTGCACGCCGTAGGTCAGG	Hammouda et al. [2021]
<i>pomt2-tag-C-T7</i>	CAAGGATAACTAGAAGTCCCAGG	This work
<i>pomt2-tag-C-T9</i>	TGTGACATCTTAATCAAACAAGG	This work

Alias	target sequence (incl. PAM)	Source
<i>pomt2-MIRmotif-T2</i>	TCATGGAGACATCATTCTGACTGG	This work
<i>pomt2-MIRmotif-T3</i>	CATTTTCAGGTGACCGGCTACGG	This work
<i>dag1-T330</i>	CAACACGCCAACTCCCATTCTGG	This work
<i>dag1-T332</i>	GCCAACTCCCATTCTGGCAGTGG	This work
<i>dag1-crispr-sgRNA2</i>	CACCACAGGGTATCCCAGCTTGG	This work
<i>SUCO-crispr-sgRNA1</i>	ATCCGGTTATCACGGTAGATAGG	This work
<i>SUCO-crispr-sgRNA2</i>	TATATATAGCTGTAGTATGCTGG	This work
<i>pomt2-D92</i>	AGCTGGGATGAAACGCACTTTGG	This work
<i>SUCO-T811</i>	GCCCACTTATTCTGCTCAATCGG	This work
<i>pomt2-ex2-SD</i>	TTTCTCACTTTCCCGAGAGGCGG	This work
<i>pomt1-ex1-SD</i>	AACTCACACCACCGCGTTGGGG	This work
<i>dag1-T408</i>	CCAGCACCATCCAGCCAACAGGG	This work
<i>dag1-Q410</i>	CCATCCAGCCAACAGGGACCAGG	This work
<i>oca2-Q22</i>	TCATCAGTGCAGGAGCAGCCTGA	This work
<i>oca2-Q271</i>	ACTCAACAGGTGAGGACCTCGAT	This work
<i>KIAA1549-crispr-sgRNA2</i>	TATCCAACAGTGGCTCCAGAAGG	This work
<i>KIAA1549-crispr-sgRNA1</i>	CCTTCTTATTTGACTAAAATCGG	This work

crRNAs

All crRNAs were ordered from IDT.

Table 5.15: crRNAs used in this thesis with sequences in 5' to 3' direction.

Alias	target sequence	PAM
<i>crRNA57_oca2-Q333_NGG PAM</i>	ACTCAACAGGTGAGGACCTC	AGG
<i>crRNA92_oca2-Q271_NAN PAM</i>	GAAACCCAGGTGGCCATTGC	GAT
<i>crRNA87_oca2-Q22_NGN PAM</i>	TCATCAGTGCAGGAGCAGCC	NGA
<i>crRNA100_oca2-Q15_NCN PAM</i>	ACTCAGACTTCTGCCTCAGG	TCA

Alias	target sequence	PAM
<i>crRNA101_oca2-W385_NTN PAM</i>	AGTCGATCCACTCCACCACA	GTA
<i>crRNA105_tbxta-D7_NTN PAM</i>	CCCGGACCAGCGCCTGGAGC	ATC
<i>crRNA106_tbxta-Q8_NCN PAM</i>	GACCAGCGCCTGGAGCATCT	CCT
<i>crRNA107_tbxta-Q22_NAN PAM</i>	AGTTCCAGAAGGGCAGCGAG	AAG
<i>crRNA115_KIAA1549-T568_NAN PAM</i>	TTTACTGATTTACATCCCA	CAA
<i>crRNA116_dag1-T412_NAN PAM</i>	CAGCCAACAGGGACCAGGCC	AAT
<i>crRNA119_SUCO-S806_NGG PAM</i>	ACAGAAAACAGATCTTGTGT	CGG

gRNAs (RfxCas13d)

Table 5.16: gRNAs (RfxCas13d) used in this thesis with sequences in 5' to 3' direction.

Alias	target sequence	PAM
<i>pomt2_Cas13d_gRNA_1</i>	CGGGAAAATGCTGATTGGTTTT	This work
<i>pomt2_Cas13d_gRNA_2</i>	TTCAACCAGCAGAGATACAGGC	This work
<i>pomt2_Cas13d_gRNA_3</i>	TGCTTGCTCGAGTGGCTGGGCT	This work
<i>dag1_Cas13d_gRNA_1</i>	GGTTTGGTTCTCGCTGCAGCGG	This work
<i>dag1_Cas13d_gRNA_2</i>	GGTGGAGGATTCTTACATGGGG	This work
<i>dag1_Cas13d_gRNA_3</i>	GCACAATTCTGCAGGGTCTGCC	This work

mRNAs

Table 5.17: mRNAs used in this thesis.

Alias	Plasmid	Internal plasmid number	Source of mRNA
<i>GFP</i>	pCS2+_GFP	#883	Lab stock

Alias	Plasmid	Internal plasmid number	Source of mRNA
<i>H2A-mCherry</i>	pCS2+_H2A-mCherry	#1924	Lab stock
<i>heiCas9</i>	pCS2+_heiCas9	#5197	Lab stock / Thumberger et al. [2022]
<i>BE4-Gam</i>	pGGEV_4_BE4-Gam	#5400	This work / Thumberger et al. [2022]
<i>evoBE4max</i>	pCS2+_evoBE4max	#5797	This work / Cornean et al. [2022]
<i>ancBE4max</i>	pCMV_ancBE4max	#5811	Koblan et al. [2018]
<i>ABE8e</i>	pCMV_ABE8e	#5812	Richter et al. [2020]
<i>evoBE4max-NG</i>	pCS2+_evoBE4max-NG	#5800	This work
<i>evoBE4max-SpRY</i>	pCS2+_evoBE4max-SpRY	#5868	This work
<i>ancBE4max-NG</i>	pCS2+_ancBE4max-NG	#5869	This work
<i>ancBE4max-SpRY</i>	pCS2+_ancBE4max-SpRY	#5867	This work
<i>ABE8e-NG</i>	pCMV_ABE8e-NG	#5862	Richter et al. [2020]
<i>ABE8e-SpRY</i>	pCS2+_ABE8e-SpRY	#5866	This work
<i>RfxCas13d</i>	pT3TS-RfxCas13d-HA	#5810	Kushawah et al. [2020]
<i>dag1</i>	pCS2+_dag1-CDS	#5628	This work

5.1.5 Antibodies

Table 5.18: Primary antibodies used in this thesis. Abbreviations: Mc. – monoclonal; Pc. – polyclonal; Cat. – Catalog; nr. – number; W - wholemounts; S - sections; WB – Western blot.

Lab nr.	Target	Host	Dilution	Type	Source	Cat. nr.
37	GFP	rabbit	1:1000 (WB)	Pc	Invitrogen	A11122
38	GFP	chicken	1:100 (W), 1:500 (S)	Pc	Invitrogen	A10262

Lab nr.	Target	Host	Dilution	Type	Source	Cat. nr.
87	Zpr1	mouse	1:200 (S)	Mc	ZIRC (Eugene, Oregon, USA)	RRID: AB_10013803
149	acetylated-tubulin	mouse	1:50 (W)	Mc	Sigma-Aldrich	T7451
165	Rx2	rabbit	1:200 (W), 1:500 (S)	Pc	homemade, Reinhardt et al. [2015]	homemade
171	α -Dystroglycan Antibody, clone I1H6C4	mouse	1:50 (S)	Mc	Merck/Millipore	05-593
194	NCL-b-DG	mouse	1:200 (WB)	Mc	Leica	B-DG-CE
	POMT1	rabbit	1:500 (WB)	Pc	Sigma-Aldrich	HPA065252
	POMT2	rabbit	1:250 (WB)	Pc	Willer et al. [2002]	Strahl lab, homemade
	Sec61	rabbit	1:2000 (WB)	Mc	Cell Signaling	D7Q6V

Table 5.19: Secondary antibodies used in this thesis. Abbreviations: Pc. – polyclonal; AF. – Alexa Fluor; Cat. – Catalog; nr. – number; conj. – conjugate; W - wholemounts; S - sections; WB – Western blot.

Target	Host	Dilution	Type	Source	Cat. nr.
chicken	donkey	1:100 (W), 1:500 (S)	Pc, AF 488-conj.	Jackson/ Dianova	703-545-155
chicken	donkey	1:100 (W), 1:500 (S)	Pc, AF 647-conj.	Jackson Immuno	703-496-155
mouse	goat	1:100 (W), 1:500 (S)	Pc, AF 488-conj.	Life Technologies	A-11029
mouse	donkey	1:100 (W), 1:500 (S)	Pc, AF 647-conj.	Jackson/ Dianova	715-605-151
mouse	goat	1:5000 (WB)	Pc, Peroxidase AffiniPure (HRP), IgG (H&L)	Jackson Immuno	115-035-044
rabbit	goat	1:100 (W), 1:500 (S)	Pc, DyLight 549-conj.	Jackson Immuno	112-505-144

Target	Host	Dilution	Type	Source	Cat. nr.
rabbit	goat	1:10000 (WB)	Pc, HRP-conjugated IgG (H&L)	Agrisera	AS09602

5.1.6 Antibiotics

Table 5.20: Antibiotics used in this thesis for bacterial selection.

Antibiotic	Stock concentration	Working concentration	Supplier
Ampicillin	100 mg/ml	100 μ g/ml	Roth
Kanamycin	50 mg/ml	50 μ g/ml	Roth

5.1.7 Kits

Table 5.21: Kits used in this thesis.

Kit	Company
Agilent RNA Nano 6000 kit	Agilent Technologies
Agilent TapeStation D1000 assay	Agilent Technologies
Amersham ECL select substrate	Cytiva
Amersham ECL prime substrate	Cytiva
Direct-zol DNA/RNA Miniprep Kit	Zymo Research
Direct-zol RNA Microprep Kit	Zymo Research
innuPREP DOUBLEpure Kit	Analytik Jena
In situ Cell Death Detection Kit, TMR red	Roche
mMESSAGE mMACHINE Sp6 Transcription Kit	Thermo Fisher Scientific
mMESSAGE mMACHINE T3 Transcription Kit	Thermo Fisher Scientific
mMESSAGE mMACHINE T7 Transcription Kit	Thermo Fisher Scientific
NEBNext UltraTM II Directional RNA Library Prep Kit for Illumina	New England Biolabs

Kit	Company
PCR DIG Probe Synthesis Kit	Roche
MEGAscript T7 Transcription Kit	Thermo Fisher Scientific
MinElute QIAquick Gel Extraction Kit	Qiagen
Monarch DNA Gel Extraction Kit	New England Biolabs
NEBuilder HiFi DNA Assembly Cloning Kit	New England Biolabs
pGEM-T easy cloning system	Promega
Plasmid Maxi Kit	Qiagen
QIAprep Spin Miniprep Kit	Qiagen
QIAquick Gel Extraction Kit	Qiagen
QIAquick PCR Purification Kit	Qiagen
Qubit RNA High Sensitivity Assay	Thermo Fisher Scientific
RevertAid First Strand cDNA Synthesis Kit	Thermo Fisher Scientific
RNeasy Mini Kit	Qiagen
SensiFAST SYBR Hi-ROX Kit	Bioline
SuperSignal West Femto Trial Kit	Thermo Fisher Scientific

5.1.8 Enzymes and buffers

Table 5.22: Enzymes and buffers used in this thesis.

Enzyme	Buffer (concentration)	Source
BamHI-HF (20 U/ μ l)	CutSmart buffer (10x)	New England Biolabs
Benzonase nuclease (250 U/ μ l)		Sigma-Aldrich
BsaI-HF v2 (20 U/ μ l)	CutSmart buffer (10x)	New England Biolabs
DNaseI (1 U/ μ l)	DNase I buffer (10x)	Thermo Fisher Scientific
DraI FD	FastDigest Green buffer (10x)	Thermo Fisher Scientific
EcoRI-HF (20 U/ μ l)	CutSmart buffer (10x)	New England Biolabs

Enzyme	Buffer (concentration)	Source
EcoRV-HF (20 U/ μ l)	CutSmart buffer (10x)	New England Biolabs
Hatching enzyme		Homemade
KpnI-HF (20 U/ μ l)	CutSmart buffer (10x)	New England Biolabs
NotI-HF (20 U/ μ l)	CutSmart buffer (10x)	New England Biolabs
OneTaq DNA polymerase (5 U/ μ l)	OneTaq buffer (5x)	New England Biolabs
Proteinase K powder, stock solution 20 mg/ml		Roche
PvuI-HF (20 U/ μ l)	CutSmart buffer (10x)	New England Biolabs
Q5 High-Fidelity DNA Polymerase (2 U/ μ l)	Q5 Reaction buffer (5x)	New England Biolabs
Q5 Hot Start High-Fidelity DNA polymerase (2 U/ μ l)	Q5 Reaction buffer (5x)	New England Biolabs
RNase A, DNase- and proteasefree (10 mg/ml)		Thermo Fisher Scientific
RNaseH (5 U/ μ l)		Thermo Fisher Scientific
Sall-HF (20 U/ μ l)	CutSmart buffer (10x)	New England Biolabs
SapI (10 U/ μ l)	CutSmart buffer (10x)	New England Biolabs
SphI (10 U/ μ l)	CutSmart buffer (10x)	New England Biolabs
T4 Ligase (5 U/ μ l)	T4 DNA Ligase buffer	Thermo Fisher Scientific
Taq DNA polymerase (5 U/ μ l)	ThermoPol reaction buffer (10x)	New England Biolabs
TaqI-v2 (20 U/ μ l)	CutSmart buffer (10x)	New England Biolabs
TURBO DNase (2 U/ μ l)	DNase I buffer (10x)	Invitrogen

Enzyme	Buffer (concentration)	Source
XbaI-FD	FastDigest buffer (10x)	Thermo Fisher Scientific

5.1.9 Chemicals and reagents

Table 5.23: Chemicals and Reagents used in this thesis.

Chemical or Reagent	Supplier
Alexa Fluor 647 Phalloidin	Thermo Fisher Scientific
2-mercaptoethanol (β -mercaptoethanol)	Roth
2-propanol (isopropanol)	Sigma-Aldrich
4',6-Diamidino-2-Phenyindole, Dilactate (DAPI)	Roth
Acetone	Sigma-Aldrich
Acrylamide, 30% (29:1)	Bio-Rad
Agar	Roth
Agarose	Sigma-Aldrich
Agarose low melting	Roth
Ampicillin	Roth
APS (ammonium persulfate)	Roth
ATP (100 mM)	Thermo Fisher Scientific
dATP (100 mM)	Thermo Fisher Scientific
Bacto-Trypton	Gibco
BCIP (5-bromo-4-chloro-3-indolyl phosphate)	Roche
Blocking reagent	Roche
Bovine Serum Albumin (BSA)	Sigma-Aldrich
Bromphenol Blue	Sigma-Aldrich
Calcium chloride (CaCl_2)	AppliChem
Calcium chloride dihydrate ($\text{CaCl}_2 \cdot 2 \text{H}_2\text{O}$)	AppliChem
CDP-Star	Roche
Chloroform	Sigma-Aldrich
DigUTP (100 mM)	Roche

Chemical or Reagent	Supplier
Dimethyl sulfoxide (DMSO)	Roth
Disodium hydrogen phosphate (Na_2HPO_4)	Sigma-Aldrich
Disodium hydrogen phosphate dihydrate ($\text{Na}_2\text{HPO}_4 \cdot 2 \text{H}_2\text{O}$)	Sigma-Aldrich
dNTPs (10 mM)	Sigma-Aldrich
DTT (dithiothreitol) (100 mM)	Thermo Fisher Scientific
Ethanol 70% (denatured)	Roth
Ethanol 96% (denatured)	Roth
Ethanol 99%	Sigma-Aldrich
Ethidium bromide (EtBr) , 10 mg ml	Roth
Ethylenediamine tetraacetic acid (EDTA)	AppliChem
Ficoll Type 400	Amersham Biosciences
Formamide	Sigma-Aldrich
Glacial acetic acid	Merck
Glucose	Sigma
Glycerol	Merck
Glycine	Sigma-Aldrich
Glycogen, molecular biology grade	Thermo Fisher Scientific
H_2O , 0.1 μm sterile filtered	Sigma-Aldrich
Heparin	Gibco
HEPES (4-(2-hydroxyethyl)-1-piperazineethanesulfonic acid)	Roth
Hydrochloric acid (HCl)	Merck
Hydrogen peroxide (H_2O_2)	Sigma-Aldrich
Kanamycin	Roth
Lithium chloride (LiCl)	Sigma-Aldrich Magnesium chloride (MgCl_2)
AppliChem	
Magnesium sulfate heptahydrate ($\text{MgSO}_4 \cdot 7 \text{H}_2\text{O}$)	AppliChem
Maleic acid 99%	Roth
Methanol (MeOH)	Roth

Chemical or Reagent	Supplier
Methylene blue trihydrate	Sigma-Aldrich
Nail polish	essence
NBT (4-nitro blue tetrazolium chloride)	Roche
Normal Goat Serum (NGS)	Gibco
N-Phenylthiourea (PTU)	Sigma-Aldrich
Orange G	Sigma-Aldrich
Paraformaldehyde (PFA)	Sigma-Aldrich
Penicillin-Streptomycin (Pen/Strep)	Sigma-Aldrich
Phenol-Chloroform-Isoamylalcohol (25:24:1) pH 8 (PCI)	Roth
Poly(ethylene glycol) (PEG) 4000	Thermo Fisher Scientific
Ponceau S solution 0.2% in 3% TCA	Serva
Potassium acetate (CH ₃ CO ₂ K)	AppliChem
Potassium chloride (KCl)	AppliChem
Potassium dihydrogen phosphate (KH ₂ PO ₄)	Merck
Potassium hydrogen phosphate (K ₂ HPO ₄)	Merck
Potassium hydroxide (KOH)	Merck
rNTPs (ATP, CTP, GTP, UTP, 100mM each)	Roche
Sheep Serum	Sigma-Aldrich
Skimmed Milk Powder, Blotting Grade	Roth
SOC Outgrowth Medium	New England Biolabs
Sodium acetate NaAc	Grüssing
Sodium chloride (NaCl)	Sigma-Aldrich
Sodium dodecyl sulfate (SDS), 20%	Roth
Sodium hydrogen carbonate (NaHCO ₃)	Merck
Sodium hydroxide (NaOH)	AppliChem
Sucrose	Sigma-Aldrich
TEMED (tetramethylethylenediamine)	Roth
Tricaine (C ₉ H ₁₁ NO ₂ · CH ₄ SO ₃ , MS-222)	Sigma-Aldrich
Tris base	Roth

Chemical or Reagent	Supplier
Tri-sodium citrate dihydrate ($C_6H_5Na_4O_7 \cdot 2 H_2O$)	Sigma-Aldrich
Triton X-100	Sigma-Aldrich
TRIzol reagent	Life Technologies
Tryptone bacterial	Roth
Tween 20	Sigma-Aldrich
X-Gal (5-bromo-4-chloro-3-indolyl-beta-D-galactopyranoside)	Roth
Xylene Cyanol FF	Serva
Yeast extract	Roth

5.1.10 Molecular Materials

Table 5.24: Molecular materials used in this thesis.

Material	Supplier
Agencourt Ampure XP beads	Beckman Coulter
Alt-R CRISPR-Cas9 crRNA	Integrated DNA Technologies, Inc. (IDT)
Alt-R CRISPR-Cas9 tracrRNA	Integrated DNA Technologies, Inc. (IDT)
Anti-Digoxigenin-AP Fab fragments	Roche
cOmplete, Mini, EDTA-free Protease Inhibitor Cocktail	Roche
DNA Loading Dye	homemade
Gel Loading Dye, Purple (6X)	New England Biolabs
GeneRuler DNA Ladder Mix	Thermo Fisher Scientific
Nuclease-Free Duplex Buffer	Integrated DNA Technologies, Inc. (IDT)
Nuclease-free water	Sigma-Aldrich
PageRuler Prestained Protein Ladder	Thermo Fisher Scientific
RiboLock RNase Inhibitor	Thermo Fisher Scientific
Precision Plus Protein Standards, dual color	Bio-Rad

Material	Supplier
RNA from torula yeast Type VI	Sigma-Aldrich
RNA Loading Dye 2x Rapid	Thermo Fisher Scientific
TriTrack DNA Loading Dye (6X)	Thermo Fisher Scientific
Wheat Germ Agglutinin (WGA), Agarose bound	Vector Laboratories

5.1.11 Consumables

Table 5.25: Consumables used in this thesis.

Consumable	Supplier
24 Well Plate with #1.5 glass-like polymer coverslip bottom	Cellvis
96 Fast PCR plate Halbrand	Sarstedt
Blades to cut from agarose gels	Roth
Cell saver tips 200 μ l, 1000 μ l	Biozym
Cell strainer	Greiner
Cover slips	Roth
Cryosection Superfrost Plus slides	Thermo Fisher Scientific
D1000 ScreenTape	Agilent Technologies
Filter paper	Whatman
Filter tips 10 μ l, 20 μ l, 200 μ l, 1.25 ml	Starlab
Filter Tips TipOne RPT (sterile), 10 μ l, 20 μ l, 200 μ l	Starlab
Folded filters	Sartorius
Glass beads	Roth
Glass dishes for microscopy	MatTek
Glass petri dishes STERIPLAN 4 cm, 9 cm	Roth
Glass vials for hatching enzyme treatment	Roth
Injection moulds	homemade
Injection needles GC100F-10	Harvard Apparatus
Latex gloves	Semperguard
Low protein binding microcentrifuge tubes 1.5 ml and 2.0 ml	Thermo Fisher Scientific
Microloader tips for microinjection	Eppendorf
Microloader tips for Western Blot	VWR
Micro pestles 0.5/1.5 ml	Laborversand Hartenstein
Micro pestles 1.5/2.0 ml	Eppendorf
Microscopy slides	Roth
Mini-PROTEAN TGX precast protein gels, 4-20%	Bio-Rad

Consumable	Supplier
Molding cups	Polysciences
Needles BD Microlance, 0.3 mm x 13 mm	BD
Nitrile gloves	Starlab
MicroAmp Optical Adhesive Film, 96 well plate	Applied Biosystems
Parafilm M	Bemis
PCR stripes	Sarstedt
PCR tubes	Kisker
PCR tubes, thin-walled, 0.2 ml	Eppendorf
Petri dishes 3.5 cm, 6 cm, 9 cm	Sarstedt
Pipette tips	Kisker
Plastic pipettes 2 ml, 5 ml, 10 ml, 25 ml	Sarstedt
Nitrocellulose membrane, 0.45 μm	Bio-Rad
Reaction tubes 1.5 ml, 2 ml, 5 ml	Sarstedt
Sandpaper 1000 grit	Bauhaus
Syringe	BD
Syringe filters 0.22 μm , 0.44 μm	Millipore
Syringe filter 0.2 μm	Whatman
Tissue Freezing Medium	Jung, Leica
Transparent 24-well plate	Co-star
Transplantation moulds	homemade
Tubes 15 ml, 50 ml	Sarstedt
Well plates, 6-well, 12-well, 24-well, 96-well	Roth, Corning
Whatman Paper	Whatman

5.1.12 Media, buffers and solutions

Ingredients for the following buffers, media and solutions were dissolved in H₂O unless indicated otherwise.

Solutions for fish work

Table 5.26: Solutions for fish rearing used in this thesis.

Solution	Ingredients
1.5% agarose in water	1.5% (w/v), bring to boil
1% agarose (low-melt) in 1x PBS	1% (w/v), heat to 80 °C
1x ERM	17 mM NaCl, 0.4 mM KCl, 0.27 mM CaCl ₂ · 2 H ₂ O, 0.66 mM MgSO ₄ · 7 H ₂ O, 17 mM HEPES pH 7.3; pH 7.1
Hatch medium	2 mg/L Methylene blue in 1x ERM
1x PBS	137 mM NaCl, 2.7 mM KCl, 1.44 g/L Na ₂ HPO ₄ , 240 mg/L mM KH ₂ PO ₄ ; pH 7.4
50x PTU	1.65 g/L PTU, stir under hood at 40 °C
20x tricaine	4 g/L tricaine, 10 g/L Na ₂ HPO ₄ · H ₂ O in 1x ERM, pH 7-7.5

Solutions for general use

Table 5.27: Solutions of general use used in this thesis.

Solution	Ingredients
75% EtOH, RNase-free	75% (v/v) EtOH (99%) in RNase-free water
70% EtOH, RNase-free	70% (v/v) EtOH (99%) in RNase-free water
70% EtOH	70% (v/v) EtOH (99%)
0.1 M NaOH	4 g/L NaOH
16% PFA	160 g/L PFA, adjust pH to 7.0
4% PFA/PTw	25% (v/v) 16% PFA in 1x PTw, adjust pH to 7-7.5
1% PFA/PTw	25% (v/v) 4% PFA in 1x PTw

Solution	Ingredients
10x PBS	1.37 M NaCl, 27 mM KCl, 14.4 g/L Na ₂ HPO ₄ , 2.4 g/L mM KH ₂ PO ₄ ; pH 7.4
1x PTw	10% (v/v) 10x PBS, 0.1% (v/v) Tween 20

Solutions for bacterial work

Table 5.28: Solutions for bacterial work used in this thesis.

Solution	Ingredients
LB medium	10 g/L Bacto-Tryptone, 5 g/L Yeast Extract, 5 g/L NaCl
LB plates	15 g/L Agar, boil in LB medium containing 10 g/L NaCl
TB Medium	12 g/L Bacto-Tryptone, 24 g/L Yeast Extract, 0.4% (v/v) Glycerol, 2.13 g/L KH ₂ PO ₄ , 12.54 g/L K ₂ HPO ₄
X-Gal	20 mg/ml X-Gal in DMSO

Solutions for molecular biology

Table 5.29: Solutions for molecular biology work used in this thesis.

Solution	Ingredients
0.8-2.0% agarose in TAE	0.8%-2% (w/v), bring to boil
6x DNA loading dye	15% (w/v) Ficoll, 0.05% (w/v) Xylene cyanol, 0.05% (w/v) Bromphenol Blue, 0.2% (w/v) Orange G, 0.2% (w/v) Ponceau S
10x DNA orange loading dye	40% (w/v) sucrose, 2 mg/ml Organge G in RNase-free water
EtBr bath	0.02% (v/v) EtBr
Fin-Clip buffer	100 mM Tris [pH 8.5], 10 mM EDTA [pH 8], 200 mM NaCl, 2% (v/v) SDS
3 M NaAc	246.1 g/L NaAC in RNase-free water
Oligo annealing buffer	10 mM Tris, 30 mM NaCl; pH 7.5-8
P1 buffer	50 mM glucose, 25 mM Tris-HCl, 10 mM EDTA, 100 µg/ml RNaseA; pH 8.0; stored at 4°C

Solution	Ingredients
P2 buffer	0.2 N NaOH, 1% (v/v) SDS
P3 buffer	5 M Potassium acetate; pH 5.5
2x RNA loading dye	0.25% (w/v) Xylene cyanol, 0.25% (w/v) Bromphenol Blue, 0.025% (v/v) SDS, 5 mM EDTA [pH 8.0], 95% (v/v) Formamide
50x TAE	2 M Tris-base, 1 M glacial acetic acid, 500 mM EDTA; pH 8.5
TE buffer	10 mM Tris-HCl [pH 8.0], 1 mM EDTA

Solutions for *in situ* hybridisation

Table 5.30: Solutions for *in situ* hybridisation used in this thesis.

Solution	Ingredients
Blocking Buffer	1x Maleate Buffer, 2% (v/v) Blocking Reagent, 0.1% (v/v) Tween 20
10% Blocking Reagent	10% (w/v) Blocking Reagent in 2x Maleate Buffer
Hybridisation Mix (HYB mix)	50% (v/v) Formamide, 5X SSC, 150 μ g/ml Heparin, 5 mg/ml Ribonucleic acid from <i>Torula yeast</i> Typ VI, 0.1% (v/v) Tween20
2x Maleate Buffer	200 mM Maleic acid, 300 mM NaCl, 0.1% (v/v) Tween 20; pH 7.5
Pre-staining buffer	0.1 M Tris-HCl [pH 7.5], 0.1 M NaCl, 0.1% (v/v) Tween 20
20x SSC (saline sodium citrate)	3 M NaCl, 300 mM Tri-sodium citrate dihydrate; pH 7.0
4x SSCT	4x SSC, 0.1% (v/v) Tween 20
2x SSCT	2x SSC, 0.1% (v/v) Tween 20
0.2x SSCT	0.2x SSC, 0.1% (v/v) Tween 20
Staining buffer	0.1 M Tris-HCl [pH 9.5], 0.1 M NaCl, 50 mM MgCl ₂ , 0.1% (v/v) Tween 20

Solutions for Western Blot

Table 5.31: Solutions for Western Blot used in this thesis.

Solution	Ingredients
20% APS	20% (w/v) APS, store at -20 °C
10x Blotting buffer	480 mM Tris, 1.92 M glycine
WB homogenisation buffer	50 mM Tris-HCl [pH 7.6], 150 mM NaCl, 1% (v/v) TritonX-100, 1x tablet Protease Inhibitor Cocktail
Hypotonic protease inhibitor (HPI) buffer	20 mM Tris, 10 mM NaCl, 1.5 mM MgCl ₂ , 0.05 U Benzonase, 1x tablet Protease Inhibitor Cocktail
2.5x Laemmli sample buffer	5% (v/v) SDS, 25% (v/v) glycerol, 157.5 mM Tris-HCl [pH 6.8], 0.08% (w/v) Bromphenol blue, 12.5% (v/v) β -mercaptoethanol (always added fresh)
5x SDS loading buffer	312.5 mM Tris-HCl [pH 6.8], 10% (v/v) SDS, 50% (v/v) Glycerol, 25% (v/v) β -mercaptoethanol, 0.08% (w/v) Bromphenol blue
1x SDS running buffer	25 mM Tris, 192 mM glycine, 0.1% (v/v) SDS
4x Separation buffer	1.5 M Tris-HCl, 1% (v/v) SDS; pH 8.8, store at 4 °C
4x Stacking buffer	0.5 M Tris-HCl, 0.4% SDS; pH 6.8, store at 4 °C
Stripping buffer	200 mM Glycine, 1% (v/v) Tween 20, 0.1% (v/v) SDS; adjust to pH 2.2 with HCl
1x TBS-T	50 mM Tris-HCl [pH 7.5], 150 mM NaCl, 0.1% (v/v) Tween 20; pH 7.4, store at 4 °C
0.5x TBS-T	25 mM Tris-HCl [pH 7.5], 75 mM NaCl, 0.05% (v/v) Tween 20; pH 7.4, store at 4 °C
Transfer buffer	20% (v/v) methanol, 0.03% (v/v) SDS, 1X Blotting buffer
WB wash buffer	50 mM Tris-HCl [pH 7.6], 150 mM NaCl, 0.1% (v/v) TritonX-100, 1x tablet Protease Inhibitor Cocktail
WB blocking buffer	5% (w/v) skim milk powder in 0.5X TBS-T; re-adjust pH to 7.4

Solutions for immunohistochemistry

Table 5.32: Solutions for immunohistochemistry used in this thesis.

Solution	Ingredients
Blocking buffer	59 mM Maleic acid [pH 7.5], 88 mM NaCl, 1.165% (w/v) Blocking reagent, 0.0587% (v/v) Tween20
2 mg/ml DAPI solution	2 mg/ml DAPI in DMSO
60% glycerol	60% (v/v) glycerol in PTw
1% and 10% NGS	diluted (v/v) in PTw
Permeabilisation solution	0.1% Tri-sodium citrate dihydrate, 0.1% (v/v) TritonX-100
30% sucrose	30% sucrose in PTw
whole mount blocking buffer	0.1% (v/v) BSA, 1% (v/v) DMSO, 4% (v/v) Sheep Serum in 1x PTw

5.1.13 Equipment and Instruments

Table 5.33: Equipment and instruments used in this thesis.

Equipment	Supplier
Advanced fluorescence and ECL Imager	Intas
Bacterial Shaker INNOVA 44	New Brunswick
Bioanalyzer 2100	Agilent Technologies
Camera Nikon DS-Ri1	Nikon
Cat S20 shaker	neoLab
Centrifuges 5417C, 5425, 5430R, 5810R	Eppendorf
Centrifuge MC 6	Sarstedt
Centrifuge for PCR tubes	Steinbrenner Laborsysteme
Cold light source for stereomicroscope KL1500 LCD	Schott
Cryostat CM 3050S	Leica
DanioVision with Top light unit and Temperature control unit	Noldus
DeNovix DS-11+ spectrophotometer	DeNovix

Equipment	Supplier
Electrophoresis chambers and combs for agarose gels	homemade and Peqlab
FemtoJet express and Microinjector 5242	Eppendorf
Fish incubator	Heraeus instruments
Fish incubator	RuMed
Forceps 5, 55 Inox stainless steel	Dumont
Freezer -20°C	Liebherr
Freezer -80°C	Thermo Fisher Scientific
Fridge 4°C	Liebherr
Incubator 32°C, 37°C, 60°C	BINDER
InjectMan NI2	Eppendorf
Leica TCS SP8	Leica
LockMailer microscope slide jar	Simport
MacBook Pro (2.7 GHz Intel Core i7, 16 GB 2133 MHz LPDDR3/Radeon Pro 455 2048 MB/Intel HD Graphics 5301536 MB)	Apple
Microwave	Sharp
Microscope Leica DM5000B DIC	Leica
Microplate centrifuge	Roth
Milli-Q water filtration station	Millipore Corporation
Mini-centrifuge	Sarstedt
Mini Protean Tetra Cell, 2 gel system	Bio-Rad
Mini Trans-Blot Cell Module	Bio-Rad
Mortar and Pestle	Roth
MS1Minishaker	IKA
Multitemp II Thermostatic circulator 2219 LKB	Bromma
Multipette plus	Eppendorf
Narrow-douncer, 1 ml	Wheaton
NEBNext Poly(A) mRNA Magnetic Isolation Module	New England Biolabs
Needle puller P-30	Sutter Instrument Co USA
NextSeq 2000 system	Illumina

Equipment	Supplier
Nikon SMZ18 stereomicroscope	Nikon
Olympus SZX7	Olympus
PCR C100 Touch Thermal Cycler	Bio-Rad
pH-Meter	Sartorius
Pipetboy acu	Integra biosciences
Pipettes 20 μ l, 1 ml	Gilson
Pipettes 2.5 μ l, 10 μ l, 200 μ l	Eppendorf
Power supply Power-PAC Basic	Bio-Rad
Qubit	Thermo Fisher Scientific
Rocking shaker DRS-12	neoLab
Rotating Arm	homemade
Scale	Sartorius
SDS-PAGE gel chamber and combs	Bio-Rad
Shaker CAT S 20, DRS-12, GFL 3005	neoLab
Sorvall Evolution RC Centrifuge with FiberLite F10-6x500y Fixed Angle Rotor	Thermo Fisher Scientific
Staining container for immunohistochemistry on cryosections	Biozym, Empty 200 μ l cell saver tip box
Stereo microscope SZX7	Olympus
Stereomicroscopes Zeiss Stemi 2000, Stemi SV11	Zeiss
Step-One Plus Real-Time PCR system	Applied Biosystems
TapeStation 4200	Agilent Technologies
Thermomixer Compact	Eppendorf
ThermoMixer F1.5	Eppendorf
UV-Gel Documentation System INTAS iX20 SmartViewer Imager	Intas
UV transilluminator ECX-F20.L	Vilber Lourmat
Vortex Genie 2	Scientific Industries
Water bath	GFL mbH
Zeiss Axio Imager M1	Zeiss

5.1.14 Software

Table 5.34: Consumables used in this thesis.

Software	Reference / Vendor
ACEofBASEs	Cornean et al. [2022]
Adobe Illustrator	Adobe, Inc.
AlphaFold Protein Structure Database	Jumper et al. [2021]; Varadi et al. [2022]
Anaconda Navigator	Anaconda, Inc.
CCTop	Stemmer et al. [2015]
CRISPResso2	Clement et al. [2019]
EditR	Kluesner et al. [2018]
Ensemble	Cunningham et al. [2022]
EnzymeX 3	Nucleobytes
EthoVision XT	Noldus
FastQC	Andrews [2010]
Fiji distribution of ImageJ	Schindelin et al. [2012]
FileMaker Pro	FileMaker, Inc.
Geneious	Biomatters Limited
InterProScan	Jones et al. [2014]
Kallisto	Bray et al. [2016]
LasX	Leica
Mendeley Desktop	Mendeley, Ltd
Microsoft Office	Microsoft
MultiQC	Ewels et al. [2016]
NIS-Elements AR	Nikon
R/Bioconductor	Huber et al. [2015]
RStudio	RStudio, PBC
Sublime Text	Sublime HQ Pty Ltd
Texmaker	Pascal Brachet

5.2 Methods

5.2.1 General embryo and fish procedures

Fish husbandry

Medaka (*Oryzias latipes*) stocks were raised and maintained as previously described [Loosli et al., 2000]. Fish were maintained in closed stocks and constant recirculating systems at 28°C on a 14 h light/10 h dark cycle at Heidelberg University. Fish husbandry and experiments were performed in following German animal welfare standards (Tierschutzgesetz §11, Abs. 1, Nr. 1) and with European Union animal welfare guidelines [Bert et al., 2016] in accordance with the following permits:

1. fish husbandry permit (number 35–9185.64/BH Wittbrodt)
2. experiments permit (numbers 35-9185.81/G-271/20 Wittbrodt)
3. terminal experimentation (numbers T-71/17)

The fish facility is under the supervision of the local representative of the animal welfare agency.

Microinjection into Medaka zygotes

Embryos were injected at the one-cell stage as previously described [Rembold et al., 2006]. Note, that ABE8e injections with the *GFP-C71* sgRNA into the *myl7::EGFP*, *myl7::H2A-mCherry* transgenic reporter line, were additionally performed into a single cell of the four-cell stage embryo [Cornean et al., 2022]. The following concentrations were used: *heiCas9* and base editor mRNA 150 ng/μl, *RfxCas13d* mRNA 450 ng/μl, sgRNAs 30 ng/μl, crRNA::tracrRNA duplexes 4 μM, *dag1* mRNA 150 ng/μl, three *Cas13d* gRNAs at 90 ng/μl each, tracer fluorophores (GFP, H2A-mCherry) 20 ng/μl. All components were diluted in nuclease-free water.

The evening before injection male fish were separated from the females. On the morning of the next day, the fish were put back together for mating. Fish were left to mate for 10-20 min. An injection plate was prepared by pouring 1.5% agarose (H₂O) into a 9 cm Petri dish. A plastic mould was placed into the agarose to create grooves for positioning of embryos for injection. After the agarose was solidified, the mould was removed and the agarose was covered with ice-cold 1x ERM. Injection needles were always freshly prepared from borosilicate glass capillaries by gravity pull with a P-30 needle puller. The

injection mix was prepared while minding RNase-free procedures. Fertilised eggs were collected after mating, separated with two 10 μ l pipette tips and sorted into the grooves of the injection plate. The microloader capillaries were filled with 3-4 μ l injection mix and loaded into the needle from the open while avoiding air bubbles. For injections a Eppendorf Microinjector 5242 injection system was used. The needle was opened by gently touching the chorion. A pressure injector with a holding pressure of 200-300 hPa (=P3) and an injection pressure of 1000-1400 hPa (=P2) was adjusted according to the needle used. To inject the needle was pierced through the chorion into the cytoplasm of one-cell stage embryos and a small amount (30-50% of the visually estimated cell volume) of the injection mix was released. After injection, the embryos were raised in 1xERM for 5-7 hours. The tracer fluorophore fluorescence was then used to screen for positively injected embryos under a fluorescent stereomicroscope. Care was taken to sort out malformed embryos as well as embryos with above or below average fluorescent signal. at either 28°C or 18°C to the appropriate stage for further analysis.

Fish fixation

Embryos from the respective wild-type or mutant strain were reared to the desired stage following stage description according to Iwamatsu [2004]. Staged embryos or hatchlings were fixed with 4% PFA. Prior to fixation hatchlings were euthanised with 20x Tricaine. Fish samples were rinsed with 1x PTw and then incubated in 4% PFA/1x PTw at 4°C overnight for embryos and hatchlings or up to 2 days for 2 weeks old fish. Samples were washed three times with 1x PTw and stored in 1% PFA/1x PTw at 4°C until use. Samples were washed three times with 1x PTw and for embryos eggshells were removed mechanically by dissection with forceps at a stereoscopic microscope. In case genotyping of samples was required, a piece of tissue, usually the tail was dissected for genomic DNA extraction. Samples were kept in 1% PFA/1x PTw until their genotype was established. Samples were then either prepared for cryosectioning, whole-mount immunohistochemistry or whole-mount *in situ* hybridisation. For longer storage samples were washed 3x in 1x PTw, three times with water and then dehydrated in consecutive dilutions (25%, 50%, 75% and 100%) in either ethanol in water (for whole-mount immunohistochemistry) or methanol in 1x PTw (for *in situ* hybridisation) for 5 min each and stored in ethanol or methanol, respectively at -20°C.

5.2.2 Extraction and clean-up of genomic DNA

Extraction of genomic DNA from medaka tissue

From embryos. Staged embryos were transferred to individually or as pools of up to ten to 1.5 ml microfuge tubes and washed twice with 1 ml water. After completely removing the medium 100 μl fin-clip buffer containing 1/20th volume Proteinase K (final concentration 1 mg/ml) were added and embryos were homogenised with clean 0.5/1.5 ml micro pestles. Samples were then incubated overnight at 60°C. After briefly collecting the liquid by short centrifugation, 200 μl water were added, the samples were gently mixed by inverting the tubes several tubes, centrifuged briefly and then incubated 20 min at 95°C to inactivate the Proteinase K. Samples were finally collected by centrifugation for 1 min at 20,800 x g and then either stored for later analysis at 4°C, precipitated with ethanol/sodium acetate or directly used for PCR.

From tails of fixed embryos or tails from dechorionated embryos prior to RNA-sequencing. The samples were either: 1) Tails from previously fixed embryos. 2) Tails from dechorionated embryos from which heads were dissected for RNA sequencing. Tail samples were transferred in as little volume as possible to 1.5 ml microfuge tubes containing 25 μl fin-clip buffer containing 1/20th volume Proteinase K (final concentration 1 mg/ml) and incubated overnight at 60°C. After briefly collecting the liquid by short centrifugation, 50 μl water was added, the samples were gently mixed by inverting the tubes several tubes, centrifuged briefly and then incubated 20 min at 95°C to inactivate the Proteinase K. Samples were finally collected by centrifugation for 1 min at 20,800 x g and then precipitated with ethanol/sodium acetate.

From 1-14 day old hatchlings. After the fish were euthanised with 20x Tricaine, either the tail, head or a small tailpiece was cut off with a scalpel and transferred to a 1.5 ml microfuge tube (depending on which tissue was needed for additional characterisation, e.g. for retinal sections, the head was cut off and the tail was used for genomic DNA extraction). Samples were washed twice with 1 ml water. After completely removing the medium 100 μl fin-clip buffer containing 1/20th volume Proteinase K (final concentration 1 mg/ml) were added and embryos were homogenised with clean 0.5/1.5 ml micro pestles. Samples were then incubated overnight at 60°C. After briefly collecting the liquid by short centrifugation, 200 μl water were added, the samples were

gently mixed by inverting the tubes several tubes, centrifuged briefly and then incubated 20 min at 95°C to inactivate the Proteinase K. Samples were finally collected by centrifugation for 1 min at 20,800 x g and then either stored for later analysis at 4°C, precipitated with sodium acetate or directly used for PCR.

From adult fish. Fish were sedated in 1x Tricaine. A piece of the tail fin was cut off with a scalpel and collected in a 1.5 ml microfuge tube containing 100 μ l fin-clip buffer with 1/20th volume Proteinase K (final concentration 1 mg/ml). Samples were then incubated overnight at 60°C. After briefly collecting the liquid by short centrifugation, 200 μ l water were added, the samples were gently mixed by inverting the tubes several tubes, centrifuged briefly and then incubated 20 min at 95°C to inactivate the Proteinase K. Samples were finally collected by centrifugation for 1 min at 20,000 x g and then either stored for later analysis at 4°C, precipitated with sodium acetate or directly used for PCR.

Ethanol/sodium acetate precipitation of genomic DNA samples

50-200 μ l supernatant was transferred to a fresh microfuge tube. For precipitation of DNA, 10% (v/v) 3 M sodium acetate and 3x volumes absolute ethanol were added to individual samples. Samples were mixed by inverting several times and cooled 10 min at -80°C. Precipitates were collected by centrifugation at 20,800 x g at 4°C for 30 min and washed with 1x volume 70% ethanol at 20,800 x g at 4°C for 15 min. The supernatant was discarded, residual ethanol was removed using a pipette tip and the pellet was air dried for 10 min before dissolving it in 30 μ l 1x TE buffer.

5.2.3 PCR and cloning procedures incl. RNA *in vitro* transcription

Software for *in silico* cloning

The Geneious 8.1.9 software was used for *in silico* cloning and the analysis of Sanger sequencing results. To calculate ligation reactions EnzymeX 3 software was used.

General PCR protocol

Q5 polymerase PCR. Standard PCR was performed with the commercial high-fidelity Q5 polymerase (NEB). Desalted primers were obtained from Eurofins Genomics. In brief, 1x Q5 buffer, 200 μM dNTPs, 0.5 μM forward primer (FWD, F), 0.5 μM reverse primer (REV, R), 0.01 U/ μl Q5 polymerase and 0.1 ng plasmid or 1-20 ng gDNA or cDNA template were mixed in nuclease-free H_2O in thin-walled 200 μl PCR tubes. For cloning purposes, 50 μl reactions were used, whereas 25 μl were used for standard genotyping. Standard cycling conditions were 2 min initial denaturation at 98°C; 35x/30x (cloning/genotyping) cycles at 98°C for 30 sec and respective annealing temperature for 20 sec and 72°C at 20-30 sec/kb; a final elongation of 5 min at 72°C. Annealing temperatures were calculated using the NEB Tm calculator® (<https://tmcalculator.neb.com/#!/main/>).

Taq polymerase PCR. PCRs for direct A-tailing for subsequent were carried out using Taq polymerase. In brief, ThermoPol buffer, 200 μM dNTPs, 0.5 μM forward primer (FWD, F), 0.5 μM reverse primer (REV, R), 2 U Taq polymerase and 1-20 ng cDNA template were mixed in nuclease-free H_2O in thin-walled 200 μl PCR tubes in a final volume of 50 μl . Standard cycling conditions were 2 min initial denaturation at 95°C; 35x cycles at 95°C for 30 sec and respective annealing temperature for 20 sec and 68°C at 60 sec/kb; a final elongation of 5 min at 68°C. Annealing temperatures were adjusted for Taq polymerase use with the NEB Tm calculator® (<https://tmcalculator.neb.com/#!/main/>).

Agarose gel electrophoresis

DNA samples were mixed with 6X DNA Loading Dye and loaded into slots of 0.8-2% agarose gels (in 1x TAE) in 1x TAE containing gel chambers. Gene Ruler DNA ladder mix was added to an individual lane to allow for the estimation of band sizes. Electrophoresis was performed at 90-130 V. Following electrophoresis, gels were stained in 0.2 $\mu\text{g}/\text{ml}$ of the intercalating agent ethidium bromide (in 1X TAE) for 20 min. DNA was visualised and gels were photographed using a UV light-based ($\lambda=254$ nm) gel documentation system.

Gel extraction

Respective DNA bands were visualised and excised on a UV-gel cutting table using a scalpel. The DNA was extracted using either, the

1. **innuPREP DOUBLEpure Kit** for standard cloning
2. **Monarch DNA Gel Extraction Kit** for subsequent Sanger sequencing samples
3. **MiniElute Gel Extraction Kit** for clean-up of linearised sgRNA templates,

according to the manufacturer's instructions. The DNA was eluted in 10-18 μ l prewarmed (50°C) nuclease-free water. The concentration of purified DNA samples was measured with a spectrophotometer.

Gibson assembly cloning to construct pCS2+ base editor plasmids

Gibson assembly cloning was performed using the NEBuilder HiFi DNA Assembly kit (NEB) following the manufacturer's instructions. In brief, the plasmid backbone was PCR amplified using the following two oligos JW9274 and JW9275. The 5' ends of the amplified PCR served completely as homologous region for annealing with desired inserts, i.e. the sequence of overlap for the inserts and the boundary to the pCS2+ backbone were 100% derived from the pCS2+ backbone. Melting temperatures of overlapping regions were at least 50°C and at least 19 bp. All PCRs were carried out using Q5 polymerase with the standard 35x cycle protocol in 50 μ l volume. PCR products were purified via 0.8% agarose gel electrophoresis and the Monarch DNA Gel Extraction Kit. For the assembly, fragments smaller than 200 bp were provided in 5-fold excess. 0.01 pmol of PCR-purified pCS2+ backbone and 0.02 pmol were entered into the reaction per individual insert and added to the NEBuilder HiFi MM 1:1 (v/v) in 20 μ l total volume in PCR tubes. The reaction was carried out in a thermocycler for 2 hours at 50°C.

pGEMt-easy cloning of in situ probe plasmids

PCR was carried with Q5 polymerase (35x cycles) and up to 12 μ l purified PCR products were A-tailed with 1.25 U Taq DNA polymerase in 1x ThermoPol buffer with 0.2 mM dATP in a volume of 20 μ l. The reaction mixture was incubated at 72°C for 20 min and then directly used for ligation with the pGEM-T easy cloning vector system. Alternatively, PCR for direct A-tailing was carried out with Taq polymerase. 1.7 μ l of the A-tailed PCR product were then ligated with 25 ng pGEM-T easy vector using 2.5 U T4 DNA ligase in Rapid Ligation buffer in a total volume of 10 μ l for 1 hour at room temperature.

DNA ligation

Standard ligations were carried out with 25 fmol linearised vector and 75 fmol insert (1:3), 1x T4 ligase buffer and 0.5 U T4 Ligase for 1 h at room temperature. To calculate the necessary amount of vector and insert the software EnzymeX 3 was used.

Transformation of chemically competent cells

Mach1T1 chemically competent *E. coli* cells were thawed on ice for 10 min. 2-5 μl of ligation reaction were added to 50 μl of cells, stirred gently and incubated on ice for 20 min. A heat shock was performed at 42°C for 30 sec. The cells were snap-cooled on ice for 2 min. 300 μl TB medium was added and tubes were incubated 45-60 min on a horizontal shaker at 180 rpm. LB-Agar plates were prepared with appropriate antibiotics for bacterial selection (ampicillin or kanamycin) and 50 μl X-gal, in case blue-white selection was desired. Agar plates were prewarmed to 37°C and between 50-200 μl of transformed bacteria were plated out and incubated overnight at 37°C. Grown colonies were selected for plasmid preparation.

Transformation of chemically competent cells for HiFi assembly cloning

For cloning with the NEBbuilder HiFi DNA Assembly chemically competent NEB Turbo Competent *E. coli* cells were used. Cells were thawed on ice for 10 minutes. The HiFi assembly was diluted 1:4 of which 1 μl was added to 50 μl cells. The cells were gently mixed and incubated on ice for 30 min. A heat shock was performed at 42°C for 30 sec. The cells were snap-cooled on ice for 5 min. 950 μl SOC medium was added and tubes were incubated 60 min on a horizontal shaker at 180 rpm. LB-Agar plates were prepared with appropriate antibiotics for bacterial selection (ampicillin or kanamycin) and prewarmed to 37°C. 50-200 μl of transformed bacteria were plated out and incubated overnight at 37°C. Grown colonies were selected for plasmid preparation.

Preparation of plasmid DNA from liquid bacterial cultures

For small-scale plasmid preparations (**Miniprep**) single, white bacterial colonies were used to inoculate 3 ml of LB-medium with the respective antibiotics, LB-Amp or LB-Kan. Bacterial cultures were incubated on a horizontal shaker for 12-14 hours at 37°C and 180 rpm. Cells from overnight

2 ml bacterial culture were harvested for 2 min at 20,800 x g and the pellet was dissolved in 200 μ l cold P1 buffer. For cell lysis, 200 μ l P2 buffer were added and the tubes were inverted several times. 200 μ l P3 buffer were added to neutralise the basic pH and the tubes were inverted several times. Insoluble cell fractions were collected at 20,800 x g and 4°C for 15 min. Supernatants were then transferred to new 1.5 ml microfuge tubes. 500 μ l 2-propanol were to precipitate DNA by centrifugation at 20,800 x g and 4°C for 15 min. Cell pellets were washed with 500 μ l 70% ethanol and collected at 20,800 x g at 4°C for 5 min. The ethanol was completely decanted, excessive ethanol was removed by pipetting and the purified DNA pellets were air-dried at room temperature for 5 min. DNA was dissolved in 40 μ l nuclease-free H₂O and stored at -20°C or used directly.

For medium-scale plasmid preparations ("**Big Mini**") 20 ml LB-medium with respective antibiotics were inoculated with 20 μ l of bacterial culture of a positively identified colony and grown at 37°C and 180 rpm overnight. 8 ml of culture was used as input for a Plasmid Mini Kit (Qiagen) purification following the manufacturer's instructions. The following changes were made: The 8 ml culture was split up into two 2 ml microfuge tubes, collecting the first 4 ml of bacterial cells for 2 min at 6,000 x g, decanting the supernatant and repeating the procedure with the remaining 4 ml culture. Following the collection of cell debris after neutralisation with Buffer N3, the supernatant of the first 2 ml tube was applied to the spin column by pipetting (800 μ l), followed by a centrifugation step for 1 min at 17,000 x g at room temperature. The flow-through was discarded and the supernatant of the second corresponding microfuge tube was applied to the same spin column by pipetting. Purified plasmid DNA was eluted in 50 μ l nuclease-free water or 0.2x TE and either stored at -20°C or used directly.

For large-scale plasmid preparations (**Maxiprep**) 200 ml LB-medium containing the respective antibiotic were inoculated with single bacterial clones or 200 μ l of bacterial culture of a positively identified colony. Bacterial cultures were incubated on a horizontal shaker for 12-14 hours at 37°C and 180 rpm. Purification of plasmid DNA was carried out using the Plasmid Maxi Kit (Qiagen) according to the manufacturer's instructions. The following changes were made: The centrifugation step after the addition of P3 was replaced by filtration of the solution using filter paper. DNA was eluted from the QIAGEN-tip into a 50 ml tube and precipitated by adding 10.5 ml

2-propanol and centrifuging 60 min at 3,200 xg and 4°C. The pellet was washed with 5 ml 70% ethanol and collected by centrifuging for 30 min at 3,200 xg and 4°C. After removing all residual ethanol, the air-dried pellet was resuspended in 100 μl 1x TE overnight at 4°C. The concentration was measured spectrophotometrically, adjusted to 1 $\mu\text{g}/\mu\text{l}$ with 1x TE and the plasmid DNA stored at -20°C or used directly.

Enzymatic digest

Digestion for quality control. A quality control digest or test digest was performed using an aliquot of the DNA sample of interest to verify that the correct insert DNA was introduced to the plasmid backbone. The digestion mix contains 1x enzyme buffer (1x CutSmart, NEB or 1x Fast Digest, Thermo), 2 U per restriction enzyme used and up to 1 μg of DNA of interest in a final volume of 20 μl . The digestion mix was incubated for 2 hours at 37°C (65°C for TaqI-v2) and was loaded on a gel to visualise the band pattern. For plasmid DNA, a single sample derived from one clone that generated the correct band pattern was further validated by Sanger sequencing.

Digestion for cloning/linearisation of template DNA for mRNA transcription. When larger quantities of digested DNA samples were required reactions were set up containing 1x enzyme buffer (1x CutSmart, NEB or 1x Fast Digest, Thermo), 10 U per restriction enzyme used and up to 10 μg of DNA of interest in a final volume of 50-100 μl . The digest was incubated at 37°C for 14 hours and then either loaded on a gel to extract the desired band via the innuPREP DOUBLEpure Kit or the MiniElute Gel Extraction Kit; alternatively, for mRNA templates, the digest was directly cleaned up using the QIAquick PCR Purification Kit (Qiagen) following the manufacturer's instructions and eluting with 20 μl nuclease-free water.

sgRNA target site selection and preparation

sgRNAs for CRISPR/Cas9 experiments were designed with CCTop [Stemmer et al., 2015], whereas base editing sgRNAs were designed using ACEofBASES [Cornean et al., 2022]. For sgRNAs, oligonucleotide pairs for identified targets were ordered with 5' substitution. Cloning of sgRNA templates and in vitro transcription was performed as previously described [Stemmer et al., 2015]. In brief, the sgRNA target was cloned into the sgRNA template backbone (DR274,

#3632) by annealed oligo cloning. The plasmid DNA from medium-scale preparations was linearized with *Dra*I, the template band purified over a 1.5% agarose gel (in 1x TAE), excised and purified using the MiniElute Gel Extraction Kit (Qiagen). 120 ng of template DNA were transcribed *in vitro* using the MEGAscript T7 Transcription Kit (Thermo) according to the manufacturer's instructions, however, setting up 10 μ l reactions (instead of 20 μ l). DNA template was removed with Turbo DNase and the sgRNAs were purified using the RNeasy Mini Kit (Qiagen) according to the manufacturer's instructions. RNA quality was assessed with a test gel and the concentration was adjusted to 300 ng/ μ l.

Alternatively, synthetic crRNAs were ordered from IDT. In brief, a target-specific, crRNA oligonucleotide (36 nucleotides), covering 20 target nucleotides, was designed and ordered together with the 67 nucleotides tracrRNA. Oligonucleotides were resuspended in Nuclease-Free Duplex Buffer to 100 μ M stocks. Resuspended oligonucleotides were stored at -20°C. To prepare a 40 μ M crRNA:tracrRNA duplex mix, 4 μ l of each 100 μ M crRNA and 100 μ M tracrRNA were mixed with 2 μ l Nuclease-Free Duplex Buffer, mixed gently, heated to 95°C and cooled down at room temperature for 15 min. The duplex was either directly used in microinjections, using 1 μ l in a 10 μ l injection for 4 μ M final concentrations, or stored up to 6 months at -20°C.

Selection and preparation of gRNAs for RfxCas13d knockdown

gRNAs for RfxCas13d mediated mRNA knockdown were designed following previously published instructions [Kushawah et al., 2020]. In brief, the full mRNA sequence of the target gene was extracted (including 5' and 3' UTRs), and the minimum free energy prediction tool RNAfold was used to select three accessible gRNAs [Lorenz et al., 2011]. Two oligos were then used for fill-in PCR and cloning-free transcription of gRNAs: a universal oligo containing a 19 nt T7 promoter sequence and a 30 nt direct repeat sequence (JW9731_Cas13d_Universal_t7), a targeting oligo that contains a complementary sequence to the repeat region as well as the 22 nt target binding sequence (specific oligo). Fill-in PCR was performed as follows: OneTaq buffer, 10 μ M universal oligo, 10 μ M specific oligo, 200 μ M dNTPs and 1.5 U OneTaq polymerase were mixed in a total volume of 50 μ l in a thin-wall PCR tube and the PCR was run on the following cycling conditions: 4 min initial denaturation at 94°C, 30x cycles of 30 sec denaturation at 94°C, 40 sec annealing at 60°C

and 30 sec extension at 72°C; a final elongation of 10 min at 72°C. The gRNA donor product was purified using the QIAquick PCR Purification Kit (Qiagen) and gRNAs were in vitro transcribed using the MEGAscript T7 Transcription Kit (Thermo). Transcribed gRNAs were then cleaned up by sodium acetate – ethanol precipitation. Nuclease-free water was added to a total volume of 100 μ l, then 10% (v/v) 3M sodium acetate and 3x volumes ethanol (95-100%) were added and RNA cooled by 1 hour incubation at -80°C and precipitated at 20,800 x g at 4°C for 30 min, followed by a washing step with 75% ethanol. The air-dried RNA pellet was reconstituted in 50 μ l RNase-free water and the RNA concentration was determined by spectrophotometry and the quality of the RNA was assessed electrophoretically. gRNAs were stored at -80°C.

***In vitro* transcription and purification of mRNA for microinjection**

Plasmids (Table 5.35) containing SP6, T7 or T3 promoters, specific coding sequences and stabilising, untranslated structures (e.g. poly-A tails) were linearised by enzymatic digest. Linearised plasmids were purified using the QIAquick PCR Purification Kit (Qiagen) and transcribed in vitro using the respective Transcription Kit. Transcribed mRNA was purified using the RNeasy Mini Kit (Qiagen) according to the manufacturer’s instructions and RNA quality was assessed with a test gel.

Table 5.35: Linearisation and transcription of mRNA. Abbreviations: Nr. – number; Rs. – Restriction site; Pol. – polymerase.

Alias	Plasmid	Internal plasmid Nr	Rs for linearisation	RNA pol for transcription
<i>heiCas9</i>	pCS2+_heiCas9	#5197	NotI	SP6
<i>BE4-Gam</i>	pGGEV_4_BE4-Gam	#5400	SpeI	SP6
<i>evoBE4max</i>	pCS2+_evoBE4max	#5797	NotI	SP6
<i>ancBE4max</i>	pCMV_AncBE4max	#5811	SapI	T7
<i>ABE8e</i>	pCMV_ABE8e	#5812	SapI	T7
<i>evoBE4max-NG</i>	pCS2+_evoBE4max-NG	#5800	NotI	SP6
<i>evoBE4max-SpRY</i>	pCS2+_evoBE4max-SpRY	#5868	NotI	SP6

Alias	Plasmid	Internal plasmid Nr	Rs for linearisation	RNA pol for transcription
<i>ancBE4max-NG</i>	pCS2+_ancBE4max-NG	#5869	NotI	SP6
<i>ancBE4max-SpRY</i>	pCS2+_ancBE4max-SpRY	#5867	NotI	SP6
<i>ABE8e-NG</i>	pCMV_ABE8e-NG	#5862	SapI	T7
<i>ABE8e-SpRY</i>	pCS2+_ABE8e-SpRY	#5866	NotI	SP6
<i>RfxCas13d</i>	pT3TS_RfxCas13d-HA	#5810	XbaI	T3
<i>dag1</i>	pCS2+_dag1-CDS	#5628	NotI	SP6

5.2.4 DNA sequencing

Sanger sequencing

Sanger sequencing was performed with Eurofins Genomics according to the manufacturer's instructions for the TubeSeq service. For quality assessment of DNA plasmids 75 ng/ μ l were prepared in a total volume of 15 μ l with or without an additional 2 μ l of 10 μ M sequencing oligos. For genotyping, PCR products were purified via gel electrophoresis and using the Monarch DNA Gel Extraction Kit (NEB) and 5 ng/ μ l were prepared in a total volume of 15 μ l with an additional 2 μ l of 10 μ M target-specific sequencing oligos.

Sequence analysis following Sanger sequencing was performed in Geneious 8.1.9 and the transition rates of base editing experiments were estimated using EditR [Kluesner et al., 2018], by uploading .ab1 sequencing files into the EditR online tool (https://moriaritylab.shinyapps.io/editr_v10/), with at least 90 bp to the 5' and 3' termini and standard p -value cutoff ($p=.01$). Base editing rates were exported to R for subsequent plotting.

Targeted amplicon sequencing

Amplicon deep sequencing (Illumina sequencing) was performed as previously described [Cornean et al., 2022]. In brief, locus-specific primers with Illumina

adapters were used for amplification of target loci from gDNA using Q5 Hot Start High-Fidelity DNA polymerase and purified via gel electrophoresis and the Monarch DNA Gel Extraction Kit. Samples were submitted either pooled or as one PCR product at 25 ng/ μ l to GeneWiz (Azenta Life Sciences) for sequencing using the Amplicon-EZ service (Illumina MiSeq, 2 x 250 bp sequencing, paired-end). Amplicon sequencing data were analysed as previously described [Cornean et al., 2022] using CRISPResso2 v.2.1.2 [Clement et al., 2019].

5.2.5 Wholemout *in situ* hybridisation procedures

Probe synthesis

Qiagen Plasmid “Big Mini” template plasmids (#5820 for *pomt1*, #5821 for *pomt2*, #5822 for *KIAA1549*, #5964 for *dag1*, #5968 for *dag1b* and #6108 for *SUCO*) were linearised with Sall (*pomt1*) or SphI (*pomt2*, *KIAA1549*, *dag1*, *dag1b*, *SUCO*). Plasmid linearisation was assessed by running a sample aliquot on a test gel. The DNA was then purified using the QIAquick PCR Purification Kit (Qiagen) according to the manufacturer’s instructions. Linearised DNA was eluted with 20 μ l nuclease-free water.

Transcription reactions were set up containing 1 μ g linearised template DNA, 10 mM DTT, rNTP-mix (1 mM final concentration for ATP, CTP and GTP, each and 0.65 mM UTP), 35 mM Digoxigenin-11-UTP, 20 U RiboLock RNase Inhibitor, 1x Transcription buffer, 40 U T7 (*pomt1*) or SP6 RNA Polymerase (*pomt2*, *KIAA1549*, *dag1*, *dag1b*, *SUCO*) in a total volume of 20 μ l. The mix was incubated for 6 hours at 37°C. To remove template DNA 2 U Turbo DNase were added and the mix was incubated at 37°C for 15 min. Transcribed RNA was purified by LiCl precipitation. In brief, the precipitation mix contained RNA sample, 91 mM LiCl and 3x volumes ethanol (v/v), was mixed gently and cooled to -20°C for 20 min. The RNA was then pelleted at 20,800 x g and 4°C for 20 min, the supernatant carefully removed and the pellet washed with 75% ethanol by centrifugation for 5 min at 20,800 x g and 4°C. After removing all ethanol and air-drying the sample at room temperature for 10 min the RNA was resuspended in 20 μ l nuclease-free water. For quality control, a aliquot (600 ng) was mixed with 2x RNA loading dye, incubated 10 min at 80°C and run on a 1% agarose gel (1x TAE). 150 μ l HYB mix were added to the remaining RNA, the sample gently mixed and stored at -20°C.

Wholemount *in situ* hybridisation (WISH)

Proteinase K digestion and post-fixation. WISH was performed on embryos and larvae from the albino heino line. Embryos or hatchlings were rehydrated sequentially by transfer from methanol to 75% methanol/1xPTw, to 50% methanol/1xPTw, to 25% methanol/1xPTw, and finally to 1xPTw, each for 5 min at room temperature with gentle agitation on a horizontal shaker in 9 cm dishes. Samples were washed 1x more for 5 min with 1xPTw. To permeabilise the tissue, samples were digested in 10 $\mu\text{g}/\text{ml}$ Proteinase K/1xPTw solution without agitation. The duration of the digest depended on the stage of the embryos: stage 24: 8 min; stage 28: 15 min; stage 34: 1 hour; stage 39: 1.5 hours. To stop Proteinase K activity, embryos were rinsed twice with 2 mg/ml glycine/1xPTw, followed by post-fixation in 4% PFA/1xPTw for 20 min. Prior to hybridization embryos were washed 5x5 min in 1xPTw at room temperature.

Sample hybridisation and staining. The samples were then pre-hybridised in HYB mix at 65°C for 2 hours in 2 ml microfuge tubes in a water bath. 10 μl of Digoxigenin-labelled probe were mixed with 190 μl HYB mix and denatured at 80°C for 10 min. The HYB mix was carefully removed leaving enough to cover the samples and the denatured hybridisation probe was immediately added. Hybridisation was performed overnight at 65°C in a water bath.

Reagents for washing (50% formamide/2xSCCT, 2xSCCT, 0.2xSCCT) were preheated to 65°C. Samples were washed 2x30 min at 65°C with 50% formamide/2xSSCT, 15 min at 65°C with 2xSSCT and 2x30 min at 65°C. Samples were washed 3x5 min with 1xPTw and blocked at room temperature for 1 hour with Blocking Buffer with gentle rotation. Samples were incubated overnight at 4°C with Anti-Digoxigenin-AP Fab fragments (dilution: 1:2000) in Blocking Buffer. Unbound antibodies were washed 6x10 min each with 1xPTw in a 6-well plate on a horizontal shaker. Samples were equilibrated 2x5 min each with Pre-staining buffer and 2x5 min each with Staining buffer. Samples were stained in the dark in a 6-well plate by incubation with 4.5 μl NBT (final: 337.5 $\mu\text{g}/\text{ml}$) and 3.5 μl BCIP (final: 175 $\mu\text{g}/\text{ml}$) in 1 ml staining buffer without shaking. Colour development was assessed every 5 min and the reaction was stopped by rinsing 3x with 1xPTw and washing 3x5 min with 1xPTw with gentle shaking. Samples were de-yolked and stored in a

multi-well plate in glycerol at 4°C overnight. Stained embryos were transferred to a coverglass, with a vaseline ring prepared as a spacer, to prevent squeezing of embryos, and a coverslip was added and samples were imaged.

5.2.6 RNA Extraction and cDNA analysis

Total RNA extraction from medaka embryos

Embryos were collected from the desired cross and raised at 28°C to the desired stage [Iwamatsu, 2004].

RNA extraction of individual embryos using the Direct-zol DNA/RNA Miniprep kit (A). Individual embryos were transferred to 1.5 ml RNase-free microfuge tubes and washed twice with 1 ml nuclease-free water. Clean 0.5/1.5 ml micro pestles were used to crack the chorion of embryos in 500 μ l Trizol reagent and homogenise embryos thoroughly. After a one hour incubation at room temperature, the tissue debris was collected by centrifugation for 1 min at 16,000 x g at room temperature and the supernatant was transferred to a fresh 1.5 ml RNase-free microfuge tube. All subsequent centrifugation steps were performed at room temperature at 16,000 x g and flow-throughs were discarded after each centrifugation. An equal volume of ethanol (95-100%, 500 μ l) was added to the supernatant, mixed by pipetting up and down twice and swiftly transferring the samples onto a Zymo-Spin IICR Column in a Collection Tube and centrifuging for 30 sec. As the volume exceeded the 700 μ l capacity of the column the mixture was applied in two steps, each followed by centrifugation. Samples were washed by adding 400 μ l RNA Prep Buffer to the column and centrifuging for 30 sec. 700 μ l RNA Wash Buffer was then added to the column and centrifuged for 1 min. The column was then carefully transferred to a fresh 1.5 ml RNase-free microfuge tube and the RNA was eluted by applying 30 μ l nuclease-free water directly to the matrix and centrifuging for 1 min. To wash the column prior to DNA elution, first 700 μ l of Direct-zol DNA Wash 1 Buffer was added to the column followed by a centrifugation step for 30 sec and then Direct-zol DNA Wash 2 Buffer was added followed by centrifugation for 30 sec. The column was then carefully transferred to a fresh 1.5 ml RNase-free microfuge tube and the DNA was eluted by applying 50 μ l Direct-zol DNA Elution Buffer directly to the matrix and centrifuging for 1 min. The DNA was then directly used for genotyping. The concentration of RNA was determined spectrophotometrically and then stored at -80°C until further processed.

RNA extraction of pools of embryos using the TRIzol method [Chomczynski, 1993] (B). Staged medaka embryos were collected in a 1.5 ml RNase-free microfuge tube and washed three times with 1x PBS. 1 ml TRIzol reagent was added for tissue lysis and homogenization which was aided by using clean 0.5/1.5 ml micro pestles to crack open the chorion. After incubating the lysates for five min at room temperature 20% (v/v) chloroform was added (200 μ l), followed by mixing and 3 min incubation at room temperature. Organic and aqueous phases were separated by centrifugation at 12,000 x g at 4°C for 15 min, after which the aqueous (upper) phase was transferred into a 1.5 ml RNase-free microfuge tube. To remove all traces of phenol, the chloroform extraction step was repeated. To precipitate the RNA from the aqueous phase 2-propanol was added at 2.5x vol. chloroform (500 μ l), as well as 1 μ g glycogen, mixed and incubated 10 min at room temperature. Precipitates were collected at 12,000 x g at 4°C for 10 min and washed with 70 μ l ethanol; followed by brief centrifugation at 7,500 x g at 4°C for 10 min. The pellet was air-dried at room temperature for 10 min and dissolved in 20-30 μ l RNase-free water for 5 min at 37°C. The RNA concentration was determined by spectrophotometry and samples were stored at -80°C.

DNaseI treatment and RNA precipitation (for A and B). To circumvent potential contamination of RNA samples by genomic DNA, RNA extracts were treated with DNaseI. In brief, up to 6 μ g of total RNA was treated with 2 U Turbo DNase in Turbo DNase buffer in a final volume of 50 μ l for 30 min at 37°C. Inactivation of DNase activity was achieved by incubating samples in 3.5 mM EDTA for 10 min at 65°C. To precipitate RNA from the sample nuclease-free water was added to a total volume of 100 μ l, then 10% (v/v) 3 M sodium acetate, 3x volumes ethanol (95-100%) and 1 μ g glycogen were added and the sample mixed thoroughly by inverting the tube several times. The mixture was cooled to -80°C for one hour and RNA was collected by centrifugation for 30 min at 20,800 x g at 4°C and washed with 70% ethanol; followed by brief centrifugation at 20,800 x g at 4°C for 10 min. The pellet was air-dried at room temperature for 10 min and dissolved in 20 μ l RNase-free water for 5 min at 37°C. The RNA concentration was determined by spectrophotometry and the quality of the RNA was assessed electrophoretically: by subjecting an aliquot of the RNA sample to a 1% agarose gel by gel electrophoresis with the gel system cleaned prior using 0.1 M NaOH. In brief, 400 ng of RNA sample was diluted to a volume of 6 μ l with nuclease-free water

and mixed with 2xRNA loading dye. The sample was denatured for 10 min at 80°C to remove secondary structures and was loaded onto a freshly-made 1% agarose in TAE gel at 90 V for 45 min. The RNA sample passed the quality control step if strong ribosomal bands with little to no smearing were visible and stored at -80°C until further processing.

RNA extraction of dissected tissue using the Direct-zol RNA Microprep kit. Embryos or hatchlings were used for tissue dissection. Embryos were dechorionated first and hatchlings were euthanised with 20x Tricaine and washed three times with 1xERM. To perforate the chorion of embryos, embryos were rolled on sandpaper (1000 grit) until no more hairs were visible on the chorion. Embryos were then treated with hatching enzyme for 30-45 min at 28°C until the chorion was dissolved for some but not all embryos and the enzymatic reaction stopped by washing the embryos three times with 1xERM. Dechorionated embryos were transferred to glass Petri dishes filled with 1xERM and inspected for damage; damaged embryos were discarded from sample processing. To dissect the desired tissue a 0.3 mm needle (0.3 mm A~13 mm) or a scalpel were used. The desired tissue sample was then transferred to a 1.5 ml RNase-free microfuge tube containing 1 ml ice-cold 1xPBS using cell saver tips in as little liquid as possible (roughly 5-10 μ l) and placed on ice until the remaining samples were dissected. The remainder tissue of the embryo was transferred to a 1.5 ml RNase-free microfuge tube containing 100 %l fin-clip buffer containing 1/20th volume Proteinase K and later processed to obtain the genotype identity of the sample, as described above. After all the samples were dissected, the 1xPBS was completely removed and 300 μ l Trizol reagent was added and samples were incubated 5 min at room temperature, followed by a centrifugation step at 20,800 x g (room temperature) and the transfer of the supernatant of samples to a 1.5 ml RNase-free microfuge tube. Samples were stored until genotypes were determined. Samples were thawed and 300 μ l ethanol (96-100%; 1x volume sample) was added, the sample was mixed by pitting up and down twice and swiftly transferred to a Zymo-Spin IC Column in a Collection Tube. All following centrifugation steps were performed at room temperature at 16,000 x g and flow-throughs were discarded after each centrifugation. Samples were centrifuged for 30 sec and columns were placed into a fresh collection tube. Samples were washed by adding 400 μ l RNA Wash Buffer to the column and centrifuging for 30 sec. To remove DNA, 30 U DNaseI (5 μ l of 6 U/ μ l) was mixed with DNA digestion buffer and applied to the matrix of the column for 15 min at room temperature. To remove

DNaseI 400 μl RNA Prep Buffer was added to the column and centrifuged for 30 sec. This step was repeated once. Finally, 700 μl RNA Wash Buffer was added to the column and centrifuged for 1 min. The column was then carefully transferred to a fresh 1.5 ml RNase-free microfuge tube and RNA was eluted by applying 20 μl nuclease-free water directly to the matrix and centrifuging for 1 min. The concentration of RNA was determined spectrophotometrically and then stored at -80°C until further processed.

cDNA synthesis

The RevertAid First Strand cDNA synthesis kit was used for the reverse transcription of previously purified total RNA for the generation of cDNA. In brief, up to 1 μg purified total RNA were incubated with either 1) for cloning full length transcripts: 0.5 μl oligo dT₁₈ and 0.5 μl random hexamers; 2) for quantification of transcripts: 0.5 μl oligo dT₁₈; in a total volume of 12 μl at 65°C for 5 min in a thin-walled 200 μl PCR tube. After 1-2 min incubation on ice, 4 μl 5x RT buffer, 1 μl RiboLock (20 U/ μl), 2 μl dNTP-mix (10 mM) and RevertAid M-MuLV Reverse Transcriptase (200 U/ μl) were added in the given order to a final volume of 20 μl . Samples were gently mixed, briefly collected by centrifugation and then samples were subjected to the following cycling conditions in a thermocycler: Maximum lid temperature: 45°C ; 10 min at 25°C , 1 hr at 42°C , 5 min at 72°C . Samples were briefly placed on ice, gently spun down and 1 μl RNaseH was added to remove residual RNA in RNA/DNA heteroduplexes. Samples were incubated 20 min at 37°C and RNaseH was inactivated by 10 minutes incubation at 65°C . The cDNA was then diluted with nuclease-free water depending on the amount of RNA used as a template for the reverse transcription, aiming to obtain a cDNA concentration of approximately 15 ng/ μl .

semi-quantitative RT-PCR

For semi-quantitative reverse-transcription PCR total RNA was extracted from embryos from heterozygous *pomt2*^{+/Cterm-fs} incrosses and DNA and RNA were extracted using the Direct-zol DNA/RNA Miniprep kit and genotypes were determined by PCR. cDNA was synthesised and 25 ng cDNA were used to determine expression levels. A 15 μl PCR reaction using Q5 polymerase was assembled with primers for the house-keeping gene *GAPDH*, and for *pomt1* and *pomt2*. Primers were designed such that forward and reverse primers were on

different exons. *GAPDH* expression was determined with 32x cycles and PCRs for *pomt1* and *pomt2* were 35x cycles. PCRs for *GAPDH* and *pomt2* were loaded on the same 2% agarose gel, *pomt1* PCRs were loaded separately and samples were analysed by gel electrophoresis. The band density was documented digitally, bands dark on white background, and analysed in Fiji. Images were cropped to include only the band sizes between 0 bp to 500 bp and from ladder to ladder. The Subtract Background function was used, with a rolling ball radius of 50.0 pixels (light background ticked). The images were then inverted cropped narrower, using one defined rectangle to fit all band sizes. Then using the Select first lane tool bands were subsequently selected and plotted using the Plot lanes function. The resulting values were used to normalise *pomt1* and *pomt2* to the corresponding *GAPDH* and the wild-type mean of expression was set to 1.

quantitative RT-PCR (qPCR)

To quantify the levels of *pomt1* and *pomt2* mRNA upon RfxCas13d mediated knockdown cDNA from one control and two knockdown samples were used. The housekeeping gene *B2M* was used for normalisation.

In brief, in a 96 well PCR plate 20 μ l of final volume per well was compiled of SensiFAST SYBR HI-ROX Mix, 10 or 20 ng of the respective cDNA, 0.4 μ M forward primer and 0.4 μ M reverse primer in RNase-free water. Empty wells were loaded with 20 μ l RNase-free water. An optical adhesive cover was added and the plate was sealed and a short spin was carried out on a centrifuge with a 96-well plate adapter. Cycling conditions were as follows: initial denaturation program (95°C for 2 min), amplification and quantification program repeated for 40x cycles (95°C for 20 sec, 60°C for 1 min with a single fluorescence measurement), melting curve program (60-95°C with a heating rate of 0.3°C/sec, 15 sec at 95°C and continuous fluorescence measurement) and finally a cooling step. Cycling was performed and signals were detected with a Step-One Plus Real-Time PCR system.

The relative change was calculated using the obtained C_T values using the comparative C_T method (also known as $2^{-\Delta\Delta C_T}$ method, Schmittgen and Livak [2008]). First, C_T means were calculated from technical replicates. Then, the ΔC_T value was calculated (Equation 5.1), which gives a normalisation of

each sample to the reference gene control, here *B2M*.

$$\Delta C_T = C_T(\textit{pomt1 or pomt2}) - C_T(\textit{GADPH}) \quad (5.1)$$

The $\Delta\Delta C_T$ value was then calculated by subtracting the mean of the control treatment ΔC_T from the ΔC_T of each treatment sample (Equation 5.2), here the *pomt2* knockdown.

$$\Delta\Delta C_T = \Delta C_T(\textit{pomt2 knockdown}) - \Delta C_T(\textit{control condition}) \quad (5.2)$$

The relative fold change was used to create visually descriptive graphs (Equation 5.3).

$$\textit{Fold change (gene expression level)} = 2^{-\Delta\Delta C_T} \quad (5.3)$$

5.2.7 RNA Sequencing

Head dissection from embryos

To prepare samples for RNA sequencing, heads of stage 22, stage 24 and stage 28 embryos were dissected at the midbrain-hindbrain boundary. Embryos were collected from heterozygous *pomt2*^{+/*Cterm-fs*} incrosses and raised at 26°C until one hour prior to reaching the desired stage [Iwamatsu, 2004]. To perforate the chorion, embryos were rolled on sandpaper (1000 grit) until no more hairs were visible on the chorion. Embryos were then treated with hatching enzyme for 30-45 min at 28°C until the chorion was dissolved for some but not all embryos and the enzymatic reaction stopped by washing the embryos 3x with 1xERM. Dechorionated embryos were transferred to glass Petri dishes filled with 1xERM and inspected for damage; damaged embryos were discarded from sample processing. To dissect the desired head region a 0.3 mm needle (0.3 mm A~13 mm) was used. The head sample was then transferred to a 1.5 ml RNase-free microfuge tube using cell saver tips in as little liquid as possible (roughly 5-10 μ l) and placed on ice. The remainder tissue of the embryo was transferred to a 1.5 ml RNase-free microfuge tube containing 25 μ l fin-clip buffer containing 1/20th volume Proteinase K and later processed to obtain the genotype identity of the sample, as described above. After 5 samples were dissected 50 μ l Trizol reagent was added and samples were incubated 5 min at room temperature, followed by a 5 min centrifugation step at 20,800 x g (room temperature) and the transfer of samples to -80°C. In this fashion, 30 samples

were dissected in one day.

RNA extraction (Direct-zol RNA micro kit)

After samples were genotyped they were pooled as follows: 5 samples were pooled for stage 22 pools and for stage 28 *pomt2* mutant pools; 4 samples were pooled for stage 24 pools; 2 samples were pooled for stage 28 wild-type pools. Where necessary additional Trizol reagent was added to reach a volume of 250 μ l. Pooled samples were then homogenised using clean 0.5/1.5 ml micro pestles, incubated 10 min at room temperature and then collected by 5 min centrifugation at 20,800 x g at room temperature. The supernatant was transferred to a fresh 1.5 ml RNase-free microfuge tube. 250 μ l ethanol (96-100%; 1x volume sample) was added, the sample was mixed by pitting up and down twice and swiftly transferred to a Zymo-Spin IC Column in a Collection Tube. Following steps of the RNA extraction protocol were performed as described earlier. The concentration of RNA was determined spectrophotometrically and samples were stored at -80°C until processed further.

Library preparation and high-throughput transcriptome sequencing)

Total RNA integrity was initially quality controlled using an Agilent RNA Nano 6000 chip on an Agilent 2100 Bioanalyzer. Samples were quantified using the Qubit RNA High Sensitivity Assay on a Qubit. The polyA RNA was enriched from 100 ng of total RNA using the NEBNext Poly(A) mRNA Magnetic Isolation Module. Libraries for RNA-Seq were prepared with the NEBNext Ultra II Directional RNA Library Prep Kit for Illumina in conjunction with NEBNext Unique Dual Index oligos. The quality of libraries was assessed with the Qubit HS DNA assay and the Agilent TapeStation D1000 assay. To remove excess adaptor dimers samples were re-purified with Ampure XP beads in a 1:1 (v/v) ratio. Samples were pooled equimolarly and sequenced on the NextSeq 2000 Sequencer (with 80 cycles of sequencing using P3 reagents using the 75 bases single end plus barcode read (dual index 16 bases, 8+8) protocol. Sequencing depth was 72 million reads on average and at least 39 million reads per sample.

RNAseq analysis)

Initial QC, index building and pseudoalignment. Analysis was performed following the course descriptions of the DIYtranscriptomics course

(<https://diytranscriptomics.com/>) [Berry et al., 2021]. Sequencing data were retrieved from gigamove and unzipped using the bash function (in Terminal) “unzip” due to size and file complexity (68 GB). The package environment was first set up as follows in Anaconda using the Anaconda Navigator 2.0.4. Channels were installed using the following bash commands in the Terminal:

```
conda config --add channels defaults
conda config --add channels defaults
conda config --add channels bioconda
conda config --add channels conda-forge
conda config --set offline false
```

The tools FastQC, MultiQC and Kallisto were installed and added to a created conda environment “rnaseq”, as follows:

```
conda create --name rnaseq
conda activate rnaseq
conda install -c bioconda fastqc
conda install -c bioconda multiqc
conda install -c bioconda kallisto
```

The medaka reference genome was obtained from Ensemble (release 105) (http://ftp.ensembl.org/pub/release-105/fasta/oryzias_latipes/cdna/) (Oryzias_latipes.ASM223467v1.cdna.all.fa.gz) and used to build an index file using Kallisto (v0.46.2) [Bray et al., 2016] using the following command:

```
Kallisto index -i Oryzias_latipes.ASM223467v1.cdna.all.index
↳ Oryzias_latipes.ASM223467v1.cdna.all.fa
```

Data quality of fastq files was assessed using FastQC (v0.11.9) [Andrews, 2010], pseudoalignment was performed using Kallisto (v0.46.2) [Bray et al., 2016] and FastQC and Kallisto mapping results for all samples were summarised in a single html file using MultiQC (v.1.11) [Ewels et al., 2016]. The commands were run using a shellscript (.sh) written in the text editor Sublime Text to include the following lines of code which was run in the rnaseq environment (Terminal):

```
# first use fastqc to check the quality of our fastq files:
fastqc *.gz -t 8
# now map reads to the indexed reference host transcriptome
# use as many 'threads' as your machine will allow in order to speed up the
↳ read mapping process.
```

```
# note that we're also including the '€>' at the end of each line
# this takes the information that would've been printed to our terminal, and
  ↪ outputs this in a log file
kallisto quant -i Oryzias_latipes.ASM223467v1.cdna.all.index -o Sample1
  ↪ -t 8 --single -l 75 -s 30 Sample_1St22wt1_sequence.txt.gz &>
  ↪ Sample1.log
kallisto quant -i Oryzias_latipes.ASM223467v1.cdna.all.index -o Sample2
  ↪ -t 8 --single -l 75 -s 30 Sample_2St22wt2_sequence.txt.gz &>
  ↪ Sample2.log
kallisto quant -i Oryzias_latipes.ASM223467v1.cdna.all.index -o Sample3
  ↪ -t 8 --single -l 75 -s 30 Sample_3St22wt3_sequence.txt.gz &>
  ↪ Sample3.log
kallisto quant -i Oryzias_latipes.ASM223467v1.cdna.all.index -o Sample4
  ↪ -t 8 --single -l 75 -s 30 Sample_4St22hom1_sequence.txt.gz &>
  ↪ Sample4.log
kallisto quant -i Oryzias_latipes.ASM223467v1.cdna.all.index -o Sample5
  ↪ -t 8 --single -l 75 -s 30 Sample_5St22hom2_sequence.txt.gz &>
  ↪ Sample5.log
kallisto quant -i Oryzias_latipes.ASM223467v1.cdna.all.index -o Sample6
  ↪ -t 8 --single -l 75 -s 30 Sample_6St22hom3_sequence.txt.gz &>
  ↪ Sample6.log
kallisto quant -i Oryzias_latipes.ASM223467v1.cdna.all.index -o Sample7
  ↪ -t 8 --single -l 75 -s 30 Sample_7St24wt1_sequence.txt.gz &>
  ↪ Sample7.log
kallisto quant -i Oryzias_latipes.ASM223467v1.cdna.all.index -o Sample8
  ↪ -t 8 --single -l 75 -s 30 Sample_8St24wt1_sequence.txt.gz &>
  ↪ Sample8.log
kallisto quant -i Oryzias_latipes.ASM223467v1.cdna.all.index -o Sample9
  ↪ -t 8 --single -l 75 -s 30 Sample_9St24wt1_sequence.txt.gz &>
  ↪ Sample9.log
kallisto quant -i Oryzias_latipes.ASM223467v1.cdna.all.index -o Sample10
  ↪ -t 8 --single -l 75 -s 30 Sample_10St24hom1_sequence.txt.gz &>
  ↪ Sample10.log
kallisto quant -i Oryzias_latipes.ASM223467v1.cdna.all.index -o Sample11
  ↪ -t 8 --single -l 75 -s 30 Sample_11St24hom2_sequence.txt.gz &>
  ↪ Sample11.log
kallisto quant -i Oryzias_latipes.ASM223467v1.cdna.all.index -o Sample12
  ↪ -t 8 --single -l 75 -s 30 Sample_12St24hom3_sequence.txt.gz &>
```

```

↪ Sample12.log
kallisto quant -i Oryzias_latipes.ASM223467v1.cdna.all.index -o Sample13
↪ -t 8 --single -l 75 -s 30 Sample_13St28wt1_sequence.txt.gz &>
↪ Sample13.log
kallisto quant -i Oryzias_latipes.ASM223467v1.cdna.all.index -o Sample14
↪ -t 8 --single -l 75 -s 30 Sample_14St28wt2_sequence.txt.gz &>
↪ Sample14.log
kallisto quant -i Oryzias_latipes.ASM223467v1.cdna.all.index -o Sample15
↪ -t 8 --single -l 75 -s 30 Sample_15St28wt3_sequence.txt.gz &>
↪ Sample15.log
kallisto quant -i Oryzias_latipes.ASM223467v1.cdna.all.index -o Sample16
↪ -t 8 --single -l 75 -s 30 Sample_16St28hom1_sequence.txt.gz &>
↪ Sample16.log
kallisto quant -i Oryzias_latipes.ASM223467v1.cdna.all.index -o Sample17
↪ -t 8 --single -l 75 -s 30 Sample_17St28hom2_sequence.txt.gz &>
↪ Sample17.log
kallisto quant -i Oryzias_latipes.ASM223467v1.cdna.all.index -o Sample18
↪ -t 8 --single -l 75 -s 30 Sample_18St28hom3_sequence.txt.gz &>
↪ Sample18.log
# summarize fastqc and kallisto mapping results in a single summary html
↪ using MultiQC:
multiqc -d .
echo "Finished"

```

Analysis of aligned data. Downstream analysis and graphical data visualization were performed in R (v.3.6.3)/Bioconductor (v.3.10.1) [Huber et al., 2015] using the R studio IDE. For citations and details on the general R packages used please see the section Analysis and data visualisation. The bioMart package [Durinck et al., 2009] was used to obtain gene-level information for medaka transcripts from Ensemble using also using the ensemblDb package [Rainer et al., 2019]. Kallisto transcripts were imported into R using the tximport package [Soneson et al., 2015]. Differential gene expression analysis was performed using the Bioconductor library EdgeR implemented in R for filtering of genes with low expression [Robinson et al., 2009]. Filtering was performed on $\text{cpm} > 1$ adjusting for replicates, data was normalised using the `calcNormFactors` edgeR function using the TMM method and the `cpm` edgeR function was used to obtain counts per million from normalised data. The `VOOM` function from Limma package

to model the mean-variance relationship [Ritchie et al., 2015]. Differentially expressed genes were clustered unsupervised by hierarchical clustering using the Pearson method (complete linkage) using $k=2$. Samples were clustered by hierarchical clustering using the Spearman method (complete linkage). The `heatmap.2` function of the Bioconductor `gplots` package [Warnes et al., 2022] was used to generate the heatmap. Only genes with $FDR < 0.01$ (adjusted p -value) after Benjamini–Hochberg adjustment were considered to be significantly differentially expressed and of these, only genes with a \log_2 fold change ≥ 2 were plotted.

5.2.8 Locomotion assay

Preparation of larvae

For assessing changes in the swimming behaviour of *pomt1*^{*Y33(ins)*}, *pomt2*^{*S56(ins)*}, *dag1*^{*T330M*} and *dag1*^{*Q410X/T330M*} mutants, as well as *pomt2*^{*D92G*} and *dag1*^{*T330A/T408I*} editants a medium-throughput assay of swimming behaviour was performed. Hatchlings were fed twice daily and raised to 2 dph. Typically, a transparent 24-well plate was used. For *pomt2*^{*D92G*} editants a back-walled 24 Well Plate with #1.5 glass-like polymer coverslip bottom was used. Larvae were transferred to individual wells and 1xERM was added to 1.2 ml. The 24-well plate was then transferred to a 28°C incubator for at least 3 hours to acclimatise larvae.

Tracking and assay set-up

Tracking of the swimming behaviour and distance quantification was performed with a DanioVision system coupled on-line to a PC running the EthoVision XT 16.0 tracking software. The temperature control unit was set to 28°C. The desktop power supply of the Top light unit was set to 16.3 V (0.3 A). The 24-well plate containing the larvae was transferred, without lid, to the observation chamber of the DanioVision system. Assay parameters were adjusted for medaka larvae from a previously published protocol [Zada et al., 2019]: 30 fps; dynamic subtraction was used as detection method with “subject is darker than background”, dark contrast: 5-100, frame weight = 1, Video Pixel Smoothing = Medium, Detection Reference Image = ”Background” → “Start learning (C)”, wait 10 sec → “Stop learning (C)” → close. Unless otherwise stated the following loop was defined for the “constant top light assay”

in the Trial control settings: Rule Begin:Start-stop trial → Action:Top light ON → Condition: After a time of 15 min → Action:Start track → Action:Top light ON → Condition: After a time of 30 min → Action:Stop track → Rule End:Start-stop trial. Unless otherwise stated the following loop was defined for the “stress routine assay” in the Trial control settings: Begin:Start-stop trial → Action:Start track → 15 min loop [Action:Top light ON → Condition: After a time of 10 sec → Action:Top light OFF → Condition: After a time of 10 sec → Action:Top light ON → (...)] → Action:Stop track → Rule End:Start-stop trial.

The two assays were set up consecutively in the Trial list as follows: constant top light assay (15 min light adjustment + 30 min constant light tracking) → stress routine assay (15 min stress light tracking). The following data parameters were used for export and subsequent analysis: Total distance travelled, binned to 1 min for the stress routine assay and binned to 5 min for the constant top light assay and the Trial Statistics were saved.

Time-course locomotion assay and analysis

Tracked larvae were either directly used for subsequent analysis (e.g. genotyping / fixation) or raised to 6 dph and 14 dph, maintaining larvae separated. From 2-6 dph larvae were maintained individually in a well of a 6-well plate in Hatch medium and fed twice daily. From 6-14 dph larvae were maintained individually in a 6 cm dish in Hatch medium and fed twice daily. Data was analysed in R and using R studio and total distances were compared using the One-way ANOVA test and Student's T test.

5.2.9 Western blot

***β*-DG and GFP blot on 1 dpf *dag1* crispants**

Sample preparation. Pools of 20x 1 dpf embryos were transferred to 1.5 ml low protein binding microcentrifuge tubes, washed 2x with 500 μ l cold 1x PBS and homogenised with clean 0.5/1.5 ml micro pestles in 500 μ l cold 1x PBS. Tubes were spun down 2 min at 960 x g at 4°C and the supernatant containing yolk protein was carefully removed. Samples were frozen in liquid nitrogen and stored at -80°C until further analysed. The frozen tissue was homogenised in 500 μ l WB homogenisation buffer by incubation for 15 min at 4°C with mild agitation. 50 μ l of WGA agarose in 1:1 slurry per sample were washed 2x with

250 μ l WB homogenisation buffer, thereby collecting the WGA beads gently at 425 x g at 4°C for 5 min, each in a 1.5 ml low protein binding microcentrifuge tube. Homogenised samples were centrifuged at 20,800 x g at 4°C for 5 min to remove cell debris and supernatants were added to the washed WGA beads and incubated overnight at 4°C on a turning wheel. WGA samples were collected at 425 x g at 4°C for 5 min and washed again 3x at 425 x g at 4°C for 5 min with 1 ml WB wash buffer. The buffer was completely removed and 20 μ l 2.5x Laemmli buffer were added and samples were incubated at 60°C for 3 min. WGA beads were collected at 20,800 x g, 1 min and the supernatant was transferred to a 1.5 ml low protein binding microcentrifuge tube. Samples were stored at -20°C.

SDS-PAGE. A SDS / discontinuous polyacrylamide (PAA) gel was run using the 4-20% Mini-PROTEAN TGX precast protein gels. Samples were incubated at 60°C for 3 min and 15x embryo equivalents (15 μ l) were loaded individually as well as 10 μ l Precision Plus Protein Standards. Empty wells were loaded with 1x Laemmli buffer. The gel was run in 1x SDS running buffer at 110 V for 30 min and then at 160 V until the 25 kDa marker almost reached the bottom.

Wet blot. The gel apparatus was dismantled, both stacking gel and the lower part of the separating gel were cut away and the gel was incubated 5 min in Transfer buffer. The size of the gel was precisely measured and a Nitrocellulose membrane (0.45 μ m) and 6x Whatman papers were prepared with equal dimensions and then also placed into Transfer buffer for 5 min. The Wet blot was mounted and the samples were blotted for 2 hours at 4°C while stirring, at 100 V (fixed voltage).

Immunoblotting and detection. The blot was carefully disassembled, the membrane was sliced in two pieces just below the 37 kDa marker and washed 3x with 0.5x TBS-T for 5 min. The membrane was then blocked in WB blocking buffer for 30 min with gentle agitation. Immunoblots were then decorated with 1:200 primary mouse anti- β -Dystroglycan antibody or 1:1000 primary rabbit anti-GFP in WB blocking buffer and incubated overnight at 4°C with gentle agitation. The membrane was rinsed 2x with 0.5x TBS-T and then washed 6x with 0.5x TBS-T for 5 min each with gentle agitation. The respective secondary antibodies, 1:5000 HRP-goat anti-mouse or 1:10000 goat anti-rabbit HRP, were incubated for 1 hour in WB blocking buffer with gentle agitation, washed again 6x with 0.5x TBS-T for 5 min each and finally developed using the Super Signal West Femto Chemiluminescent substrate and

imaged using an Advanced fluorescence and ECL Imager.

POMT1 and POMT2 western blots on stage 34 wild-type and homozygous *pomt2*^{Cterm-fs} mutants

Sample preparation. Embryos from wild-type Cab incrosses (=WT samples) and heterozygous *pomt2*^{+/*Cterm-fs*} incrosses were raised to stage 34. Homozygous *pomt2*^{+/*Cterm-fs*} mutants were identified by phenotype (=mutant samples). Embryos of both WT and mutant samples were dechorionated manually, the yolk was pierced, the yolk sac was removed and the embryos were transferred to 1.5 ml low protein binding microcentrifuge tubes containing 1 ml cold 1x PBS. Up to 20x embryos of the same genotype were collected and then centrifuged at 960 *x g* and 4°C for 5 min, washed again with 1 ml cold PBS and centrifuged again to remove remaining yolk. The liquid was completely removed and samples were frozen in liquid nitrogen and stored at -80°C until processed further. 20 WT embryos and 40 mutant embryos were pooled and considered a sample. 3x samples were prepared per genotype. Samples were transferred to a 1 ml narrow-douncer and homogenised thoroughly in 500 μ l HPI buffer, transferred to fresh 1.5 ml low protein binding microcentrifuge tubes and incubated 10 min on ice. Samples were vortexed briefly to obtain a homogenous suspension and centrifuged at 16,000 *x g* and 4°C for 15 min. The pellet was resuspended in 100 μ l HPI buffer by pipetting up and down several times and brief vortexing and then split onto two aliquots of 50 μ l and stored at -80°C until further use.

SDS-PAGE, immunoblotting and detection. Samples were denatured in 5x SDS sample buffer for 5 min at room temperature. 30 μ g protein were loaded onto an 8% SDS PAA gel and the gel was run 10 min at 110 V and then 30 min at 200 V. Nitrocellulose membranes were blotted for 75 min at 100 V and sliced just below the 55 kDa marker. The membranes were blocked for 1 hour with 5% milk in 1x TBS-T and incubated with the first primary antibody rabbit anti-POMT2 [Willer et al., 2002] at 1:250 (upper slice) in 5% milk in 1x TBS-T or 1:2000 rabbit anti-Sec61 overnight at 4°C. The membrane was washed 3x with 1x TBS-T and incubated with 1:10,000 secondary anti-rabbit HRP antibody in 5% milk in 1x TBS-T for 1 hour at room temperature. The membrane was washed again 3x with 1x TBS-T and detected using the Amersham ECL select substrate for POMT2 or the Amersham ECL prime substrate for Sec61. The upper slice was then stripped for 15 min in Stripping buffer, washed 3x with 1x TBS-T and then re-blocked, the second primary

rabbit anti-POMT1 antibody incubated 1:500 in 5% milk in 1x TBS-T overnight at 4°C. Washes and secondary antibody incubation as well as detection were repeated as before.

5.2.10 Immunohistochemistry

Wholemout immunohistochemistry

Fixed samples stored in 1% PFA/1x PTw were washed 3x for 10 min with 1x PTw. Alternatively, samples dehydrated in ethanol were rehydrated sequentially by transfer from ethanol to 75% ethanol (in H₂O), to 50% ethanol (in H₂O), to 25% ethanol (in H₂O), and finally to 1x PTw, each for 5 min at room temperature. Samples were then washed 3x more for 5 min with 1x PTw. For permeabilisation, tail or head samples were incubated in pre-cooled acetone for 12 min at -20°C in 1.5 ml microfuge tubes. Samples were rinsed 2x with H₂O, transferred to 6-well plates and washed 2x 5 min in 1x PTw on a horizontal shaker. Samples were transferred to 1.5 ml microfuge tubes and blocked with 1 ml wholemount blocking buffer on a rotating arm (no overhead rotation) for 2 hours. Samples were transferred to a PCR tube and incubated in primary antibodies diluted in wholemount blocking buffer for 3 nights at 4°C on a tube revolver. The primary antibody solution was removed by washing 6x for 30 min, each in 1x PTw in a 6-well plate on a horizontal shaker at room temperature. Samples were transferred to a new PCR tube and incubated with secondary antibodies and DAPI (1:500 dilution) in wholemount blocking buffer overnight at 4°C on a tube revolver in the dark. The secondary antibody solution was removed by washing 6x for 30 min, each in 1x PTw in a 6-well plate on a horizontal shaker at room temperature in the dark. Until imaging, samples were stored in 1% PFA/1x PTw at 4°C in the dark. For imaging, the samples were mounted in 1% low melting agarose in 1x PBS on glass-bottom dishes.

Phalloidin staining on wholemount samples

Phalloidin (AF647) stainings on wholemount samples were performed after secondary antibody washes. In brief, the required volume of phalloidin stock was transferred to a reaction tube and the methanol was left to evaporate in the dark. Phalloidin was then diluted 1:50 in 1x PTw and applied to the samples for 4 hours at room temperature in the dark. The samples were then rinsed with 1x PTw and stored or mounted as described above.

TUNEL staining on wholemount samples

TUNEL stainings on wholemount samples were performed after secondary antibody washes. Samples were permeabilised in 10 $\mu\text{g}/\text{ml}$ Proteinase K / 1x PTw solution without agitation and re-fixed in 4% PFA / 1x PTw for 20 min at room temperature. Samples were washed 4x 5 min with 1x PTw in a 6-well plate and permeabilised with 33% acetone/67% ethanol at -20°C in a 1.5 ml microfuge tube. Samples were rinsed 2x with 1x PTw and transferred to a 0.2 ml PCR tube. The TUNEL reaction mix from the In situ Cell Death Detection Kit, TMR red was prepared by mixing 90 μl Label Solution with 10 μl Enzyme Solution, gently mixing the solution and incubating the samples with the TUNEL mix for 2 hours at 37°C in the dark. Samples were washed 3x 5 min with 1x PTw in the dark and stored and mounted as described above.

Immunohistochemistry on cryosections

Fixed samples were washed 5x 5 min each with 1x PTw and cryoprotected in 30% sucrose in 1x PTw at 4°C for ≥ 3 days. To improve section quality the samples were then incubated in a 50:50 mixture of 30% sucrose and Tissue Freezing Medium for ≥ 3 days at 4°C . Heads were mounted in mounting molds that were halfway filled with Tissue Freezing Medium, with the mouth facing down towards the bottom of the mold. Samples were frozen in liquid nitrogen and equilibrated in the cryostat. Mounting molds were filled up with Tissue Freezing Medium and solidified again in the cryostat. 16 μm (for all samples until 6 dph) or 20 μm (for 14 dph samples) serial sections were obtained on a cryostat, collected on Superfrost Plus slides and dried overnight in the dark at 4°C . The sections were then rehydrated in 1x PTw for 30 min at room temperature in a humidified pipette tip box. During all subsequent incubation steps, sections were covered with Parafilm. Blocking was performed for 2 hours with 10% NGS in 1x PTw at room temperature. The blocking solution was removed by washing 2x 5 min with 1x PTw. The respective primary antibodies were in the corresponding dilution in 1% NGS overnight to 3x overnight at 4°C . To remove residual, unbound primary antibody sections were washed 6x 10 min with 1x PTw. The secondary antibody was applied in 1% NGS together with DAPI (1:500 dilution) for 2 hours at 37°C in the dark. Unbound secondary antibody was washed off 3x 10 min with 1x PTw in the dark. 60 μl of 60% glycerol was then added to mount the slides, after which the coverslip was lowered slowly and sealed with nail polish. The slides were then kept at 4°C in the dark until imaging.

Phalloidin staining on cryosections

Phalloidin (AF647) stainings on cryosections were performed after secondary antibody washes and before sealing the slides. In brief, the required volume of phalloidin stock was transferred to a reaction tube and the methanol was left to evaporate in the dark. Phalloidin was then diluted 1:100 in 1xPTw and applied to slides for 30 min at room temperature in the dark, followed by one 5 min wash with 1xPTw in the dark and mounted and stored as described above.

TUNEL staining on cryosections

TUNEL stainings on cryosections were performed after secondary antibody washes and before sealing the slides. In brief, sections were re-fixed in 4% PFA / 1xPTw for 20 min at room temperature. Slides were washed 3x 10 min with 1xPTw. The slides were then incubated in Permeabilisation solution in microscope slide jars on ice for 2 min, rinsed 2x with 1xPTw and transferred back to the humidified pipette tip box. The TUNEL reaction mix from the In situ Cell Death Detection Kit, TMR red was prepared by mixing 45 μ l Label Solution with 5 μ l Enzyme Solution, gently mixing the solution and incubating the slides with the TUNEL mix covered with Parafilm for 1 hour at 37°C in the dark. Slides were washed 3x 10 min with 1xPTw in the dark and mounted and stored as described above.

5.2.11 Microscopy

Gross morphology and heart dynamics of embryos were assessed with a **Nikon SMZ18 Stereomicroscope** (Nikon) equipped with or without a Nikon DS-Ri1 camera. The colourimetric in situ hybridisations were imaged under a **Leica DIC DB5000 microscope** with 5x (dry) and 20x (dry) objectives (Leica). All **immunohistochemistry stainings** (cryosections and whole-mount) were acquired using the inverted confocal laser scanning microscope **Leica TCS Sp8** (ACS APO objective lenses: 10x/0.30 dry, 20x/0.75 multi-immersion, and 63x/1.30 glycerol; laser lines: 405 nm, 488 nm, 532 nm and 638 nm) imaged using matching laser and PMT settings. The acquisition using the Leica Application Suite Software was adjusted to avoid overexposure. *In vivo* imaging of hearts of medaka embryos experiments were performed as previously described [Cornean et al., 2022] with a **Leica TCS Sp8**.

5.2.12 Analysis, visualisation and writing

Image and data analysis

Images were processed with the Fiji distribution of ImageJ (v.2.0.0-rc-69/1.52n) [Schindelin et al., 2012], including adjustments in brightness and contrast. Analysis and graphical data visualization were performed, unless otherwise stated, in R (v.3.6.3) [R Core Team, 2020] (<https://www.R-project.org/>) using the RStudio IDE with the following packages: Tidyverse [Wickham et al., 2019], ggplot2 [Wickham, 2016], ggpubr [Kassambara, 2020], plyr [Wickham, 2011], dplyr [Wickham et al., 2020], matrixStats [Bengtsson, 2021], cowplot [Wilke, 2020] and viridis [Garnier et al., 2021]. Sample size (n) and statistical tests are provided in the respective figure/figure legend or the main text. If not otherwise stated provided values were given as mean±standard deviation.

Figure assembly

All figures presented in this work were composed in Adobe Illustrator (v.23.1.1). Images (.tiff) and plots (.pdf) obtained from external programs were embedded into the Illustrator canvas, cropped and resized if necessary. Graphical elements of plots (line size, font size) were adapted to improve aesthetics. Images or plots were not modified in any way to falsify any of the presented content or leave room for misinterpretation.

Thesis writing

This thesis was written in Microsoft Word for Mac (v.16.16.27) and assembled and typeset in L^AT_EX(pdfTeX 3.14159265-2.6-1.40.19; TeX Live 2018; kpathsea version 6.3.0) using Texmaker 5.0.2. Referencing was preformed in L^AT_EX with the eLife citation format using BibTeX files compiled in Mendeley Dektop (v1.19.8).

6

References

- Akasaka-Manyá K**, Manyá H, Endo T. Mutations of the POMT1 gene found in patients with Walker-Warburg syndrome lead to a defect of protein O-mannosylation. *Biochemical and Biophysical Research Communications*. 2004; 325(1):75–79. <https://doi.org/10.1016/j.bbrc.2004.10.001>, doi: 10.1016/j.bbrc.2004.10.001.
- Akasaka-Manyá K**, Manyá H, Hayashi M, Endo T. Different roles of the two components of human protein O-mannosyltransferase, POMT1 and POMT2. *Biochemical and Biophysical Research Communications*. 2011; 411(4):721–725. <http://dx.doi.org/10.1016/j.bbrc.2011.07.012>, doi: 10.1016/j.bbrc.2011.07.012.
- Akasaka-Manyá K**, Manyá H, Nakajima A, Kawakita M, Endo T. Physical and functional association of human protein O-mannosyltransferases 1 and 2. *Journal of Biological Chemistry*. 2006; 281(28):19339–19345. <http://dx.doi.org/10.1074/jbc.M601091200>, doi: 10.1074/jbc.M601091200.
- Andrews S**, FastQC: A Quality Control Tool for High Throughput Sequence Data [Online].; 2010. <http://www.bioinformatics.babraham.ac.uk/projects/fastqc/>.
- Anzalone AV**, Koblan LW, Liu DR. Genome editing with CRISPR–Cas nucleases, base editors, transposases and prime editors. *Nature Biotechnology*. 2020; 38(7):824–844. <https://doi.org/10.1038/s41587-020-0561-9>, doi: 10.1038/s41587-020-0561-9.
- Anzalone AV**, Randolph PB, Davis JR, Sousa AA, Koblan LW, Levy JM, Chen PJ, Wilson C, Newby GA, Raguram A, Liu DR. Search-and-replace genome editing without double-strand breaks or donor DNA. *Nature*. 2019; 576(7785):149–157. <http://dx.doi.org/10.1038/s41586-019-1711-4>, doi: 10.1038/s41586-019-1711-4.
- Arbab M**, Shen MW, Mok B, Wilson C, Matuszek Ż, Cassa CA, Liu DR. Determinants of Base Editing Outcomes from Target Library Analysis and Machine Learning. *Cell*. 2020; 182(2):463–480.e30. <https://doi.org/10.1016/j.cell.2020.05.037>, doi: 10.1016/j.cell.2020.05.037.
- Arnaut R**, Ferrer T, Huisken J, Spitzer K, Stainier DYR, Tristani-Firouzi M, Chi NC. Zebrafish model for human long QT syndrome. *Proceedings of the National Academy of Sciences*. 2007 jul; 104(27):11316 LP – 11321. <http://www.pnas.org/content/104/27/11316.abstract>, doi: 10.1073/pnas.0702724104.
- Avşar-Ban E**, Ishikawa H, Manyá H, Watanabe M, Akiyama S, Miyake H, Endo T, Tamaru Y. Protein O-mannosylation is necessary for normal embryonic development

-
- in zebrafish. *Glycobiology*. 2010; 20(9):1089–1102. <https://doi.org/10.1093/glycob/cwq069>, doi: 10.1093/glycob/cwq069.
- Bai L**, Kovach A, You Q, Kenny A, Li H. Structure of the eukaryotic protein O-mannosyltransferase Pmt1Pmt2 complex. *Nature Structural and Molecular Biology*. 2019; 26(8):704–711. <http://dx.doi.org/10.1038/s41594-019-0262-6>, doi: 10.1038/s41594-019-0262-6.
- Balci B**, Uyanik G, Dincer P, Gross C, Willer T, Talim B, Haliloglu G, Kale G, Hehr U, Winkler J, Topaloğlu H. An autosomal recessive limb girdle muscular dystrophy (LGMD2) with mild mental retardation is allelic to Walker-Warburg syndrome (WWS) caused by a mutation in the POMT1 gene. *Neuromuscular Disorders*. 2005; 15(4):271–275. <https://doi.org/10.1016/j.nmd.2005.01.013>, doi: 10.1016/j.nmd.2005.01.013.
- Barrangou R**, Fremaux C, Deveau H, Richards M, Boyaval P, Moineau S, Romero DA, Horvath P. CRISPR Provides Acquired Resistance Against Viruses in Prokaryotes. *Science*. 2007; 315(5819):1709–1712. <https://www.science.org/doi/abs/10.1126/science.1138140>, doi: 10.1126/science.1138140.
- Barresi R**, Campbell KP. Dystroglycan: From biosynthesis to pathogenesis of human disease. *Journal of Cell Science*. 2006; 119(2):199–207. <https://doi.org/10.1242/jcs.02814>, doi: 10.1242/jcs.02814.
- Bartels MF**, Winterhalter PR, Yu J, Liu Y, Lommel M, Möhrlen F, Hu H, Feizi T, Westerlind U, Ruppert T, Strahl S. Protein O-mannosylation in the murine brain: Occurrence of Mono-O-Mannosyl glycans and identification of new substrates. *PLoS ONE*. 2016; 11(11). <https://doi.org/10.1242/jcs.02814>, doi: 10.1371/journal.pone.0166119.
- Bausewein D**, Engel J, Jank T, Schoedl M, Strahl S. Functional Similarities between the Protein O -Mannosyltransferases Pmt4 from Bakers' Yeast. *The Journal of Biological Chemistry*. 2016; 291(34):18006–18015. <https://doi.org/10.1074/jbc.M116.739128>, doi: 10.1074/jbc.M116.739128.
- Becher B**, Waisman A, Lu LF. Conditional Gene-Targeting in Mice: Problems and Solutions. *Immunity*. 2018; 48(5):835–836. <https://doi.org/10.1016/j.immuni.2018.05.002>, doi: 10.1016/j.immuni.2018.05.002.
- Beltrán-Valero de Bernabé D**, Currier S, Steinbrecher A, Celli J, van Beusekom E, van der Zwaag B, Kayserili H, Merlini L, Chitayat D, Dobyns WB, Cormand B, Lehesjoki AE, Cruces J, Voit T, Walsh CA, van Bokhoven H, Brunner HG. Mutations in the O-Mannosyltransferase Gene POMT1 Give Rise to the Severe Neuronal Migration Disorder Walker-Warburg Syndrome. *The American Journal of Human Genetics*. 2002; 71(5):1033–1043. <https://doi.org/10.1086/342975>, doi: 10.1086/342975.
- Bengtsson H**, matrixStats: Functions that Apply to Rows and Columns of Matrices (and to Vectors); 2021. <https://cran.r-project.org/package=matrixStats>.
- Bensellam M**, Chan JY, Lee K, Joglekar MV, Hardikar AA, Loudovaris T, Thomas HE, Jonas JC, Laybutt DR. Phlda3 regulates beta cell survival during stress. *Scien-*

- tific Reports. 2019; 9(1):1–13. <https://dx.doi.org/10.1038/s41598-019-49289-5>, doi: 10.1038/s41598-019-49289-5.
- Berry ASF**, Amorim CF, Berry CL, Syrett CM, English ED, Beiting DP. An open-source toolkit to expand bioinformatics training in infectious diseases. *mBio*. 2021; 12(4):1–6. <https://doi.org/10.1128/mBio.01214-21>, doi: 10.1128/mBio.01214-21.
- Bert B**, Chmielewska J, Bergmann S, Busch M, Driever W, Finger-Baier K, Hößler J, Köhler A, Leich N, Misgeld T, Nöldner T, Reiher A, Scharl M, Seebach-Sproedt A, Thumberger T, Schönfelder G, Grune B. Considerations for a European animal welfare standard to evaluate adverse phenotypes in teleost fish. *The EMBO Journal*. 2016 jun; 35(11):1151–1154. <https://doi.org/10.15252/embj.201694448>, doi: 10.15252/embj.201694448.
- Biancheri R**, Falace A, Tessa A, Pedemonte M, Scapolan S, Cassandrini D, Aiello C, Rossi A, Broda P, Zara F, Santorelli FM, Minetti C, Bruno C. POMT2 gene mutation in limb-girdle muscular dystrophy with inflammatory changes. *Biochemical and Biophysical Research Communications*. 2007; 363(4):1033–1037. <https://doi.org/10.1016/j.bbrc.2007.09.066>, doi: 10.1016/j.bbrc.2007.09.066.
- Bigotti MG**, Brancaccio A. High degree of conservation of the enzymes synthesizing the laminin-binding glycoepitope of α -dystroglycan. *Open Biology*. 2021; 11(9). <https://doi.org/10.1098/rsob.210104>, doi: 10.1098/rsob.210104.
- Billon P**, Bryant EE, Joseph SA, Nambiar TS, Hayward SB, Rothstein R, Ciccia A. CRISPR-Mediated Base Editing Enables Efficient Disruption of Eukaryotic Genes through Induction of STOP Codons. *Molecular Cell*. 2017; 67(6):1068—1079.e4. <http://dx.doi.org/10.1016/j.molcel.2017.08.008>, doi: 10.1016/j.molcel.2017.08.008.
- Bleckmann C**, Geyer H, Lieberoth A, Splittstoesser F, Liu Y, Feizi T, Schachner M, Kleene R, Reinhold V, Geyer R. O-glycosylation pattern of CD24 from mouse brain. *Biological Chemistry*. 2009; 390(7):627–645. <https://doi.org/10.1515/BC.2009.044>, doi: 10.1515/BC.2009.044.
- Bolotin A**, Quinquis B, Sorokin A, Dusko Ehrlich S. Clustered regularly interspaced short palindrome repeats (CRISPRs) have spacers of extrachromosomal origin. *Microbiology*. 2005; 151(8):2551–2561. <https://doi.org/10.1099/mic.0.28048-0>, doi: 10.1099/mic.0.28048-0.
- Brady S**, Morfini G. A perspective on neuronal cell death signaling and neurodegeneration. *Molecular Neurobiology*. 2010; 42(1):25–31. doi: 10.1007/s12035-010-8128-2.
- Bray NL**, Pimentel H, Melsted P, Pachter L. Near-optimal probabilistic RNA-seq quantification. *Nature Biotechnology*. 2016; 34(5):525–527. doi: 10.1038/nbt.3519.
- Bredesen DE**, Rao RV, Mehlen P. Cell death in the nervous system. *Nature*. 2006; 443(7113):796–802.
- Briggs DC**, Yoshida-Moriguchi T, Zheng T, Venzke D, Anderson ME, Strazzulli A, Moracci M, Yu L, Hohenester E, Campbell KP. Structural basis of laminin binding to the LARGE glycans on dystroglycan. *Nature Chemical Biology*. 2016; 12(10):810–814. <https://doi.org/10.1038/nchembio.2146>, doi: 10.1038/nchembio.2146.

-
- Brooks SA.** Appropriate glycosylation of recombinant proteins for human use: Implications of choice of expression system. *Applied Biochemistry and Biotechnology - Part B Molecular Biotechnology*. 2004; 28(3):241–255. <https://doi.org/10.1385/mb:28:3:241>, doi: 10.1385/MB:28:3:241.
- Brooks SA.** Strategies for analysis of the glycosylation of proteins: Current status and future perspectives. *Molecular Biotechnology*. 2009; 43(1):76–88. <https://doi.org/10.1007/s12033-009-9184-6>, doi: 10.1007/s12033-009-9184-6.
- Buisson N, Sirour C, Moreau N, Denker E, Bouffant RL, Goullancourt A, Darribère T, Bello V, Le Bouffant R, Goullancourt A, Darribère T, Bello V.** An adhesome comprising laminin, dystroglycan and myosin IIA is required during notochord development in *Xenopus laevis*. *Development*. 2014 dec; 141(23):4569–4579. <https://doi.org/10.1242/dev.116103>, doi: 10.1242/dev.116103.
- Burger A, Lindsay H, Felker A, Hess C, Anders C, Chiavacci E, Zaugg J, Weber LM, Catena R, Jinek M, Robinson MD, Mosimann C.** Maximizing mutagenesis with solubilized CRISPR-Cas9 ribonucleoprotein complexes. *Development (Cambridge)*. 2016; 143(11):2025–2037. <https://doi.org/10.1242/dev.134809>, doi: 10.1242/dev.134809.
- Burgoyne LA.** The Mechanisms of Pyknosis: Hypercondensation and Death. *Experimental Cell Research*. 1999; 248(1):214–222. <https://doi.org/10.1006/excr.1999.4406>, doi: 10.1006/excr.1999.4406.
- Carrington B, Weinstein RN, Sood R.** BE4max and AncBE4max Are Efficient in Germline Conversion of C:G to T:A Base Pairs in Zebrafish. *Cells*. 2020 jul; 9(7):1690. <https://www.mdpi.com/2073-4409/9/7/1690>, doi: 10.3390/cells9071690.
- Chai W, Yuen CT, Kogelberg H, Carruthers RA, Margolis RU, Feizi T, Lawson AM.** High prevalence of 2-mono- and 2,6-di-substituted manol-terminating sequences among O-glycans released from brain glycopeptides by reductive alkaline hydrolysis. *European Journal of Biochemistry*. 1999; 263(3):879–888. <https://doi.org/10.1046/j.1432-1327.1999.00572.x>, doi: 10.1046/j.1432-1327.1999.00572.x.
- Chen J.** Impaired cardiovascular function caused by different stressors elicits a common pathological and transcriptional response in zebrafish embryos. *Zebrafish*. 2013; 10(3):389–400. <https://www.liebertpub.com/doi/10.1089/zeb.2013.0875>, doi: 10.1089/zeb.2013.0875.
- Chen L, Park JE, Paa P, Rajakumar PD, Prekop HT, Chew YT, Manivannan SN, Chew WL.** Programmable C:G to G:C genome editing with CRISPR-Cas9-directed base excision repair proteins. *Nature Communications*. 2021; 12(1). <http://dx.doi.org/10.1038/s41467-021-21559-9>, doi: 10.1038/s41467-021-21559-9.
- Chen S, Liu Z, Lai L, Li Z.** Efficient C-to-G Base Editing with Improved Target Compatibility Using Engineered Deaminase-nCas9 Fusions. *The CRISPR journal*. 2022; 5(2):1–8. <http://www.ncbi.nlm.nih.gov/pubmed/35238619>, doi: 10.1089/crispr.2021.0124.
- Cheung EV, Tidball JG.** Administration of the non-steroidal anti-inflammatory drug ibuprofen increases macrophage concentrations but reduces necrosis during

- modified muscle use. *Inflammation Research*. 2003; 52(4):170–176. <https://doi.org/10.1007/s000110300068>, doi: 10.1007/s000110300068.
- Chiapparino A**, Grbavac A, Jonker HRA, Hackmann Y, Mortensen S, Zatorska E, Schott A, Stier G, Saxena K, Wild K, Schwalbe H, Strahl S, Sinning I. Functional implications of mir domains in protein O-mannosylation. *eLife*. 2020; 9:1–23. <https://doi.org/10.7554/eLife.61189>, doi: 10.7554/eLife.61189.
- Chiba A**, Matsumura K, Yamada H, Inazu T, Shimizu T, Kusunoki S, Kanazawa I, Kobata A, Endo T. Structures of sialylated O-linked oligosaccharides of bovine peripheral nerve α -dystroglycan. The role of a novel O-mannosyl-type oligosaccharide in the binding of α -dystroglycan with laminin. *Journal of Biological Chemistry*. 1997; 272(4):2156–2162. <https://doi.org/10.1074/jbc.272.4.2156>, doi: 10.1074/jbc.272.4.2156.
- Chomczynski P**. A reagent for the single-step simultaneous isolation of RNA, DNA and proteins from cell and tissue samples. *BioTechniques*. 1993 sep; 15(3):532–4, 536–7. <http://europepmc.org/abstract/MED/7692896>.
- Chowdhury K**, Lin S, Lai SL. Comparative Study in Zebrafish and Medaka Unravels the Mechanisms of Tissue Regeneration. *Frontiers in Ecology and Evolution*. 2022; 10(February):1–27. <https://doi.org/10.3389/fevo.2022.783818>, doi: 10.3389/fevo.2022.783818.
- Clement E**, Mercuri E, Godfrey C, Smith J, Robb S, Kinali M, Straub V, Bushby K, Manzur A, Talim B, Cowan F, Quinlivan R, Klein A, Longman C, McWilliam R, Topaloglu H, Mein R, Abbs S, North K, Barkovich AJ, et al. Brain involvement in muscular dystrophies with defective dystroglycan glycosylation. *Annals of Neurology*. 2008 nov; 64(5):573–582. <https://doi.org/10.1002/ana.21482>, doi: 10.1002/ana.21482.
- Clement K**, Rees H, Canver MC, Gehrke JM, Farouni R, Hsu JY, Cole MA, Liu DR, Joung JK, Bauer DE, Pinello L. CRISPResso2 provides accurate and rapid genome editing sequence analysis. *Nature Biotechnology*. 2019; 37(3):224–226. <https://doi.org/10.1038/s41587-019-0032-3>, doi: 10.1038/s41587-019-0032-3.
- Clements R**, Turk R, Campbell KP, Wright KM. Dystroglycan Maintains Inner Limiting Membrane Integrity to Coordinate Retinal Development. *The Journal of Neuroscience*. 2017 aug; 37(35):8559 LP – 8574. <http://www.jneurosci.org/content/37/35/8559.abstract>, doi: 10.1523/JNEUROSCI.0946-17.2017.
- Cohn RD**, Henry MD, Michele DE, Barresi R, Saito F, Moore SA, Flanagan JD, Skwarchuk MW, Robbins ME, Mendell JR, Williamson RA, Campbell KP. Disruption of *Dag1* in differentiated skeletal muscle reveals a role for dystroglycan in muscle regeneration. *Cell*. 2002; 110(5):639–648. [https://doi.org/10.1016/S0092-8674\(02\)00907-8](https://doi.org/10.1016/S0092-8674(02)00907-8), doi: 10.1016/S0092-8674(02)00907-8.
- Cong L**, Ran FA, Cox D, Lin S, Barretto R, Habib N, Hsu PD, Wu X, Jiang W, Marraffini LA, Zhang F. Multiplex Genome Engineering Using CRISPR/Cas Systems. *Science*. 2013; 339(6121):819–823. <https://www.science.org/doi/abs/10.1126/science.1231143>, doi: 10.1126/science.1231143.

-
- Cornean A.** Establishing Tools for the study of protein O-mannosylation in vertebrate development. Master's thesis, Heidelberg University; 2017.
- Cornean A,** Gierten J, Welz B, Mateo JL, Thumberger T, Wittbrodt J. Precise in vivo functional analysis of DNA variants with base editing using ACEofBASEs target prediction. *eLife*. 2022 apr; 11:e72124. <https://doi.org/10.7554/eLife.72124>, doi: 10.7554/eLife.72124.
- Cunningham F,** Allen JE, Allen J, Alvarez-Jarreta J, Amode MR, Armean IM, Austine-Orimoloye O, Azov AG, Barnes I, Bennett R, Berry A, Bhai J, Bignell A, Billis K, Boddu S, Brooks L, Charkhchi M, Cummins C, Da Rin Fioretto L, Davidson C, et al. Ensembl 2022. *Nucleic Acids Research*. 2022; 50(D1):D988–D995. <https://doi.org/10.1093/nar/gkab1049>, doi: 10.1093/nar/gkab1049.
- Daghsni M,** Aldiri I. Building a Mammalian Retina: An Eye on Chromatin Structure. *Frontiers in Genetics*. 2021; 12(October):1–13. <https://doi.org/10.3389/fgene.2021.775205>, doi: 10.3389/fgene.2021.775205.
- De Bruijn SE,** Verbakel SK, De Vrieze E, Kremer H, Cremers FPMM, Hoyng CB, van den Born LI, Roosing S, Ingeborgh Van Den Born L, Roosing S, van den Born LI, Roosing S. Homozygous variants in KIAA1549, encoding a ciliary protein, are associated with autosomal recessive retinitis pigmentosa. *Journal of Medical Genetics*. 2018; 55(10):705–712. <https://jmg.bmj.com/content/55/10/705>, doi: 10.1136/jmedgenet-2018-105364.
- Dekkers MPJ,** Nikolettou V, Barde YA. Death of developing neurons: New insights and implications for connectivity. *Journal of Cell Biology*. 2013; 203(3):385–393. doi: 10.1083/jcb.201306136.
- Devisme L,** Bouchet C, Gonzals M, Alanio E, Bazin A, Bessires B, Bigi N, Blanchet P, Bonneau D, Bonnires M, Bucourt M, Carles D, Clarisse B, Delahaye S, Fallet-Bianco C, Figarella-Branger D, Gaillard D, Gasser B, Delezoide AL, Guimiot F, et al. Cobblestone lissencephaly: Neuropathological subtypes and correlations with genes of dystroglycanopathies. *Brain*. 2012; 135(2):469–482. <https://doi.org/10.1093/brain/awr357>, doi: 10.1093/brain/awr357.
- Dobyns WB,** Pagon RA, Armstrong D, Curry CJR, Greenberg F, Grix A, Holmes LB, Laxova R, Michels VV, Robinow M, Zimmerman RL, Opitz JM, Reynolds JF. Diagnostic criteria for Walker-Warburg syndrome. *American Journal of Medical Genetics*. 1989 feb; 32(2):195–210. <https://doi.org/10.1002/ajmg.1320320213>, doi: <https://doi.org/10.1002/ajmg.1320320213>.
- Doman JL,** Raguram A, Newby GA, Liu DR. Evaluation and minimization of Cas9-independent off-target DNA editing by cytosine base editors. *Nature Biotechnology*. 2020; 38(5):620–628. <http://dx.doi.org/10.1038/s41587-020-0414-6>, doi: 10.1038/s41587-020-0414-6.
- Durinck S,** Spellman PT, Birney E, Huber W. Mapping identifiers for the integration of genomic datasets with the R/ Bioconductor package biomaRt. *Nature Protocols*. 2009; 4(8):1184–1191. <https://doi.org/10.1038/nprot.2009.97>, doi: 10.1038/nprot.2009.97.
- Dwyer CA,** Baker E, Hu H, Matthews RT. RPTP ζ /phosphacan is abnormally

- glycosylated in a model of muscle-eye-brain disease lacking functional POMGnT1. *Neuroscience*. 2012; 220:47–61. <https://doi.org/10.1016/j.neuroscience.2012.06.026>, doi: 10.1016/j.neuroscience.2012.06.026.
- El-Brolosy MA**, Kontarakis Z, Rossi A, Kuenne C, Günther S, Fukuda N, Kikhi K, Boezio GLM, Takacs CM, Lai SL, Fukuda R, Gerri C, Giraldez AJ, Stainier DYR. Genetic compensation triggered by mutant mRNA degradation. *Nature*. 2019; 568(7751):193–197. doi: 10.1038/s41586-019-1064-z.
- Ellis K**, Bagwell J, Bagnat M. Notochord vacuoles are lysosome-related organelles that function in axis and spine morphogenesis. *Journal of Cell Biology*. 2013; 200(5):667–679. <https://doi.org/10.1083/jcb.201212095>, doi: 10.1083/jcb.201212095.
- Endo T**. O-Mannosyl glycans in mammals. *Biochimica et Biophysica Acta (BBA) - General Subjects*. 1999; 1473(1):237–246. <https://www.sciencedirect.com/science/article/pii/S0304416599001828>, doi: [https://doi.org/10.1016/S0304-4165\(99\)00182-8](https://doi.org/10.1016/S0304-4165(99)00182-8).
- Endo T**. Glycobiology of α -dystroglycan and muscular dystrophy. *Journal of Biochemistry*. 2015; 157(1):1–12. <https://doi.org/10.1093/jb/mvu066>, doi: 10.1093/jb/mvu066.
- Ervasti JM**, Campbell KP. A role for the dystrophin-glycoprotein complex as a transmembrane linker between laminin and actin. *Journal of Cell Biology*. 1993; 122(4):809–823. <https://doi.org/10.1083/jcb.122.4.809>, doi: 10.1083/jcb.122.4.809.
- Ewels P**, Magnusson M, Lundin S, Källner M. MultiQC: Summarize analysis results for multiple tools and samples in a single report. *Bioinformatics*. 2016; 32(19):3047–3048. <https://doi.org/10.1093/bioinformatics/btw354>, doi: 10.1093/bioinformatics/btw354.
- Ferreira da Silva J**, Oliveira GP, Arasa-Verge EA, Kagiou C, Moretton A, Timelthaler G, Jiricny J, Loizou JL. Prime editing efficiency and fidelity are enhanced in the absence of mismatch repair. *Nature Communications*. 2022; 13(1):1–11. <https://doi.org/10.1038/s41467-022-28442-1>, doi: 10.1038/s41467-022-28442-1.
- Freeze HH**, Eklund EA, Ng BG, Patterson MC. Neurological Aspects of Human Glycosylation Disorders. *Annual Review of Neuroscience*. 2015; 38:105–125. <https://doi.org/10.1146/annurev-neuro-071714-034019>, doi: 10.1146/annurev-neuro-071714-034019.
- Fu JL**, Kanno T, Liang SC, Matzke AJM, Matzke M. GFP Loss-of-Function Mutations in *Arabidopsis thaliana*. *G3: Genes|Genomes|Genetics*. 2015 sep; 5(9):1849–1855. <http://www.g3journal.org/content/5/9/1849.abstract>, doi: 10.1534/g3.115.019604.
- Furutani-Seiki M**, Wittbrodt J. Medaka and zebrafish, an evolutionary twin study. *Mechanisms of Development*. 2004; 121(7-8):629–637. <https://doi.org/10.1016/j.mod.2004.05.010>, doi: 10.1016/j.mod.2004.05.010.
- Ganz J**, Kaslin J, Freudenreich D, Machate A, Geffarth M, Brand M. Subdivisions

-
- of the adult zebrafish subpallium by molecular marker analysis. *Journal of Comparative Neurology*. 2011; 520(3):633–655. <https://doi.org/10.1002/cne.22757>, doi: 10.1002/cne.22757.
- Garnier S**, Ross N, Rudis R, Camargo PA, Sciaini M, Scherer C, viridis - Colorblind-Friendly Color Maps for R; 2021. <https://sjmgarnier.github.io/viridis/>, doi: 10.5281/zenodo.4679424.
- Gasiunas G**, Barrangou R, Horvath P, Siksnyš V. Cas9-crRNA ribonucleoprotein complex mediates specific DNA cleavage for adaptive immunity in bacteria. *Proceedings of the National Academy of Sciences of the United States of America*. 2012; 109(39):2579–2586. <https://doi.org/10.1073/pnas.1208507109>, doi: 10.1073/pnas.1208507109.
- Gaudelli NM**, Komor AC, Rees HA, Packer MS, Badran AH, Bryson DI, Liu DR. Programmable base editing of A•T to G•C in genomic DNA without DNA cleavage. *Nature*. 2017; 551(7681):464–471. <https://doi.org/10.1038/nature24644>, doi: 10.1038/nature24644.
- Gee SH**, Montanaro F, Lindenbaum MH, Carbonetto S. Dystroglycan-x3b1; a dystrophin-associated glycoprotein, is a functional agrin receptor. *Cell*. 1994 jun; 77(5):675–686. [https://doi.org/10.1016/0092-8674\(94\)90052-3](https://doi.org/10.1016/0092-8674(94)90052-3), doi: 10.1016/0092-8674(94)90052-3.
- Geis T**, Rödl T, Topaloğlu H, Balci-Hayta B, Hinreiner S, Müller-Felber W, Schoser B, Mehraein Y, Hübner A, Zirn B, Hoopmann M, Reutter H, Mowat D, Schuierer G, Schara U, Hehr U, Kölbel H. Clinical long-time course, novel mutations and genotype-phenotype correlation in a cohort of 27 families with POMT1-related disorders. *Orphanet Journal of Rare Diseases*. 2019; 14(1):1–17. <https://doi.org/10.1186/s13023-019-1119-0>, doi: 10.1186/s13023-019-1119-0.
- Gentzsch M**, Immervoll T, Tanner W. Protein O-glycosylation in *Saccharomyces cerevisiae*: the protein O-mannosyltransferases Pmt1p and Pmt2p function as heterodimer. *FEBS Letters*. 1995; 377(2):128–130. [https://doi.org/10.1016/0014-5793\(95\)01324-5](https://doi.org/10.1016/0014-5793(95)01324-5), doi: 10.1016/0014-5793(95)01324-5.
- Gentzsch M**, Strahl-bolsing S, Tanner W. A new DOL-P-man:protein O-D-mannosyltransferase activity from *Saccharomyces cerevisiae*. *Glycobiology*. 1995; 5(1):77–82. <https://doi.org/10.1093/glycob/5.1.77>, doi: 10.1093/glycob/5.1.77.
- Gentzsch M**, Tanner W. The PMT gene family: Protein O-glycosylation in *saccharomyces cerevisiae* is vital. *EMBO Journal*. 1996; 15(21):5752–5759. <https://doi.org/10.1002/j.1460-2075.1996.tb00961.x>, doi: 10.1002/j.1460-2075.1996.tb00961.x.
- Gierten J**, Pylatiuk C, Hammouda OT, Schock C, Stegmaier J, Wittbrodt J, Gehrig J, Loosli F. Automated high-throughput heartbeat quantification in medaka and zebrafish embryos under physiological conditions. *Scientific Reports*. 2020; 10(1):1–12. <https://doi.org/10.1038/s41598-020-58563-w>, doi: 10.1038/s41598-020-58563-w.
- Girrbach V**, Strahl S. Members of the evolutionarily conserved PMT family of protein O-mannosyltransferases form distinct protein complexes among themselves.

- Journal of Biological Chemistry. 2003; 278(14):12554–12562. <https://doi.org/10.1074/jbc.M212582200>, doi: 10.1074/jbc.M212582200.
- Goddeeris MM**, Wu B, Venzke D, Yoshida-Moriguchi T, Saito F, Matsumura K, Moore SA, Campbell KP. LARGE glycans on dystroglycan function as a tunable matrix scaffold to prevent dystrophy. *Nature*. 2013; 503(7474):136–140. <http://dx.doi.org/10.1038/nature12605>, doi: 10.1038/nature12605.
- Godfrey C**, Clement E, Mein R, Brockington M, Smith J, Talim B, Straub V, Robb S, Quinlivan R, Feng L, Jimenez-Mallebrera C, Mercuri E, Manzur AY, Kinali M, Torelli S, Brown SC, Sewry CA, Bushby K, Topaloglu H, North K, et al. Refining genotype-phenotype correlations in muscular dystrophies with defective glycosylation of dystroglycan. *Brain*. 2007; 130(10):2725–2735. <https://doi.org/10.1093/brain/awm212>, doi: 10.1093/brain/awm212.
- Godfrey C**, Foley AR, Clement E, Muntoni F. Dystroglycanopathies: Coming into focus. *Current Opinion in Genetics and Development*. 2011; 21(3):278–285. <http://dx.doi.org/10.1016/j.gde.2011.02.001>, doi: 10.1016/j.gde.2011.02.001.
- Gomez Toledo A**, Raducu M, Cruces J, Nilsson J, Halim A, Larson G, Rüetschi U, Grahn A. O-mannose and O-N-acetyl galactosamine glycosylation of mammalian α -dystroglycan is conserved in a region-specific manner. *Glycobiology*. 2012; 22(11):1413–1423. <https://doi.org/10.1093/glycob/cws109>, doi: 10.1093/glycob/cws109.
- Götzke H**, Kilisch M, Martínez-Carranza M, Sograte-Idrissi S, Rajavel A, Schlichthaerle T, Engels N, Jungmann R, Stenmark P, Opazo F, Frey S. The ALFA-tag is a highly versatile tool for nanobody-based bioscience applications. *Nature Communications*. 2019; 10(1):1–12. <http://dx.doi.org/10.1038/s41467-019-12301-7>, doi: 10.1038/s41467-019-12301-7.
- Gray RS**, Wilm TP, Smith J, Bagnat M, Dale RM, Topczewski J, Johnson SL, Solnica-Krezel L. Loss of col8a1a function during zebrafish embryogenesis results in congenital vertebral malformations. *Developmental Biology*. 2014; 386(1):72–85. <http://dx.doi.org/10.1016/j.ydbio.2013.11.028>, doi: 10.1016/j.ydbio.2013.11.028.
- Gücüm S**, Sakson R, Hoffmann M, Grote V, Becker C, Pakari K, Beedgen L, Thiel C, Rapp E, Ruppert T, Thumberger T, Wittbrodt J. A patient-based medaka *alg2* mutant as a model for hypo- N -glycosylation. *Development*. 2021; 148(11). <https://doi.org/10.1242/dev.199385>, doi: 10.1242/dev.199385.
- Gupta V**, Kawahara G, Gundry SR, Chen AT, Lencer WI, Zhou Y, Zon LI, Kunkel LM, Beggs AH. The zebrafish *dag1* mutant: A novel genetic model for dystroglycanopathies. *Human Molecular Genetics*. 2011; 20(9):1712–1725. <https://doi.org/10.1093/hmg/ddr047>, doi: 10.1093/hmg/ddr047.
- Gutierrez-Triana JA**, Tavhelidse T, Thumberger T, Thomas I, Wittbrodt B, Kellner T, Anlas K, Tsingos E, Wittbrodt J. Efficient single-copy HDR by 5' modified long dsDNA donors. *eLife*. 2018; 7(6221):1–15. <https://doi.org/10.7554/eLife.39468>, doi: 10.7554/eLife.39468.
- Halpern ME**, Ho RK, Walker C, Kimmel CB. Induction of muscle pioneers and floor plate is distinguished by the zebrafish no tail mutation. *Cell*. 1993; 75(1):99–

-
111. [https://doi.org/10.1016/S0092-8674\(05\)80087-X](https://doi.org/10.1016/S0092-8674(05)80087-X), doi: 10.1016/S0092-8674(05)80087-X.
- Haltiwanger RS**, Lowe JB. Role of glycosylation in development. *Annual Review of Biochemistry*. 2004; 73:491–537. <https://doi.org/10.1146/annurev.biochem.73.011303.074043>, doi: 10.1146/annurev.biochem.73.011303.074043.
- Hammouda OT**, Wu MY, Kaul V, Gierten J, Thumberger T, Wittbrodt J. In vivo identification and validation of novel potential predictors for human cardiovascular diseases. *PLOS ONE*. 2021 dec; 16(12):e0261572. <https://doi.org/10.1371/journal.pone.0261572>, doi: 10.1371/journal.pone.0261572.
- Han R**, Kanagawa M, Yoshida-Moriguchi T, Rader EP, Ng RA, Michele DE, Muirhead DE, Kunz S, Moore SA, Iannaccone ST, Miyake K, McNeil PL, Mayer U, Oldstone MBA, Faulkner JA, Campbell KP. Basal lamina strengthens cell membrane integrity via the laminin G domain-binding motif of α -dystroglycan. *Proceedings of the National Academy of Sciences of the United States of America*. 2009; 106(31):12573–12579. <https://doi.org/10.1073/pnas.0906545106>, doi: 10.1073/pnas.0906545106.
- Hang J**, Wang J, Lu M, Xue Y, Qiao J, Tao L. Protein O-mannosylation across kingdoms and related diseases: From glycobiology to glycopathology. *Biomedicine and Pharmacotherapy*. 2022; 148(February):112685. <https://doi.org/10.1016/j.biopha.2022.112685>, doi: 10.1016/j.biopha.2022.112685.
- Hara Y**, Kanagawa M, Kunz S, Yoshida-Moriguchi T, Satz JS, Kobayashi YM, Zhu Z, Burden SJ, Oldstone MBAA, Campbell KP. Like-acetylglucosaminyltransferase (LARGE)-dependent modification of dystroglycan at Thr-317/319 is required for laminin binding and arenavirus infection. *Proceedings of the National Academy of Sciences*. 2011 oct; 108(42):17426 LP – 17431. <http://www.pnas.org/content/108/42/17426.abstract>, doi: 10.1073/pnas.1114836108.
- Haselbeck A**, Tanner W. O-Glycosylation in *Saccharomyces cerevisiae* is initiated at the endoplasmic reticulum. *FEBS Letters*. 1983; 158(2):335–338. [https://doi.org/10.1016/0014-5793\(83\)80608-5](https://doi.org/10.1016/0014-5793(83)80608-5), doi: 10.1016/0014-5793(83)80608-5.
- Hassel D**, Scholz EP, Trano N, Friedrich O, Just S, Meder B, Weiss DL, Zitron E, Marquart S, Vogel B, Karle CA, Seemann G, Fishman MC, Katus HA, Rotbauer W. Deficient zebrafish ether-à-go-go-related gene channel gating causes short-QT syndrome in zebrafish reggae mutants. *Circulation*. 2008; 117(7):866–875. <https://doi.org/10.1161/CIRCULATIONAHA.107.752220>, doi: 10.1161/CIRCULATIONAHA.107.752220.
- Holt KH**, Crosbie RH, Venzke DP, Campbell KP. Biosynthesis of dystroglycan: Processing of a precursor propeptide. *FEBS Letters*. 2000; 468(1):79–83. [https://doi.org/10.1016/S0014-5793\(00\)01195-9](https://doi.org/10.1016/S0014-5793(00)01195-9), doi: 10.1016/S0014-5793(00)01195-9.
- Hoshijima K**, Jurynek MJ, Grunwald DJ. Precise Editing of the Zebrafish Genome Made Simple and Efficient. *Developmental Cell*. 2016; 36(6):654–667. <http://dx.doi.org/10.1016/j.devcel.2016.02.015>, doi: 10.1016/j.devcel.2016.02.015.
- Hoshijima K**, Jurynek MJ, Klatt Shaw D, Jacobi AM, Behlke MA, Grunwald DJ. Highly Efficient CRISPR-Cas9-Based Methods for Generating Deletion Mu-

- tations and F0 Embryos that Lack Gene Function in Zebrafish. *Developmental Cell*. 2019; 51(5):645–657.e4. <https://www.sciencedirect.com/science/article/pii/S1534580719308135>, doi: <https://doi.org/10.1016/j.devcel.2019.10.004>.
- Hou L**, Liu K, Li Y, Ma S, Ji X, Liu L. Necrotic pyknosis is a morphologically and biochemically distinct event from apoptotic pyknosis. *Journal of Cell Science*. 2016; 129(16):3084–3090. <https://doi.org/10.1242/jcs.184374>, doi: 10.1242/jcs.184374.
- Hsu PD**, Scott DA, Weinstein JA, Ran FA, Konermann S, Agarwala V, Li Y, Fine EJ, Wu X, Shalem O, Cradick TJ, Marraffini LA, Bao G, Zhang F. DNA targeting specificity of RNA-guided Cas9 nucleases. *Nature Biotechnology*. 2013; 31(9):827–832. <https://doi.org/10.1038/nbt.2647>, doi: 10.1038/nbt.2647.
- Hu H**, Candiello J, Zhang P, Ball SL, Cameron DA, Halfter W. Retinal ectopias and mechanically weakened basement membrane in a mouse model of muscle-eye-brain (MEB) disease congenital muscular dystrophy. *Molecular Vision*. 2010; 16(March):1415–1428. <http://www.molvis.org/molvis/v16/a155/>.
- Hu H**, Li J, Gagen CS, Gray NW, Zhang Z, Qi Y, Zhang P. Conditional knockout of protein O-mannosyltransferase 2 reveals tissue-specific roles of O-mannosyl glycosylation in brain development. *Journal of Comparative Neurology*. 2011; 519(7):1320–1337. <https://doi.org/10.1002/cne.22572>, doi: 10.1002/cne.22572.
- Huang TP**, Newby GA, Liu DR. Precision genome editing using cytosine and adenine base editors in mammalian cells. *Nature Protocols*. 2021; 16(2):1089–1128. <http://dx.doi.org/10.1038/s41596-020-00450-9>, doi: 10.1038/s41596-020-00450-9.
- Huber W**, Carey VJ, Gentleman R, Anders S, Carlson M, Carvalho BS, Bravo HC, Davis S, Gatto L, Girke T, Gottardo R, Hahne F, Hansen KD, Irizarry RA, Lawrence M, Love MI, Macdonald J, Obenchain V, Oles AK, Pagès H, et al. Orchestrating high-throughput genomic analysis with Bioconductor. *Nature Methods*. 2015; 12(2):115–121. <http://dx.doi.org/10.1038/nmeth.3252>, doi: 10.1038/nmeth.3252.
- Hwang WY**, Fu Y, Reyon D, Maeder ML, Tsai SQ, Sander JD, Peterson RT, Yeh JRJ, Joung JK. Efficient genome editing in zebrafish using a CRISPR-Cas system. *Nature Biotechnology*. 2013; 31(3):227–229. <http://dx.doi.org/10.1038/nbt.2501>, doi: 10.1038/nbt.2501.
- Ichikawa K**, Tomioka S, Suzuki Y, Nakamura R, Doi K, Yoshimura J, Kumagai M, Inoue Y, Uchida Y, Irie N, Takeda H, Morishita S. Centromere evolution and CpG methylation during vertebrate speciation. *Nature Communications*. 2017; 8(1):1833. <http://dx.doi.org/10.1038/s41467-017-01982-7><https://doi.org/10.1038/s41467-017-01982-7>, doi: 10.1038/s41467-017-01982-7.
- Inamori KI**, Hara Y, Willer T, Anderson ME, Zhu Z, Yoshida-Moriguchi T, Campbell KP. Xylosyl- and glucuronyltransferase functions of LARGE in α -dystroglycan modification are conserved in LARGE2. *Glycobiology*. 2013; 23(3):295–302. <https://doi.org/10.1093/glycob/cws152>, doi: 10.1093/glycob/cws152.
- Ishikawa T**, Kashima M, Nagano AJ, Ishikawa-Fujiwara T, Kamei Y, Todo T, Mori K. Unfolded protein response transducer IRE1-mediated signaling independent of XBP1 mRNA splicing is not required for growth and development of

medaka fish. *eLife*. 2017; 6:1–29. <https://doi.org/10.7554/eLife.26845.001>, doi: 10.7554/eLife.26845.001.

Ivanov D. Notch Signaling-Induced Oscillatory Gene Expression May Drive Neurogenesis in the Developing Retina. *Frontiers in Molecular Neuroscience*. 2019; 12(September):1–20. <https://doi.org/10.3389/fnmol.2019.00226>, doi: 10.3389/fnmol.2019.00226.

Iwamatsu T. Stages of normal development in the medaka *Oryzias latipes*. *Mechanisms of development*. 2004; 121(7-8):605–618. <https://doi.org/10.1016/j.mod.2004.03.012>, doi: 10.1016/j.mod.2004.03.012.

Jimenez-Mallebrera C, Torelli S, Feng L, Kim J, Godfrey C, Clement E, Mein R, Abbs S, Brown SC, Campbell KP, Kröger S, Talim B, Topaloglu H, Quinlivan R, Roper H, Childs AM, Kinali M, Sewry CA, Muntoni F. A comparative study of α -dystroglycan glycosylation in dystroglycanopathies suggests that the hypoglycosylation of α -dystroglycan does not consistently correlate with clinical severity. *Brain Pathology*. 2009; 19(4):596–611. <https://doi.org/10.1111/j.1750-3639.2008.00198.x>, doi: 10.1111/j.1750-3639.2008.00198.x.

Jinek M, Chylinski K, Fonfara I, Hauer M, Doudna JA, Charpentier E. A Programmable Dual-RNA-Guided DNA Endonuclease in Adaptive Bacterial Immunity. *Science*. 2012; 337(6096):816–822. <https://doi.org/10.1126/science.1225829>, doi: 10.1126/science.1225829.

Jones P, Binns D, Chang HY, Fraser M, Li W, McAnulla C, McWilliam H, Maslen J, Mitchell A, Nuka G, Pesseat S, Quinn AF, Sangrador-Vegas A, Scheremetjew M, Yong SY, Lopez R, Hunter S. InterProScan 5: Genome-scale protein function classification. *Bioinformatics*. 2014; 30(9):1236–1240. <https://doi.org/10.1093/bioinformatics/btu031>, doi: 10.1093/bioinformatics/btu031.

Jumper J, Evans R, Pritzel A, Green T, Figurnov M, Ronneberger O, Tunyasuvunakool K, Bates R, Žídek A, Potapenko A, Bridgland A, Meyer C, Kohl SAAA, Ballard AJ, Cowie A, Romera-Paredes B, Nikolov S, Jain R, Adler J, Back T, et al. Highly accurate protein structure prediction with AlphaFold. *Nature*. 2021; 596(7873):583–589. <https://doi.org/10.1038/s41586-021-03819-2>, doi: 10.1038/s41586-021-03819-2.

Kanagawa M. Dystroglycanopathy: From elucidation of molecular and pathological mechanisms to development of treatment methods. *International Journal of Molecular Sciences*. 2021; 22(23). <https://doi.org/10.3390/ijms222313162>, doi: 10.3390/ijms222313162.

Kanagawa M, Saito F, Kunz S, Yoshida-Moriguchi T, Barresi R, Kobayashi YM, Muschler J, Dumanski JP, Michele DE, Oldstone MBA, Campbell KP. Molecular recognition by LARGE is essential for expression of functional dystroglycan. *Cell*. 2004; 117(7):953–964. doi: 10.1016/j.cell.2004.06.003.

Kassambara A. ggpubr: 'ggplot2' Based Publication Ready Plots; 2020, <https://cran.r-project.org/package=ggpubr>.

Kim J, Koo BK, Knoblich JA. Human organoids: model systems for human biology

- and medicine. *Nature Reviews Molecular Cell Biology*. 2020; 21(10):571–584. <http://dx.doi.org/10.1038/s41580-020-0259-3>, doi: 10.1038/s41580-020-0259-3.
- Kim N**, Yoo JC, Han JY, Hwang EM, Kim YS, Jeong EY, Sun CH, Yi GS, Roh GS, Kim HJ, Kang SS, Cho GJ, Park JY, Choi WS. Human nuclear clusterin mediates apoptosis by interacting with Bcl-XL through C-terminal coiled coil domain. *Journal of Cellular Physiology*. 2011; 227(3):1157–1167. <https://doi.org/10.1002/jcp.22836>, doi: 10.1002/jcp.22836.
- Kirchmaier S**, Lust K, Wittbrodt J. Golden GATEway cloning—a combinatorial approach to generate fusion and recombination constructs. *PloS one*. 2013; 8(10):1–9. <https://doi.org/10.1371/journal.pone.0076117>, doi: 10.1371/journal.pone.0076117.
- Kluesner MG**, Lahr WS, Lin Lonetree C, Smeester BA, Qiu X, Slipek NJ, Claudio Vázquez PN, Pitzten SP, Pomeroy EJ, Vignes MJ, Lee SC, Bingea SP, Andrew AA, Webber BR, Moriarity BS. CRISPR-Cas9 cytidine and adenosine base editing of splice-sites mediates highly-efficient disruption of proteins in primary and immortalized cells. *Nature Communications*. 2021; 12(1):1–12. <http://dx.doi.org/10.1038/s41467-021-22009-2>, doi: 10.1038/s41467-021-22009-2.
- Kluesner MG**, Nedveck DA, Lahr WS, Garbe JR, Abrahante JE, Webber BR, Moriarity BS. EditR: A Method to Quantify Base Editing from Sanger Sequencing. *The CRISPR Journal*. 2018; 1(3):239–250. <https://doi.org/10.1089/crispr.2018.0014>, doi: 10.1089/crispr.2018.0014.
- Koblan LW**, Arbab M, Shen MW, Hussmann JA, Anzalone AV, Doman JL, Newby GA, Yang D, Mok B, Replogle JM, Xu A, Sisley TA, Weissman JS, Adamson B, Liu DR. Efficient C•G-to-G•C base editors developed using CRISPRi screens, target-library analysis, and machine learning. *Nature Biotechnology*. 2021; 39(11):1414–1425. <https://doi.org/10.1038/s41587-021-00938-z>, doi: 10.1038/s41587-021-00938-z.
- Koblan LW**, Doman JL, Wilson C, Levy JM, Tay T, Newby GA, Maianti JP, Raguram A, Liu DR. Improving cytidine and adenine base editors by expression optimization and ancestral reconstruction. *Nature Biotechnology*. 2018; 36(9):843–846. <https://doi.org/10.1038/nbt.4172><http://dx.doi.org/10.1038/nbt.4172>, doi: 10.1038/nbt.4172.
- Komor AC**, Kim YB, Packer MS, Zuris JA, Liu DR. Programmable editing of a target base in genomic DNA without double-stranded DNA cleavage. *Nature*. 2016; 533(7603):420–424. <https://doi.org/10.1038/nature17946><http://dx.doi.org/10.1038/nature17946>, doi: 10.1038/nature17946.
- Komor AC**, Zhao KT, Packer MS, Gaudelli NM, Waterbury AL, Koblan LW, Kim YB, Badran AH, Liu DR. Improved base excision repair inhibition and bacteriophage Mu Gam protein yields C:G-to-T:A base editors with higher efficiency and product purity. *Science Advances*. 2017; 3(8):eaao4774. <https://doi.org/10.1126/sciadv.aao4774>, doi: 10.1126/sciadv.aao4774.
- Konermann S**, Lotfy P, Brideau NJ, Oki J, Shokhirev MN, Hsu PD. Transcriptome Engineering with RNA-Targeting Type VI-D CRISPR Effectors. *Cell*. 2018; 173(3):665–676.e14. <https://doi.org/10.1016/j.cell.2018.02.033>, doi: 10.1016/j.cell.2018.02.033.

-
- Kontarakis Z**, Stainier DYR. Genetics in Light of Transcriptional Adaptation. *Trends in Genetics*. 2020; 36(12):926–935. <https://doi.org/10.1016/j.tig.2020.08.008>, doi: 10.1016/j.tig.2020.08.008.
- Kraeussling M**, Wagner TU, Scharl M. Highly Asynchronous and Asymmetric Cleavage Divisions Accompany Early Transcriptional Activity in Pre-Blastula Medaka Embryos. *PLOS ONE*. 2011 jul; 6(7):e21741. <https://doi.org/10.1371/journal.pone.0021741>, doi: 10.1371/journal.pone.0021741.
- Kroll F**, Powell GT, Ghosh M, Gestri G, Antinucci P, Hearn TJ, Tunbak H, Lim S, Dennis HW, Fernandez JM, Whitmore D, Dreosti E, Wilson SW, Hoffman EJ, Rihel J. A simple and effective f0 knockout method for rapid screening of behaviour and other complex phenotypes. *eLife*. 2021 jan; 10:1–34. <https://elifesciences.org/articles/59683>, doi: 10.7554/eLife.59683.
- Kurt IC**, Zhou R, Iyer S, Garcia SP, Miller BR, Langner LM, Grünewald J, Joung JK. CRISPR C-to-G base editors for inducing targeted DNA transversions in human cells. *Nature Biotechnology*. 2021; 39(1):41–46. <https://doi.org/10.1038/s41587-020-0609-x>, doi: 10.1038/s41587-020-0609-x.
- Kushawah G**, Hernandez-Huertas L, Abugattas-Nuñez del Prado J, Martinez-Morales JR, DeVore ML, Hassan H, Moreno-Sanchez I, Tomas-Gallardo L, Diaz-Moscoso A, Monges DE, Guelfo JR, Theune WC, Brannan EO, Wang W, Corbin TJ, Moran AM, Sánchez Alvarado A, Málaga-Trillo E, Takacs CM, Bazzini AA, et al. CRISPR-Cas13d Induces Efficient mRNA Knockdown in Animal Embryos. *Developmental Cell*. 2020 sep; 54(6):805–817.e7. <https://doi.org/10.1016/j.devcel.2020.07.013>, doi: 10.1016/j.devcel.2020.07.013.
- Larsen ISB**, Narimatsu Y, Joshi HJ, Siukstaite L, Harrison OJ, Brasch J, Goodman KM, Hansen L, Shapiro L, Honig B, Vakhrushev SY, Clausen H, Halim A. Discovery of an O-mannosylation pathway selectively serving cadherins and protocadherins. *Proceedings of the National Academy of Sciences*. 2017; 114(42):11163–11168. <https://doi.org/10.1073/pnas.1708319114>, doi: 10.1073/pnas.1708319114.
- Larsen ISB**, Narimatsu Y, Joshi HJ, Yang Z, Harrison OJ, Brasch J, Shapiro L, Honig B, Vakhrushev SY, Clausen H, Halim A. Mammalian O-mannosylation of cadherins and plexins is independent of protein O-mannosyltransferases 1 and 2. *Journal of Biological Chemistry*. 2017; 292(27):11586–11598. <https://doi.org/10.1074/jbc.M117.794487>, doi: 10.1074/jbc.M117.794487.
- Li J**, Yu M, Feng G, Hu H, Li X. Breaches of the pial basement membrane are associated with defective dentate gyrus development in mouse models of congenital muscular dystrophies. *Neuroscience Letters*. 2011; 505(1):19–24. <http://dx.doi.org/10.1016/j.neulet.2011.09.040>, doi: 10.1016/j.neulet.2011.09.040.
- Li X**, Zhang G, Ngo N, Zhao X, Kain SR, Huang CC. Deletions of the *Aequorea victoria* Green Fluorescent Protein Define the Minimal Domain Required for Fluorescence. *Journal of Biological Chemistry*. 1997; 272(45):28545–28549. <https://www.sciencedirect.com/science/article/pii/S0021925818386897>, doi: <https://doi.org/10.1074/jbc.272.45.28545>.
- Li Y**, Liu Y, Yang H, Zhang T, Naruse K, Tu Q. Dynamic transcriptional and chromatin accessibility landscape of medaka embryogenesis. *Genome Research*.

- 2020 Jun; 30(6):924–937. <http://genome.cshlp.org/content/30/6/924.abstract>, doi: 10.1101/gr.258871.119.
- Lien HW**, Yuan RY, Chou CM, Chen YC, Hung CC, Hu CH, Hwang SPL, Hwang PP, Shen CN, Chen CL, Cheng CH, Huang CJ. Zebrafish cyclin Dx is required for development of motor neuron progenitors, and its expression is regulated by hypoxia-inducible factor 2 α . *Scientific Reports*. 2016; 6(March):1–12. <https://doi.org/10.1038/srep28297>, doi: 10.1038/srep28297.
- Lischik CQ**, Adelman L, Wittbrodt J. Enhanced in vivo-imaging in medaka by optimized anaesthesia, fluorescent protein selection and removal of pigmentation. *PLoS ONE*. 2019; 14(3):e0212956. <https://doi.org/10.1371/journal.pone.0212956>, doi: 10.1371/journal.pone.0212956.
- Liu K**, Chen Y, Ai F, Li YQ, Zhang K, Zhang WT. PHLDA3 inhibition attenuates endoplasmic reticulum stress-induced apoptosis in myocardial hypoxia/reoxygenation injury by activating the PI3K/AKT signaling pathway. *Experimental and Therapeutic Medicine*. 2021; 21(6):1–9. <https://doi.org/10.3892/etm.2021.10045>, doi: 10.3892/etm.2021.10045.
- Liu Y**, Yu M, Shang X, Nguyen MHH, Balakrishnan S, Sager R, Hu H. Eyes shut homolog (EYS) interacts with matriglycan of O-mannosyl glycans whose deficiency results in EYS mislocalization and degeneration of photoreceptors. *Scientific Reports*. 2020; 10(1):7795. <https://doi.org/10.1038/s41598-020-64752-4>, doi: 10.1038/s41598-020-64752-4.
- Lommel M**, Schott A, Jank T, Hofmann V, Strahl S. A conserved acidic motif is crucial for enzymatic activity of protein O-mannosyltransferases. *Journal of Biological Chemistry*. 2011; 286(46):39768–39775. <https://doi.org/10.1074/jbc.M111.281196>, doi: 10.1074/jbc.M111.281196.
- Lommel M**, Strahl S. Protein O-mannosylation: Conserved from bacteria to humans. *Glycobiology*. 2009; 19(8):816–828. <https://doi.org/10.1093/glycob/cwp066>, doi: 10.1093/glycob/cwp066.
- Lommel M**, Willer T, Strahl S. POMT2, a key enzyme in Walker-Warburg syndrome: Somatic sPOMT2, but not testis-specific tPOMT2, is crucial for mannosyltransferase activity in vivo. *Glycobiology*. 2008; 18(8):615–625. <https://doi.org/10.1093/glycob/cwn042>, doi: 10.1093/glycob/cwn042.
- Loosli F**, Köster RW, Carl M, Kühnlein R, Henrich T, Mücke M, Krone A, Wittbrodt J. A genetic screen for mutations affecting embryonic development in medaka fish (*Oryzias latipes*). *Mechanisms of Development*. 2000; 97(1-2):133–139. [https://doi.org/10.1016/S0925-4773\(00\)00406-8](https://doi.org/10.1016/S0925-4773(00)00406-8), doi: 10.1016/S0925-4773(00)00406-8.
- Lorenz R**, Bernhart SH, Höner zu Siederdisen C, Tafer H, Flamm C, Stadler PF, Hofacker IL. ViennaRNA Package 2.0. *Algorithms for Molecular Biology*. 2011; 6(1):26. <https://doi.org/10.1186/1748-7188-6-26>, doi: 10.1186/1748-7188-6-26.
- Lust K**, Sinn R, Pérez Saturnino A, Centanin L, Wittbrodt J. De novo neurogenesis by targeted expression of *atoh7* to Müller glia cells. *Development (Cambridge)*. 2016; 143(11):1874–1883. <https://doi.org/10.1242/dev.135905>, doi: 10.1242/dev.135905.

-
- Manya H**, Chiba A, Yoshida A, Wang X, Chiba Y, Jigami Y, Margolis RU, Endo T. Demonstration of mammalian protein O-mannosyltransferase activity: Coexpression of POMT1 and POMT2 required for enzymatic activity. *Proceedings of the National Academy of Sciences*. 2004; 101(2):500–505. <https://doi.org/10.1073/pnas.0307228101>, doi: 10.1073/pnas.0307228101.
- Manya H**, Bouchet C, Yanagisawa A, Vuillaumier-Barrot S, Quijano-Roy S, Suzuki Y, Maugenre S, Richard P, Inazu T, Merlini L, Romero NB, Leturcq F, Bezier I, Topaloglu H, Estournet B, Seta N, Endo T, Guicheney P. Protein O-mannosyltransferase activities in lymphoblasts from patients with α -dystroglycanopathies. *Neuromuscular Disorders*. 2008; 18(1):45–51. <https://doi.org/10.1016/j.nmd.2007.08.002>, doi: 10.1016/j.nmd.2007.08.002.
- Marijanovic Z**, Laubner D, Möller G, Gege C, Husen B, Adamski J, Breitling R. Closing the gap: Identification of human 3-ketosteroid reductase, the last unknown enzyme of mammalian cholesterol biosynthesis. *Molecular Endocrinology*. 2003; 17(9):1715–1725. <https://doi.org/10.1210/me.2002-0436>, doi: 10.1210/me.2002-0436.
- Marlétaz F**, Firbas PN, Maeso I, Tena JJ, Bogdanovic O, Perry M,), Gómez-Skarmeta JL, Irimia M. Amphioxus functional genomics and the origins of vertebrate gene regulation. *Nature*. 2018; 564(7734):64–70. <https://doi.org/10.1038/s41586-018-0734-6>, doi: 10.1038/s41586-018-0734-6.
- Martin PT**. The dystroglycanopathies: The new disorders of o-linked glycosylation. *Seminars in Pediatric Neurology*. 2005; 12(3):152–158. <https://doi.org/10.1016/j.spn.2005.10.003>, doi: 10.1016/j.spn.2005.10.003.
- Martinez HR**, Craigen WJ, Ummat M, Adesina AM, Lotze TE, Jefferies JL. Novel cardiovascular findings in association with a POMT2 mutation: Three siblings with α -dystroglycanopathy. *European Journal of Human Genetics*. 2014; 22(4):486–491. <https://doi.org/10.1038/ejhg.2013.165>, doi: 10.1038/ejhg.2013.165.
- Mayr C**. What are 3 utrs doing? *Cold Spring Harbor Perspectives in Biology*. 2019; 11(10). <https://doi.org/10.1101/cshperspect.a034728>, doi: 10.1101/cshperspect.a034728.
- McClenahan FK**, Sharma H, Shan X, Eyermann C, Colognato H. Dystroglycan Suppresses Notch to Regulate Stem Cell Niche Structure and Function in the Developing Postnatal Subventricular Zone. *Developmental Cell*. 2016; 38(5):548–566. <http://dx.doi.org/10.1016/j.devcel.2016.07.017><https://www.sciencedirect.com/science/article/pii/S153458071630510X>, doi: <https://doi.org/10.1016/j.devcel.2016.07.017>.
- Mercuri E**, Messina S, Bruno C, Mora M, Pegoraro E, Comi GP, D'Amico A, Aiello C, Biancheri R, Berardinelli A, Boffi P, Cassandrini D, Laverda A, Moggio M, Morandi L, Moroni I, Pane M, Pezzani R, Pichiecchio A, Pini A, et al. Congenital muscular dystrophies with defective glycosylation of dystroglycan: A population study. *Neurology*. 2009; 72(21):1802–1809. <https://doi.org/10.1212/01.wnl.0000346518.68110.60>, doi: 10.1212/01.wnl.0000346518.68110.60.
- Meyer HV**, Dawes TJWW, Serrani M, Bai W, Tokarczuk P, Cai J, de Marvao A, Henry A, Lumbers RT, Gierten J, Thumberger T, Wittbrodt J, Ware JS,

- Rueckert D, Matthews PM, Prasad SK, Costantino ML, Cook SA, Birney E, O'Regan DP. Genetic and functional insights into the fractal structure of the heart. *Nature*. 2020; 584(7822):589–594. <https://doi.org/10.1038/s41586-020-2635-8>, doi: 10.1038/s41586-020-2635-8.
- Michele DE**, Barresi R, Kanagawa M, Saito F, Kelley RI, Somer H, Straub V, Mathews KD, Moore SA, Campbell KP. Post-translational disruption of dystroglycan–ligand interactions in congenital muscular dystrophies. *Nature*. 2002; 418(6896):417–422. <https://doi.org/10.1038/nature00837>, doi: 10.1038/nature00837.
- Mojica FJM**, Díez-Villaseñor C, García-Martínez J, Soria E. Intervening sequences of regularly spaced prokaryotic repeats derive from foreign genetic elements. *Journal of Molecular Evolution*. 2005; 60(2):174–182. <https://doi.org/10.1038/nature00837>, doi: 10.1007/s00239-004-0046-3.
- Moldovan GL**, Dejsuphong D, Petalcorin MIR, Hofmann K, Takeda S, Boulton SJ, D'Andrea AD. Inhibition of homologous recombination by the PCNA-interacting protein PARI. *Molecular Cell*. 2012; 45(1):75–86. <http://dx.doi.org/10.1016/j.molcel.2011.11.010>, doi: 10.1016/j.molcel.2011.11.010.
- Molla KA**, Yang Y. CRISPR/Cas-Mediated Base Editing: Technical Considerations and Practical Applications. *Trends in Biotechnology*. 2019; 37(10):1121–1142. <https://doi.org/10.1016/j.tibtech.2019.03.008>, doi: 10.1016/j.tibtech.2019.03.008.
- Moore CJ**, Goh HT, Hewitt JE. Genes required for functional glycosylation of dystroglycan are conserved in zebrafish. *Genomics*. 2008; 92(3):159–167. <https://doi.org/10.1016/j.ygeno.2008.05.008>, doi: 10.1016/j.ygeno.2008.05.008.
- Moore SA**, Saito F, Chen J, Michele DE, Henry MD, Messing A, Cohn RD, Ross-Barta SE, Westra S, Williamson RA, Hosl T, Campbell KP. Deletion of brain dystroglycan recapitulates aspects of congenital muscular dystrophy. *Nature*. 2002; 418(6896):422–425. <https://doi.org/10.1038/nature00838>, doi: 10.1038/nature00838.
- Moremen KW**, Tiemeyer M, Nairn AV. Vertebrate protein glycosylation: diversity, synthesis and function. *Nature Reviews Molecular Cell Biology*. 2012; 13(7):448–462. <http://dx.doi.org/10.1038/nrm3383>, doi: 10.1038/nrm3383.
- Morlacchi S**, Sciandra F, Bigotti MG, Bozzi M, Hübner W, Galtieri A, Giardina B, Brancaccio A. Insertion of a myc-tag within α -dystroglycan domains improves its biochemical and microscopic detection. *BMC Biochemistry*. 2012; 13(1). <https://doi.org/10.1186/1471-2091-13-14>, doi: 10.1186/1471-2091-13-14.
- Myshrall TD**, Moore SA, Ostendorf AP, Satz JS, Kowalczyk T, Nguyen H, Daza RAM, Lau C, Campbell KP, Hevner RF. Dystroglycan on radial glia end feet is required for pial basement membrane integrity and columnar organization of the developing cerebral cortex. *Journal of Neuropathology and Experimental Neurology*. 2012; 71(12):1047–1063. <https://doi.org/10.1097/NEN.0b013e318274a128>, doi: 10.1097/NEN.0b013e318274a128.
- Nakano I**, Funahashi M, Takada K, Toda T. Are breaches in the glia limitans the primary cause of the micropolygyria in Fukuyama-type congenital muscular

-
- dystrophy (FCMD)? - Pathological study of the cerebral cortex of an FCMD fetus. *Acta Neuropathologica*. 1996; 91(3):313–321. <https://doi.org/10.1007/s004010050431>, doi: 10.1007/s004010050431.
- Nambiar TS**, Baudrier L, Billon P, Ciccia A. CRISPR-based genome editing through the lens of DNA repair. *Molecular Cell*. 2022; 82(2):348–388. <https://doi.org/10.1016/j.molcel.2021.12.026>, doi: 10.1016/j.molcel.2021.12.026.
- Nelson JW**, Randolph PB, Shen SP, Everette KA, Chen PJ, Anzalone AV, An M, Newby GA, Chen JC, Hsu A, Liu DR. Engineered pegRNAs improve prime editing efficiency. *Nature Biotechnology*. 2021; <http://dx.doi.org/10.1038/s41587-021-01039-7>, doi: 10.1038/s41587-021-01039-7.
- Neubert P**, Halim A, Zauser M, Essig A, Joshi HJ, Zatorska E, Larsen ISB, Loibl M, Castells-Ballester J, Aebi M, Clausen H, Strahl S. Mapping the O-Mannose glycoproteome in *saccharomyces cerevisiae*. *Molecular and Cellular Proteomics*. 2016; 15(4):1323–1337. doi: 10.1074/mcp.M115.057505.
- Nguyen H**, Ostendorf AP, Satz JS, Westra S, Ross-Barta SE, Campbell KP, Moore SA. Glial scaffold required for cerebellar granule cell migration is dependent on dystroglycan function as a receptor for basement membrane proteins. *Acta Neuropathologica Communications*. 2013; 1(1):58. <https://doi.org/10.1186/2051-5960-1-58>, doi: 10.1186/2051-5960-1-58.
- Nickolls AR**, Bönemann CG. The roles of dystroglycan in the nervous system: insights from animal models of muscular dystrophy. *Disease Models Mechanisms*. 2018 dec; 11(12):dmm035931. <https://doi.org/10.1242/dmm.035931>, doi: 10.1242/dmm.035931.
- Nilsson J**, Nilsson J, Larson G, Grahn A. Characterization of site-specific O-glycan structures within the mucin-like domain of α -dystroglycan from human skeletal muscle. *Glycobiology*. 2010; 20(9):1160–1169. <https://doi.org/10.1093/glycob/cwq082>, doi: 10.1093/glycob/cwq082.
- Nishimasu H**, Shi X, Ishiguro S, Gao L, Hirano S, Okazaki S, Noda T, Abudayyeh OO, Gootenberg JS, Mori H, Oura S, Holmes B, Tanaka M, Seki M, Hirano H, Aburatani H, Ishitani R, Ikawa M, Yachie N, Zhang F, et al. Engineered CRISPR-Cas9 nuclease with expanded targeting space. *Science*. 2018; 361(6408):1259–1262. <https://doi.org/10.1126/science.aas9129>, doi: 10.1126/science.aas9129.
- Pacharra S**, Hanisch FG, Mühlenhoff M, Faissner A, Rauch U, Breloy I. The lecticans of mammalian brain perineural net are O-mannosylated. *Journal of Proteome Research*. 2013; 12(4):1764–1771. <https://doi.org/10.1021/pr3011028>, doi: 10.1021/pr3011028.
- Palmieri V**, Bozzi M, Signorino G, Papi M, De Spirito M, Brancaccio A, Maulucci G, Sciandra F. α -Dystroglycan hypoglycosylation affects cell migration by influencing β -dystroglycan membrane clustering and filopodia length: A multiscale confocal microscopy analysis. *Biochimica et Biophysica Acta (BBA) - Molecular Basis of Disease*. 2017; 1863(9):2182–2191. <https://www.sciencedirect.com/science/article/pii/S0925443917301916>, doi: <https://doi.org/10.1016/j.bbadis.2017.05.025>.
- Parsons MJ**, Campos I, Hirst EMA, Stemple DL. Removal of dystroglycan causes

- severe muscular dystrophy in zebrafish embryos. *Development*. 2002; 129(14):3505–3512. doi: 10.1242/dev.129.14.3505.
- Patterson GH**, Knobel SM, Sharif WD, Kain SR, Piston DW. Use of the green fluorescent protein and its mutants in quantitative fluorescence microscopy. *Biophysical Journal*. 1997; 73(5):2782–2790. <https://www.sciencedirect.com/science/article/pii/S0006349597783073>, doi: [https://doi.org/10.1016/S0006-3495\(97\)78307-3](https://doi.org/10.1016/S0006-3495(97)78307-3).
- Pavoni E**, Cacchiarelli D, Tittarelli R, Orsini M, Galtieri A, Giardina B, Brancaccio A. Duplication of the dystroglycan gene in most branches of teleost fish. *BMC Molecular Biology*. 2007; 8:1–10. <https://doi.org/10.1186/1471-2199-8-34>, doi: 10.1186/1471-2199-8-34.
- Peng HB**, Afshan Ali A, Daggett DF, Rauvala H, Hassell JR, Smalheiser NR. The Relationship between Perlecan and Dystroglycan and its Implication in the Formation of the Neuromuscular Junction. *Cell Communication and Adhesion*. 1998; 5(6):475–489. doi: 10.3109/15419069809005605.
- Petri K**, Zhang W, Ma J, Schmidts A, Lee H, Horng JE, Kim DY, Kurt IC, Clement K, Hsu JY, Pinello L, Maus MV, Joung JK, Yeh JRJ. CRISPR prime editing with ribonucleoprotein complexes in zebrafish and primary human cells. *Nature Biotechnology*. 2021; <http://dx.doi.org/10.1038/s41587-021-00901-y>, doi: 10.1038/s41587-021-00901-y.
- Porto EM**, Komor AC, Slaymaker IM, Yeo GW. Base editing: advances and therapeutic opportunities. *Nature Reviews Drug Discovery*. 2020; 19(12):839–859. <http://dx.doi.org/10.1038/s41573-020-0084-6>, doi: 10.1038/s41573-020-0084-6.
- Pourcel C**, Salvignol G, Vergnaud G. CRISPR elements in *Yersinia pestis* acquire new repeats by preferential uptake of bacteriophage DNA, and provide additional tools for evolutionary studies. *Microbiology*. 2005; 151(3):653–663. <https://doi.org/10.1099/mic.0.27437-0>, doi: 10.1099/mic.0.27437-0.
- Qin W**, Lu X, Liu Y, Bai H, Li S, Lin S. Precise A•T to G•C base editing in the zebrafish genome. *BMC Biology*. 2018; 16(1):139. <https://doi.org/10.1186/s12915-018-0609-1>, doi: 10.1186/s12915-018-0609-1.
- R Core Team**, R: A Language and Environment for Statistical Computing. Vienna, Austria; 2020. <https://www.r-project.org/>.
- Rainer J**, Gatto L, Weichenberger CX. `ensemldb`: an R package to create and use Ensembl-based annotation resources. *Bioinformatics*. 2019; <https://academic.oup.com/bioinformatics/advance-article/doi/10.1093/bioinformatics/btz031/5301311>, doi: 10.1093/bioinformatics/btz031.
- Ravindran S**. Got mutation? 'Base editors' fix genomes one nucleotide at a time. *Nature*. 2019; 575(7783):553–555. <https://doi.org/10.1038/d41586-019-03536-x>, doi: 10.1038/d41586-019-03536-x.
- Rees HA**, Liu DR. Base editing: precision chemistry on the genome and transcriptome of living cells. *Nature Reviews Genetics*. 2018; 19(12):770–788. <http://dx.doi.org/10.1038/s41576-018-0059-1>, doi: 10.1038/s41576-018-0059-1.

-
- van Reeuwijk J**, Janssen M, van den Elzen C, Beltran-Valero de Bernabé D, Sabatelli P, Merlini L, Boon M, Scheffer H, Brockington M, Muntoni F, Huynen MA, Verrips A, Walsh CA, Barth PG, Brunner HG, van Bokhoven H. POMT2 mutations cause alpha-dystroglycan hypoglycosylation and Walker-Warburg syndrome. *Journal of medical genetics*. 2005 dec; 42(12):907–912. <https://pubmed.ncbi.nlm.nih.gov/15894594><https://www.ncbi.nlm.nih.gov/pmc/articles/PMC1735967/>, doi: 10.1136/jmg.2005.031963.
- Reinhardt R**, Centanin L, Tavhelidse T, Inoue D, Wittbrodt B, Concordet J, Martinez-Morales JR, Wittbrodt J. Sox2, Tlx, Gli3, and Her9 converge on Rx2 to define retinal stem cells in vivo. *The EMBO Journal*. 2015; 34(11):1572–1588. <https://doi.org/10.15252/embj.201490706>, doi: 10.15252/embj.201490706.
- Rembold M**, Loosli F, Adams RJ, Wittbrodt J. Individual cell migration serves as the driving force for optic vesicle evagination. *Science*. 2006; 313(5790):1130–1134. <https://doi.org/10.1126/science.1127144>, doi: 10.1126/science.1127144.
- Richter MF**, Zhao KT, Eton E, Lapinaite A, Newby GA, Thuronyi BW, Wilson C, Koblan LW, Zeng J, Bauer DE, Doudna JA, Liu DR. Phage-assisted evolution of an adenine base editor with improved Cas domain compatibility and activity. *Nature Biotechnology*. 2020; 38(7):883–891. <http://dx.doi.org/10.1038/s41587-020-0453-z>, doi: 10.1038/s41587-020-0453-z.
- Ritchie ME**, Phipson B, Wu D, Hu Y, Law CW, Shi W, Smyth GK. Limma powers differential expression analyses for RNA-sequencing and microarray studies. *Nucleic Acids Research*. 2015; 43(7):e47. <https://doi.org/10.1093/nar/gkv007>, doi: 10.1093/nar/gkv007.
- Robinson MD**, McCarthy DJ, Smyth GK. edgeR: A Bioconductor package for differential expression analysis of digital gene expression data. *Bioinformatics*. 2009; 26(1):139–140. <https://doi.org/10.1093/bioinformatics/btp616>, doi: 10.1093/bioinformatics/btp616.
- Rosello M**, Serafini M, Mione MC, Concordet JP, Del Bene F. Disease modeling by efficient genome editing using a near PAM-less base editor in vivo. *bioRxiv*. 2021 jun; p. 2021.06.28.450169. <http://biorxiv.org/content/early/2021/06/29/2021.06.28.450169.abstract>, doi: 10.1101/2021.06.28.450169.
- Rosello M**, Voungny J, Czarny F, Mione MC, Concordet JP, Albadri S, Del Bene F. Precise base editing for the in vivo study of developmental signaling and human pathologies in zebrafish. *eLife*. 2021; 10:1–27. <https://doi.org/10.7554/eLife.65552>, doi: 10.7554/eLife.65552.
- Rubio-Fernández M**, Uribe ML, Vicente-Tejedor J, Germain F, Susín-Lara C, Quereda C, Montoliu L, De La Villa P, Martín-Nieto J, Cruces J. Impairment of photoreceptor ribbon synapses in a novel Pomt1 conditional knockout mouse model of dystroglycanopathy. *Scientific Reports*. 2018; 8(1):1–15. <https://doi.org/10.1038/s41598-018-26855-x>, doi: 10.1038/s41598-018-26855-x.
- Runge K**, Mathieu R, Bugeon S, Lafi S, Beurrier C, Sahu S, Schaller F, Loubat A, Herauld L, Gaillard S, Pallesi-Pocachard E, Montheil A, Bosio A, Rosenfeld JA, Hudson E, Lindstrom K, Mercimek-Andrews S, Jeffries L, van Haeringen A, Vanakker O, et al. Disruption of NEUROD2 causes a neurodevelopmental syndrome with autistic

- features via cell-autonomous defects in forebrain glutamatergic neurons. *Molecular Psychiatry*. 2021; 26(11):6125–6148. <https://doi.org/10.1038/s41380-021-01179-x>, doi: 10.1038/s41380-021-01179-x.
- Rupp RA**, Snider L, Weintraub H. Xenopus embryos regulate the nuclear localization of XMyoD. *Genes Development*. 1994 jun; 8(11):1311–1323. <http://genesdev.cshlp.org/content/8/11/1311.abstract>, doi: 10.1101/gad.8.11.1311.
- Sasaki T**, Yamada H, Matsumura K, Shimizu T, Kobata A, Endo T. Detection of O-mannosyl glycans in rabbit skeletal muscle α -dystroglycan. *Biochimica et Biophysica Acta - General Subjects*. 1998; 1425(3):599–606. [https://doi.org/10.1016/S0304-4165\(98\)00114-7](https://doi.org/10.1016/S0304-4165(98)00114-7), doi: 10.1016/S0304-4165(98)00114-7.
- Sato S**, Omori Y, Katoh K, Kondo M, Kanagawa M, Miyata K, Funabiki K, Koyasu T, Kajimura N, Miyoshi T, Sawai H, Kobayashi K, Tani A, Toda T, Usukura J, Tano Y, Fujikado T, Furukawa T. Pikachurin, a dystroglycan ligand, is essential for photoreceptor ribbon synapse formation. *Nature Neuroscience*. 2008; 11(8):923–931. <https://doi.org/10.1038/nn.2160>, doi: 10.1038/nn.2160.
- Saturnino AP**, Lust K, Wittbrodt J. Notch signalling patterns retinal composition by regulating *atoh7* during post-embryonic growth. *Development (Cambridge)*. 2018; 145(21). <https://doi.org/10.1242/dev.169698>, doi: 10.1242/dev.169698.
- Satz JS**, Barresi R, Durbeej M, Willer T, Turner A, Moore SA, Campbell KP. Brain and eye malformations resembling Walker-Warburg syndrome are recapitulated in mice by dystroglycan deletion in the epiblast. *Journal of Neuroscience*. 2008; 28(42):10567–10575. <https://doi.org/10.1523/JNEUROSCI.2457-08.2008>, doi: 10.1523/JNEUROSCI.2457-08.2008.
- Satz JS**, Ostendorf AP, Hou S, Turner A, Kusano H, Lee JC, Turk R, Nguyen H, Ross-Barta SE, Westra S, Hoshi T, Moore SA, Campbell KP. Distinct functions of glial and neuronal dystroglycan in the developing and adult mouse brain. *Journal of Neuroscience*. 2010; 30(43):14560–14572. <https://doi.org/10.1523/JNEUROSCI.3247-10.2010>, doi: 10.1523/JNEUROSCI.3247-10.2010.
- Satz JS**, Philp AR, Nguyen H, Kusano H, Lee J, Turk R, Riker MJ, Hernández J, Weiss RM, Anderson MG, Mullins RF, Moore SA, Stone EM, Campbell KP. Visual impairment in the absence of dystroglycan. *Journal of Neuroscience*. 2009; 29(42):13136–13146. <https://doi.org/10.1523/JNEUROSCI.0474-09.2009>, doi: 10.1523/JNEUROSCI.0474-09.2009.
- Schartl M**. Beyond the zebrafish: Diverse fish species for modeling human disease. *DMM Disease Models and Mechanisms*. 2014; 7(2):181–192. <https://doi.org/10.1242/dmm.012245>, doi: 10.1242/dmm.012245.
- Schindelin J**, Arganda-Carreras I, Frise E, Kaynig V, Longair M, Pietzsch T, Preibisch S, Rueden C, Saalfeld S, Schmid B, Tinevez JY, White DJ, Hartenstein V, Eliceiri K, Tomancak P, Cardona A. Fiji: an open-source platform for biological-image analysis. *Nature Methods*. 2012; 9(7):676–682. <https://doi.org/10.1038/nmeth.2019>, doi: 10.1038/nmeth.2019.
- Schjoldager KT**, Narimatsu Y, Joshi HJ, Clausen H. Global view of human protein glycosylation pathways and functions. *Nature Reviews Molecular Cell*

-
- Biology. 2020; 21(12):729–749. <http://dx.doi.org/10.1038/s41580-020-00294-x>, doi: 10.1038/s41580-020-00294-x.
- Schmittgen TD**, Livak KJ. Analyzing real-time PCR data by the comparative CT method. *Nature Protocols*. 2008; 3(6):1101–1108. <https://doi.org/10.1038/nprot.2008.73>, doi: 10.1038/nprot.2008.73.
- Scott A**, Stemple D. Zebrafish Notochordal Basement Membrane: Signaling and Structure. In: *Current Topics in Developmental Biology*, vol. 65 Academic Press; 2004.p. 229–253. <https://www.sciencedirect.com/science/article/pii/S0070215304650095>, doi: 10.1016/S0070-2153(04)65009-5.
- Sehnert AJ**, Huq A, Weinstein BM, Walker C, Fishman M, Stainier DYR. Cardiac troponin T is essential in sarcomere assembly and cardiac contractility. *Nature Genetics*. 2002; 31(1):106–110. <https://doi.org/10.1038/ng875>, doi: 10.1038/ng875.
- Seleit A**, Aulehla A, Paix A. Endogenous protein tagging in medaka using a simplified CRISPR/Cas9 knockin approach. *eLife*. 2021; 10:1–28. doi: 10.7554/eLife.75050.
- Sentandreu R**, Northcote DH. The structure of a glycopeptide isolated from the yeast cell wall. *Biochemical Journal*. 1968 sep; 109(3):419–432. <https://doi.org/10.1042/bj1090419>, doi: 10.1042/bj1090419.
- Serafini PR**, Feyder MJ, Hightower RM, Garcia-Perez D, Vieira NM, Lek A, Gibbs DE, Moukha-Chafiq O, Augelli-Szafran CE, Kawahara G, Widrick JJ, Kunkel LM, Alexander MS. A limb-girdle muscular dystrophy 2I model of muscular dystrophy identifies corrective drug compounds for dystroglycanopathies. *JCI Insight*. 2018; 3(18). <https://doi.org/10.1172/jci.insight.120493>, doi: 10.1172/jci.insight.120493.
- Sheikh MO**, Halmo SM, Wells L. Recent advancements in understanding mammalian O-mannosylation. *Glycobiology*. 2017; 27(9):806–819. <https://doi.org/10.1093/glycob/cwx062>, doi: 10.1093/glycob/cwx062.
- Shimizu T**, Hibi M. Formation and patterning of the forebrain and olfactory system by zinc-finger genes *Fezf1* and *Fezf2*. *Development Growth and Differentiation*. 2009; 51(3):221–231. <https://doi.org/10.1111/j.1440-169X.2009.01088.x>, doi: 10.1111/j.1440-169X.2009.01088.x.
- Silva AC**, Pereira C, Fonseca ACRG, Pinto-do Ó P, Nascimento DS. Bearing My Heart: The Role of Extracellular Matrix on Cardiac Development, Homeostasis, and Injury Response. *Frontiers in Cell and Developmental Biology*. 2021; 8(January):1–18. doi: 10.3389/fcell.2020.621644.
- Smalheiser NR**, Haslam SM, Sutton-Smith M, Morris HR, Dell A. Structural analysis of sequences O-linked to mannose reveals a novel Lewis X structure in crinin (dystroglycan) purified from sheep brain. *Journal of Biological Chemistry*. 1998; 273(37):23698–23703. <https://doi.org/10.1074/jbc.273.37.23698>, doi: 10.1074/jbc.273.37.23698.
- Sohaskey ML**, Jiang Y, Zhao JJ, Mohr A, Roemer F, Harland RM. Osteopotenia regulates osteoblast maturation, bone formation, and skeletal integrity in mice. *Journal of Cell Biology*. 2010; 189(3):511–525. <https://doi.org/10.1083/jcb.201003006>, doi: 10.1083/jcb.201003006.

- Soneson C**, Love MI, Robinson MD. Differential analyses for RNA-seq: transcript-level estimates improve gene-level inferences. *F1000Research*. 2015; 4(1521). <https://doi.org/10.12688/f1000research.7563.1>, doi: 10.12688/f1000research.7563.1.
- Song M**, Kim HK, Lee S, Kim Y, Seo SY, Park J, Choi JW, Jang H, Shin JH, Min S, Quan Z, Kim JH, Kang HC, Yoon S, Kim HH. Sequence-specific prediction of the efficiencies of adenine and cytosine base editors. *Nature Biotechnology*. 2020; 38(9):1037–1043. <https://doi.org/10.1038/s41587-020-0573-5>, doi: 10.1038/s41587-020-0573-5.
- Song M**, Lim JM, Min S, Oh JS, Kim DY, Woo JS, Nishimasu H, Cho SR, Yoon S, Kim HH. Generation of a more efficient prime editor 2 by addition of the Rad51 DNA-binding domain. *Nature Communications*. 2021; 12(1):1–8. <http://dx.doi.org/10.1038/s41467-021-25928-2>, doi: 10.1038/s41467-021-25928-2.
- Song S**, Landsbury A, Dahm R, Liu Y, Zhang Q, Quinlan RA. Functions of the intermediate filament cytoskeleton in the eye lens. *Journal of Clinical Investigation*. 2009; 119(7):1837–1848. <https://doi.org/10.1172/JCI38277>, doi: 10.1172/JCI38277.
- Spence HJ**, Dhillon AS, James M, Winder SJ. Dystroglycan, a scaffold for the ERK-MAP kinase cascade. *EMBO Reports*. 2004; 5(5):484–489. <https://doi.org/10.1038/sj.embor.7400140>, doi: 10.1038/sj.embor.7400140.
- Stalnaker SH**, Hashmi S, Lim JM, Aoki K, Porterfield M, Gutierrez-Sanchez G, Wheeler J, Ervasti JM, Bergmann C, Tiemeyer M, Wells L. Site mapping and characterization of O-glycan structures on α -dystroglycan isolated from rabbit skeletal muscle. *Journal of Biological Chemistry*. 2010; 285(32):24882–24891. <https://doi.org/10.1074/jbc.M110.126474>, doi: 10.1074/jbc.M110.126474.
- Stalnaker SH**, Stuart R, Wells L. Mammalian O-mannosylation: Unsolved questions of structure/function. *Current Opinion in Structural Biology*. 2011; 21(5):603–609. doi: 10.1016/j.sbi.2011.09.001.
- Steffen LS**, Guyon JR, Vogel ED, Beltre R, Pusack TJ, Zhou Y, Zon LI, Kunkel LM. Zebrafish orthologs of human muscular dystrophy genes. *BMC Genomics*. 2007; 8. <https://doi.org/10.1186/1471-2164-8-79>, doi: 10.1186/1471-2164-8-79.
- Stemmer M**, Thumberger T, del Sol Keyer M, Wittbrodt J, Mateo JL. CCTop: An Intuitive, Flexible and Reliable CRISPR/Cas9 Target Prediction Tool. *PLOS ONE*. 2015 apr; 10(4):e0124633. <https://doi.org/10.1371/journal.pone.0124633>, doi: 10.1371/journal.pone.0124633.
- Sudo A**, Kanagawa M, Kondo M, Ito C, Kobayashi K, Endo M, Minami Y, Aiba A, Toda T. Temporal requirement of dystroglycan glycosylation during brain development and rescue of severe cortical dysplasia via gene delivery in the fetal stage. *Human Molecular Genetics*. 2018; 27(7):1174–1185. <https://doi.org/10.1093/hmg/ddy032>, doi: 10.1093/hmg/ddy032.
- Sugita S**, Saito F, Tang J, Satz J, Campbell K, Südhof TC. A stoichiometric complex of neurexins and dystroglycan in brain. *Journal of Cell Biology*. 2001; 154(2):435–445. doi: 10.1083/jcb.200105003.
- Sun X**, Zhou Y, Zhang R, Wang Z, Xu M, Zhang D, Huang J, Luo F, Li F,

-
- Ni Z, Zhou S, Chen H, Chen S, Chen LL, Du X, Chen B, Huang H, Liu P, Yin L, Qiu J, et al. Dstyk mutation leads to congenital scoliosis-like vertebral malformations in zebrafish via dysregulated mTORC1/TFEB pathway. *Nature Communications*. 2020; 11(1):1–17. <http://dx.doi.org/10.1038/s41467-019-14169-z>, doi: 10.1038/s41467-019-14169-z.
- Taniguchi-Ikeda M**, Koyanagi-Aoi M, Maruyama T, Takaori T, Hosoya A, Tezuka H, Nagase S, Ishihara T, Kadoshima T, Muguruma K, Ishigaki K, Sakurai H, Mizoguchi A, Novitch BG, Toda T, Watanabe M, Aoi T. Restoration of the defect in radial glial fiber migration and cortical plate organization in a brain organoid model of Fukuyama muscular dystrophy. *iScience*. 2021; 24(10):103140. <https://doi.org/10.1016/j.isci.2021.103140>, doi: 10.1016/j.isci.2021.103140.
- Tham DKL**, Joshi B, Moukhles H. Aquaporin-4 cell-surface expression and turnover are regulated by dystroglycan, dynamin, and the extracellular matrix in astrocytes. *PLoS ONE*. 2016; 11(10):1–22. <https://doi.org/10.1371/journal.pone.0165439>, doi: 10.1371/journal.pone.0165439.
- Thumberger T**, Tavheliidse-Suck T, Gutierrez-Triana JA, Cornean A, Medert R, Welz B, Freichel M, Wittbrodt J. Boosting targeted genome editing using the hei-tag. *eLife*. 2022 mar; 11:e70558. <https://doi.org/10.7554/eLife.70558>, doi: 10.7554/eLife.70558.
- Thuronyi BW**, Koblan LW, Levy JM, Yeh WHH, Zheng C, Newby GA, Wilson C, Bhaumik M, Shubina-Oleinik O, Holt JR, Liu DR. Continuous evolution of base editors with expanded target compatibility and improved activity. *Nature Biotechnology*. 2019; 37(9):1070–1079. <https://doi.org/10.1038/s41587-019-0193-0>, doi: 10.1038/s41587-019-0193-0.
- Trinidad JC**, Schoepfer R, Burlingame AL, Medzihradzsky KF. N- and O-Glycosylation in the murine synaptosome. *Molecular and Cellular Proteomics*. 2013; 12(12):3474–3488. <https://doi.org/10.1074/mcp.M113.030007>, doi: 10.1074/mcp.M113.030007.
- Uribe ML**, Quereda C, Rubio-fern M, Janssen GMC, Ru AHD, Veelen PAV, Hensbergen PJ, Martín-Nieto J, Quereda C, Rubio-Fernández M, Cruces J, Janssen GMC, de Ru AH, van Veelen PA, Hensbergen PJ. Retinal Proteomics of a Mouse Model of Dystroglycanopathies Reveals Molecular Alterations in Photoreceptors. *Journal of Proteome Research*. 2021 jun; 20(6):3268–3277. <https://doi.org/10.1021/acs.jproteome.1c00126>, doi: 10.1021/acs.jproteome.1c00126.
- Varadi M**, Anyango S, Deshpande M, Nair S, Natassia C, Yordanova G, Yuan D, Stroe O, Wood G, Laydon A, Žídek A, Green T, Tunyasuvunakool K, Petersen S, Jumper J, Clancy E, Green R, Vora A, Lutfi M, Figurnov M, et al. AlphaFold Protein Structure Database: massively expanding the structural coverage of protein-sequence space with high-accuracy models. *Nucleic Acids Research*. 2022 jan; 50(D1):D439–D444. <https://doi.org/10.1093/nar/gkab1061>, doi: 10.1093/nar/gkab1061.
- Varki A**. Biological roles of glycans. *Glycobiology*. 2017; 27(1):3–49. <https://doi.org/10.1093/glycob/cww086>, doi: 10.1093/glycob/cww086.
- Varki A**, Kornfeld S. Essentials of Glycobiology: Historical Background and

- Overview. In: Varki A, Cummings RD, Esko J, Stanley P, Hart GW, Aebi M, Darvill AG, Kinoshita T, Packer NH, Prestegard JH, Schnaar RL, Seeberger PH, editors. *Essentials of Glycobiology, 3rd edition*, 3rd editio ed. Cold Spring Harbor (NY): Cold Spring Harbor Laboratory Press; 2017. <https://www.ncbi.nlm.nih.gov/books/NBK316258/?report=classic>, doi: 10.1101/glycobiology.3e.001.
- Verkman AS**, Tradtrantip L, Smith AJ, Yao X. Aquaporin Water Channels and Hydrocephalus. *Pediatric Neurosurgery*. 2017; 52(6):409–416. <https://doi.org/10.1159/000452168>, doi: 10.1159/000452168.
- Vester-Christensen MB**, Halim A, Joshi HJ, Steentoft C, Bennett EP, Lavery SB, Vakhrushev SY, Clausen H. Mining the O-mannose glycoproteome reveals cadherins as major O-mannosylated glycoproteins. *Proceedings of the National Academy of Sciences of the United States of America*. 2013; 110(52):21018–21023. <https://doi.org/10.1073/pnas.1313446110>, doi: 10.1073/pnas.1313446110.
- Vicencio J**, Sánchez-Bolaños C, Moreno-Sánchez I, Brena D, Vejnar CE, Kukhtar D, Ruiz-López M, Cots-Ponjoan M, Rubio A, Melero NR, Crespo-Cuadrado J, Carolis C, Pérez-Pulido AJ, Giráldez AJ, Kleinstiver BP, Cerón J, Moreno-Mateos MA, Vejnar CE, Rubio A, Melero NR, et al. Genome editing in animals with minimal PAM CRISPR-Cas9 enzymes. *Nature Communications*. 2022; 13(1):2601. <https://doi.org/10.1038/s41467-022-30228-4>, doi: 10.1038/s41467-022-30228-4.
- Walko G**, Wögenstein KL, Winter L, Fischer I, Feltri ML, Wiche G. Stabilization of the dystroglycan complex in Cajal bands of myelinating Schwann cells through plectin-mediated anchorage to vimentin filaments. *Glia*. 2013; 61(8):1274–1287. <https://doi.org/10.1002/glia.22514>, doi: 10.1002/glia.22514.
- Walton RT**, Christie KA, Whittaker MN, Kleinstiver BP. Unconstrained genome targeting with near-PAMless engineered CRISPR-Cas9 variants. *Science*. 2020 apr; 368(6488):290–296. <https://doi.org/10.1126/science.aba8853>, doi: 10.1126/science.aba8853.
- Wang W**, MacKinnon R. Cryo-EM Structure of the Open Human Ether-à-go-go-Related K⁺ Channel hERG. *Cell*. 2017; 169(3):422–430.e10. <http://dx.doi.org/10.1016/j.cell.2017.03.048>, doi: 10.1016/j.cell.2017.03.048.
- Warnes GR**, Bolker B, Bonebakker L, Gentleman R, Huber W, Liaw A, Lumley T, Maechler M, Magnusson A, Moeller S, Schwartz M, Venables B, gplots: Various R Programming Tools for Plotting Data; 2022. <https://cran.r-project.org/package=gplots>.
- Wickham H**. The Split-Apply-Combine Strategy for Data Analysis. *Journal of Statistical Software*. 2011; 40(1):1–29. <http://www.jstatsoft.org/v40/i01/>.
- Wickham H**. *ggplot2: Elegant Graphics for Data Analysis*. Springer-Verlag New York; 2016. <https://ggplot2.tidyverse.org>.
- Wickham H**, Averick M, Bryan J, Chang W, McGowan LD, François R, Golemund G, Hayes A, Henry L, Hester J, Kuhn M, Pedersen TL, Miller E, Bache SM, Müller K, Ooms J, Robinson D, Seidel DP, Spinu V, Takahashi K, et al. Welcome to the tidyverse. *Journal of Open Source Software*. 2019; 4(43):1686. <https://doi.org/10.21105/joss.01686>, doi: 10.21105/joss.01686.

-
- Wickham H**, François R, Henry L, Müller K. dplyr: A Grammar of Data Manipulation; 2020, <https://cran.r-project.org/package=dplyr>.
- Wilke CO**, cowplot: Streamlined Plot Theme and Plot Annotations for 'ggplot2'; 2020. <https://cran.r-project.org/package=cowplot>.
- Willer T**, Amselgruber W, Deutzmann R, Strahl S. Characterization of POMT2, a novel member of the PMT protein O-mannosyltransferase family specifically localized to the acrosome of mammalian spermatids. *Glycobiology*. 2002; 12(11):771–783. <https://doi.org/10.1093/glycob/cwf086>, doi: 10.1093/glycob/cwf086.
- Willer T**, Prados B, Falcón-Pérez JM, Renner-Müller I, Przemeczek GKH, Lommel M, Coloma A, Valero MC, De Angelis MH, Tanner W, Wolf E, Strahl S, Cruces J. Targeted disruption of the Walker-Warburg syndrome gene *Pomt1* in mouse results in embryonic lethality. *Proceedings of the National Academy of Sciences of the United States of America*. 2004; 101(39):14126–14131. <https://www.pnas.org/doi/full/10.1073/pnas.0405899101>, doi: 10.1073/pnas.0405899101.
- Williams SE**, Noel M, Lehoux S, Cetinbas M, Xavier RJ, Sadreyev RI, Scolnick EM, Smoller JW, Cummings RD, Mealer RG. Mammalian brain glycoproteins exhibit diminished glycan complexity compared to other tissues. *Nature Communications*. 2022; 13(1). <https://doi.org/10.1038/s41467-021-27781-9>, doi: 10.1038/s41467-021-27781-9.
- Williamson RA**, Henry MD, Daniels KJ, Hrstka RF, Lee JC, Sunada Y, Ibraghimov-Beskrovnyaya O, Campbell KP. Dystroglycan is essential for early embryonic development: Disruption of Reichert's membrane in *Dag1*-null mice. *Human Molecular Genetics*. 1997; 6(6):831–841. <https://doi.org/10.1093/hmg/6.6.831>, doi: 10.1093/hmg/6.6.831.
- Wittbrodt J**, Shima A, Scharl M. Medaka - A model organism from the Far East. *Nature Reviews Genetics*. 2002; 3(1):53–64. <https://doi.org/10.1038/nrg704>, doi: 10.1038/nrg704.
- Wopereis S**, Lefeber DJ, Morava É, Wevers RA. Mechanisms in protein O-glycan biosynthesis and clinical and molecular aspects of protein O-glycan biosynthesis defects: A review. *Clinical Chemistry*. 2006; 52(4):574–600. <https://doi.org/10.1373/clinchem.2005.063040>, doi: 10.1373/clinchem.2005.063040.
- Xu C**, Wang S, Thibault G, Ng DTW. Futile protein folding cycles in the ER are terminated by the unfolded protein O-mannosylation pathway. *Science*. 2013; 340(6135):978–982. <https://doi.org/10.1126/science.1234055>, doi: 10.1126/science.1234055.
- Xu J**, Wang T, Wu Y, Jin W, Wen Z. Microglia Colonization of Developing Zebrafish Midbrain Is Promoted by Apoptotic Neuron and Lysophosphatidylcholine. *Developmental Cell*. 2016; 38(2):214–222. <https://doi.org/10.1016/j.devcel.2016.06.018>, doi: 10.1016/j.devcel.2016.06.018.
- Yagi H**, Nakagawa N, Saito T, Kiyonari H, Abe T, Toda T, Wu SWW, Khoo KHH, Oka S, Kato K. AGO1-dependent GlcNAc modification primes the formation of functional glycans on α -dystroglycan. *Scientific Reports*. 2013; 3(1):3288. <https://doi.org/10.1038/srep03288>, doi: 10.1038/srep03288.

- Yanagisawa A**, Bouchet C, Van den Bergh PYK, Cuisset JM, Viollet L, Leturcq F, Romero NB, Quijano-Roy S, Fardeau M, Seta N, Guicheney P. New POMT2 mutations causing congenital muscular dystrophy. *Neurology*. 2007 sep; 69(12):1254–1260. <https://doi.org/10.1212/01.wnl.0000268489.60809.c4>, doi: 10.1212/01.wnl.0000268489.60809.c4.
- Yanagisawa A**, Bouchet C, Quijano-Roy S, Vuillaumier-Barrot S, Clarke N, Odent S, Rodriguez D, Romero NB, Osawa M, Endo T, Lia TA, Seta N, Guicheney P. POMT2 intragenic deletions and splicing abnormalities causing congenital muscular dystrophy with mental retardation. *European Journal of Medical Genetics*. 2009; 52(4):201–206. doi: 10.1016/j.ejmg.2008.12.004.
- Yang Y**, Yamada T, Hill KK, Hemberg M, Reddy NC, Cho HY, Guthrie AN, Oldenburg A, Heiney SA, Ohmae S, Medina JF, Holy TE, Bonni A, Yang H, Many H, Kobayashi K, Jiao H, Fu X, Xiao J, Li X, et al. Analysis of phenotype, enzyme activity and genotype of Chinese patients with POMT1 mutation. *Journal of Human Genetics*. 2016; 61(8):753–759. <https://doi.org/10.1038/jhg.2016.42>, doi: 10.1038/jhg.2016.42.
- Yoshida-Moriguchi T**, Willer T, Anderson ME, Venzke D, Whyte T, Muntoni F, Lee H, Nelson SF, Yu L, Campbell KP. SGK196 Is a Glycosylation-Specific O-Mannose Kinase Required for Dystroglycan Function. *Science*. 2013; 341(6148):896–899. <https://www.science.org/doi/abs/10.1126/science.1239951>, doi: 10.1126/science.1239951.
- Yıldırım M**, Eker HK, Doğan MT. A homozygous mutation in the pomt2 gene in four siblings with limb-girdle muscular dystrophy 2n. *Turk Pediatri Arsivi*. 2021; 56(1):68–71. <https://doi.org/10.14744/TurkPediatriArs.2020.37880>, doi: 10.14744/TurkPediatriArs.2020.37880.
- Zada D**, Bronshtein I, Lerer-Goldshtein T, Garini Y, Appelbaum L. Sleep increases chromosome dynamics to enable reduction of accumulating DNA damage in single neurons. *Nature Communications*. 2019; 10(1). <http://dx.doi.org/10.1038/s41467-019-08806-w>, doi: 10.1038/s41467-019-08806-w.
- Zhang M**, Liu J, Tseng GN. Gating Charges in the Activation and Inactivation Processes of the hERG Channel. *Journal of General Physiology*. 2004 nov; 124(6):703–718. <https://doi.org/10.1085/jgp.200409119>, doi: 10.1085/jgp.200409119.
- Zhang Y**, Qin W, Lu X, Xu J, Huang H, Bai H, Li S, Lin S. Programmable base editing of zebrafish genome using a modified CRISPR-Cas9 system. *Nature Communications*. 2017; 8(1):6–10. <https://doi.org/10.1038/s41467-017-00175-6>, doi: 10.1038/s41467-017-00175-6.
- Zhao Y**, Shang D, Ying R, Cheng H, Zhou R. An optimized base editor with efficient C-to-T base editing in zebrafish. *BMC Biology*. 2020; 18(1):190. <https://doi.org/10.1186/s12915-020-00923-z>, doi: 10.1186/s12915-020-00923-z.
- Zilova L**, Weinhardt V, Tavhelidse T, Schlagheck C, Thumberger T, Wittbrodt J. Fish primary embryonic pluripotent cells assemble into retinal tissue mirroring in vivo early eye development. *eLife*. 2021; 10:1–26. <https://doi.org/10.7554/elife.66998>, doi: 10.7554/elife.66998.

Publications

Cornean A*, Gierten J*, Welz B*, Mateo JL, Thumberger T, Wittbrodt. 2022. Precise in vivo functional analysis of DNA variants with base editing using ACEofBASEs target prediction. *Elife* 11:e72124. doi:10.7554/eLife.72124

Thumberger T*, Tavhelidse-Suck T*, Gutierrez-Triana JA*, **Cornean A**, Medert R, Welz B, Freichel M, Wittbrodt J. 2022. Boosting targeted genome editing using the hei-tag. *Elife* 11:e70558. doi:10.7554/eLife.70558

* joint first authorship

Acknowledgments

First, I want to thank you **Jochen** for supporting me along this long journey. I believe it started almost 7 years ago, when you agreed to take me in for an internship, even before I started the Master's program in Heidelberg, when I was still green behind the ears. You always knew which kind of support I needed, encouraging me to explore and learn freely but also being a great source of inspiration and motivation when times were dire. I thank you for challenging me, being a great mentor, scientist and foremost, a great human being. I am grateful for all the opportunities you enabled. It was a pleasure.

I would also like to thank you **Jun.-Prof. Dr. Steffen Lemke**, for having accompanied me throughout my time in Heidelberg. You were a fantastic second supervisor and I am ever grateful for your time, enthusiasm and support.

I would like to thank the members of my Thesis Advisory Committee **Jun.-Prof. Dr. Steffen Lemke, Prof. Dr. Sabine Strahl** and **Prof. Dr. Irmgard Sinning**. I am grateful for you being part of my TAC meetings and all the input you provided.

I am very grateful for the fantastic support on organisational matters in the lab by **Frederike Seibold, Ute Volbehrr, Kevin Verweyen**. Also, I would like to thank **Beate Wittbrodt** for all her help and advice on fish related issues. I am also grateful for the support by the Fish team, **Sven Erny, Erik Leist, Marzena Majewski** and **Antonino Saraceno**.

Lena Appel, Tanja Kellner, Natalia Sokolova, Tinatini Tavheliidse-Suck, Venera Weinhardt, Jørgen Benjaminsen, Omar Hammouda I am very happy and grateful for your fantastic and very helpful feedback on my thesis.

Thank you to my co-authors **Jakob Gierten, Bettina Welz, Juan Mateo** and **Thomas Thumberger** for the collaboration on the base editing project. I was a great learning experience and I am glad we managed to conclude the project together. Thank you **Prof. Dr. Sabine Strahl** and

Daniel Sturm for the collaboration on the *pomt2* mutants. I hope we can bring this project to paper before I leave.

Thank you **Tanja Kellner**, for being a constant source of stability and support over the past 6 years, ever since joined Bay 2. I was a pleasure to have worked next to you.

Thank you **Nithyapriya Kumar** for the great support and collaboration during the last four months. I am very grateful to have worked alongside such a great and hard-working scientist. I would also like to thank all the students I had the privilege to work with, **Oi Pui Hoang, Svenja Kling, Celine Roelse, Linda Kloß** and **Nick Marschlich**.

Over the past years the 5th floor has become something like a second home for me. I am grateful for all the people that were part of this experience past and present, from COS parties, defense parties, coffee breaks, retreats or intense scientific discussions. Especially, I would like to thank **Leonie Adelmann, Clara Becker, Jørgen Benjaminsen, Jakob Gierten, Ann-Kathrin Heilig, Nithyapriya Kumar, Colin Lischik, Christina Schlagheck, Risa Suzuki, Tinatini Tavhelidse-Suck, Thomas Thumberger, Erika Tsingos, Philip Watson, Venera Weinhardt** and **Lucie Zilova** and as well as all members of the Centanin, Lemke and Wittbrodt labs for the awesome working environment and stimulating discussions.

Omar and **Colin**, I thank you for all the fun we had together in the lab and now, ever more, outside the lab. Thank you for being supportive friends and fantastic scientist, always keen to help out. I am sure we will continue our board game events and many others and I am very much looking forward to spending more time with you as well as **Shaymaa** and **Miri** and your F1 Rayaan Marlene.

I would like to thank my dear friends **Luke and Katy** for being such an important part of my life, despite the distance. Thank you **Luke** for always being there. I am very much looking forward to what's coming next with you guys, **Luke, Joe** and **Freddy!**

Lena, ich bin sehr froh, dass du mich in den vergangenen 4 Jahren über die Höhen und Tiefen meiner Promotion begleitet hast. Unsere Mini-Urlaube an den Wochenenden waren die Oasen nach denen ich mich oft gesehnt habe. Ich danke dir für deine Unterstützung und dein Verständnis während des langen Endspurts und freue mich schon auf all das was noch auf uns zukommt.

Zu guter Letzt möchte ich meiner ganzen Familie, Mama, Papa, Bia, Oma, Buni, Darya Luki, von ganzem Herzen danken. Ich danke euch für eure Unterstützung und eure uneingeschränkte Liebe. Oma, von dir habe ich gelernt wie wichtig es ist jede Möglichkeit etwas neues zu Lernen zu ergreifen. Auch wenn du nicht zum Anlass meiner Verteidigung mit mir feiern kannst, du bist und wirst für immer bei mir sein.

Declaration

Herewith I declare that I prepared the PhD thesis "The role of the medaka protein O-mannosyltransferase 2 across tissues, development and dystroglycanopathies" on my own and with no other sources and aids than quoted.

Heidelberg, 2022

List of Figures

1.1	Principle of protein <i>O</i> -mannosylation by the POMT1-POMT2 complex in vertebrates.	4
1.2	The role of <i>O</i> -mannosylation for the function of α -dystroglycan (α -DG) and the dystrophin-glycoprotein complex (DGC).	7
1.3	Overview of the symptoms in dystroglycanopathies.	9
1.4	CRISPR/Cas9-mediated generation of loss-of-function alleles.	14
1.5	The principle of base editing is exemplified by the target C-to-T conversion through cytosine base editors.	16
2.1	Somatic cytosine and adenine base editing at the <i>oca2</i> locus allows for direct functional assessment.	22
2.2	Somatic cytosine and adenine base editing at the <i>oca2</i> locus is highly efficient.	25
2.3	ABE8e efficiently introduces a function-altering C71R missense mutation in F0.	28
2.4	Introducing a PTC in <i>tnnt2a</i> gene accurately recreates complex mutant phenotypes in F0.	31
2.5	<i>In vivo</i> cytosine and adenine base editing modelling of the ERG channel gene <i>kcnh6a</i> reveals that p.R512G completely abolishes the protein's function.	33
2.6	Expression of the substrates of the POMT1-POMT2 complex across stages and tissues.	36
2.7	Overview of <i>pomt1</i> and <i>pomt2</i> mutant medaka alleles generated in this thesis.	39
2.8	The <i>pomt2</i> knockout by knockin strategy used to generate N-terminal mutant alleles results in <i>pomt2</i> ^{S56(<i>ins</i>)} allele with mild postembryonic phenotypes.	42
2.9	MZT <i>pomt2</i> ^{S56(<i>ins</i>)} mutants display severe developmental defects.	43
2.10	Normal retinal architecture in zygotic <i>pomt2</i> ^{S56(<i>ins</i>)} mutants is accompanied by changes in splicing.	46
2.11	Splice-donor editants of <i>pomt2</i> recapitulate moderate embryonic, CMD-like phenotypes	48
2.12	A 3'UTR deletion strategy leads to the isolation of the severe <i>pomt2</i> ^{Cterm-<i>fs</i>} allele.	50

2.13	Reduced levels of <i>pomt1/pomt2</i> transcript and POMT1/POMT2 protein in stage 34 <i>pomt2^{Cterm-fs}</i> mutants.	52
2.14	Time course of <i>pomt2^{Cterm-fs}</i> mutant embryonic development.	54
2.15	<i>Pomt2^{Cterm-fs}</i> mutants display inter-hemispheric fissure defects in the forebrain at stage 22.	55
2.16	Striking forebrain and midbrain defects of stage 24 <i>pomt2^{Cterm-fs}</i> mutants are accompanied by increased levels of apoptosis in the brain and the retina.	57
2.17	Striking brain and eye defects in stage 28 <i>pomt2^{Cterm-fs}</i> mutants are a consequence of widespread cell death.	59
2.18	A transcriptome of <i>pomt2^{Cterm-fs}</i> mutant development.	60
2.19	A simple locomotion assay can determine the swimming behaviour of freely swimming medaka larvae.	64
2.20	Larval movement across post-embryonic stages in wild-type medaka.	65
2.21	Larval movement across post-embryonic stages in <i>pomt1^{Y33(ins)}</i> and <i>pomt2^{S56(ins)}</i> mutants shows no quantifiable changes.	67
2.22	Reducing maternal <i>pomt2</i> transcript results in a low frequency of DGpathy phenotypes.	68
2.23	Zygotic aspartate 92 of the POMT2 acidic DE motif is dispensable for muscular and retinal function in post-embryonic medaka larvae.	71
2.24	Expression of the substrates of the POMT1/2 complex across stages and tissues.	74
2.25	Conservation of <i>O</i> -mannosylation sites and concept of <i>O</i> -man site base editing.	76
2.26	Conservation of <i>O</i> -mannosylation sites.	78
2.27	Synthetic crRNAs achieve higher base editing efficiencies of the <i>oca2</i> gene as indicated by the loss of eye pigment.	81
2.28	NG and SpRY CBEs can efficiently edit <i>oca2</i> NGN PAM as indicated by the loss of eye pigmentation.	82
2.29	SpRY base editor variants can efficiently edit <i>oca2</i> NAN PAM sites as indicated by the loss of eye pigmentation.	84
2.30	SpRY base editor variants can efficiently edit <i>oca2</i> NCN and NTN PAM sites using synthetic crRNAs.	85
2.31	SpRY cytosine base editor variants are versatile tools that allow PAM-decoupled base editing of <i>tbxta</i> NAN, NCN and NTN PAM sites.	87

2.32	Medaka <i>dag1</i> crispants reveal DGpathy-like phenotypes in post-embryonic development.	89
2.33	Cytosine base editing of the <i>dag1</i> gene reveals the functional importance of a proline at position 333 in F0.	91
2.34	The loss of <i>dag1</i> function by CRISPR/Cas9-mediated NHEJ or ABE8e single amino acid change can be assayed with great precision in F0.	93
2.35	ancBE4max-SpRY mediates editing of a highly conserved T412 <i>O</i> -man site with a NAN PAM.	95
2.36	<i>dag1</i> ^{+/<i>T330M</i>} and <i>dag1</i> ^{+/<i>Q410X</i>} crossing schemes and genotyping in F2.	97
2.37	F2 analysis on the progressive effect of <i>dag1</i> p.T330M and a p.Q410X on larval locomotion.	99
2.38	<i>SUCO</i> crispants and editants show striking spinal abnormalities.	101
2.39	Low levels of unspecific developmental defects in <i>KIAA1549</i> editants and crispants indicate a dispensable role during early embryogenesis.	103
3.1	Differential POMT-complex activity requirements of organs affected in DGpathies.	111
3.2	Comprehensive overview of the functional roles of POMT substrates in DGpathy.	121

List of Tables

5.1	Fish lines used in this thesis.	129
5.2	Bacteria used in this thesis.	130
5.3	Plasmids used for mRNA synthesis in this thesis.	130
5.4	Plasmids used for sgRNA synthesis in this thesis.	131
5.5	Plasmids used for <i>in situ</i> probe synthesis in this thesis.	133
5.6	Miscellaneous plasmids used in this thesis.	133
5.7	Genotyping and Sanger sequencing primers used in this thesis.	134
5.8	Illumina sequencing primers used in this thesis.	136
5.9	Oligonucleotides for sgRNA cloning used in this thesis.	136
5.10	qRT-PCR primers used in this thesis.	138
5.11	RT-PCR primers used in this thesis.	139
5.12	Oligonucleotides for gRNA (Cas13d) donors used in this thesis.	139
5.13	Miscellaneous cloning primers used in this thesis.	140
5.14	sgRNAs used in this thesis.	141
5.15	crRNAs used in this thesis.	142
5.16	gRNAs (RfxCas13d) used in this thesis.	143
5.17	mRNAs used in this thesis.	143
5.18	Primary antibodies used in this thesis.	144
5.19	Secondary antibodies used in this thesis.	145
5.20	Antibiotics used in this thesis.	146
5.21	Kits used in this thesis.	146
5.22	Enzymes and buffers used in this thesis.	147
5.23	Chemicals and Reagents used in this thesis.	149
5.24	Molecular materials used in this thesis.	152
5.25	Consumables used in this thesis.	154
5.26	Solutions for fish rearing used in this thesis.	156
5.27	Solutions of general use used in this thesis.	156
5.28	Solutions for bacterial work used in this thesis.	157
5.29	Solutions for molecular biology work used in this thesis.	157
5.30	Solutions for <i>in situ</i> hybridisation used in this thesis.	158
5.31	Solutions for Western Blot used in this thesis.	159
5.32	Solutions for immunohistochemistry used in this thesis.	160
5.33	Equipment and instruments used in this thesis.	160

5.34 Consumables used in this thesis.	163
5.35 Linearisation and transcription of mRNA.	174